HELLENIC REPUBLIC
National and Kapodistrian University of Athens
EST. 1837

$BiVO_4$ inverse opal photonic catalysts

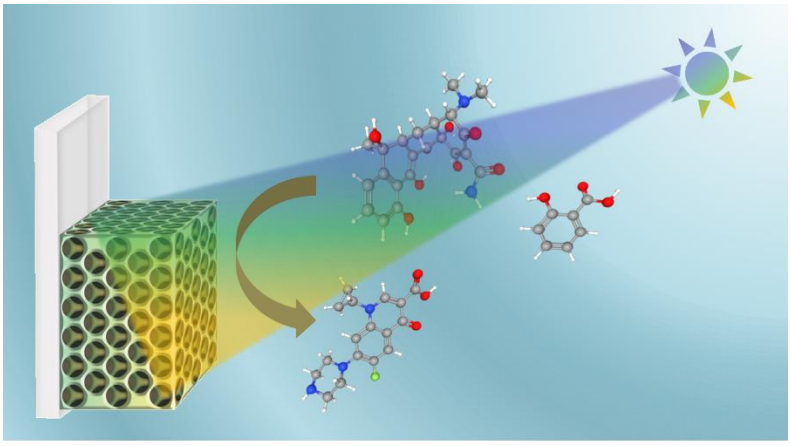

PYLARINOU MARTHA

PhD Thesis

Athens 2024

NATIONAL AND KAPODISTRIAN UNIVERSITY OF ATHENS

PHYSICS DEPARTMENT, SECTION OF CONDENSED MATTER PHYSICS

$BiVO_4$ inverse opal photonic catalysts

PhD Thesis

Pylarinou Martha

ADVISORY COMMITTEE
Likodimos Vlassios (supervisor)
Associate Professor
Physics Department NKUA
Spiros Gardelis
Associate Professor
Physics Department NKUA
Stefanou Nikolaos
Professor
Physics Department NKUA

EXAMINATION BOARD
Spiros Gardelis
Associate Professor
Physics Department NKUA
Kontos Athanassios
Professor
Department of Physics, NTUA
Likodimos Vlassios (supervisor)
Associate Professor
Physics Department NKUA
Papanikolaou Nikolaos
Research Director,
INN, NCSR "Demokritos"
Sakellis Elias
Assistant Professor
Physics Department NKUA
Sarlis Nikolaos
Professor
Physics Department NKUA
Stefanou Nikolaos
Professor
Physics Department NKUA

Athens 2024

ΕΘΝΙΚΟ ΚΑΙ ΚΑΠΟΔΙΣΤΡΙΑΚΟ ΠΑΝΕΠΙΣΤΗΜΙΟ ΑΘΗΝΩΝ

ΤΜΗΜΑ ΦΥΣΙΚΗΣ, ΤΟΜΕΑΣ ΦΥΣΙΚΗΣ ΣΥΜΠΥΚΝΩΜΕΝΗΣ ΥΛΗΣ

Φωτονικοί καταλύτες αντίστροφων οπαλίων $BiVO_4$

Διδακτορική Διατριβή

Πυλαρινού Μάρθα

ΤΡΙΜΕΛΗΣ ΣΥΜΒΟΥΛΕΥΤΙΚΗ ΕΠΙΤΡΟΠΗ

Λυκοδήμος Βλάσιος (Επιβλέπων)
Αναπληρωτής Καθηγητής Τμήματος Φυσικής ΕΚΠΑ
Γαρδέλης Σπυρίδων
Αναπληρωτής Καθηγητής Τμήματος Φυσικής ΕΚΠΑ
Στεφάνου Νικόλαος
Καθηγητής Τμήματος Φυσικής ΕΚΠΑ

ΕΠΤΑΜΕΛΗΣ ΕΞΕΤΑΣΤΙΚΗ ΕΠΙΤΡΟΠΗ

Γαρδέλης Σπυρίδων
Αναπληρωτής Καθηγητής Τμήματος Φυσικής ΕΚΠΑ
Κόντος Αθανάσιος
Καθηγητής Τμήματος Φυσικής Σ.Ε.Μ.Φ.Ε. ΕΜΠ
Λυκοδήμος Βλάσιος
Αναπληρωτής Καθηγητής, Τμήματος Φυσικής ΕΚΠΑ
Παπανικολάου Νικόλαος
Ερευνητής Α', Ινστιτούτου Νανοεπιστήμης και Νανοτεχνολογίας, ΕΚΕΦΕ «Δ»
Σακέλλης Ηλίας
Επίκουρος Καθηγητής Τμήματος Φυσικής ΕΚΠΑ
Σαρλής Νικόλαος
Καθηγητής Τμήματος Φυσικής ΕΚΠΑ
Στεφάνου Νικόλαος
Καθηγητής Τμήματος Φυσικής ΕΚΠΑ

Αθήνα 2024

Acknowledgments

First and foremost, I would like to express my gratitude to my supervisor Associate Professor Vlassis Likodimos for giving me the opportunity to work in this particular field of research, but also for his continuous guidance and support throughout my PhD study. I would also like to thank the rest of my advisory committee: Associate Professor Spiros Gardelis and Professor Nikolaos Stefanou, for their insightful comments. Further, I would like to thank the examination board for their suggestions, which improved the content of this Thesis.

I would also like to thank all those who helped in conducting the experiments, Assistant Professor Elias Sakellis and Dr. Nikolaos Boukos for the electron microscopy measurements, Dr. Athanasios Dimoulas and Dr. Polychronis Tsipas for the XPS-UPS measurements, Associate Professor Spiros Gardelis for the quantum efficiency and photoluminescence measurements, Dr. Thomas Stergiopoulos for photoluminescence measurements, Dr. Vassilis Psycharis for the X-ray diffraction measurements and Dr. Marios G. Kostakis for chromatography measurements.

The thesis was carried out in the framework of the program entitled "Advanced photocatalytic Slow Photon nanostructures"- SLOWPHOTON, which was funded by the Hellenic Foundation for Research and Innovation (EL.I.D.E.K.) in the context of "First Call for H.F.R.I. Research Projects for Support Members and Researchers and the procurement of high-cost research equipment grant" (Project Number: HFRI-FM17-543).

Finally, I would like to express my gratitude to my husband Giannis and my family for their continuous support and for being always there.

Abstract

Bismuth vanadate ($BiVO_4$) is an n-type semiconductor that has attracted significant research interest among transition metal oxides because of its high efficiency as a photoanode in the photoelectrochemical water splitting under visible light irradiation that is largely due to its indirect energy gap of size ~2.4 eV and the appropriate energy band potentials. Current research on $BiVO_4$ photocatalysts is focused on the development of nanostructured materials and the modification of their electronic properties through doping with metal ions and the formation of heterojunctions with plasmonic nanoparticles and other semiconducting nanomaterials that reduce the strong recombination of photoinduced carriers caused by the low electron mobility in $BiVO_4$. Photonic crystals have been established as unique periodic structures for controlling light propagation in materials. Their application in semiconductor photocatalysis has emerged as an advanced structural modification aimed at enhancing light harvesting from photocatalytic materials via "slow" photons. The design of photonic photocatalysts in the form of inverse opals attracts great research interest as it enables combining the morphological features of macroporous periodic structures to enhance the photoinduced process via slow photons with targeted synthetic modifications of the materials aimed at improved light harvesting and charge carrier separation that are key factors in photocatalytic applications.

The subject of this thesis was the development of $BiVO_4$ photonic crystals with controlled optical and electronic properties for photocatalytic applications in the visible range. $BiVO_4$ inverse opals of variable photonic band gap were fabricated by applying the method of successive deposition of colloidal polymer spheres of different diameters followed by infiltration of the colloidal matrix with an inorganic salt precursor solution and removal of the colloidal substrate to form the inverse structure. X-ray diffraction, Raman spectroscopy, scanning and transmission electron microscopy measurements as well as diffuse and specular reflectance optical spectroscopy showed the formation of well-ordered periodic reverse opal structures in the monoclinic $BiVO_4$ phase. Comparative evaluation of the films performance on the photocatalytic degradation of the standard aqueous pollutant salicylic acid as a function of the diameter of the inverse opals, allowed tuning of the photonic band gap in relation to the electronic absorption edge of $BiVO_4$ and the utilization of blue slow photons for improved collection of visible light and enhanced photocatalytic activity. Doping the optimal photonic $BiVO_4$ films with molybdenum and calcium impurities was performed to improve electron transport and charge separation. Systematic study of the composition, structural, optical and electronic properties of the fabricated Mo-$BiVO_4$ and Ca-$BiVO_4$ photonic films showed that these impurities enter the crystal lattice of $BiVO_4$ as Mo^{6+} and Ca^{2+} ions that replace V^{5+} and Bi^{3+} ions creating shallow donor levels and acceptors, respectively. These dopants caused weak effects on the monoclinic structure and energy gap of $BiVO_4$ but significant modifications in the donor concentration and the positions of the conduction and valence bands. These changes were exploited in the sequential deposition of Mo-$BiVO_4$/Ca-$BiVO_4$ photonic

films with the optimal dopant concentration determined from salicylic acid photocatalytic degradation experiments. The creation of multiple interfaces between Mo-$BiVO_4$ and Ca-$BiVO_4$ nanoparticles with different donor concentrations resulted in a wide distribution of type II n-n^+ homojunctions in the framework of Mo-$BiVO_4$/Ca-$BiVO_4$ photonic crystals, which led to the efficient photoelectrocatalytic decomposition of emerging pharmaceuticals pollutants, and in particular the broad-spectrum antibiotics tetracycline and ciprofloxacin as well as salicylic acid. This behavior was confirmed by photoelectrochemical measurements of current density as a function of potential and time in an aqueous electrolyte, where the Mo-$BiVO_4$/Ca-$BiVO_4$ homojunctions presented the best performance, while electrochemical impedance, Mott-Schottky and photoluminescence measurements showed a decrease of electron-hole recombination and an increase in the donor concentration that were combined with the photonic amplification due to slow light.

In addition, the surface modification of Mo-$BiVO_4$ inverse opals with plasmonic Ag and Au metallic nanoparticles was studied with the aim of increasing the photocatalytic efficiency that was evaluated in the photo(electro)catalytic degradation of ibuprofen and tetracycline antibiotics under a potential bias in the visible range. Surface modification of photonic crystals with Ag and Au nanoparticles may cause sensitization of the semiconductors to the visible range and enhance light absorption through the excitation of localized surface plasmon resonances, which can lead to the injection of high-energy electrons into the semiconductor combined with further enhancement due to slow photons and/or better charge separation. Evaluation of the photonic films in photoelectrochemical water splitting showed a significant contribution from local field enhancement, particularly for Ag/Mo-$BiVO_4$ photonic films due to the spectral overlap of the plasmonic with the electronic absorption and the blue slow photons (high-energy edge) of the Mo-$BiVO_4$ photonic films, in contrast to the weak plasmonic sensitization effect of the photonic films modified with Au. The variation of energy bands in the metal-semiconductor heterojunctions due to the different work functions of Ag and Au nanoparticles in relation to Mo-$BiVO_4$, led to differences in interfacial electron transfer, resulting in higher photoelectrocatalytic degradation of tetracycline and ibuprofen by Ag/Mo-$BiVO_4$ and (Ag, Au)/Mo-$BiVO_4$ films, respectively. Moreover, the formation of a bilayer heterojunction TiO_2/Mo-$BiVO_4$ was studied using the most efficient Mo-$BiVO_4$ photonic films as a substrate combined with a mesoporous titania coating. The bilayer films showed significantly improved performance in the photoelectrocatalytic degradation of ibuprofen compared to the additive performance of their components, which is related to the enhanced light harvesting through backscattering from the mesoporous TiO_2 layer combined with the photoinduced charge transfer at the interface between TiO_2 and Mo-$BiVO_4$, promoting charge separation and photocatalytic activity.

Εκτεταμένη Περίληψη

Το βαναδικό βισμούθιο ($BiVO_4$) είναι ημιαγωγός τύπου-n που έχει προσελκύσει σημαντικό ερευνητικό ενδιαφέρον μεταξύ των οξειδίων των μετάλλων μετάπτωσης λόγω της υψηλής του απόδοσης ως φωτοάνοδος για τη φωτοηλεκτροχημική διάσπαση του νερού υπό ακτινοβόληση στο ορατό που οφείλεται σε μεγάλο βαθμό στο έμμεσο ενεργειακό του χάσμα μεγέθους ~2.4 eV και τα κατάλληλα δυναμικά ενεργειακών ζωνών. Η σύγχρονη έρευνα των φωτοκαταλυτών $BiVO_4$ εστιάζεται στην ανάπτυξη νανοδομημένων υλικών και την τροποποίηση των ηλεκτρονικών τους ιδιοτήτων μέσω νόθευσης με μεταλλικά ιόντα και του σχηματισμού ετεροεπαφών με πλασμονικά νανοσωματίδια και άλλα ημιαγώγιμα νανοϋλικά που περιορίζουν την ισχυρή επανασύνδεση φωτοεπαγόμενων φορέων λόγω της μικρής ευκινησίας ηλεκτρονίων στο $BiVO_4$. Οι φωτονικοί κρύσταλλοι έχουν καθιερωθεί ως πρότυπες περιοδικές δομές ελέγχου της διάδοσης του φωτός στα υλικά. Η εφαρμογή τους στη φωτοκατάλυση ημιαγωγών έχει αναδειχθεί σε μια προηγμένη δομική τροποποίηση που στοχεύει στην ενίσχυση της συλλογής φωτός από φωτοκαταλυτικά υλικά μέσω "αργών" φωτονίων. Ο σχεδιασμός φωτονικών φωτοκαταλυτών με τη μορφή αντίστροφων οπαλίων προσελκύει μεγάλο ερευνητικό ενδιαφέρον καθώς δίνει τη δυνατότητα να συνδυαστούν τα μορφολογικά χαρακτηριστικά μακροπορωδών περιοδικών δομών για την ενίσχυση της φωτοεπαγόμενης διεργασίας μέσω αργών φωτονίων με στοχευμένες συνθετικές τροποποιήσεις των υλικών με στόχο την αποδοτική συλλογή φωτός και τον αποτελεσματικό διαχωρισμό φορέων που αποτελούν καθοριστικούς παράγοντες σε φωτοκαταλυτικές εφαρμογές.

Αντικείμενο της παρούσας διατριβής ήταν η ανάπτυξη φωτονικών κρυστάλλων $BiVO_4$ με ελεγχόμενες οπτικές και ηλεκτρονικές ιδιότητες για φωτοκαταλυτικές εφαρμογές στο ορατό. Κατασκευάσθηκαν αντίστροφα οπάλια $BiVO_4$ μεταβλητού φωτονικού χάσματος εφαρμόζοντας τη μέθοδο διαδοχικής εναπόθεσης κολλοειδών πολυμερικών σφαιρών διαφορετικών διαμέτρων ακολουθούμενη από την πλήρωση της κολλοειδούς μήτρας με πρόδρομο διάλυμα ανόργανων αλάτων και την απομάκρυνση του κολλοειδούς υποστρώματος για τον σχηματισμό της αντίστροφης δομής. Μετρήσεις περίθλασης ακτίνων-Χ, φασματοσκοπίας Raman, ηλεκτρονικής μικροσκοπίας σάρωσης και διέλευσης καθώς και οπτική φασματοσκοπία διάχυτης και κατοπτρικής ανακλαστικότητας έδειξαν τον σχηματισμό καλά οργανωμένων περιοδικών δομών αντίστροφων οπαλίων στη μονοκλινή φάση $BiVO_4$. Συγκριτική αξιολόγηση της απόδοσης των υμενίων στη φωτοκαταλυτική διάσπαση του πρότυπου υδατικού ρύπου σαλικυλικού οξέος συναρτήσει της διαμέτρου των αντίστροφων οπαλίων, επέτρεψε τη ρύθμιση του φωτονικού χάσματος σε σχέση με την ακμή ηλεκτρονικής απορρόφησης του $BiVO_4$ και την αξιοποίηση κυανών αργών φωτονίων για την καλύτερη συλλογή ορατού φωτός και ενισχυμένη φωτοκαταλυτική δράση. Για τη βελτίωση της μεταφοράς ηλεκτρονίων και του διαχωρισμού φορτίου πραγματοποιήθηκε εμπλουτισμός των βέλτιστων φωτονικών υμενίων $BiVO_4$ με προσμίξεις μολυβδαινίου και ασβεστίου. Συστηματική μελέτη της σύστασης, των δομικών, οπτικών και ηλεκτρονικών ιδιοτήτων των νοθευμένων φωτονικών υμενίων Mo-$BiVO_4$ και Ca-$BiVO_4$ έδειξαν ότι οι προσμίξεις αυτές υπεισέρχονται στο

κρυσταλλικό πλέγμα του $BiVO_4$ ως ιόντα Mo^{6+} και Ca^{2+} που αντικαθιστούν τα ιόντα V^{5+} και Bi^{3+} δημιουργώντας ρηχές στάθμες δοτών και αποδεκτών, αντίστοιχα, με μικρή επίδραση στη μονοκλινή δομή και το ενεργειακό χάσμα του $BiVO_4$ αλλά σημαντική μεταβολή της συγκέντρωσης δοτών και μετατοπίσεις των ζωνών αγωγιμότητας και σθένους. Οι μεταβολές αυτές αξιοποιήθηκαν στη διαδοχική εναπόθεση φωτονικών υμενίων Mo-$BiVO_4$/Ca-$BiVO_4$ με τη βέλτιστη συγκέντρωση προσμίξεων που προσδιορίστηκε από πειράματα φωτοκαταλυτικής απεικοδόμησης σαλικυλικού οξέος. Η δημιουργία πλήθους διεπιφανειών μεταξύ νανοσωματιδίων Mo-$BiVO_4$ και Ca-$BiVO_4$ με διαφορετικές συγκεντρώσεις δοτών οδήγησε σε μια ευρεία κατανομή ομοεπαφών n-n^+ τύπου II στον σκελετό των φωτονικών κρυστάλλων Mo-$BiVO_4$/Ca-$BiVO_4$, η οποία οδήγησε την αποδοτική φωτοηλεκτροκαταλυτική διάσπαση αναδυόμενων φαρμακευτικών ρύπων, και ειδικότερα των αντιβιοτικών ευρέως φάσματος τετρακυκλίνη και σιπροφλοξασίνη καθώς και του σαλικυλικού οξέος. Η συμπεριφορά αυτή επιβεβαιώθηκε με φωτοηλεκτροχημικές μετρήσεις πυκνότητας ρεύματος συναρτήσει του δυναμικού και του χρόνου σε υδατικό ηλεκτρολύτη όπου οι ομοεπαφές Mo-$BiVO_4$/Ca-$BiVO_4$ παρουσίασαν την βέλτιστη απόδοση, ενώ μετρήσεις ηλεκτροχημικής εμπέδησης, Mott-Schottky και φωτοφωταύγειας έδειξαν μείωση της επανασύνδεσης ηλεκτρονίων-οπών και αύξηση της συγκέντρωσης δοτών που συνδυάζονται με τη φωτονική ενίσχυση λόγω αργού φωτός.

Επίσης, μελετήθηκε η επιφανειακή τροποποίηση των αντίστροφων οπαλίων Mo-$BiVO_4$ με πλασμονικά μεταλλικά νανοσωματίδια Ag και Au με στόχο την αύξηση της φωτοκαταλυτικής απόδοσης που αξιολογήθηκε στη φωτο(ηλεκτρο)καταλυτική διάσπαση των αντιβιοτικών ιβουπροφένη και τετρακυκλίνη υπό την επίδραση δυναμικού στο ορατό. Η επιφανειακή τροποποίηση των φωτονικών κρυστάλλων με νανοσωματίδια Ag και Au μπορεί να προκαλέσει ευαισθητοποίηση των ημιαγωγών στο ορατό και την ενίσχυση της απορρόφησης φωτός μέσω της διέγερσης εντοπισμένων επιφανειακών πλασμονικών συντονισμών, η οποία μπορεί να οδηγήσει σε έγχυση ηλεκτρονίων υψηλής ενέργειας στον ημιαγωγό σε συνδυασμό με περαιτέρω ενίσχυση λόγω αργών φωτονίων ή/και καλύτερου διαχωρισμού φορτίου. Αξιολόγηση των φωτονικών υμενίων στη φωτοηλεκτροχημική στη διάσπαση του νερού έδειξε σημαντική συνεισφορά από την τοπική ενίσχυση πεδίου, ιδιαίτερα για τα φωτονικά υμένια Ag/Mo-$BiVO_4$ λόγω της φασματικής επικάλυψης της πλασμονικής με την ηλεκτρονική απορρόφηση και τα κυανά αργά φωτόνια (ακμή υψηλής ενέργειας) των φωτονικών υμενίων Mo-$BiVO_4$, σε αντίθεση με την ασθενή πλασμονική ευαισθητοποίηση των φωτονικών υμενίων που τροποποιήθηκαν με Au. Η μεταβολή των ενεργειακών ζωνών στις ετεροεπαφές μετάλλου-ημιαγωγού λόγω των διαφορετικών έργων εξόδου των νανοσωματιδίων Ag και Au σε σχέση με το Mo-$BiVO_4$, οδήγησε σε διαφορές στη διεπιφανειακή μεταφορά ηλεκτρονίων που οδήγησαν στην υψηλότερη φωτοηλεκτροκαταλυτική αποικοδόμηση της τετρακυκλίνης και της ιβουπροφαίνης από τα υμένια Ag/Mo-$BiVO_4$ και (Ag,Au)/Mo-$BiVO_4$, αντίστοιχα. Επιπλέον, μελετήθηκε ο σχηματισμός διστρωματικής ετεροεπαφής TiO_2/Mo-$BiVO_4$ χρησιμοποιώντας τα αποδοτικότερα φωτονικά υμένια Mo-$BiVO_4$ ως υπόστρωμα σε συνδυασμό με μια επίστρωση μεσοπορώδους τιτανίας. Τα διστρωματικά υμένια έδειξαν σημαντικά βελτιωμένη απόδοση στη φωτοηλεκτροκαταλυτική διάσπαση της

ιβουπροφαίνης σε σύγκριση με την αθροιστική απόδοση των συστατικών τους, η οποία σχετίζεται με τη βελτιωμένη συλλογή φωτός μέσω οπισθοσκέδασης από το μεσοπορώδες στρώμα TiO_2 σε συνδυασμό με τη μεταφορά φωτοεπαγόμενων φορέων στη διεπιφάνεια της ετεροεπαφής μεταξύ TiO_2 και Mo-$BiVO_4$ που προάγει το διαχωρισμό φορτίου και τη φωτοκαταλυτική δράση.

Η παρούσα διατριβή αποτελείται από 5 κεφάλαια:

Στο **Κεφάλαιο 1** παρουσιάζονται συνοπτικά ο μηχανισμός της φωτοκατάλυσης ημιαγωγών, οι ιδιότητες του βαναδικού βισμουθίου καθώς και οι συνθετικές τροποποιήσεις του υλικού που έχουν μελετηθεί τα τελευταία χρόνια για την ενίσχυση της φωτοκαταλυτικής απόδοσης. Ειδικότερα, περιγράφεται η νόθευση του $BiVO_4$ με μεταλλικά ιόντα με στόχο τη βελτίωση της μεταφοράς και διαχωρισμού φορτίου καθώς και ο σχηματισμός ετεροεπαφών με νανοδομημένα υλικά με έμφαση στα πλασμονικά νανοσωματίδια και τους διαφορετικούς μηχανισμούς ενίσχυσης της φωτοκαταλυτικής διεργασίας μέσω της ενίσχυσης του τοπικού πεδίου και της μεταφοράς φορτίου ή/και ενέργειας στον ημιαγωγό. Επίσης, γίνεται σύντομη εισαγωγή στις ιδιότητες των φωτονικών κρυστάλλους και ιδιαίτερα στην αξιοποίηση των αργών φωτονίων στην ενίσχυση της φωτοκαταλυτικής διεργασίας καθώς και την εφαρμογή τους στην περίπτωση του $BiVO_4$.

Στο **Κεφάλαιο 2** περιγράφονται αναλυτικά οι μέθοδοι κατασκευής των φωτονικών κρυστάλλων αντίστροφου οπαλίου $BiVO_4$ με ελεγχόμενα φωτονικά χάσματα μέσω της αυτό-οργάνωσης μονοδιεσπαρμένων πολυμερικών σφαιρών από κολλοειδή εναιωρήματα (κάθετη και οριζόντια εναπόθεση), η μέθοδος πλήρωσης της κολλοειδούς μήτρας με σύνθετο πρόδρομο διάλυμα, η νόθευση με μεταλλικά ιόντα Mo και Ca, η επιφανειακή τροποποίηση με πλασμονικά νανοσωματίδια Ag και Au και η εναπόθεση διστρωματικών υμενίων TiO_2/Mo-$BiVO_4$. Επιπλέον, παρουσιάζονται οι πειραματικές διατάξεις και τεχνικές που χρησιμοποιήθηκαν στη μελέτη των δομικών, οπτικών και ηλεκτρονικών ιδιοτήτων των φωτονικών υμενίων και την αξιολόγηση της φωτοκαταλυτικής και φωτοηλεκτροχημικής τους δράσης.

Στο **Κεφάλαιο 3** μελετάται η τροποποίηση φωτονικών κρυστάλλων βαναδικού βισμουθίου μέσω νόθευσης με προσμίξεις μολυβδαινίου (Mo-$BiVO_4$) και ασβεστίου (Ca-$BiVO_4$) και ο σχηματισμός ομοεπαφών Mo-$BiVO_4$/Ca-$BiVO_4$ με στόχο τον συνδυασμό της φωτονικής ενίσχυσης με τη μείωση της επανασύνδεσης ηλεκτρονίων-οπών για τη βελτίωση της φωτοκαταλυτικής απόδοσης στην αποδόμηση φαρμακευτικών ρύπων. Για την κατασκευή μη-τροποποιημένων φωτονικών υμενίων $BiVO_4$ με τη δομή αντίστροφων οπαλίων εφαρμόσθηκε η μέθοδος κάθετης εναπόθεσης κολλοειδών εναιωρημάτων σφαιρών πολυστυρενίου διαφορετικών διαμέτρων για τη ρύθμιση του φωτονικού χάσματος σε συνδυασμό με πλήρωση της πολυμερικής μήτρας οπαλίου στην υγρή φάση με πρόδρομο διάλυμα ανόργανων αλάτων, $Bi(NO_3)_3$ και NH_4VO_3, και πύρωση. Συστηματική ανάλυση της μορφολογίας και σύστασης καθώς και των δομικών και οπτικών ιδιοτήτων των φωτονικών υμενίων με διαφορετικές πειραματικές τεχνικές έδειξε τον σχηματισμό περιοδικών δομών αντίστροφου οπαλίου στη μονοκλινή φάση $BiVO_4$ με ενεργειακό χάσμα 2.59 eV και μεταβλητό φωτονικό χάσμα στο ορατό. Συγκριτική αξιολόγηση της φωτοκαταλυτικής απόδοσης των αντίστροφων οπαλίων στην αποικοδόμηση του σαλικυλικού οξέος ως άχρωμου

υδατικού φαρμακευτικού ρύπου έδειξε επιλεκτική ενίσχυση της φωτοκαταλυτικής διεργασίας στην περίπτωση συντονισμού της φασματικής περιοχής αργού φωτός υψηλής ενέργειας (*κυανά αργά φωτόνια*) με την ηλεκτρονική απορρόφησης του $BiVO_4$, επιτρέποντας να προσδιοριστεί η βέλτιστη φωτονική δομή για τη συλλογή ορατού φωτός. Κατόπιν, πραγματοποιήθηκε νόθευση των βέλτιστων φωτονικών υμενίων $BiVO_4$ με προσμίξεις Mo και Ca αντικαθιστώντας μέρος των ανόργανων αλάτων του πρόδρομου διαλύματος πλήρωσης με κατάλληλα άλατα που περιείχαν μολυβδαίνιο και ασβέστιο σε διαφορετικές συγκεντρώσεις. Συστηματική μελέτη των τροποποιημένων αντίστροφων οπαλίων $BiVO_4$ με περίθλαση ακτίνων-Χ, ηλεκτρονική μικροσκοπία διέλευσης σε συνδυασμό με στοιχειακή ανάλυση EDX, φασματοσκοπίες Raman, απορρόφησης υπερύθρου FT-IR καθώς και φωτοηλεκτρονίων ακτινών-Χ έδειξαν την εισαγωγή ιόντων Mo^{6+} και Ca^{2+} τα οποία αντικαθιστούν τα ιόντα V^{5+} και Bi^{3+} στο κρυσταλλικό πλέγμα του $BiVO_4$ που διατηρεί τη μονοκλινή δομή σχηλίτη με μικρή διαταραχή. Οι βέλτιστες συγκεντρώσεις νόθευσης Mo^{6+} και Ca^{2+}, οι οποίες προσδιορίστηκαν μέσω συγκριτικής αξιολόγησης στη φωτοκαταλυτική αποικοδόμηση του σαλικυλικού οξέος υπό ορατή ακτινοβολία, χρησιμοποιήθηκαν για την ταυτόχρονη νόθευση του βαναδικού βισμουθίου (Mo,Ca)-$BiVO_4$ καθώς και την εναπόθεση ομοεπαφών Mo-$BiVO_4$/Ca-$BiVO_4$. Επιπλέον, φωτοηλεκτρονιακή φασματοσκοπία υπεριώδους και οπτικές μετρήσεις έδειξαν τη δημιουργία ρηχών ενεργειακών σταθμών δοτών και αποδεκτών στα φωτονικά υμένια Mo-$BiVO_4$ και Ca-$BiVO_4$, αντίστοιχα, και μετατοπίσεις των ζωνών αγωγιμότητας και σθένους με μικρή μείωση του ενεργειακού χάσματος του $BiVO_4$. Μετρήσεις ηλεκτροχημικής εμπέδησης σε συνδυασμό με ανάλυση Mott-Schottky και φωτοφωταύγεια έδειξαν μείωση της επανασύνδεσης ηλεκτρονίων-οπών ιδιαίτερα στις ομοεπαφές Mo-$BiVO_4$/Ca-$BiVO_4$ και σημαντική μεταβολή της συγκέντρωσης δοτών μετά τη νόθευση με ετεροάτομα Mo και Ca. Συγκριτική αξιολόγηση των φωτονικών υμενίων Mo-$BiVO_4$, Ca-$BiVO_4$, (Mo,Ca)-$BiVO_4$ και Mo-$BiVO_4$/Ca-$BiVO_4$ στη φωτοηλεκτροκαταλυτική διάσπαση αναδυόμενων φαρμακευτικών ρύπων, και ειδικότερα των αντιβιοτικών ευρέως φάσματος τετρακυκλίνη και σιπροφλοξασίνη καθώς και του σαλικυλικού οξέος αλλά και την παραγωγή φωτορεύματος σε υδατικό ηλεκτρολύτη έδειξαν ότι τα φωτονικά υμένια ομοεπαφών παρουσιάζουν την υψηλότερη απόδοση. Η ενίσχυση αυτή αποδόθηκε στη δημιουργία διεπιφανειών μεταξύ νανοσωματιδίων Mo-$BiVO_4$ και Ca-$BiVO_4$ που οδηγεί σε μια ευρεία κατανομή ομοεπαφών n-n^+ τύπου II στον σκελετό των φωτονικών κρυστάλλων λόγω των διαφορετικών συγκεντρώσεων δοτών, προάγοντας τον διαχωρισμό φορτίου σε συνέργεια με τη συνεισφορά αργών φωτονίων στη συλλογή φωτός.

Στο **Κεφάλαιο 4** παρουσιάζεται η επιφανειακή τροποποίηση των βέλτιστων φωτονικών υμενίων Mo-$BiVO_4$ με πλασμονικά νανοσωματίδια Ag και Au με στόχο την ενίσχυση της φωτο(ηλεκτρο)καταλυτικής αποικοδόμησης των αντιβιοτικών ιβουπροφένη και τετρακυκλίνη στο ορατό. Για την τροποποίηση αυτή επιλέχθηκε το Mo-$BiVO_4$ του οποίου το έργο εξόδου βρίσκεται μεταξύ των αντίστοιχων τιμών για τα μεταλλικά νανοσωματίδια Ag και Au με αποτέλεσμα τη δυνατότητα διερεύνησης διαφορετικών μηχανισμών μεταφοράς φορτίου στη διεπιφάνεια μετάλλου-ημιαγωγού για την ενίσχυση της φωτοκαταλυτικής δράσης. Σε αυτή την περίπτωση, η κατασκευή

φωτονικών υμενίων Mo-$BiVO_4$ αντίστροφου οπαλίου έγινε εφαρμόζοντας τη μέθοδο οριζόντιας εναπόθεσης σε αγώγιμο γυαλί που στηρίζεται στην αυτό-οργάνωση των πολυμερικών σφαιρών σε περιοδικές δομές πυκνής διάταξης *fcc* σε οριζόντιο υπόστρωμα απαιτώντας μικρότερες ποσότητες κολλοειδών εναιωρημάτων, οι οποίες στη συνέχεια πληρώνονται με το πρόδρομο διάλυμα Mo-$BiVO_4$ και απομακρύνονται μέσω πύρωσης. Κατασκευάστηκαν φωτονικά υμένια που τροποποιήθηκαν επιφανειακά με την έγχυση υδατικού εναιωρήματος νανοσωματιδίων Ag και Au με χαρακτηριστικές κορυφές εντοπισμένου επιφανειακού πλασμονικού συντονισμού στα 406 και 520 nm, αντίστοιχα. Συγκριτική δομική ανάλυση των φωτοηλεκτροδίων Ag/Mo-$BiVO_4$, Au/Mo-$BiVO_4$ και Ag-Au/Mo-$BiVO_4$ με ηλεκτρονική μικροσκοπία διέλευσης σε συνδυασμό με στοιχειακή ανάλυση EDX, περίθλαση ακτίνων-Χ και φασματοσκοπίες Raman και φωτοηλεκτρονίων ακτινών-Χ έδειξε ομοιόμορφη κατανομή των μεταλλικών νανοσωματιδίων στα τοιχώματα των φωτονικών κρυστάλλων, ενώ φασματοσκοπία διάχυτης ανάκλασης υπεριώδους-ορατού έδειξε σημαντική μείωση της ανακλαστικότητας λόγω της πλασμονικής απορρόφησης. Φωτοηλεκτροχημικές μετρήσεις πυκνότητας ρεύματος-τάσης (J-V), εξωτερικής κβαντικής απόδοσης (Incident Photon-to-Current Efficiency-IPCE), ηλεκτροχημικής εμπέδησης και ανάλυσης Mott-Schottky σε συνδυασμό με φωτοφωταύγεια έδειξαν ενισχυμένη συλλογή ορατού φωτός και βελτίωση του διαχωρισμού φορτίου. Ειδικότερα, αξιολόγηση των φωτονικών υμενίων στην παραγωγή φωτορεύματος κατά τη φωτοηλεκτροχημική διάσπαση του νερού έδειξε σημαντική συνεισφορά από την εντοπισμό του τοπικού πεδίου, ιδιαίτερα στα φωτονικά υμένια Ag/Mo-$BiVO_4$ λόγω της φασματικής επικάλυψης της πλασμονικής με την ηλεκτρονική απορρόφηση και τα κυανά αργά φωτόνια (ακμή υψηλής ενέργειας) των φωτονικών υμενίων Mo-$BiVO_4$, σε αντίθεση με την ασθενή πλασμονική ευαισθητοποίηση (έγχυση ηλεκτρονίων υψηλής ενέργειας) στα φωτονικά υμένια Au/Mo-$BiVO_4$. Τα υμένια Ag/Mo-$BiVO_4$ και Ag-Au/Mo-$BiVO_4$ παρουσίασαν τις υψηλότερες αποδόσεις στη φωτοαποικοδόμηση της τετρακυκλίνης και της ιβουπροφένης, αντίστοιχα, υπό ακτινοβόληση στο ορατό σε δυναμικό +1.0 vs Ag/AgCl. Η διαφορά αυτή αποδόθηκε στις αντίστοιχες μετατοπίσεις των ενεργειακών ζωνών των επιφανειακά τροποποιημένων φωτονικών υμενίων που προκύπτουν από τη μεταβολή της ευθυγράμμισης των ενεργειών Fermi στην ετεροπαφή μετάλλου-ημιαγωγού λόγω των διαφορετικών έργων εξόδου των νανοσωματιδίων Ag και Au σε σχέση με το Mo-$BiVO_4$, που μεταβάλει τη διεπιφανειακή μεταφορά ηλεκτρονίων, σε συμφωνία με τα αποτελέσματα πειραμάτων παγίδευσης των δραστικών ειδών ριζών υπεροξειδίου ($^{\bullet}O_2^-$) και υδροξυλίου ($^{\bullet}OH$) καθώς και φωτοεπαγόμενων οπών (h^+). Διαπιστώνεται ότι οι σχετικές θέσεις ενεργειακών ζωνών και η ρύθμιση του φωτονικού χάσματος είναι καθοριστικοί παράγοντες στον σχεδιασμό αποδοτικών πλασμονικών-φωτονικών φωτοηλεκτροκαταλυτών με βάση ετεροεπαφές φωτονικών κρυστάλλων ημιαγωγών, ενεργών στο ορατό, και πλασμονικών νανοσωματιδίων.

Στο **Κεφάλαιο 5** μελετώνται ετεροδομημένα διστρωματικά υμένια TiO_2/Mo-$BiVO_4$ με στόχο την ενίσχυση της συλλογής φωτός και της φωτοκαταλυτικής δράσης στο ορατό και το υπεριώδες. Τα υμένια κατασκευάσθηκαν με την οριζόντια εναπόθεση του βέλτιστου αντίστροφου οπαλίου Mo-$BiVO_4$ ως φωτονικό υπόστρωμα το οποίο

εμφανίζει ισχυρή εγγενή απορρόφηση σε λ<490 nm και βελτιωμένη μεταφορά φορτίου λόγω νόθευσης με Mo. Περιστροφική εναπόθεση ενός μεσοπορώδους στρώματος νανοκρυσταλλικής τιτανίας Aeroxide P25 που παρουσιάζει υψηλή φωτοκαταλυτική απόδοση στο εγγύς υπεριώδες, οδήγησε σε μια πορώδη διστρωματική ετεροδομή P25/Mo-$BiVO_4$ που δημιουργήθηκε από την κατάρρευση της δομής αντίστροφου οπαλίου του υποστρώματος μετά τη δεύτερη θερμική ανόπτηση λόγω της ανάπτυξης των νανοκρυσταλλιτών $BiVO_4$. Οι μορφολογικές, δομικές και οπτικές ιδιότητες των υμενίων μελετήθηκαν με ηλεκτρονική μικροσκοπία σε συνδυασμό με στοιχειακή ανάλυση EDX, φασματοσκοπίες Raman, διάχυτης και κατοπτρικής ανάκλασης και φωτοηλεκτροχημικές μετρήσεις πυκνότητας ρεύματος-τάσης (J-V), εξωτερικής κβαντικής απόδοσης (IPCE) ηλεκτροχημικής εμπέδησης και ανάλυσης Mott-Schottky, ενώ συγκριτική αξιολόγηση της φωτοκαταλυτικής δράσης των μονο- και δι-στρωματικών υμενίων πραγματοποιήθηκε στη φωτοηλεκτροκαταλυτική αποικοδόμηση του μη στεροειδούς αντιφλεγμονώδους φαρμάκου ιβουπροφένης υπό την επίδραση δυναμικού στο ορατό και το υπεριώδες. Τα διστρωματικά υμένια έδειξαν σημαντικά βελτιωμένη απόδοση στη φωτοηλεκτροκαταλυτική διάσπαση της ιβουπροφαίνης σε σύγκριση με την αθροιστική απόδοση των συστατικών τους, η οποία σχετίζεται με τη βελτιωμένη συλλογή φωτός μέσω οπισθοσκέδασης από το μεσοπορώδες στρώμα TiO_2 σε συνδυασμό με τη μεταφορά φωτοεπαγόμενων φορέων στη διεπιφάνεια της ετεροεπαφής μεταξύ TiO_2 και Mo-$BiVO_4$ που προάγει τον διαχωρισμό φορτίου και τη φωτοκαταλυτική δράση.

List of Publications

Papers in Peer-Reviewed Journals

G. V. Theodorakopoulos, **M. Pylarinou**, E. Sakellis, F. K Katsaros, V. Likodimos, G. Em Romanos, *Mo-$BiVO_4$ Photocatalytically modified ceramic ultrafiltration membranes for enhanced water treatment efficiency*, Membranes **14**(5), 112 (2024).

M. Pylarinou, E. Sakellis, P. Tsipas, S. Gardelis, V. Psycharis, A. Dimoulas, T. Stergiopoulos, V. Likodimos, *Light concentration and electron transfer in plasmonic–photonic Ag,Au modified Mo-$BiVO_4$ inverse opal photoelectrocatalysts*, Nanoscale **16**, 10366-10376 (2024).

M. Pylarinou, E. Sakellis, P. Tsipas, G. Em. Romanos, S. Gardelis, A. Dimoulas, V. Likodimos, *Mo-$BiVO_4$/Ca-$BiVO_4$ Homojunction nanostructure-based inverse opals for photoelectrocatalytic pharmaceutical degradation under visible light*, ACS Applied Nano Materials **6**, 6759–6771 (2023).

M. Pylarinou, A. Toumazatou, E. Sakellis, E. Xenogiannopoulou, S. Gardelis, N. Boukos, A. Dimoulas, V. Likodimos, *Visible light trapping against charge recombination in* FeO_x-TiO_2 *photonic crystal photocatalysts*, Materials **14** (23), 7117 (2021). *Editor's Choice.*

Presentations in Conferences

M. Pylarinou, E. Sakellis, S. Gardelis, V. Likodimos, *Bilayer TiO_2/Mo-$BiVO_4$ photocatalytic films for enhanced light harvesting and charge separation*, 10th International Conference on Micro-Nanoelectronics, Nanotechnology and MEMS, Micro Nano 2023, 2-5 November 2023, Athens, Greece, Book of Abstracts pp. 209-210 (poster).

M. Pylarinou, E. Sakellis, P. Tsipas, S. Gardelis, V. Likodimos, *Homojunction metal (Mo, Ca)-doped $BiVO_4$ photonic crystal photocatalysts*, 11th European Conference on Solar Chemistry and Photocatalysis: Environmental Applications (SPEA 11), Torino, Italy, 6-10 June 2022 (flash oral and poster presentation) p.395.

M. Pylarinou, S. Gardelis, V. Likodimos, E. Sakellis, P. Tsipas, N. Boukos, A. Dimoulas, *Surface modification of Mo-$BiVO_4$ photonic crystal photocatalysts by Au and Ag plasmonic nanoparticles*, XXXVI Pan-Hellenic conference on Solid-State Physics and Materials Science, 26-28 September 2022, Heraklion, Greece, Poster presentation P1.23.

M. Pylarinou, E. Sakellis, V. Likodimos, *Metal (Mo, Ca)-doped $BiVO_4$ inverse opal photonic catalysts*, XXXV Panhellenic Conference on Solid State Physics and Materials Science, Congress Center, NCSR "Demokritos", 26-29 September 2021, Athens, Greece, Poster presentation P2.11.

M. Pylarinou, A. Toumazatou, E. Sakellis, D. Palles, N. Boukos, V. Likodimos, *Visible light active FeO_x-TiO_2 photonic crystal photocatalysts*, XXXIV Panhellenic Conference on Solid State Physics and Materials Science, Patras 11-14 September 2019 (poster presentation).

Contents

Acronyms

Abs	Absorbance
Ag	Silver
ATR	Attenuated Total Reflectance
Au	Gold
BE	Bending Energy
$BiVO_4$	Bismuth Vanadate
BQ	1,4-benzoquinone
Ca	Calcium
CB	Conduction Band
CIP	Ciprofloxacin
DR	Diffuse Reflectance
EDX	Energy-dispersive X-ray analyzer
EF	Fermi Level
EFTEM	Energy-filtered Transmission Electron Microscopy
Eg	Energy gap
EIS	Electrochemical Impedance
FA	Formic Acid
FTIR	Fourier Transform Infrared Spectroscopy
FTO	Fluorine-doped tin oxide
HRTEM	High-resolution Transmission Electron Microscopy
IBU	Ibuprofen
io	Inverse opal
IPA	Isopropanol
IPCE	Incident Photon-to-Current Efficiency
IR	Infrared Spectroscopy
KE	Kinetic Energy
LSPR	Localized Surface Plasmon Energy
LSV	Linear Sweep Voltammetry
MO	Metal Oxide
Mo	Molybdenum
ms	monoclinic scheelite
NHE	Normal Hydrogen Electrode
NPs	Nanoparticles
PBG	Photonic Band Gap
PC	Photonic Crystals
PEC	Photoelectrocatalysis
PL	Photoluminescence
PMMA	Poly(methyl methacrylate)
PS	Polystyrene
R	Specular Reflectance
RHE	Reversible Hydrogen Electrode
SA	Salicylic Acid
SCL	Space Charge Layer
SEM	Scanning Electron Microscopy
T	Transmittance
TC	Tetracycline
TEM	Transmission Electron Microscopy
TiO_2	Titania
ts	tetragonal scheelite

tz	tetragonal zircon-type
UPS	Ultraviolet Photoelectron Spectroscopy
UV	Ultraviolet
VB	Valence band
Vis	Visible
VLA	Visible Light Activated
Voc	Photovoltage or open circuit voltage
WF	Work Function
XPS	X-ray Photoelectron Spectroscopy
XRD	X-ray Diffraction

CHAPTER 1

Introduction

1.1 Semiconductor photocatalysis

Semiconductor photocatalysis has been considered as one of the most promising technologies to address global concerns on environmental pollution and meet the growing energy demands by utilizing naturally abundant, renewable sources such as solar light [1]. It has accordingly sparked extensive multidisciplinary research, providing a versatile and eco-friendly approach for solar energy conversion applications that span from sustainable water and air purification [2] to the production of hydrogen and chemical fuels through processes such as water splitting and CO_2 reduction [3, 4]. These advancements rely on environmentally friendly nanostructured materials and solar energy, either as a standalone process or in conjunction with other advanced technologies [5]. This distinctive potential for solar powered technologies has spurred the development of photocatalytic semiconductor nanomaterials with tailored structural, morphological and optoelectronic properties [6] that could alleviate the two major limitations of the process efficiency, namely the low quantum efficiency arising from the recombination of photogenerated charge carriers (electrons and holes) and the poor solar light harvesting [7, 8], especially for benchmark wide band gap (>3.0 eV) semiconductor photocatalysts like titanium dioxide (TiO_2) [9].

Photocatalysis is defined as a catalytic process that accelerates the rate of a photoreaction - a chemical reaction that involves the absorption of light– in the presence of a substance, the *photocatalyst*, whose excited state repeatedly interacts with the reacting species forming intermediates and regenerates itself after each interaction cycle without being consumed [10]. Semiconductor photocatalysis is characterized as heterogeneous since the solid photocatalyst is in a different physical state from the reactants. Organic pollutant degradation and photoelectrochemical water splitting are among the most important applications. Photocatalytic decomposition of organic contaminants in water belongs to the broader category of advanced oxidation processes, which are based on the generation of hydroxyl radicals ($OH^{\bullet}$) [5], while photocatalytic water splitting, firstly reported by Fujishima and Honda [11], describes the dissociation of water molecules into hydrogen (H_2) and oxygen O_2 using a semiconducting electrode under band gap irradiation.

The primary photocatalytic process involves the absorption of photons with energy equal to or greater than the semiconductor band gap (E_g) that leads to the excitation of electrons into the conduction band (CB) and the generation of holes in the valence band (VB), followed by multiple trapping processes at bulk or surface states over a broad range of time scales [12]. Photogenerated electrons and holes that evade detrimental, radiative or non-radiative recombination can initiate secondary surface reactions via interfacial charge transfer to adsorbates at the photocatalyst surface resulting for instance in organics degradation or the evolution of H_2 and O_2 from water splitting. Surface reduction and oxidation reactions are thermodynamically driven by

photogenerated electrons and holes, respectively, provided that their reduction and oxidation potentials lie between those of the semiconductor CB and VB edges. Specifically, when light of energy $h\nu \geq E_g$ is absorbed by the semiconductor, electrons (e^-) and holes (h^+) are generated in the conduction and valence bands, respectively (Figure 1.1):

$$\text{Semiconductor photocatalyst} + h\nu \rightarrow e^- + h^+.$$

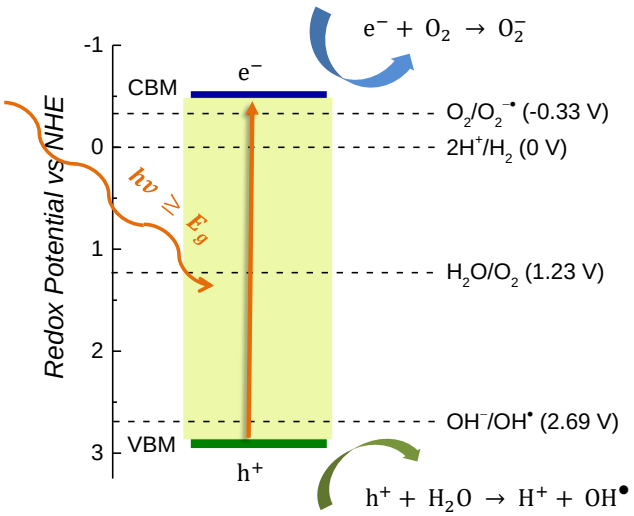

Figure 1.1 Semiconductor photocatalysis scheme and selected redox potentials with respect to normal hydrogen electrode (NHE) at pH=0. The NHE values are converted to the absolute vacuum energy scale (AVS) according to $V_{NHE} = -V_{AVS} - 4.5$ V [13].

Photogenerated e^- on the semiconductor surface can react with O_2 producing superoxide radicals ($O_2^{\bullet -}$) provided that the energy of the conduction band minimum (CBM) is more negative than the standard reduction potential of $O_2^{\bullet -}$ O_2/O_2^- (-0.33 V vs. NHE at pH = 0), whereas holes h^+ can oxidize OH^- or H_2O producing hydroxyl radicals ($OH^\bullet$) if the valence band maximum (VBM) is more positive than the standard oxidation level of $OH^-/OH^\bullet$ (2.69 V vs. NHE at pH = 0) [8]:

$$e^- + O_2 \rightarrow O_2^{\bullet -}$$

$$h^+ + H_2O \rightarrow H^+ + OH^\bullet$$

Hydroxyl radicals are extremely reactive species (redox potential as high as 2.7 V at acidic pH) that attack non-selectively, practically all organic contaminants (*indirect oxidation*), which can be sequentially transformed through a series of intermediate reactions to simpler organic molecules that are eventually mineralized to CO_2, H_2O, and inorganic salts. Shallow trapped holes may also directly oxidize chemisorbed pollutants (*direct oxidation*), while superoxide radical anions may further react with H^+ to generate hydroperoxyl radicals (•OOH) and H_2O_2 leading to the formation of reactive oxygen species that may contribute to the oxidative degradation of pollutants [1, 9]. Likewise, to achieve overall water splitting using a semiconductor, its

conduction band potential must be more negative than that of H_2 generation and its valence band potential must be more positive than that required for O_2 generation.

Semiconductors with sufficient positive VB potentials for producing the highly reactive $OH^{\bullet}$ radicals, such as TiO_2, ZnO and WO_3 (Figure 1.2) are advantageous for photocatalytic organics degradation [8, 14]. However, electron transfer from the CB to dissolved O_2^- molecules that is frequently the rate-determining step for the photocatalytic mineralization of organic pollutants is not thermodynamically favored for WO_3, where multi-electron reduction of O_2 to H_2O_2 is required [8]. On the other hand, TiO_2 and ZnO metal oxides present ideal energy band diagrams for the simultaneous formation of holes, $OH^{\bullet}$ radicals, O_2^- and H_2O_2 for the photocatalytic degradation of organic compounds.

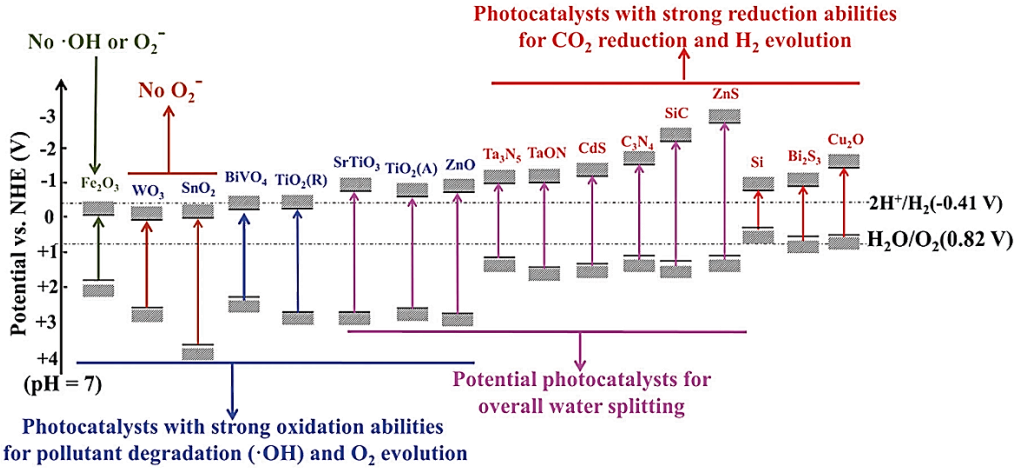

Figure 1.2 Band edge potentials of typical semiconductors in aqueous electrolytes at pH=0 for different photocatalytic applications [8].

In particular, TiO_2 (titania) has been the most extensively studied photocatalyst because of its high oxidation/reduction capacity, low-cost, photochemical stability and low toxicity [15]. Nevertheless, practical applications have been largely impaired by titania's poor light harvesting ability due to the wide band gap (3.0-3.2 eV) of most TiO_2 polymorphic phases, which absorb in the UVA spectral range accounting for only 4-5% of sun's total irradiation, and the persistent recombination of photogenerated charge carriers. Moreover, besides favorable thermodynamic driving forces dictated by the relative energies of the CB/VB potentials for the semiconductor photocatalysts and the redox potentials of reversible target reactions, the overall process efficiency is determined by the semiconductors light harvesting efficiency, charge excitation/separation, charge transport and recombination as well as surface reaction (reduction and oxidation) kinetics that depend critically on their structural, optical and electronic properties.

To reduce electron-hole recombination and improve photocatalytic performance, an electrical bias can be externally applied on the semiconducting material that is deposited onto a conductive substrate, utilized as *photoelectrode*, and connected to a counter electrode, leading to electrochemically assisted photocatalysis [16, 17]. The corresponding process, which is accordingly labelled "*photoelectrocatalysis*" (PEC), has

emerged as a competent method for both pollutants degradation and water splitting by combining heterogeneous photocatalysis and electrochemical methods. In that case, the simultaneous occurrence of both surface reduction and oxidation reactions is not thermodynamically a prerequisite as the counter electrode can assist one of them. The generation of reactive species via the reduction pathway can be facilitated by the applied bias, circumventing limitations by the energy band gaps and band edge positions of semiconductor photocatalysts.

When a semiconductor is immersed in a solution containing redox species (Figure 1.3a), electrons flow across the semiconductor/electrolyte interface until equilibration of the chemical potentials of electrons in the solid and the solution is established [18]. The interfacial electron transfer generates a space charge layer (SCL) or *depletion layer* in the semiconductor, while the CB and VB edges are bent so that a potential barrier is formed against further electron transfer across the interface (Figure 1.3b). For a n-type semiconductor, whose Fermi level (E_F) is typically higher than the redox potential of the electrolyte, electrons will transfer toward the solution to reach equilibrium, leading to an excess of positive charge arising from the ionized dopant atoms in the semiconductor after equilibration, while the electrolyte will acquire an excess negative charge. The positive charge will distribute across the SCL characterized by the depletion of the majority carriers (electrons), and the negative charge will spread over a much narrower region (Helmholtz layer) between the electrode and the electrolyte (Figure 1.3b). The SCL thickness typically ranges from 100 Å to several microns, whereas on the solution side of the semiconductor/electrolyte interface, the narrow (~1 Å) Helmholtz double layer will form by the sorption of counter-ions onto the charged surface of the semiconductor [13]. The Helmholtz layer results in an additional potential drop V_H inside the semiconductor SCL altering the extent of band bending in order to set the electron transfer rate across the interface equal to zero, at equilibrium.

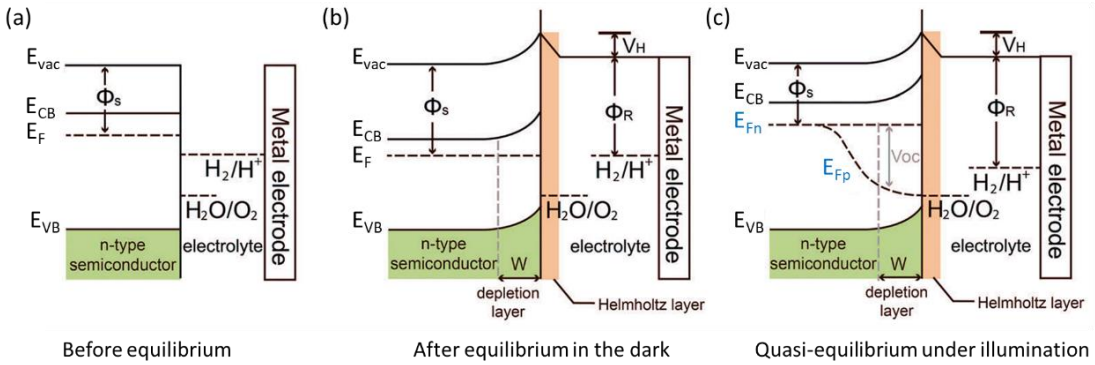

Figure 1.3 Band bending and SCL formation at the interface of an n-type semiconductor with an aqueous electrolyte with respect to the redox potentials (H_2O/O_2 and H_2/H^+), the Helmholtz layer potential drop (V_H), the semiconductor work function (Φ_s), and the electron (E_{Fn}) and hole (E_{Fp}) quasi-Fermi levels (a) before and (b) after equilibration at semiconductor/electrolyte interface in the dark, and in (c) quasi-equilibrium conditions under steady-state illumination. Adopted from ref [19].

Steady-state illumination leads to non-equilibrium electron and hole populations, which can be described by the corresponding quasi-Fermi levels, E_{Fn} and E_{Fp}, that represent the electrochemical potentials of electrons and holes under non-equilibrium conditions. The splitting of the quasi-Fermi levels results in a built-in electric field that generates the *photovoltage* or *open-circuit voltage* (V_{OC}) at the semiconductor/liquid junction, which corresponds to the potential difference between the quasi-Fermi levels E_{Fn}-E_{Fp} under no net current flow (Figure 1.3c). The magnitude of V_{OC} determines the ability of a semiconductor to initiate photoelectrochemical reactions (e.g. even if the appropriate semiconductor band-edge positions straddle the water oxidation and reduction levels, water splitting is not possible unless V_{OC} exceeds 1.23 V).

Application of an external bias voltage in a PEC system may further enhance band bending and thus improve the separation of photogenerated electrons and holes and promote surface oxidation/reduction reactions and the production of reactive species for organics degradation and water splitting, as summarized in Figure 1.4. When a bias voltage is applied between the working photoelectrode and a reference electrode, the resulting potential difference will be distributed over the SCL and Helmholtz layers.

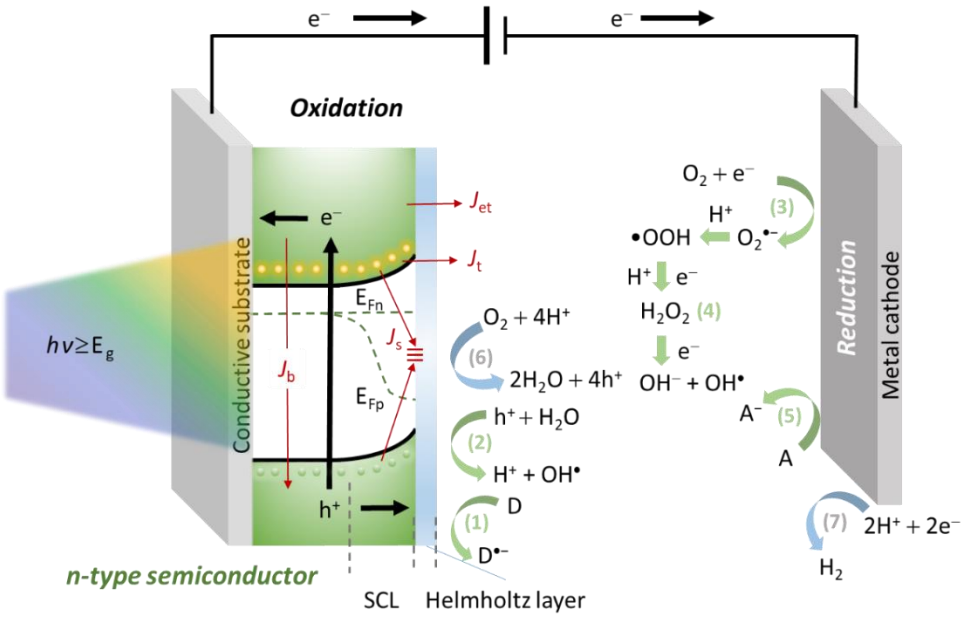

Figure 1.4 PEC processes and pathways for surface oxidation/reduction reactions and the production of reactive species for organics degradation and water splitting using an n-type semiconductor photoelectrode and a metallic counter electrode: (1) donor electron transfer, (2) hydroxyl radical formation from water oxidation, (3) oxygen reduction to superoxide radicals, (4) formation of hydrogen peroxide followed by the formation of hydroxyl radicals, (5) electron transfer to an electron acceptor, (6) oxygen evolution reaction, and (7) proton reduction to hydrogen [16]. Photogenerated e^- and h^+ can recombine by different processes associated with a current density including bulk (J_b) and surface (J_s), recombination, tunneling (J_t) and thermal electron-transfer (J_{et}) of majority carriers across the interfacial potential barrier. Detrimental recombination processes are depicted by thin red arrows as opposed to beneficial e^- and h^+ exciation/separation and collection processes toward the electrolyte and the counter electrode depicted by thick black arrows [18].

As V_H remains essentially constant due to the high charge density and relatively small width of the Helmholtz layer [13], the potential drop across the semiconductor/ electrolyte interface takes place predominantly within the semiconductor SCL. Application of a positive bias to an n-type semiconductor photoelectorde will increase the width of the SCL and lead to upward band bending. On the other hand, the degree of band bending can be reduced or even eliminated when a sufficiently negative bias is applied, leading to the condition of flat bands, where the SCL width becomes zero. The flat band potential (V_{fb}) is accordingly defined as the electrode potential measured with respect to a reference electrode (e.g. NHE) in a semiconductor/electrolyte junction, when the potential drop across the SCL becomes zero [13]. In the case of an n-type semiconductor photoanode under illumination, application of a positive potential bias greater than U_{fb} causes electron migration towards the counter electrode and hole transfer towards the solution interface. The separation of photogenerated e^- and h^+ is thereby increased, promoting surface oxidation and reduction reactions and the formation of reactive species for organics degradation or water splitting, as shown in Figure 1.4. At the counter electrode, additional reactive species can be produced, assisting the PEC process. The overall efficiency is though limited by several recombination processes that determine the corresponding electron and hole concentrations at the semiconductor/electrolyte interface under quasi-equilibrium conditions. Specifically, photogenerated charge carriers can recombine producing a current density associated with radiative or non-radiative recombination in the bulk of the semiconductor (J_b), surface recombination via defect (trap) states at the semiconductor/liquid interface (J_s), tunnel through the electric potential barrier near the surface (J_t) or thermally surmount the interfacial potential barrier (J_{et}). Significant research efforts have been thus directed towards the development and design of semiconductor nanostructures with tailored electronic and optical properties that could circumvent recombination issues and enhance PEC efficiency [20, 21].

1.2 Bismuth vanadate

Ternary transition metal oxide (MO) semiconductors have been attracting increasing interest as alternative photocatalysts that can effectively evade the intrinsic limitations of binary MOs such as the benchmark TiO_2 or Fe_2O_3 oxides for photocatalytic applications [22, 23]. Despite the favorable chemical stability and oxidation capacity of binary transition MOs composed of d^0 (Ti^{4+}, V^{5+}, Nb^{5+} and W^{6+}) or d^n (Fe^{3+}, Co^{2+}/Co^{3+}) cations, their photocatalytic performance is inherently limited by their wide band gaps determined from their O 2p valence band for the former ones and the poor polaron hopping conduction mechanism for the latter ones, impeding solar light harvesting and charge transport, respectively [6]. From a wealth of multinary oxides, bismuth vanadate ($BiVO_4$) has emerged as the most promising visible light MO photocatalyst exhibiting the highest performance among MO photoanodes for PEC water oxidation along with good chemical stability, environmental inertness and low cost [24]. Soon after the seminal work of Kudo et al. in 1998 [25] that reported on the photocatalytic O_2 evolution by $BiVO_4$ in the presence $AgNO_3$ as sacrificial electron acceptor under visible light, it was realized that the material's polymorphic phase determines its

photocatalytic activity. Early studies by Kudo et al. showed that monoclinic scheelite $BiVO_4$ largely outperforms both the tetragonal zircon [26] and tetragonal scheelite [27] phases, indicative of strong correlations with subtle electronic modifications caused by the monoclinic structural distortion.

Specifically, $BiVO_4$ occurs in nature in the form of the minerals: pucherite with orthorhombic crystal structure, dreyerite with tetragonal zircon-type (*tz*) crystal structure (space group: $I_{4_1/a}$ with $a = b = 7.30$ Å, $c = 6.584$ Å) and clinobivasnite with monoclinic scheelite (*ms*) structure (space group: $I_{2/b}$ with $a = 5.1956$ Å, $b = 5.0935$ Å, $c = 11.7045$ Å, and $\gamma = 90.383$ Å) [28], as shown in Figure 1.5 [29]. The preparation of the pucherite phase has not been reported in the laboratory, in contrast to the *tz* and *ms* polymorphs commonly prepared by low and high temperature synthesis, respectively [30]. The *tz* polymorph can be irreversibly transformed to the thermodyanmcially stable *ms* phase at 670-770 K [26]. In addition, the high temperature tetragonal scheelite (*ts*) phase can be obtained by the reversible structural phase transition of *ms* $BiVO_4$ at 528 K [31]. In the scheelite structure, each V ion is tetrahedrally coordinated by four O atoms, while each Bi ion is coordinated by eight O atoms from eight different VO_4 tetrahedral units (Figure 1.5 c). In the zircon structure, V is also stabilized by four O atoms and Bi is coordinated by eight O atoms, but each Bi is surrounded by only six VO_4 tetrahedra because two VO_4 units provide two O atoms to Bi (Figure 1.5b). In both structures, each O atom is coordinated to two Bi and one V atoms, forming a three dimensional structure.

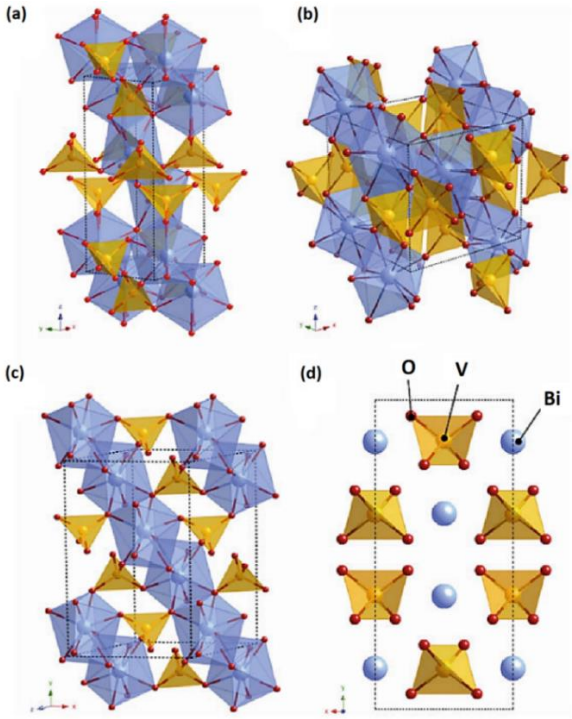

Figure 1.5 Crystal structures of (a) pucherite (orthorhombic), (b) dreyerite (tetragonal zircon-*tz*), and (c) clinobisvanite (monoclinic scheelite-*ms*) $BiVO_4$ polymorphs. (d) Side view (c-axis) of the clinobisvanite structure [29].

The symmetry lowering of the *ms* phase results in two different V–O bond lengths for the VO_4 tetrahedra (~1.69 and ~1.77 Å) in contrast to the four equal V–O bond lengths (~1.72 Å) of the more symmetric ts phase. Likewise, the two different Bi-O bond lengths of the *ts* phase (2.4 and 2.47 Å) split to four different Bi-O bond lengths (2.35, 2.37, 2.52, and 2.63 Å) in the *ms* structure, reflecting the monoclinic distortion of the local environments of V and Bi ions, which removes the four-fold symmetry of the tetragonal system.

Electronic band structure calculations in combination with spectroscopic investigations have shown that the VB of *ms* $BiVO_4$ consists primarily of O 2p states, $2p_\pi$ and hybridized sp^2 orbitals due to the distorted trigonal planar symmetry around O atoms [32], while VBM is composed of O $2p_\pi$ states with a small contribution from Bi 6s (Figure 1.6a,b). The CBM consists of V 3d, possessing primarily $d_{x^2-y^2}$ and d_{z^2} character with significant contribution from antibonding O sp^{2*} due to hybridization, while the upper region of the CB has strong Bi 6p character. The E_g of *ms* $BiVO_4$ has been established to be *indirect* with a value of ~2.5 eV (Figure 1.6c), accompanied by a *direct* transition at ~2.7 eV, very close (0.2 eV) to the indirect one [33]. This behavior accounted for earlier ambiguities on the nature of the fundamental band gap of *ms* $BiVO_4$ as well as the absence of strong band edge emission that is expected for direct band gap semiconductors due to band-to band carrier recombination.

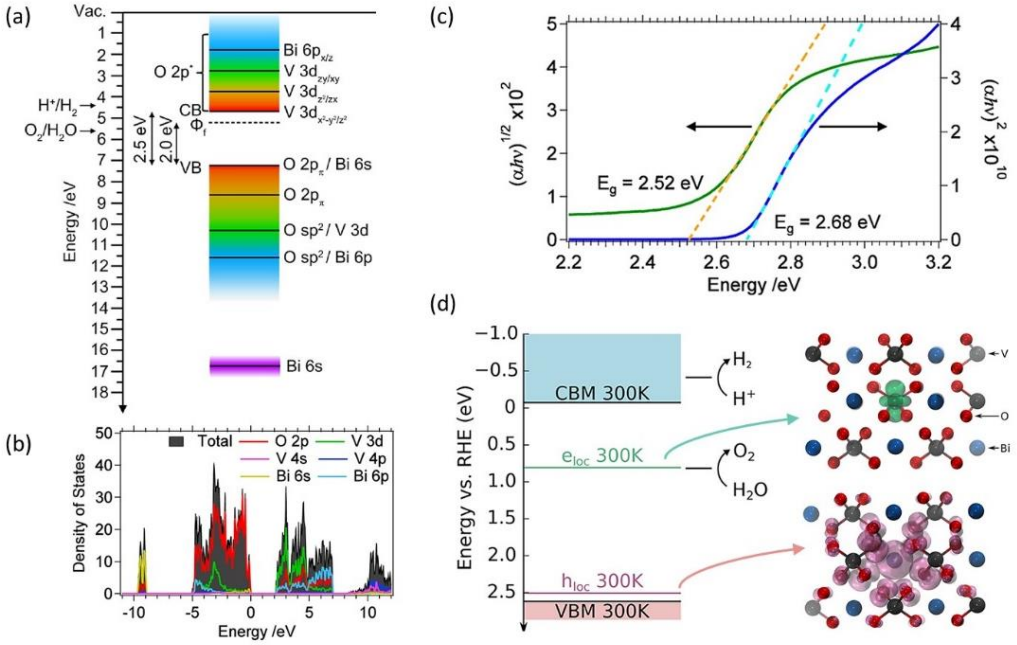

Figure 1.6 (a) Schematic electronic band structure and (b) the total and partial density of states for *ms*-$BiVO_4$ projected onto atomic wave functions [32]. (c) Tauc plots $(\alpha h\nu)^n \propto (h\nu - E_g)$ with α being the optical absorption coefficient, and the linear fits of the absorption edges for $n = 1/2$ and $n = 2$ corresponding to indirect and direct transitions, respectively [33]. (d) Energy diagram depicting the energy levels of hole and electron polarons with respect to the band edges of *ms* $BiVO_4$ 300 K and the H^+/H_2 and O_2/H_2O redox potentials at pH = 7. Arrows indicate the charge densities of electron and hole polarons localized around V and Bi atoms [34].

Charge transport investigations on $BiVO_4$ showed n-type conduction following the small polaron hopping mechanism in the range of 250 to 400 K with activation energy of about 0.3 eV and very low electron mobility of 10^{-2} cm^2 V^{-1} s^{-1} compared to other MO photoanodes [35, 36]. The resulting electron diffusion length (L_n) in *ms* $BiVO_4$ is accordingly reduced to ~10 nm at room temperature [37], whereas the hole diffusion length (L_p) was estimated to be an order of magnitude higher (~100 nm) compensating for the low mobility and accounting for the strong water oxidation efficiency of $BiVO_4$. Photogenerated e^- have been predicted to form small polarons around V atoms (most probably reflecting the localization of V 3d orbitals at the CBM due to poor overlap with Bi 6p orbitals) [38, 39], whereas weakly localized hole polarons were predicted to distribute around the BiO_8 octahedra (Figure 1.6d) [34]. It is worth noting that hole localization and the concomitant lattice distortion was predicted to be much larger in the ts $BiVO_4$ polymorphic phase, whereas the hole polaron distributes over several lattice sites in *ms* $BiVO_4$, leading to higher hole mobility and photocatalytic activity [38]. Moreover, the electron and hole polaron levels were calculated at 0.88 eV below the CBM and 0.11 eV above the VBM at 300 K (Figure 1.6d), disrupting the band alignment at the $BiVO_4/H_2O$ interface and leading to detrimental recombination between electron and hole polarons that impair the photocatalytic activity [34].

Intensive research efforts have been devoted to improve the poor charge transport of majority carriers (electrons) for *ms* $BiVO_4$ by extrinsic doping [24]. Among several intrinsic defects of *ms* $BiVO_4$, O vacancies have been the most prevalent ones with the lowest formation energy, especially under Bi rich/O poor [40] or even O moderate [41] conditions, leading to shallow donors and n-type conductivity. Weak p-type conductivity has been also predicted under Bi poor/O rich conditions via Bi vacancies and O interstitials as the dominant acceptor defects, though p-doped $BiVO_4$ has been rarely reported [41]. Among different heteroatoams (Figure 1.7a,b), the most effective extrinsic shallow donors of *ms* $BiVO_4$, are Mo^{6+} and W^{6+} substituting for V^{5+} ions [42, 43, 44] and interstitial hydrogen (H_i) [45], as well as intrinsic oxygen vacancy (V_O) defects [46, 47]. Specifically, substitutional Mo and W atoms at V lattice sites (ionic radii V^{5+}:0.54 Å, Mo^{6+}: 0.62 Å, W^{6+}: 0.65 Å), lead to marked enhancements of the donor density (N_D) and electron mobility at concentrations up to <3 %, especially for Mo-doping (Figure 1.7c) without large structural distortions or transformation of the *ms* crystal structure to the tetragonal one. At the same time, the introduction of defect states may reduce hole mobility and hole diffusion length even though the overall photocatalytic efficiency for water splitting is improved by the enhanced electron mobility, whereas excessive doping may lead to adverse effects by defect formation (Figure 1.7c). A recent study of Mo-doped $BiVO_4$ single-crystalline films [48] showed that 50 nm-thick 2% doped Mo-$BiVO_4$ films deliver larger photocurrents than the optimal (160 nm-thick) $BiVO_4$ films despite the much lower photon absorption (Figure 1.7d). Thereby, it was shown that Mo doping improves electron transport by increasing not only N_D but also electron mobility by reducing the hopping activation energy of small polarons due to the strong electrostatic interactions between positively charged $Mo^{6+}O_4$ and negatively charged $V^{4+}O_4$ tetrahedra that decrease the local structural distortion and the barrier for small polaron hopping.

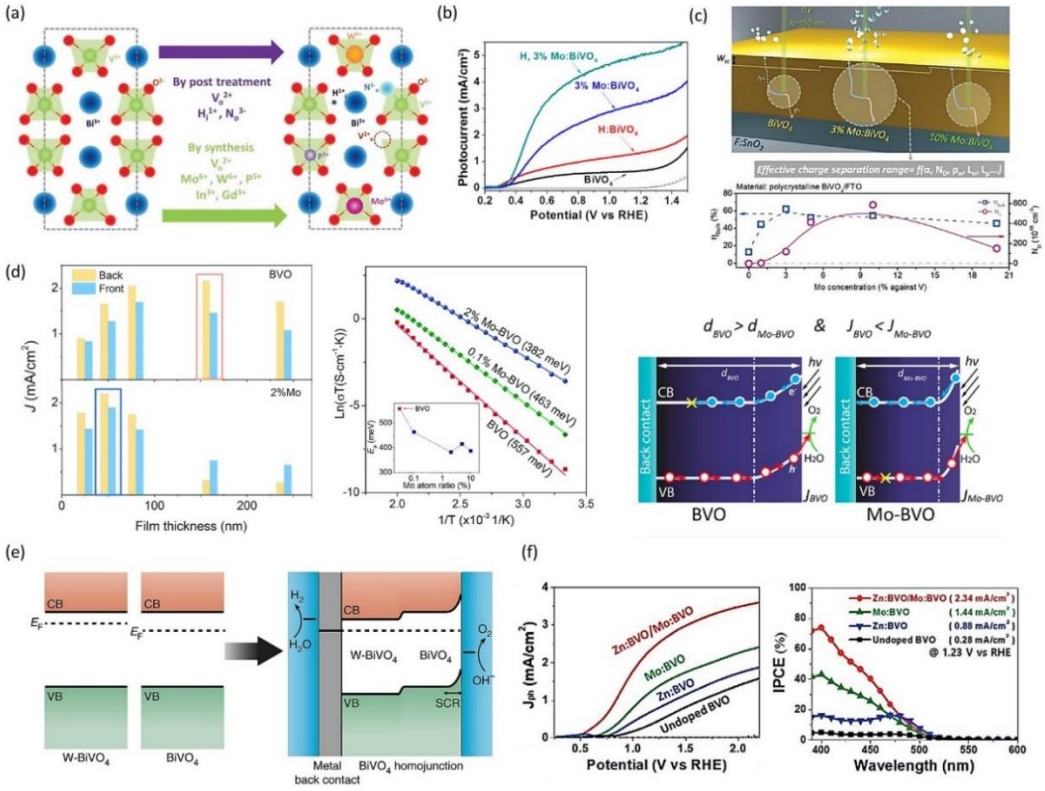

Figure 1.7 (a) Most effective dopants of $BiVO_4$ lattice [24] and (b) comparative photocurrent density vs potential curves for $BiVO_4$, H-$BiVO_4$, 3% Mo-$BiVO_4$, and co-doped H, 3% Mo-$BiVO_4$ [45]. (c) Schematic dependence of electron (L_n) and hole (L_p) diffusion lengths, bulk charge separation efficiency η_{bulk} and donor density N_D with the Mo-doping concentration [24]. (d) Photocurrent densities of pristine and 2% Mo-doped $BiVO_4$ photoanodes at 1.23 V vs RHE as a function of film thickness, temperature dependence of conductivity fitting plots of pristine, 0.1% Mo-, and 2% Mo-$BiVO_4$ films based on the small polaron transport model. The inset shows the corresponding hopping activation energy in Mo-BiVO4 as a function of the Mo atom ratio [48]. (e) Schematic of homojunction and space charge region formation between W-doped $BiVO_4$ and $BiVO_4$ [49]. (f) Enhancement of photocurrent density vs potential and Incident Photon-to-Current Efficiency (IPCE) for homojuntion Mo-$BiVO_4$/Zn-$BiVO_4$ photoanodes with respect to pristine, as well as single doped Mo- and Zn-$BiVO_4$ [50].

Furthermore, homojunction deposition has been a competent approach to boost the PEC performance of $BiVO_4$ for water splitting, evading the weak interfacial coupling and stability issues of heterojunctions. Abdi et al. [49] introduced a gradient doped W-$BiVO_4$ photoanode leading to a distributed n-n^+ homojunction that greatly improved charge separation (Figure 1.7e), while successive deposition of Mo-$BiVO_4$/Co-$BiVO_4$ [50] and Mo-$BiVO_4$/Zn-$BiVO_4$ planar photoanodes (Figure 1.7f) [51] resulted in significant enhancement of both charge transport and interfacial electron transfer for water splitting. Nanostructuring and morphology engineering of $BiVO_4$ photoanodes to hierarchical structures has been keenly pursued as a means to improve charge separation and light absorption for highly efficient PEC water splitting [52, 53] Moreover, highly effective heterojunctions have been reported for $BiVO_4$ with semiconductors such as WO_3 [54, 55], SnO_2 [56], and TiO_2 [57] that act as electron

transporting layers with higher electron transfer capacity than $BiVO_4$ and lead to type II band alignment for spontaneous cascade electron transfer. At the same time, they provide a scaffold of high aspect ratio structure like nanorods that allow high $BiVO_4$, loading amounts, while remaining relatively thin (≈100 nm) for efficient hole transport.

1.3 Photonic crystals

Among different hierarchical morphologies to improve light harvesting [8], photonic crystals (PCs) [58] have been attracting particular attention as a unique three-dimensional (3D) periodically ordered structures that can be ideally combined with judicious compositional modifications to simultaneously enable slow light propagation and charge separation for semiconductor photocatalysts [59]. PCs are periodic structures characterized by the spatial modulation of their refractive index (n) on a length scale comparable to the wavelength of light [60, 61]. The periodicity of n modifies radically light propagation, likewise the periodic lattice potential alters free electron motion in crystals. A key feature of PCs that allows for light manipulation is their capacity to create photonic band gaps (PBGs), where light propagation is prohibited, similar to E_g in semiconductors [62]. Stacks of alternating dielectric layers were long ago introduced by Lord Rayleigh [62], establishing the prototype one-dimensional (1D) PC (Figure 1.8). Interference of forward and backward propagating waves after reflection at the layer interfaces of these 1D heterostructures (Bragg mirrors), results in the formation of standing waves at frequencies fulfilling the Bragg condition i.e. at the boundaries ($k=\pm\pi/a$) of the 1st Brillouin zone for the 1D stack with lattice constant a [58]. This leads to the opening of a forbidden frequency range, i.e. a band gap, in the dispersion relation $\omega(k)$ between the photon frequency ω and wave vector k ($|\boldsymbol{k}|=k=2\pi/\lambda$ with λ being the wavelength of light). Thereby, $\omega(k)$ deviates from the linear dispersion relation $\omega(k)=(c/n)|\boldsymbol{k}|$ (c=the vacuum speed of light) expected for a homogeneous, isotropic material. The electric field antinodes (amplitude maxima) for the two possible standing waves are localized at the high/low refractive index layers, yielding the lower/higher frequency photonic bands, conventionally called "dielectric" and "air" bands, respectively (Figure 1.8). Changing the periodicity, i.e. lattice constant and/or n of the alternating layers in the 1D structure modifies the PBG spectral position and width (broadens with the increase of n contrast), respectively.

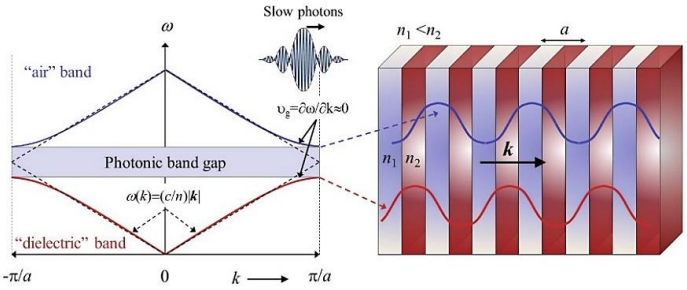

Figure 1.8 Photonic band gap formation in a 1D periodic stack consisting of alternating dielectric layers with different refractive indices ($n_2>n_1$) [59].

Although PBG's formation is common in 1D PCs with non-zero refractive index contrast, this becomes more complex when the structural periodicity extends to higher dimensions. In 2D and 3D photonic structures, forbidden frequency intervals can occur in different directions of light propagation. These spectral regions can merge into the same frequency range, creating a complete, omnidirectional PBG, only under favorable conditions such as sufficient *n* contrast, lattice symmetry, and filling factor. These partial gaps, known as "stop" bands, differ from complete PBGs, or simply "gaps," where light propagation is inhibited in all possible directions [58].

Among various PC designs, "natural" self-assembled structures have attracted particular attention due to the ease of fabrication, the most prominent being artificial opals [63, 64], prepared by the spontaneous organization of colloidal dielectric spheres to close-packed lattices, especially the thermodynamically stable face centered cubic (*fcc*) one [65]. Despite their 3D ordered structure, opals that self-assemble with their close-packed (111) planes parallel to the substrate (Figure 1.9) do not present a complete PBG, independently of the *n* contrast. In fact, their close-packed structure permits only the formation of a pseudo-PBG (stop band) between the second and third bands for wave propagation along the ΓL-direction in reciprocal space, i.e. the [111] crystal direction in real space (L-pseudogap) (Figure 1.10a). This results in a characteristic dip of the transmittance (T%) spectrum for incident light normal to the (111) planes, which are parallel to the substrate surface (Figure 1.9) [66].

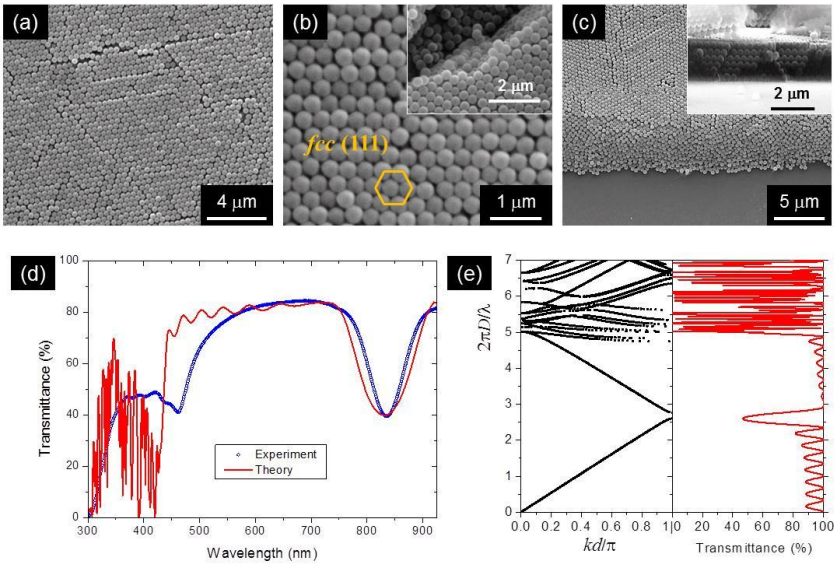

Figure 1.9 (a), (b) Top and (c) side view SEM images of opal films prepared by the self-assembly of monodisperse polystyrene spheres of 350 nm diameter, at different magnifications. (d) Experimental and theoretical transmittance (T%) spectrum for a slab of 8 (111) layers on glass substrate, and (e) photonic band structure in units of normalized frequency along the [111] direction and the corresponding transmittance for a plain 8-layers thick slab [66].

Nevertheless, using opal colloidal crystals as sacrificial templates their replica, inverse structure can be fabricated by filling the interstitial space between the spheres with the material of choice followed by the selective template removal by calcination or chemical etching [64]. The *inverse opal* structure consists of an *fcc* lattice of air spheres

within the dielectric background of the infiltrated material, and possesses a full PBG between the eighth and ninth photonic bands provided that the *n* contrast is higher than 2.8 and losses due to material's optical absorption are avoided [65, 67], as shown in Figure 1.10b [68]. The formation of a complete PBG is favored in that case because the *fcc* lattice presents the most spherical Brillouin zone of all 3D Bravais lattices. This leads to similar periodicity along different directions and significant spectral overlap of forbidden intervals for adequate *n* contrast.

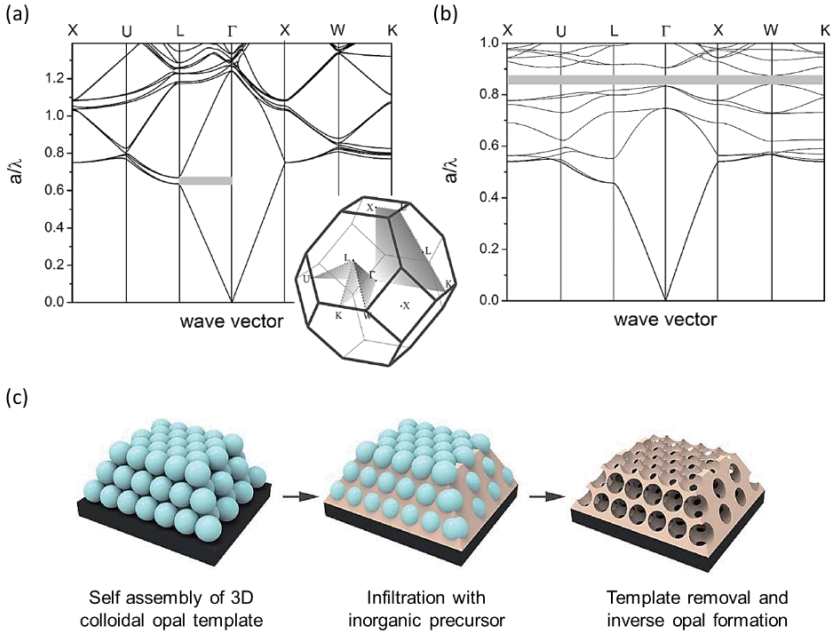

Figure 1.10 Photonic band structures of *fcc* lattices consisting of (a) dielectric spheres *n*=1.45 in air where the shaded gray region corresponds to the partial (pseudo) photonic gap created in the ΓL direction in reverse space or equivalently in the direction [111] in the regular lattice, and (b) air spheres in a dielectric matrix (*n*=3.45) where the dark gray region corresponds to the complete PBG. The inset shows the Brillouin zone for an *fcc* lattice [68]. (c) Schematic procedure of the sequential inverse opal fabrication process (adapted from [69]), including self-assembly of colloidal template, infiltration with inorganic precursor and template removal/ crystallization of the inverse replica structure.

A facile templating method that turned out to be the most prevalent for the fabrication of metal oxide inverse opals is the sequential deposition method, which is carried out in three main steps (Figure 1.10c): 1) synthesis of an opal PC substrate by the self-assembly of colloidal polymer or silica monodisperse templating spheres, 2) infiltration of the opal voids using wet impregnation or gas-phase deposition of liquid or vapor precursors of the inorganic material, followed by the chemical/physical conversion of the precursor via e.g. the sol-gel process of hydrolysis-condensation within the opal interstices, and 3) removal of the colloidal template, typically by calcination or chemical etching of the polymeric matrix that simultaneously results in the crystallization of the amorphous skeleton to the desired inverse opal structure [70]. There are several methods for the synthesis of colloidal crystal templates [64]. In this work, we have used the *vertical* and *horizontal* deposition methods. In the vertical

method, the polymeric template matrix is deposited by the self-assembly of monodispersed spheres from colloidal suspensions (Evaporation-Induced Self-Assembly/EISA). According to this technique, glass substrates are placed vertically in aqueous solutions of polystyrene (PS) or polymethyl methacrylate (PMMA) nanospheres, where the controlled evaporation of the solvent combined with the capillary forces at the interface between the substrate-solvent and air, cause the self-organization of spheres in densely packed *fcc* (opal) structure. In the horizontal method, the aqueous solution of polymeric nanospheres is deposited directly on a horizontal substrate resulting in inward convective flow and self-assembly as the evaporation rate at the periphery is much higher than that at the center leading to the *fcc* structure [71]. After the opal templates are formed, the interstitial space between the templating spheres is filled with a suitable precursor solution, using the dip-coating method. The infiltrated colloidal templates are then calcined at appropriate temperatures in order to decompose the polymer matrix and form a 3D interconnected inorganic inverse opal network.

1.4 Slow photon-assisted photocatalysis

Despite the sizable refractive index of metal oxides, e.g n=2.6-2.9 for TiO_2 at 500 nm [72], the corresponding n contrast in the inverse opal lattice remains marginally below the threshold of 2.8 predicted for full PBG formation. On the other hand, the stop band due to the L-pseudogap persists for light propagation along the [111] direction with variable frequency within the UV-Vis-NIR range depending on the void macropore diameter as well as the n contrast between the inorganic frame and the medium filling the void space (air, water or other solvent) and solid filling fraction [73, 74]. For frequencies within the L-pseudogap, the associated wave vector takes imaginary values and light propagating along [111] is exponentially attenuated, leading to enhanced reflection. The stop band can be thus identified in the transmission and reflection spectra as regions of low (high) transmission (reflection) signal at normal incidence to the film surface that is parallel to the (111) planes of the *fcc* inverse opals. Although rigorous band structure calculations are required to accurately fit the experimental optical spectra [75, 76], the stop band spectral position can be approximated by Bragg's condition of constructive interference, alike diffraction of X-rays by a periodic crystal lattice, provided that Snell's law of refraction is taken into account [77], as shown in Figure 1.11.

The modified Bragg's law for first order diffraction from the (111) planes, takes the form:

$$\lambda = 2d_{111}\sqrt{n_{eff}^2 - \sin^2\theta},$$

where λ is the stop band wavelength, $d_{111} = a/\sqrt{3} = \sqrt{2/3}\,D$ is the interplanar spacing between (111) planes, with a being the lattice constant and D the sphere diameter and n_{eff} is the volume-weighted average of the refractive indexes of the constituent spheres n_{sphere} and the material occupying the interstitial voids n_{void} defined as $n_{eff}^2 = n_{\text{sphere}}^2 f + n_{\text{void}}^2(1-f)$ with f the filling fraction ($f = 0.74$ for the *fcc* lattice), and θ is the angle between the incident beam and the plane normal. The PC is accordingly

considered as a homogeneous medium with effective refractive index n_{eff} and thickness $t = Nd_{111}$,where N is the number of sphere layers. It should be noted that this definition of n_{eff} is essentially the simplest approach among the *effective medium approximations* to the refractive index of the composite PC structure using its average dielectric constant $\varepsilon_{avg} = \varepsilon_{\text{sphere}} f + \varepsilon_{\text{void}}(1-f) \Rightarrow n_{eff} = \sqrt{n_{\text{sphere}}^2 f + n_{\text{void}}^2 (1-f)}$, which, despite its simplicity, is quite accurate for low dielectric constants (<6).

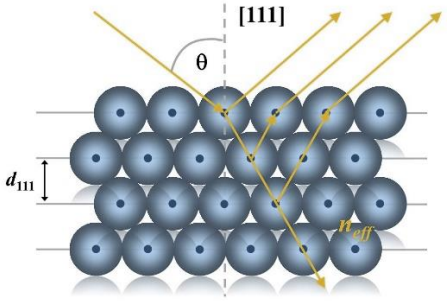

Figure 1.11 Bragg diffraction of light incident on the (111) *fcc* crystal planes of an opal at angle θ modified by refraction within the composite medium with n_{eff} refractive index.

At normal incidence $\theta = 0°$, first order diffraction from the (111) planes assumes the simple form $\lambda = 2\sqrt{2} n_{eff} D/\sqrt{3}$, which shows that the stop band varies linearly with the sphere diameter D for constant n. Moreover, this simple analytical approach based on modified Bragg´s law in combination with angle and solvent dependent optical measurements of the stop band frequencies can be used to determine independently the void sphere size and filling fraction in the inverse opal structure that commonly falls short of the theoretical value 0.26 for the *fcc* lattice due to its nanocrystalline nature and the accompanying porosity [78].

Nevertheless, the enhanced stop band reflection in inverse opals at frequencies within the L-pseudogap is a rather adverse effect for the photocatalytic process, as light absorption is diminished at these frequencies. The distinctive feature of PCs that underlies their potential to amplify light harvesting and photocatalysis, lies in their ability to retard light propagation and thus extend the path length of incident photons within the periodically structured network. This unique effect is caused by the strong reduction of the group velocity υ_g for photons propagating with energies at the edges of the stop band, which are accordingly called **slow photons**. In the simple case of 1D PCs, the group velocity of light υ_g i.e. the velocity at which a pulse propagates within a medium defined by the derivative $\upsilon_g = d\omega/dk$, becomes extremely low at frequencies near the edges of the L-pseudogap [79], as the dispersion relation $\omega(k)$ progressively flattens (Figure 1.8) and ideally should vanish within the band gap, where standing (non-propagating) waves develop for a perfect infinite PC. At frequencies approaching the stop band from the long wavelengths (red edge) side, light tends to form a standing wave that is mainly localized in the high RI (*dielectric band*) part of the PC, i.e. the inorganic skeleton of the inverse opal structure. At short wavelengths (blue edge), the light standing wave is primarily localized in the low RI

(*air band*) region of the PC. These photons are accordingly called *red*- and *blue*-edge slow photons. This unique effect that enables the structural manipulation of light propagation has been applied for the first time in 2003 by Mallouk and co-workers [79], to enhance the photocurrent of dye-sensitized solar cells by depositing a TiO_2 inverse opal film on a conventional porous nanoparticulate titania photoelectrode, by means of both the back reflection of light in the stop band region of the PC that acts as a dielectric mirror and the excitation of localized slow photon modes within the nanocrystalline absorbing layer [80, 81].

Slow photon-induced amplification of titania's photocatalytic reaction rate has been introduced by Ozin's group [82], by tuning the L-pseudogap of TiO_2 inverse opals within titania's electronic band gap so that the consequent stop band reflection is largely suppressed by the strong TiO_2 electronic absorption, while slow photons at the red edge of the stop band enhance the relatively weak optical absorption of titania near its absorption edge. In their seminal work, Chen et al. [82] demonstrated a marked improvement of photocatalytic efficiency on dye sensitized anatase TiO_2 inverse opal films with methylene blue (MB) as model pollutant, under both monochromatic UVA and white light irradiation. The photocatalytic activity was evaluated by implementing "solid-state" (dry) photodegradation experiments on the MB sensitized films to avoid contributions from molecular diffusion in the pore network and ensure high *n* contrast. Stop band reflectance of the anatase inverse opals was continuously varied from the visible to the UVA range by using polystyrene templating spheres with diameters from 380 down to 130 nm, as shown in Figure 1.12a-d.

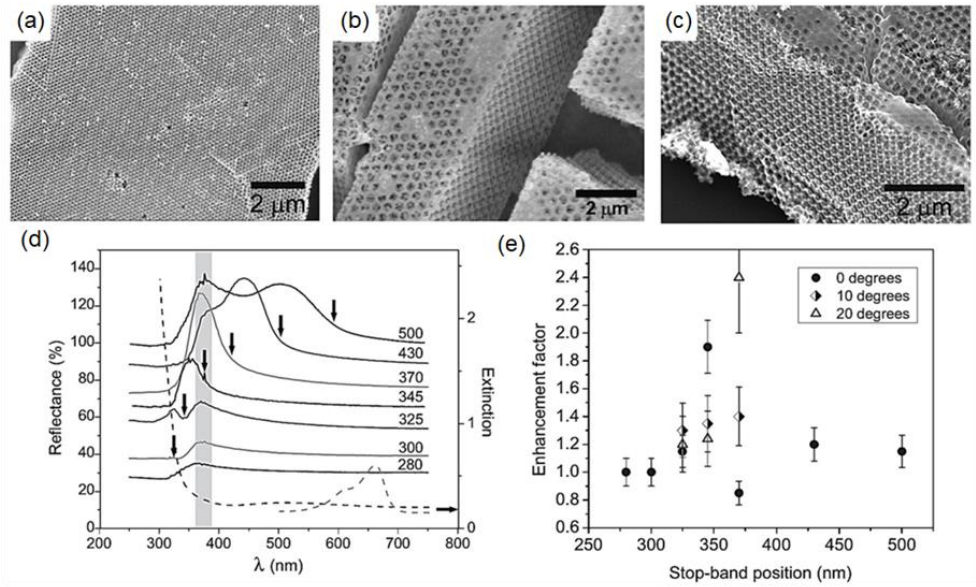

Figure 1.12 SEM images of TiO_2 inverse opals obtained from (a) 150 (b) 210 and (c) 300 nm polystyrene sphere templates. (d) Reflectance spectra (solid lines) of the inverse opals with stop bands in the range of 280-500 nm together with the extinction spectra of nanocrystalline TiO_2 films and MB (black and gray dashed lines). The shaded band indicates the narrowband UVA light applied for "dry" MB photodegradation. (e) Photocatalytic enhancement factor for the TiO_2 inverse opals as a function of stop band position and incidence angle of the monochromatic UVA irradiation [82].

Illumination with narrowband UVA light at 370±10 nm i.e. within the electronic band gap of anatase TiO_2, resulted in a marked non-monotonous variation of the MB degradation rate with the stop band frequency, which could be further adjusted by changing the irradiation incidence angle, Figure 1.12e. A two-fold enhancement of the MB degradation rate was thus reached compared to conventional nanocrystalline TiO_2 films, for the PCs with stop band at ~350 nm either at normal or 20° off-normal light incidence on the (111) planes that shifted the stop band to the same wavelength according to modified Bragg's law. For these best performing inverse opals, the monochromatic UVA excitation matched closely the red edge of the corresponding stop band, where slow photons are expected to localize in the high refractive index part of the PC (titania skeleton), leading to the increase of the optical path length and the acceleration of reaction kinetics. On the other hand, the optimal stop band frequency for dry MB phtodegradation under white light illumination (Xe lamp with cutoff filter at λ<300 nm) was blue shifted to 300 nm, where the detrimental effect of stop band reflection could be most effectively diminished by the strong electronic absorption of TiO_2. Control over the two competing photonic effects i.e. slow photons and the spectrally broader stop band reflectance by fine tuning the L-pseudogap position at energies well within TiO_2 electronic band gap to minimize reflective losses, has been considered as the key factor for the improvement of photocatalytic performance under polychromatic illumination conditions.

PC structuring has accordingly emerged as an advanced, though challenging, approach that may selectively improve light trapping at frequencies of weak materials' electronic absorption, by retarding light propagation at the red/blue edges of the fundamental photonic band gap (PBG) and higher frequency photonic bands [83] as well as by multiple light scattering due to the persistent disorder and imperfections in PCs [84]. Besides extending the optical path of incident photons, PC structures provide a macroporous scaffold that along with the secondary mesoporosity of its inorganic skeleton lead to a network of interconnected macro-mesopores that facilitate reactants adsorption and diffusion during the photocatalytic process [85]. Substantial research has been thus devoted to exploit these advantageous characteristics in combination with materials' compositional properties for the development of visible light activated (VLA) photonic catalysts [59, 86, 87].

1.5 Plasmonic-assisted photocatalysis

Plasmonic metal-semiconductor heterostructures are considered as highly promising systems to moderate the major limitations of weak visible light harvesting as well as poor charge carrier separation and transport that compromise the efficiency of semiconductor photocatalysts [88]. Radiative and non-radiative decay of the localized surface plasmon resonance (LSPR) of subwavelength metallic nanoparticles (NPs), the most common being Au and Ag, provides distinct interaction mechanisms for improving photocatalytic performance via the size-dependent local electromagnetic field enhancement and scattering [89, 90] as well as electron transfer, mostly by means of hot electron injection [91, 92], plasmon-induced resonant energy transfer [93,94] and plasmonic heating to adjacent semiconductor substrates. Specifically, scattering of

electromagnetic irradiation by a metallic sphere with radius much smaller than the incident wavelength induces multipole resonances arising from the collective oscillations of free electrons at the metal NP surface (Figure 1.13a). The most prominent mode is the dipole one, whose frequency is determined by the dielectric function as well as the size, shape and dielectric environment of the metal NPs [95]. Resonant excitation of LSPR on noble metal NPs that exhibit frequencies within the visible spectrum (Figure 1.13a) [96], gives rise to a size-dependent extinction (optical density) that increases with the NP diameter, reflecting the diverse contributions of absorption and scattering that can be tailored by the NP dimensions (Figure 1.13b) [97]. The different scaling laws for the absorption (σ_{abs}) and scattering (σ_{scat}) cross sections that vary as $\sigma_{abs} \propto R^3$ and $\sigma_{sc} \propto R^6$ with the particle radius R, lead to much higher absorption over scattering for small NPs sizes with diameters <50 nm, whereas larger NPs present more efficient scattering [98].

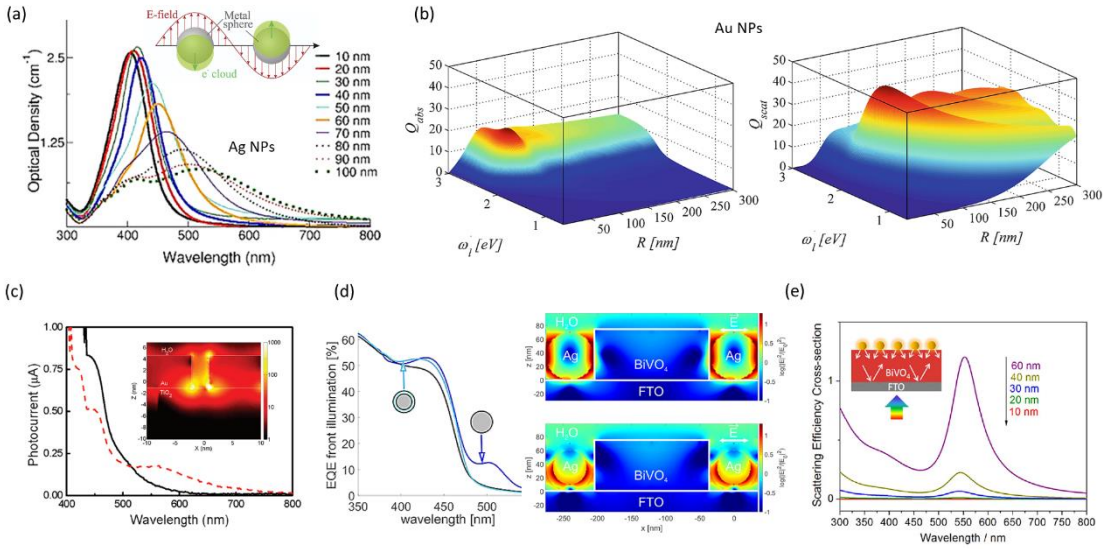

Figure 1.13. (a) Plasmon oscillation for a metallic sphere [95] and extinction spectra of Ag NPs of different diameters [96]. (b) Calculated spectral efficiencies of absorption Q_{abs} and scattering Q_{sc} defined by the ratio of the corresponding cross sections over the particle area ($\sigma/\pi R^2$) as a function of the radius for Au nanospheres [97]. (c) Enhanced photocurrent and electric field intensity (inset) at the Au-TiO_2 photoanode interface [102]. (d) Simulated external quantum efficiency (EQE, equivalent to IPCE) at 1.23 V vs RHE under front-side illumination and the correspeonding electric field intensities at 427 nm for bare Ag and Ag@SiO_2 core-shell NPs in $BiVO_4$ [99]. (e) Size-dependent scattering efficiency cross sections for Au NPs and schematic resonant photon scattering effect for Au-decorated $BiVO_4$ photoanodes under back-side illumination (inset) [100].

A key feature of LSPR is the marked electric field enhancement nearby plasmonic NPs leading to spatially non-homogenous local fields that decrease exponentially (evanescent field) within a few tens of nm from the particle surface [90]. As the rate of photogenerated e^- and h^+ formation in a semiconductor photocatalyst is proportional to the local field intensity, it can be greatly amplified in close proximity to plasmonic NPs (Figure 1.13c) [101, 102]. The LSPR-assisted amplification of the photocatalytic process has been accordingly termed as local/near-field enhancement or light

concentration mechanism [89, 90]. This can be particularly advantageous when the plasmonic NPs are placed at the semiconductor/liquid interface, facilitating e^- and h^+ separation in the semiconductor SCL, while it can be moderated by the intervention of dielectric shells surrounding the plasmonic NPs (Figure 1.13d) [99]. Light concentration at plasmonic metal-semiconductor heterostructures can be further enhanced by tailoring the morphology and spatial distribution of metallic NPs in order to create "hot spots" e.g. at the edges of polyhedral NPs or at nanometer gaps between plasmonic NPs, where enormous enhancements by several orders of magnitude can be achieved [103]. Besides light concentration that pertains to small plasmonic NPs of high σ_{abs}, larger NPs exhibiting enhanced σ_{scat} can increase light harvesting by preferential scattering of the incident light towards the semiconductor [89]. In contrast to the spherical scattering distribution that is expected for metal NPs embedded in an isotropic medium, when they are placed at the interface between two media of different refractive indexes e.g. at the semiconductor–electrolyte interface, they will preferentially scatter light towards the medium of higher *n* [104], i.e. towards the semiconductor, either for front-side illumination (i.e. incident light impinges on the plasmonic NPs first) or back-side illumination. In the latter case, light will be preferentially back-scattered by the plasmonic NPs, increasing its path length through the semiconductor and the probability of absorption, as schematically shown in the inset of Figure 1.13e. It should be noted that for both radiative LSPR enhancement mechanisms, i.e. light concentration and far-field scattering by plasmonic NPs, LSPR absorption/scattering should occur at energies higher than the semiconductor E_g in order to enhance the excitation of e^--h^+ pairs and improve the PEC efficiency.

While radiative local-field enhancement increases the rate of interband transitions in the semiconductor due to the increased local field intensity, non-radiative decay of LSPR may directly excite electron −hole pairs in the semiconductor via the plasmon-induced resonance energy transfer (PIRET) process (Figure 1.14a) [94]. It is based on the dipole-dipole interaction between the plasmonic metal (donor) and semiconductor (acceptor) leading to an upward energy transfer process, whose efficiency is determined by the spectral overlap between LSPR and the semiconductor band gap without the need of direct contact between the plasmonic and semiconductor NPs, as demonstrated for the $Au/SiO_2/Cu_2O$ core-shell particles NPs (Figure 1.14a) [93], while it can be combined with amplification effects due to scattering from large plasmonic NPs with the absorption range of the semiconductor (Figure 1.14b) [105]. Non-radiative decay of LSPR may also lead to hot electron transfer between the plasmonic NP to the semiconductor, which has been one of the most widely investigated LSPR amplification mechanisms of semiconductor photocatalysis, though the corresponding charge transfer efficiency has been rather low [106]. Specifically, non-radiative decay of LSPR may result in the generation of electron−hole pairs separated by the energy of the surface plasmon (e.g. Au and Ag surface plasmons can transfer energies between approximately 1 to 4 eV to hot electrons). The excited electron and hole relax on the fs timescale primarily via electron-electron scattering. However, in the case of a metal–semiconductor heterojunction forming a Schottky junction (when the E_F of the metal lies within the semiconductor E_g), excited electrons with energy exceeding the

corresponding Schottky barrier (tunneling is also likely but with lower probability) can be injected to the semiconductor CB before relaxation (Figure 1.14c) enabling the activation of semiconductor photocatalysts, especially wide-band gap ones, with energies lower than their E_g [107]. Hot electron transfer can be enhanced for plasmonic NPs of small size that have been reported to lower the Schottky barrier and enhance photocatalytic efficiency beyond the semiconductor band gap (Figure 1.14d) [108].

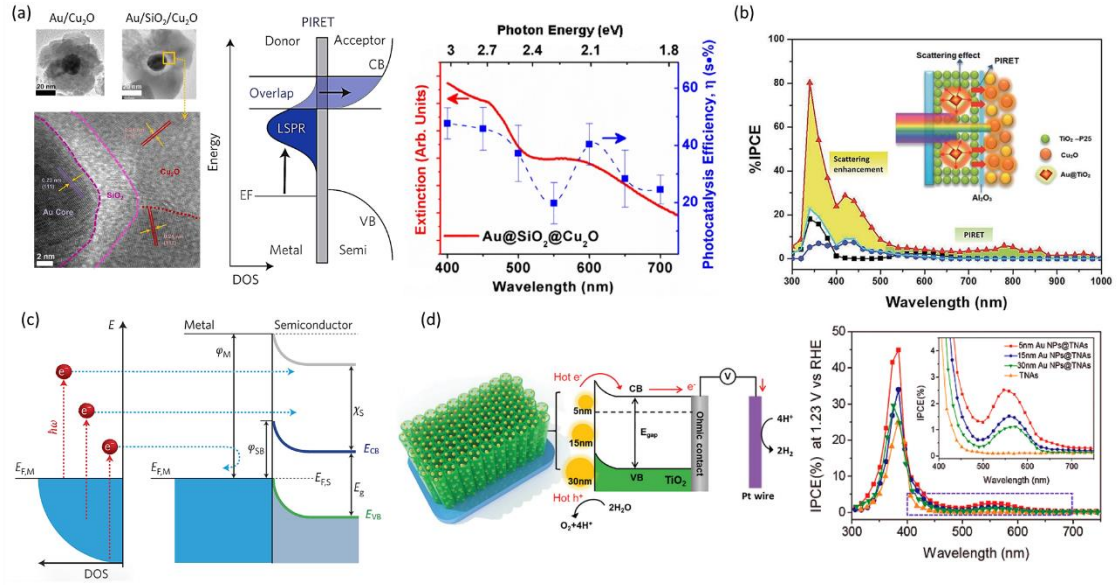

Figure 1.14 Non-radiative LSPR enhancement mechanisms of semiconductor photocatalysis. (a) (left) Schematic of PIRET for a plasmon–semiconductor coupled dipole [94], TEM images of Au@Cu_2O and Au@SiO_2@Cu_2O core-shell NPs (middle) along with their extinction and photocatalytic action spectra (right) [93]. (b) IPCE spectra for TiO_2-Au@TiO_2 (120 nm)/Al_2O_3/Cu_2O photoanodes (red triangles) with respect to their constituents, with shaded areas delineating the scattering and PIRET contributions, schematically shown in the inset [105]. (c) Schematic of hot-electron injection to a semiconductor photocatalyst [91]. (d) Schematic of Au NPs@TiO_2 nanotube (TNAs) photoanode and size-dependent hot electron transfer (left) leading to enhanced IPCE for smaller Au NPs (right) [108].

These effects have been intensely investigated and established for wide band gap MO photocatalysts coupled with plasmonic NPs, the most prominent system being Au-TiO_2, whose photocatalytic response can be extended to the visible range via hot-electron injection primarily over the Schottky barrier at the Au-TiO_2 interface [109]. However, relatively fewer efforts have been devoted to heterojunctions between plasmonic NPs and narrow band gap semiconductors [110, 111], where bi-directional electron flow between metallic and semiconductor NPs may occur depending on the interfacial band-alignment and Schottky barrier height [112], resulting in enhanced charge separation and plasmon resonant energy transfer.

1.6 $BiVO_4$ photonic photocatalysts

Mo-doped $BiVO_4$ inverse opal photoelectrodes were fabricated by using a metal salt precursor that was infiltrated in opal templates consisting of PS spheres Zhou et al. [113, 114]. Short time post heating at 110 °C was applied to increase their contact

area and enlarge the interconnecting mesopores of 30-50 nm in the inverse structure to 90-150 nm macropores after template removal (Figure 1.15a). Among the different PC films, meso-macroporous ones presented the highest performance for water splitting as well as the longest carrier lifetimes. Highly efficient $BiVO_4$ photoanodes for water splitting were reported by Zhang et al. [115] based on the synergy of PC engineering with the LSPR of Au nanoparticles (NPs) in Mo:$BiVO_4$ inverse opal films prepared from PS colloidal crystal templates with diameters of 260 and 320 nm, assembled on top of a 150 nm-thin compact Mo:$BiVO_4$ film to minimize reflection losses (Figure 1.15b). Surface modification of the PC films with 20 nm Au NPs resulted in improved photocurrent density reaching 3.1 mA cm^{-2} at 1.23 V vs RHE under solar light for the PCs with stop band reflection at 513 nm matching the electronic band gap $BiVO_4$ and Au LSPR leading to a marked enhancement of both light harvesting and charge separation by hot-electron transfer (Figure 1.15c).

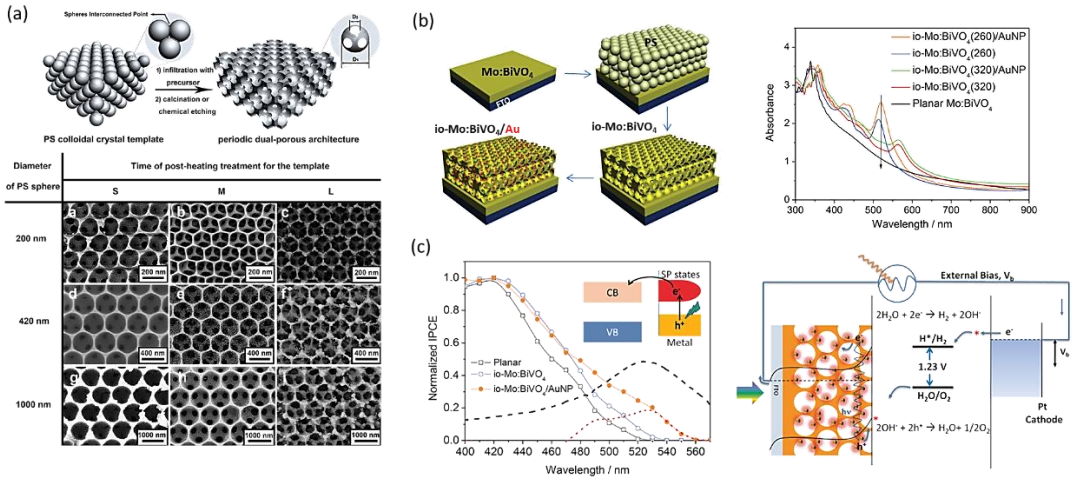

Figure 1.15 (a) Scheme of $BiVO_4$ inverse opal fabrication with controlled porosity and SEM images for templating PS spheres of different diameters and post-heating treatment times (S:0 min, M: 3-5 min, L:10-12 min) [113]. (b) Schematic of the deposition of surface modified Mo-BiVO4 inverse opals (io) by Au NPs (io-Mo:$BiVO_4$/Au) over a Mo-$BiVO_4$ thin film underlayer and the corresponding extinction spectra for two PS templating diameter. (c) Comparison of the normalized IPCE spectra to the maximum value at 420 nm for the io-Mo:$BiVO_4$ prepared from 260 nm PS template and planar Mo:$BiVO_4$ photoelectrodes modified by Au NPs at 1.1 V vs RHE. Red and black dashed lines show the difference in IPCE after Au deposition and the 20 nm Au LSPR extinction, respectively. The inset shows the hot electron injection process, while the right panel depicts the corresponding water splitting mechanism [115].

Surface modification of $BiVO_4$ inverse opal powders fabricated by the ascorbic acid-assisted PMMA-templating method using bismuth nitrate and ammonium metavanadate as metal sources was demonstrated using AgBr along with Pt, Au or Pd NPs at various loadings [116, 117]. The ternary composite 0.17 wt% Pd/AgBr/$BiVO_4$ presented the highest performance on the degradation of 4-chlorophenol under visible light, related to the combined effect of light harvesting, transport and separation of photogenerated charges. Improvement of metal NPs' dispersion and bonding in $BiVO_4$ PCs was reported for Ag/$BiVO_4$ PCs by electrodeposition from $AgNO_3$/$NaNO_3$ aqueous solution [118]. Significant increase of the photocurrent density (nearly five-

fold) and methylene blue (MB) dye degradation rate (three-fold) under visible light were observed in comparison to disordered porous $BiVO_4$ films, attributed to the overlap of the stop band red edge at ~440 nm with the $BiVO_4$ absorption edge and the LSPR of the Ag NPs (size 25-30 nm). Electrodeposition was earlier applied to modify $BiVO_4$ inverse opals with carbon quantum dots (QDs) as alternative sensitizers to metal NPs for water splitting [119]. Combination of carbon QDs' optical absorption with red slow photons matching the $BiVO_4$ electronic absorption, resulted in strong enhancement of the H_2 evolution rate, further assisted by the electron acceptor action of carbon QDs that suppress charge recombination.

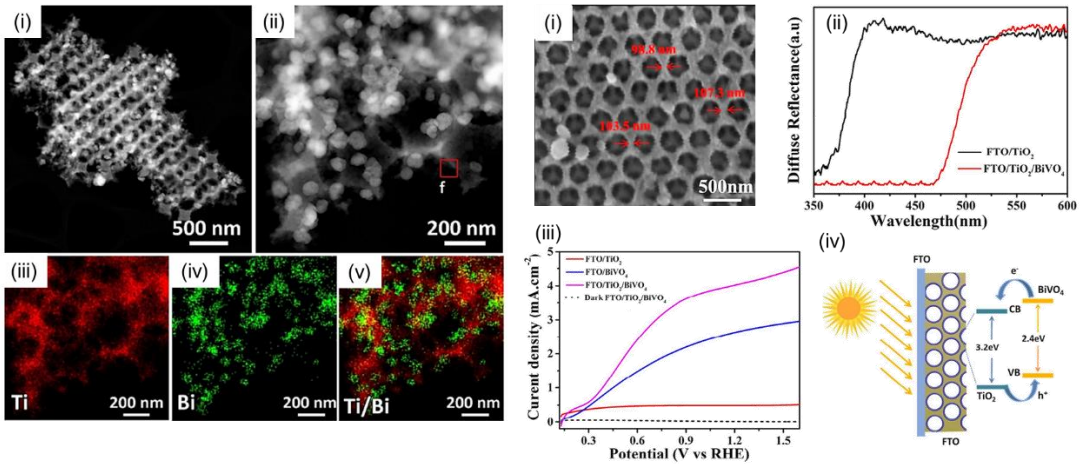

Figure 1.16 (left panel) (i) (ii) TEM images of $BiVO_4/TiO_2$ inverse opals at different magnifications and (iii)-(v) EDX elemental maps of the Ti and Bi distribution of the area shown in (ii) [121]. (right panel) (i) SEM image of $FTO/TiO_2/BiVO_4$ inverse opals, (ii) UV-vis diffuse reflectance spectra of FTO/TiO_2 and $FTO/TiO_2/BiVO_4$ PCs, and (iii) comparative photocurrent density the ternary inverse opal and its constituents. (iv) Scheme of the charge transfer mechanism for the $BiVO_4/TiO_2/FTO$ composite photoanode [122].

$BiVO_4$ was also exploited as visible light sensitizer of TiO_2 in order to improve charge separation and photocatalytic performance. Heterojunction $BiVO_4/TiO_2$ PCs were reported by Zalfani et al. [120] applying hydrothermal treatment of TiO_2 inverse opal powders prepared from 350 nm PS colloidal templates with suitable metal-vanadate solution at different molar ratios [121] leading to the dispersion of $BiVO_4$ NPs (70–90 nm) in the macroporous TiO_2 support. Significant enhancement has been achieved in the visible light photocatalytic degradation rate of rhodamine B (RhB) dye for the 0.2 $BiVO_4/TiO_2$ composite due to the optimal assembly and favorably positioned band edges of the two constituent MOs that promoted interfacial electron transfer from $BiVO_4$ CB to the TiO_2 CB under visible light. A ternary $FTO/TiO_2/BiVO_4$ core-shell inverse opal photoelectrode was fabricated by Zhang et al. [122] by the successive electrodeposition of a $BiVO_4$ film (~29 nm) over a thin (6 nm) TiO_2 layer that was deposited by atomic layer deposition on a conductive F: SnO_2 (FTO) inverse opal of 290 nm diameter prepared by the infiltration of FTO precursor in 408 nm PS colloidal opal templates. In this design, the periodically structured FTO inverse opals served as continuous porous support for TiO_2 and $BiVO_4$ consecutive layers, affording

improved light harvesting and fast electron transport, while TiO_2 acted as an electron scavenger to improve charge separation in the heterojunction with the visible light absorbing $BiVO_4$ layer. A very high photocurrent density of 4.11 mA cm^{-2} was achieved at 1.23 V vs RHE in the presence of sodium sulphite as hole scavenger. A composite $BiVO_4/WO_3$ PC photoanode has been also implemented by Zhang et al. [123] using WO_3 inverse opals of 300 nm pore size onto which a $BiVO_4$ layer was electrodeposited leading to an increase of the wall thickness from 60 to 100 nm and a decrease of macropore size to 250 nm, while leaving intact the periodic structure. Further surface modification by the electrodeposition of cobalt-phosphate (Co-Pi) as water oxidation catalyst, resulted in a marked improvement of photocurrent density to 4.5 mA cm^{-2} at 1.4 V versus Ag/AgCl. This was related to the enhanced light harvesting and interfacial charge separation between the two constituent MOs with suitable band alignment that drive visible light excited electrons from $BiVO_4$ to WO_3.

Although slow photons effects were not systematically explored in all cases, the enhanced performance of $BiVO_4$ PCs corroborates their competence for photocatalytic applications, as recently shown by the markedly improved carrier dynamics in $BiVO_4$ inverse opals due to their nanocrystalline skeleton compared to conventional plate-like materials [124]. Moreover, in spite of its moderate E_g to allow simultaneously the generation of highly reactive oxygen species such as hydroxyl radicals ($^{\bullet}OH$) and superoxide radical anions ($O^{2-\bullet}$) [125, 126, 127], single or composite $BiVO_4$ materials have been utilized for the photocatalytic degradation of organic contaminants under visible light [128, 129, 130]. However, the application of $BiVO_4$ in organics degradation under visible light has been mainly limited to dye pollutants and scarcely reported for colorless recalcitrant water contaminants such as pharmaceuticals [131], while even less results have been reported on the photoelectrocatalytic degradation of refractory emerging contaminants such as antibiotics [132].

CHAPTER 2

Experimental methods

2.1 Materials fabrication

2.1.1 $BiVO_4$ inverse opal film fabrication

$BiVO_4$ inverse opals were fabricated by the liquid phase infiltration of colloidal crystal opal templates with appropriate metal salt precursors, as schematically depicted in Scheme 2.1. Initially, the formation of polymer opal templates of different diameters was carried out by using the vertical and horizontal self-assembly methods. In the vertical method, a substrate was nearly vertically suspended in a vial containing 10 ml of 0.2 wt% suspension of monodisperse polystyrene (PS) spheres and was kept at 55 °C until the solvent fully evaporated over a period of 2 days. On the other hand, in the horizontal method 100 μl of 1.25 wt% PS sphere suspension was deposited directly on a horizontal substrate and was kept at 20 °C until the solvent fully evaporated within a few hours. As water evaporates, capillary forces induce the spontaneous organization of PS microspheres to the face centered cubic (*fcc*) close-packed lattice, yielding high-quality opal templates. Microscope glass slides or fluorine-doped tin oxide (FTO, thickness 2.2 mm, surface resistivity 7 Ω/sq, Sigma Aldrich) conductive glass slides were used as substrates, which have been cleaned prior to their use. Typically, a glass slide was cleaned in Hellmanex™ III followed by ultrasound sonication in acetone (ACS reagent, ≥ 99.5%) and ethanol (absolute, 99.8%), while an FTO slide was cleaned by ultrasound sonication in Hellmanex™ III and propanol-2 followed by dipping in water and blowing with nitrogen. The hydrophilicity of the substrate surface was enhanced by dipping in H_2O:HNO_3 (5:1) for several min. Then, liquid infiltration was applied by dip-coating the PS opal template of specific diameter in a complex metal salt precursor consisting of a mixture of two solutions [133]. The first one was prepared by mixing 0.5 mmol ammonium vanadate, NH_4VO_3 (ACS, 99.0% min), 9 ml of propanol-2 (HPLC, 99.8%) and 0.5 ml of nitric acid (puriss. p.a., 65%) under continuous stirring for 30 min at room temperature, followed by 5 min sonication and the addition of 0.5 mmol citric acid (anhydrous, ACS, 99.5+%) until dissolution. The second one was prepared by dissolving 0.5 mmol bismuth(III) nitrate pentahydrate, $Bi(NO_3)_3 \cdot 5H_2O$ (99.999% trace metals basis) with 0.5 ml acetic acid (glacial, ACS, 99.7+%) [134].

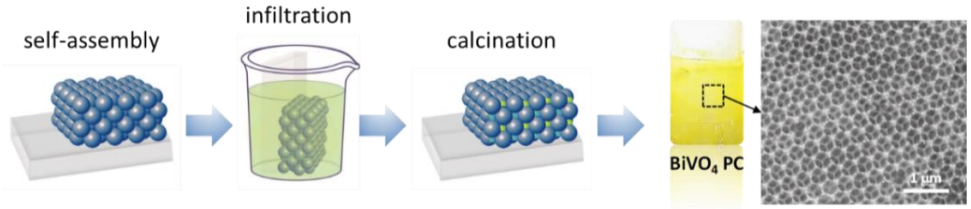

Scheme 2.1 Schematic illustration of the $BiVO_4$ inverse opal film fabrication process including a representative photo and a SEM image of typical films [134].

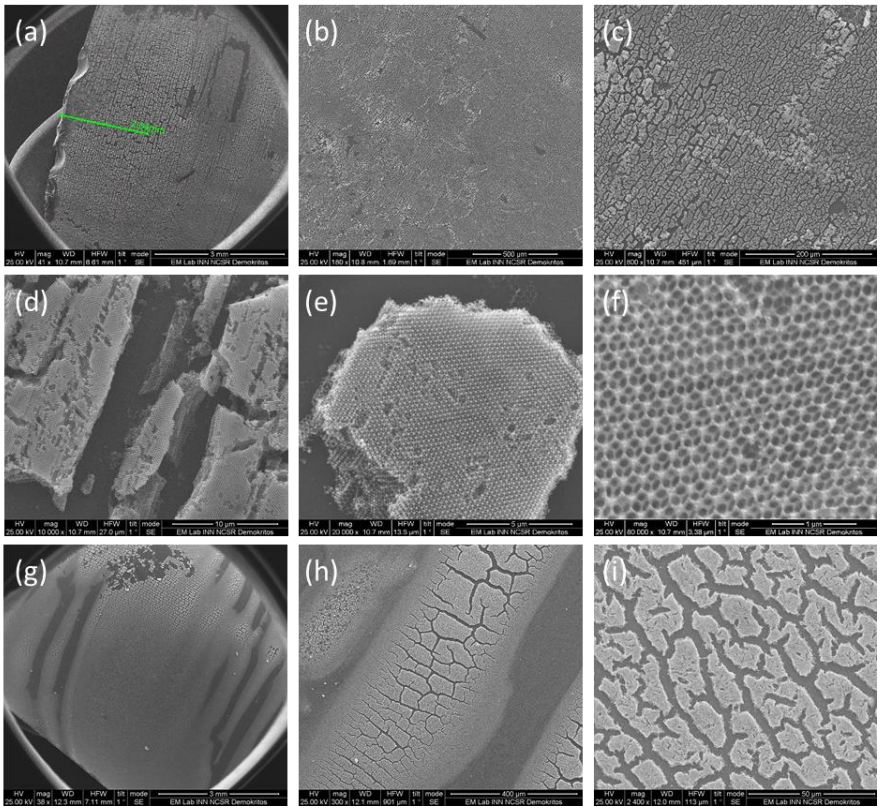

Figure 2.1 Top view SEM images of the inverse opal films obtained from PS templating spheres of (a)-(f) 300 and (g)-(i) 340 nm diameters after calcination at 400 °C at different magnifications.

The two solutions were mixed and stirred for 30 min. The PS opal films were then dipped into the metal salt precursor for 5 min, followed by drying for 1 h at 70 °C. The dip-coating process was repeated three times in order to ensure complete infiltration of the precursor to the opal interstices. Calcination of the impregnated opal films, after drying, was performed at variable temperatures in the range of 350-500 °C to remove the sacrificial PS template and crystallize the amorphous complex precursor in the inverse opal structure, while maintaining its structural integrity. The optimum calcination temperature was thus determined to be 400 °C, where excessive crystallite growth was avoided and the ordered macropore film structure remained intact with photonic domains extending over several microns though with extended cracking due to the (Figure 2.1).

2.1.2 PBG engineering and metal doping of $BiVO_4$ inverse opal films

Controlled PBG formation and tuning was implemented by using monodisperse PS templating spheres with mean diameters of 300, 340, 418 and 460 nm (Microparticles GmbH) with standard deviation SD=10-11 nm, in the form of 5% solids (w/v) colloidal dispersions in deionized water (2.7-3.0% CV) as well as 510 nm spheres (5% CV, SD=0.01 μm, 2.6% solids (w/v), Polybead® PS Microspheres). The $BiVO_4$ photonic crystal films were designated as PC300, PC340, PC418, PC460 and PC510 after the diameter of the templating PS spheres. Disordered $BiVO_4$ PC films were also deposited by mixing 300, 340, 418 and 460 nm PS spheres at equal weights in the colloidal template in order to suppress PBG formation, while preserving the films' macroporous structure and thus serve as reference for photonic enhancement effects.

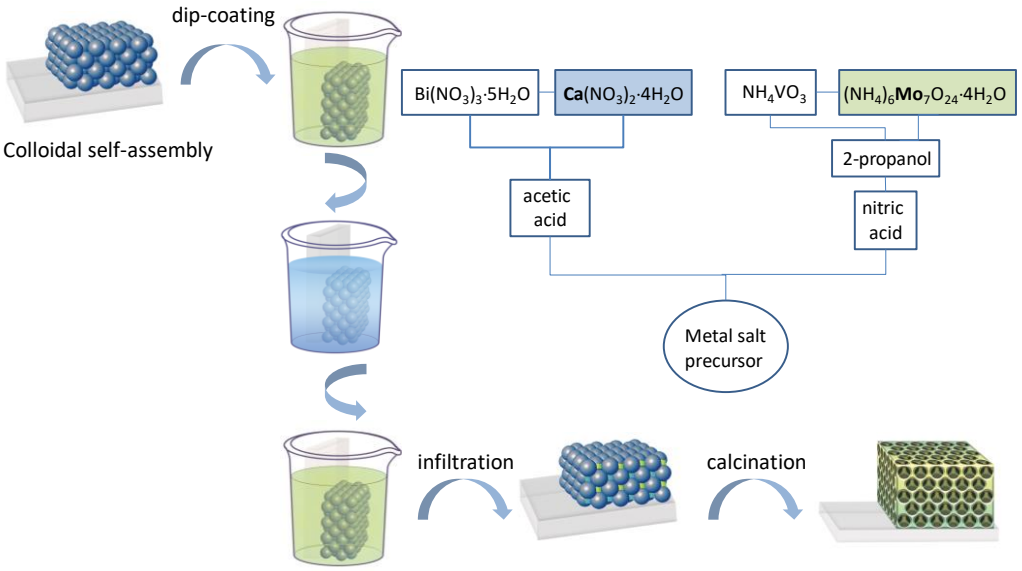

Scheme 2.2 Schematic presentation of the deposition process for metal-doped $BiVO_4$ inverse opals by successive infiltrations of the colloidal opal templates with the Mo and Ca-containing metal salt precursors [134].

Molybdenum (Mo) doping was performed by substituting part of NH_4VO_3 in the metal salt precursor with ammonium molybdate tetrahydrate $(NH_4)_6Mo_7O_{24}{\cdot}4H_2O$ (BioUltra, ≥ 99.0%) at Mo:V molar ratios of 2, 3, and 4%, while calcium (Ca) doping was carried out by replacing part of $Bi(NO_3)_3{\cdot}5H_2O$ with calcium nitrate tetrahydrate, $Ca(NO_3)_2{\cdot}4H_2O$ (ExpertQ®, ACS, 99 - 103%) at Ca:Bi molar ratios of 2, 3, 4, and 5%. Homojunction deposition was performed by three successive infiltrations of the colloidal template by the Mo and Ca-containing metal salt precursors leading to Mo-$BiVO_4$/Ca-$BiVO_4$/Mo-$BiVO_4$ PC films, designated as Mo-Ca-Mo (Scheme 2.2) [134].

2.1.3 Mo-$BiVO_4$ inverse opal films decorated with Ag and/or Au NPs

Inverse opal films were fabricated by the liquid infiltration of self-assembled colloidal templates prepared by the horizontal method using monodisperse PS spheres of 239, 287, 340 and 418 nm diameter (Microparticles GmbH, standard deviation SD=6-11 nm, 2.6-3.0% CV), in the form of 5% solids (w/v) colloidal dispersions in deionized water on cleaned FTO (thickness 2.2 mm, surface resistivity 7 Ω/sq, Sigma Aldrich) conductive glass substrates subjected to surface treatment in H_2O:HNO_3 (5:1) to increase their hydrophilicity [135]. The sacrificial PS opal templates were prepared by the material-saving convective evaporation-induced self-assembly of colloidal spheres on horizontal substrates [71], as reported above. Then, liquid infiltration of the opal films was carried out by dip-coating in the complex metal salt precursor for Mo-$BiVO_4$ at Mo:V molar ratios of 3 %, followed by drying for 1 h at 70°C. The infiltrated films were calcined at 400 °C to remove the PS opal template and crystallize the amorphous precursor in the Mo-$BiVO_4$ inverse opal structure. The fabricated PC films were labelled as Mo-$BiVO_4$ PCXXX with XXX being the templating sphere diameter.

The Mo-$BiVO_4$ PCs were decorated with 10 nm Ag NPs (Thermo Scientific, 0.02 mg/ml suspension, supplied in 2 mM sodium citrate, $4{\times}10^{12}$ NP/ml) or 5 nm Au NPs

(Sigma Aldrich, stabilized suspension in citrate buffer, 5.5×10^{13} NPs/ml) by dropping 15 μL of suspension on the films' surface, which were kept at 50 °C for 60 min, followed by washing with deionized water and ethanol, yielding the Ag/Mo-$BiVO_4$ and Au/Mo-$BiVO_4$ inverse opals, respectively (Scheme 2.3).

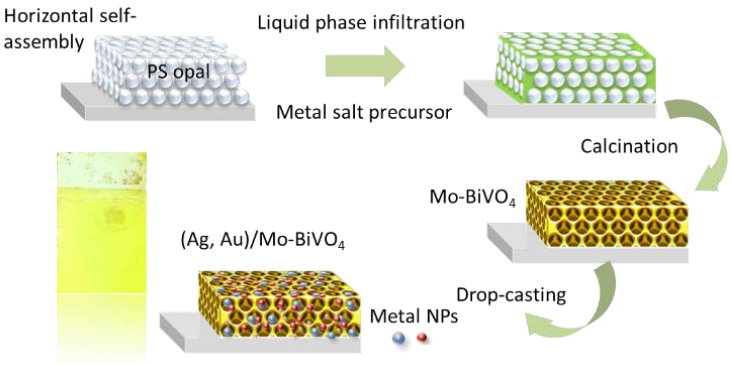

Scheme 2.3 Schematic of the deposition processes for Mo-$BiVO_4$ inverse opals [135].

This process was also applied for the fabrication of co-decorated (Ag, Au)/Mo-$BiVO_4$ films using a mixture of 15 μL with equal amounts of the plasmonic NP suspensions. Plasmonic size effects were also investigated by decorating the photonic Mo-$BiVO_4$ films using 10, 50 and 80 nm Au NP citrate stabilized dispersions (Sigma Aldrich).

2.1.4 Bilayer heterojunction P25/Mo-$BiVO_4$ inverse opals

A Mo-doped $BiVO_4$ inverse opal layer was initially deposited on clean FTO substrates using the liquid phase infiltration of a colloidal opal template of 340 nm diameter PS spheres with the appropriate metal salt precursor and optimized composition (Mo:V molar ratios of 3 %) followed by calcination at 400 °C, which provides the highest photoelectrocatalytic performance (*vide infra*). The horizontal colloidal crystallization method was applied in that case too, in order to rapidly deposit the PS template films without consuming large amounts of colloidal suspension as for the conventional self-assembly methods. The bilayer photoelectrode was then constructed by the deposition of mesoporous nanocrysalline TiO_2 layer [136, 137] on the Mo-$BiVO_4$ films in order to enhance light harvesting and charge separation. Aeroxide® P25 Degussa was utilized as the benchmark TiO_2 photocatalyst due to the mixed phase of anatase and rutile NPs and the concomitant charge transfer [15]. The deposition of the P25 paste on top of the Mo-$BiVO_4$ PC340 films was performed by spin coating (Ossila) with angular velocity 400 rpm for 30 sec followed by drying at 120 °C and post-annealing at 450 °C for 30 min with rate 5 °C/min in order to remove organics (Scheme 2.4).

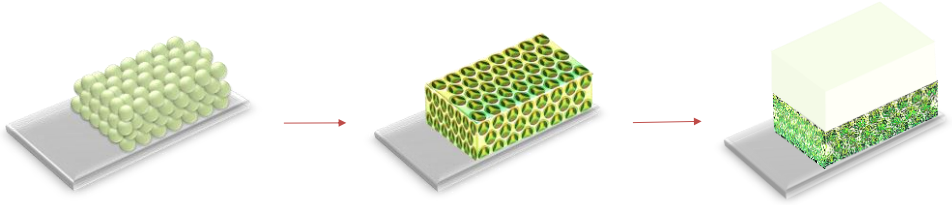

Scheme 2.4 Fabrication process of bilayer P25/Mo-$BiVO_4$ heterojunctions.

2.2 Materials characterization

2.2.1 Electron microscopy

Scanning Electron Microscopy (SEM) is one of the most powerful methods for the analysis of the surface of materials with resolution down to the nanometer scale and the quantitate determination of the sample chemical composition by detecting the energy dispersion of the produced X-rays (Energy Dispersive X-ray-EDX spectroscopy). In a typical SEM setup (Figure 2.2a) an electron beam (primary electrons with typical energies 1-30 keV) generated by the electron gun (electron source and accelerating anode) is focused on the sample surface to a nm-size spot that is scanned across the specimen to generate images of the sample surface and composition based on different electron-matter interactions such as the generation of backscattered and secondary electrons and X-rays [138].The backscattered are high energy electrons, which originate from the interior of the sample and provide information about the elemental composition of the sample, whereas the low energy secondary electrons (0-50 eV) are ejected from the conduction or valence bands of the specimen atoms by inelastic scattering interactions with the primary electrons, and thus originate from within a few nanometers below the sample surface. The signal from secondary electrons is accordingly localized at the point of impact of the primary electron beam, allowing to collect images of the sample surface with high resolution, which is largely determined by the spot size of the incident electron beam.

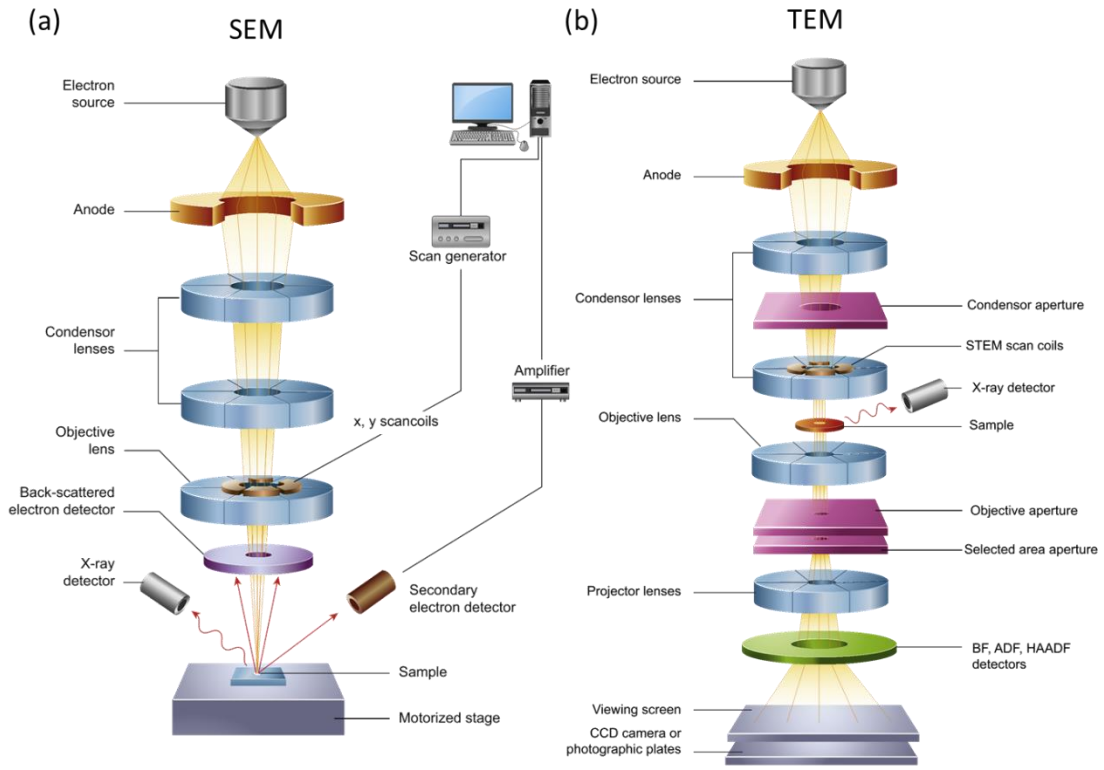

Figure 2.2 Schematic diagrams of the core components of (a) SEM and (b) TEM microscopes including the electron source and accelerating anode, electromagnetic lenses to focus the electron beam before and/or after the specimen and different detectors to collect the emitted signals from the irradiated specimen [138].

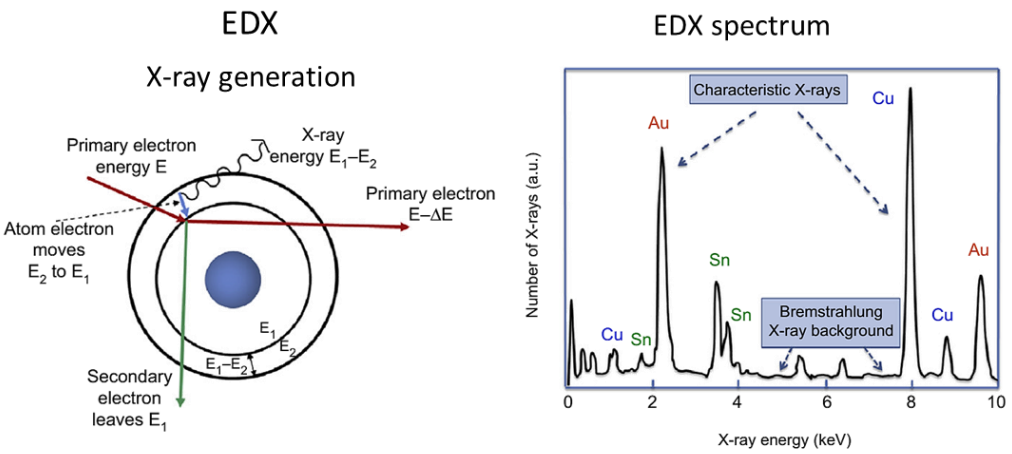

Figure 2.3 Characteristic X-ray generation when primary (incident) electrons knock an electron out of an atom, followed by the transition of an electron from an outer, higher-energy shell to the empty energy level vacated by the secondary electron, leading to characteristic X-ray emission (EDX) spectrum of the specific elements that allows quantification of the materials composition [138].

The number of secondary electrons emitted from a sample depends on the angle of incidence of the primary electron beam that determines the scattering volume. As the angle of incidence increases, the surface becomes more parallel to the beam (increased tilt) and there is a larger intersection of the electron interaction volume with the surface, and therefore enhanced emission of secondary electrons. Steep surfaces and edges tend to be brighter than flat surfaces, leading to images with a well-defined, three-dimensional appearance. In addition, the interaction of the focused electron beam with the specimen results in the emission of characteristic X-rays (Figure 2.3), whose energy dispersion can be detected by an EDX detector in line-of-sight of the specimen inside the microscope vacuum chamber. As the emitted EDX spectra are distinctly related to a specific element, this technique has evolved to a valuable tool for the spatially resolved analysis of the sample chemical composition that can supplement SEM imaging [138].

In this work, the films morphology and composition was investigated by a FEI Quanta 200 Inspect SEM coupled with an EDX analyzer (EDXDX4). The electron beam was thermionically emitted from a tungsten filament cathode and accelerated with a voltage of 25 kV on top of the microscope column. The generated beam of 3-5 nm was focused on the sample by a set of electrostatic and magnetic lenses, as well as a scanning coil. The samples were coated with thin layer of Au metal under vacuum, in order to avoid electrostatic charging for the poorly conducting specimens and distortion of the SEM images.

Transmission electron microscopy (TEM) is an analytical technique with high resolution power down to the atomic scale, where the electron gun typically accelerates electrons by applying 80-300 kV to give them sufficient energy to pass through a very thin sample, typically thinner than 200 nm Then, a set of electromagnetic lenses is used to focus the high energy electrons to the sample. The transmitted electrons that are scattered as they pass through the sample, either

elastically or inelastically, form an image that is magnified and focused by objective lens onto a fluorescent screen or is detected by charge coupled device (CCD) camera. Depending on the thickness or mass of the sample a TEM image is formed related to the absorption or scattering of electrons by the sample. Areas of greater thickness or composed of heavier elements are imaged darker because fewer electrons from these areas manage to reach the detector due to scattering or absorption by the sample. Areas without a sample are shown bright. Bright field (BF) or dark field (DF) images can be formed from unscattered and scattered electrons by using an aperture (objective aperture) positioned in the back focal plane of the objective lens (Figure 2.2b) that blocks scattered or unscattered electrons, respectively [138].

In addition, diffraction contrast image can be formed as a result of elastic (Bragg) scattering of electrons by the sample. The local diffraction pattern is formed in the back focal plane of the objective lens and magnified by the projector lenses onto the recording device. Analysis of the diffraction patterns can determine the type of crystal lattice, lattice parameters and local crystal orientation. High-Resolution Transmission Electron Microscopy (HRTEM) of ultrathin specimens provides high-resolution images at the atomic-scale by the interaction of elastically scattered electrons by different crystal planes allowing imaging of the atom positions, interfaces and crystal defects. EDX analysis can be also performed in TEM at much higher spatial resolution than in SEM, because X-rays originate from the very thin electron transparent TEM specimen (<200 nm) compared to the large interaction volume in SEM. In this work the films were characterized using a FEI Talos F200i scanning TEM operating at 200 keV, equipped with a windowless EDX microanalyzer (6T/100 Bruker).

2.2.2 X-ray diffraction

X-ray diffraction (XRD) is the basic experimental technique used to determine the crystal structure materials and all the related structural information based on the diffraction of X-rays from periodic crystal lattices. Elastic scattering of monochromatic X-rays off the (hkl) lattice planes of a crystalline material results in distinct maxima of the scattering amplitude i.e. diffraction peaks, due to constructive interference when Bragg's condition is met: $2d_{hkl}\sin\theta = n\lambda$, where d_{hkl} is the interplanar distance of successive (hkl) lattice planes θ is the angle of incidence, n the order of diffraction and λ the wavelength of the X-rays. In the case of polycrystalline or powder sample consisting of a large number of randomly oriented crystallites allowing all possible orientations of lattice planes, Bragg condition from the (hkl) crystal planes results in a diffraction cone with semi-vertex angle 2θ with respect to the constant incident wavevector of the X-ray beam (Debye-Scherrer method) [139].

In this work, XRD measurements were performed in the standard Bragg-Brentano geometry on a Siemens D5000 powder diffractometer with CuKa radiation using a step size of 0.03° and a counting time of 11 s/step. Specifically, X-rays generated in a Cu tube passes through a system of parallel metal plates (soller slit) in order to reduce the axial beam divergence and then from the aperture slits, before it is directed to the material that is placed on the sample holder at the goniometer of the instrument.

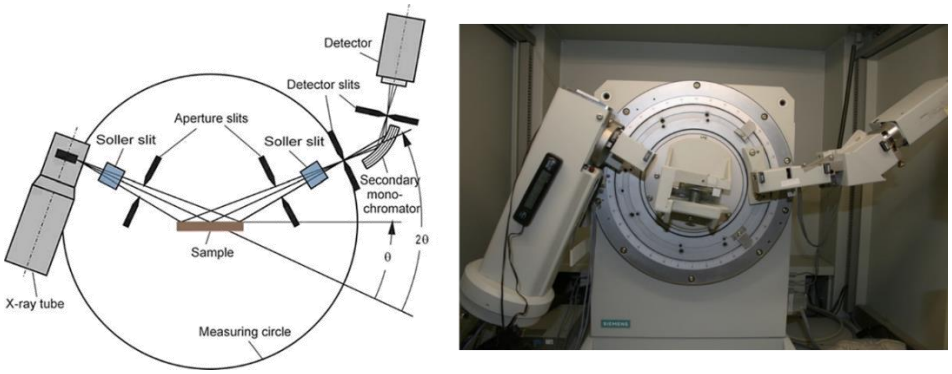

Figure 2.4 (left) The Bragg-Brentano geometry and (right) the X-ray powder diffractometer, Siemens D5000.

The scattered beam passes through the anti-scatter slit, which reduces scattering from other causes (air, fluorescence, etc.) and through the detector slit, which determines the beam width that reaches the detector and, therefore, the instrumental resolution. Finally, a graphite monochromator cuts off the CuK_β radiation and the beam enters the detector. In the Bragg-Brentano geometry, the X-ray tube is fixed, while the sample and the detector rotate simultaneously at a speed ratio of 2:1 i.e. θ-2θ scan, to vary the orientation of the lattice planes with respect to the incident X-ray beam. The scattered beam can be measured over a range of 2θ angles from 10° - 120°.

2.2.3 Raman spectroscopy

Raman spectroscopy is based on the inelastic scattering of monochromatic radiation by matter (gas, liquid, solid, amorphous or crystalline) mainly applied as vibrational spectroscopy to obtain accurate fingerprint information on molecular vibrations and phonon modes as well as lattice dynamics of the investigated material system. When monochromatic light is incident on a sample, most photons are elastically scattered (Rayleigh scattering, $\omega_{scat} = \omega_{laser}$), whereas a very small fraction of photons (about 1 in 10 million) is inelastically scattered leading to the appearance of additional spectral bands symmetrically shifted on either side of the elastic one at smaller $\omega_{scat} = \omega_{laser} - \omega_i$ (Stokes) or higher frequencies $\omega_{scat} = \omega_{laser} + \omega_i$ (anti-Stokes). The corresponding spectral shifts with respect to the laser excitation frequency ω_{laser} correspond to the frequencies of specific molecular vibrations or phonon modes of a crystal (Figure 2.5). Specifically, the Stokes and anti-Stokes sidebands for 1st-order scattering correspond to the excitation (creation) and relaxation (destruction) of a normal vibrational mode (molecule) or lattice vibrational mode (phonon) for a solid at frequency ω_i with intensities varying with ω_{laser}^4 and the Stokes lines (fundamental vibrational state) presenting the highest relative intensity [140]. Raman spectrometers rely on the utilization of highly monochromatic lasers in the UV-Vis-NIR range along with Rayleigh rejection filters (edge or notch) that attenuate elastic scattering as close as possible to the frequency of the laser line allowing the detection of the much weaker ($I_{\text{Raman}} \sim 10^{-3} I_{\text{Rayleigh}}$) Raman bands by highly sensitive detectors (the most common nowadays being charge-coupled devices CCDs) after being dispersed with suitable diffraction gratings. Combination with microscopes offers the possibility for spatially resolved measurements and spectral mapping of materials surfaces.

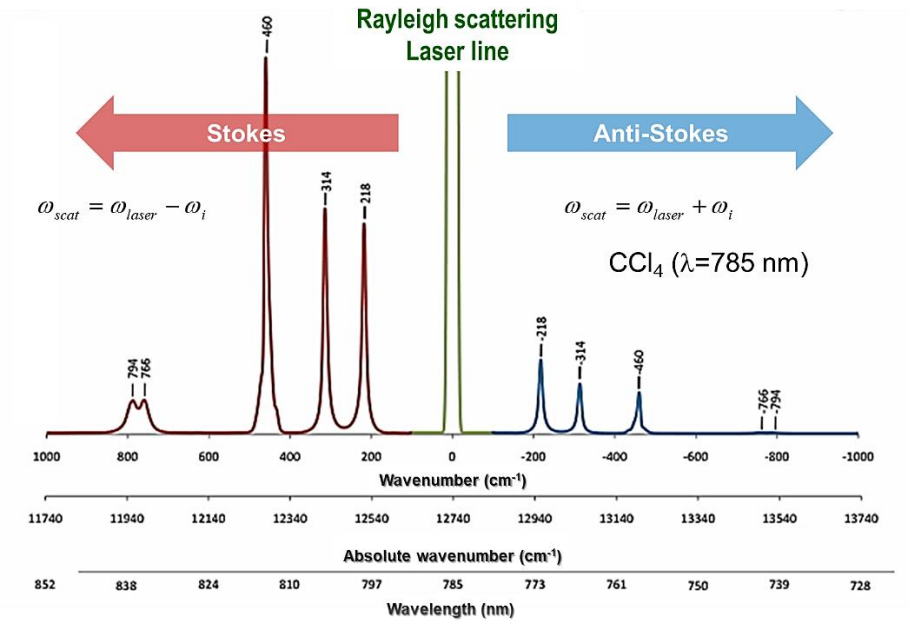

Figure 2.5 Raman spectrum of CCl_4 at 785 nm laser excitation, showing the Rayleigh and the non-elastic Stokes and anti-Stokes bands at different frequency scales

In this work, micro-Raman spectra were acquired in backscattering configuration using an inVia confocal Raman microscope by means of a ×50 (NA=0.75) objective with 785 nm laser excitation at low level power density (0.1 mW/μm²) (Figure 2.6). Specifically, a laser diode emitting at 785 nm (near infrared-NIR) produces a monochromatic beam that is guided by a series of motorized optics to the edge filter, reflected and directed to the optical microscope equipped with different objective lenses to focus the laser beam on the sample surface at a broad range of laser powers regulated by motorized neutral density filters of variable optical density. The beam is backscattered from the sample to a dielectric edge filter with Rayleigh rejection cutoff at about 100 cm^{-1} so that the Stokes bands can be measured. The inelastically scattered beam passing through the edge filter is focused by a lens into the 65 μm entrance slit.

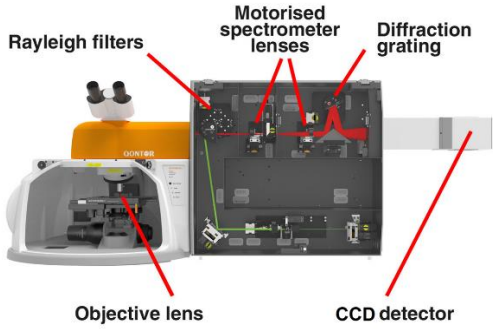

Figure 2.6 Typical setup of the inVia™ confocal Raman microscope [141].

It is then reflected on a prismatic mirror that directs it to a 1200 lines/mm diffraction grating. The diffracted beam is reflected to the other side of the mirror and focused by a lens onto the CCD detector (the focal length is 250 mm) that records the Raman spectrum of the sample. Spectra were obtained by continuous scans in the range of

100-3200 cm^{-1}, while frequency shifts were calibrated by an internal Si reference. Raman peak analysis was performed with Renishaw's WIRE program.

2.2.4 Infrared spectroscopy

Infrared (IR) spectroscopy is based on the direct absorption of IR radiation by a material, causing the excitation of normal vibrational modes or collective lattice vibrations/phonons in molecules or crystals, respectively. IR absorption by a material takes place when the frequency of the incident radiation equals the frequency of a vibrational mode for resonance to occur. The basic selection rule for a vibrational mode to be IR-active is that at least one component of the dipole moment tensor changes in relation to the distance from equilibrium position i.e. the derivative of the dipole moment with respect to the normal coordinate Q_k is non-zero $\left(\frac{\partial \mu_q}{\partial Q_k}\right)_0 \neq 0$, which is the basic selection rule for IR spectroscopy [105]. This contrasts, Raman spectroscopy, where the derivative of the molecule polarizability or the electric susceptibility for solids should be non-zero with respect to the normal coordinate, rendering the two techniques complementary, depending on the materials' symmetry.

IR absorption is commonly measured by Fourier Transform infrared (FTIR) spectrometers, where spectrum analysis is carried out by the Fourier transform of the interferogram recorded by a Michelson interferometer [142]. In that case, a collimated beam from a polychromatic IR source (usually SiC), is directed to a beam splitter causing ideally 50% light refraction towards the fixed mirror and 50% transmission towards the moving mirror (Figure 2.7a). Light is reflected from the two mirrors back to the beam splitter and some fraction of the original beam passes into the sample compartment, where it is focused on the sample. On leaving the sample compartment light is refocused on the detector. The difference in optical path length between the two arms to the interferometer is known as *retardation* or *optical path difference*. An interferogram is thus obtained by recording the signal from the detector as a function of retardation that provides the spectral information recovered by Fourier transform processing. When an absorbing sample is present the background interferogram is modulated by the presence of IR absorption bands in the sample.

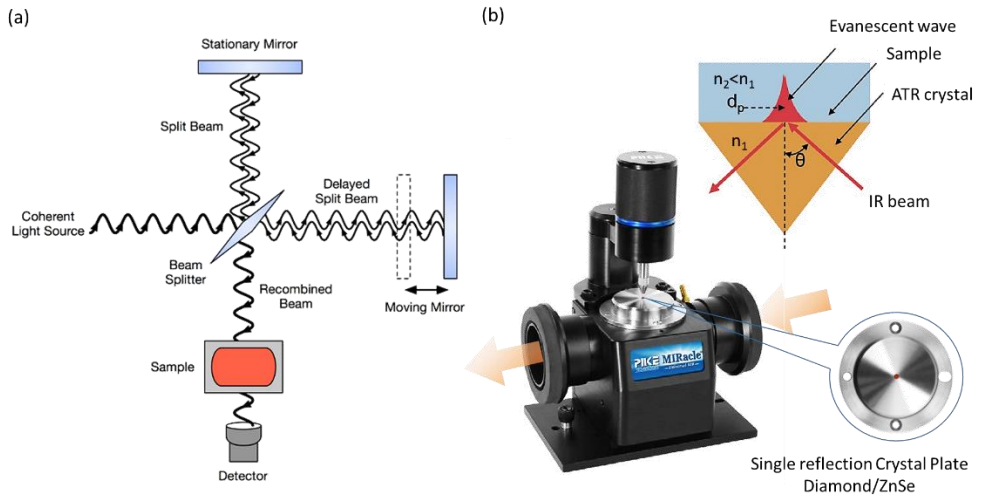

Figure 2.7 (a) Schematic diagram of a Michelson interferometer for FTIR spectroscopy and (b) Schematic of ATR and accessory using a single reflection diamond/ZnSe crystal plate.

The Attenuated Total Reflectance (ATR) technique is widely used for obtaining FTIR spectra from materials that are not transparent to IR radiation. In this technique, the sample is in contact with an internal reflection element, typically a high refractive index crystal that does not absorb in the measurement range. The IR beam is directed through the ATR crystal to the sample, which must have a lower n in order to achieve total reflection at the crystal/sample interface. Upon reflection the exponentially decaying IR beam (evanescent wave) enters the sample at a shallow depth (a few μm) and undergoes absorption resulting in the attenuation of total reflection (Figure 2.7b). The penetration depth depends on the angle of incidence, the ATR crystal refractive index as well as the wavelength, which requires correction to accurately record the absorption intensities of the material. In this work, ATR-FTIR spectra of the films were recorded on a JASCO 470Plus FT-IR spectrometer equipped with a PIKE MIRacle ATR accessory using a single reflection diamond/ZnSe crystal plate (Figure 2.7b)

2.2.5 UV-visible spectroscopy

The optical properties of the films and the monitoring of the pollutant concentration during photocatalytic tests were studied by ultraviolet-visible (UV-Vis) spectroscopy [143]. Absorbance (Abs), transmittance (T%), specular (R%), and diffuse reflectance (DR%) measurements were performed with the Agilent Cary 60 UV-vis spectrometer with the addition of accessories (Figure 2.8).

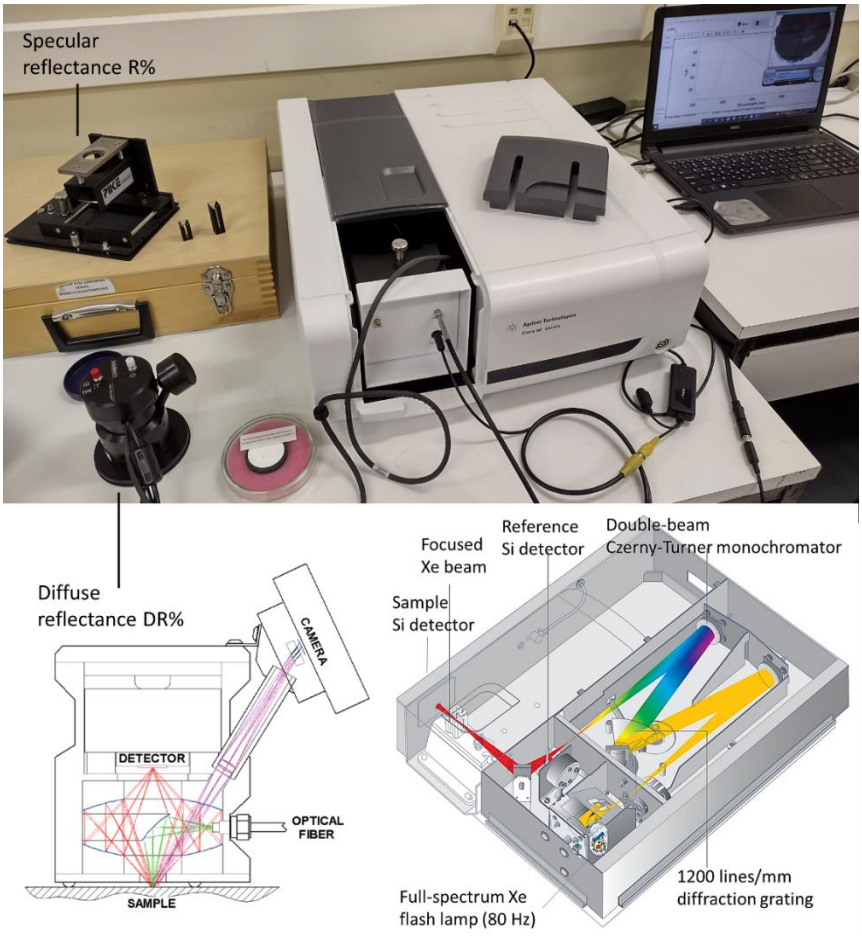

Figure 2.8 Photo and optical design of the UV-vis spectrometer with the addition of accessories for R% and DR% reflectance measurements.

The spectrophotometer consists of a pulsed Xe lamp (80 Hz), a double-beam Czerny-Turner monochromator that covers the spectral range 190–1100 nm with resolution of ≤1.5 nm, a holographic diffraction grating of 1200 lines/mm, two Si photodiodes as detectors for simultaneous measurement of the sample and reference beams as well as a scan speed of up to 24000 nm/min and a maximum rate of 80 data points/s. The pulsed Xe light beam is guided by mirrors to the monochromator and then it is focused to a beam-splitter that reflects part of the beam towards the reference Si detector that measures the reference intensity (I_0). The other part of the beam after focusing (the minimum spot size being 1.5 x 1.0 mm) is directed to the sample holder and then to the sample Si detector that measures the sample intensity (I). By measuring the intensities of the two beams I_0 and I (double beam measurement), the transmittance $T = I/I_0$ is derived, where normalization to the reference signal accounts for any fluctuations in the Xe lamp intensity.

Transmittance-absorbance measurements

According to the Lambert-Beer law, the concentration and absorbance of a substance are proportionally related as

$$\mathrm{Abs} = -\log(I/I_0) = \varepsilon L C$$

where ε is the absorption coefficient [M^{-1} cm^{-1}], C is the concentration [M] and L the optical path length [cm]. This relationship is used to determine spectrophotometrically the concentration of organic pollutants during the photocatalytic reaction based on the values of ε and L. The transmittance T% for films and absorbance Abs spectra for the pollutant solutions are acquired by the following procedure: the spectrum of air or the cell filled with the solvent is initially measured as reference spectrum (blank) that provides the baseline correction. Then, the sample is attached to a metallic sample holder or a suitable cell holder in the sample compartment, followed by spectral acquisition with the sample in the optical path. The software divides the sample by the reference spectrum, giving the final T% or Abs spectra.

Specular reflectance measurements

Specular reflectance measurements were performed by aligning the specular reflectance system 15° (PIKE, UV-Vis 15Spec) in the path of the focused Xe beam within the spectrometer compartment (Figure 2.9). The reflected beam from the surface of the film, which is placed horizontally on a suitable mask, is directed to the sample Si detector of the spectrometer to obtain the specular reflection spectrum. The reference (blank) measurement for the calibration of the R% specular reflectance spectra was done by using a UV-enhanced reflectance Al mirror.

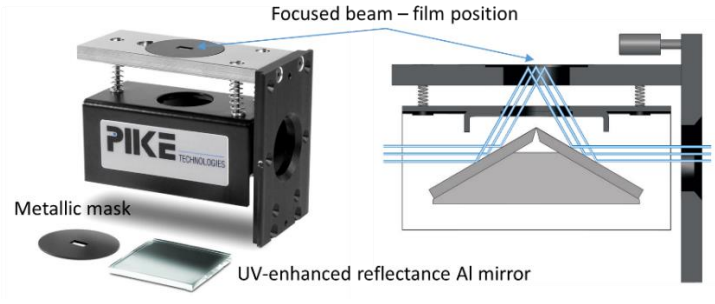

Figure 2.9 Specular reflectance accessory and optical path for 15° R% measurements.

Diffuse reflectance measurements

Diffuse reflectance measurements were performed with the remote diffuse reflectance accessory (Barrelino) that is coupled to the Cary 60 spectrometer (Figure 2.8). The Barrelino is a device for optical analysis of small-size regions (~1 mm) with diffuse response using fiber optic interface. The monochromatic beam emitted by the spectrometer is focused onto 1.5 m optical fiber that is connected to the optical system, which includes an ellipsoidal collecting mirror that focuses the beam to a spot of less than 1 mm at the surface of the sample. The diffuse reflected light from the sample, after multiple reflections on the two axisymmetric ellipsoidal mirrors surrounding the device, is focused on the upper focal point of the mirrors, where a built-in Si detector is mounted, which is electronically connected to the recording system of the Cary 60 spectrometer bypassing the internal sample Si detector. The specular reflection is not recorded as it is blocked by the collecting mirror of the beam entering via the optical fiber. The device has a built-in digital camera for the magnified view of the sample and the precise selection of the sampling point for analysis. Before the measurement, a tablet (HALON) with approximately 100% reflectance over the entire UV-vis spectrum was used as a reference (blank) measurement to calibrate the DR% spectra.

The DR% spectra were further used to estimate the films' absorbance applying the Kubelka-Munk infinite medium approximation for thick samples in which absorption and diffuse scattering are significant, using the remission function [144, 145]:

$$F(R_\infty) = \frac{K}{S} = \frac{(1 - R_\infty)^2}{2R_\infty}$$

where K is the absorption coefficient and S is the scattering coefficient, while R_∞ is the reflectivity for "infinite" film thickness, which is approximated by the experimentally measured DR % [146]. It should be noted that this relation corresponds physically to a medium that reflects the same amount of light regardless of the substrate reflectance.

2.2.6 Photoelectron spectroscopy

X-ray Photoelectron Spectroscopy (XPS) is one of the most widely used surface sensitive analytical techniques, which relies on the photoelectric effect and provides quantitative information about the surface chemical composition of materials and the concentration of individual elements. Surface analysis by XPS involves the irradiation of a material under ultrahigh vacuum conditions by a monochromatic X-ray beam that causes photoionization and emission of photoelectrons, whose kinetic energy is measured [147]. A typical spectrometer consists of a soft X-ray source (usually Al K_α or Mg K_α anodes) and a monochromator, an electrostatic lens system, a hemispherical electron analyzer and the detector (Figure 2.10a). The emitted electrons are directed through the lens to the analyzer, where they are separated depending on their kinetic energy and are directed to the detector. The X-ray energy hν is equal to the binding energy (BE) plus the kinetic energy (KE) of the emitted electrons and the spectrometer work function (Φ_{spec}). The binding energy (BE) of an electron is accordingly determined by the relation: $BE = h\nu - (KE + \Phi_{spec})$ [147].

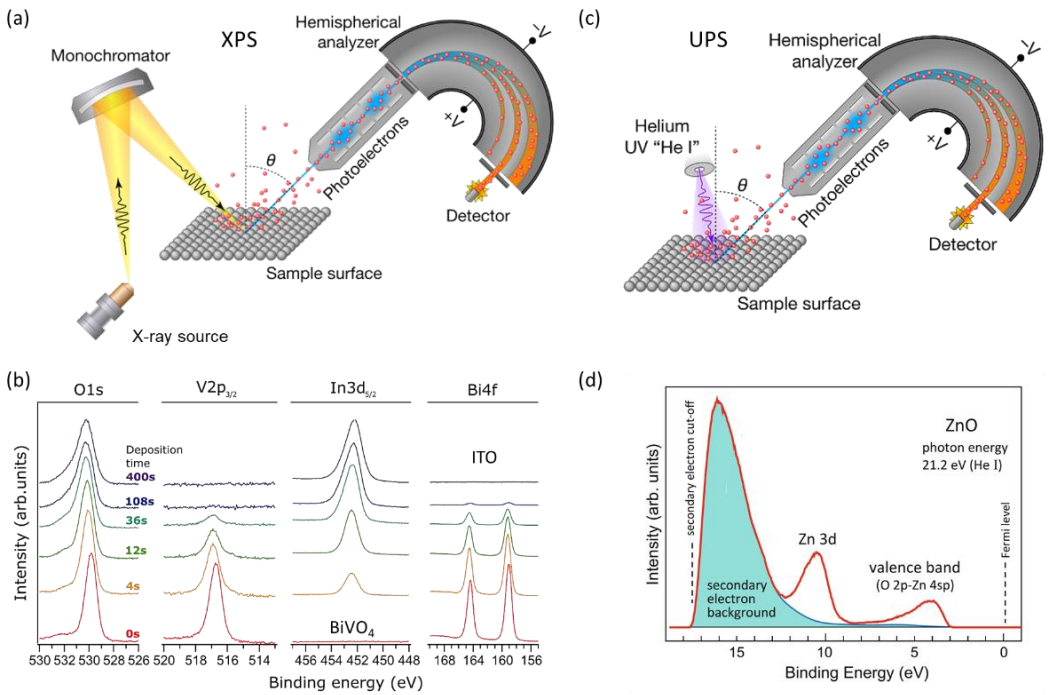

Figure 2.10 (a) Schematic diagram of XPS [148]and (b) evolution of the O 1s, V $2p_{3/2}$, In 3d5/2, and Bi 4f core-level XP spectra for the $BiVO_4$/Sn-doped In_2O_3 (ITO) interfaces for the denoted deposition times of ITO films with increasing thickness over $BiVO_4$ [149]. (c) Schematic diagram of UPS [148] and (d) UPS spectrum of a ZnO crystal using the He I resonance line (21.2 eV) as excitation source [150].

The XP spectrum represents the number of emitted photoelectrons as a function of BE, which can be used to identify each specific element according to its electron configuration, oxidation state as well as its amount within the XPS sampling volume (Figure 2.10b). To generate atomic percentage values, the raw XPS signal is corrected by dividing the intensity by a relative sensitivity factor and normalized over all of the elements detected besides hydrogen. In addition, XPS is an inherently surface sensitive technique due to the short inelastic mean free path (IMFP) of free electrons within a solid. Electrons with KE of ~1000 eV have an IMFP of a few nm. Using Beer's law, it can be shown that about 95% of the emitted electrons will escape from a depth of 10 nm or less, and 10 nm is often referred as the information depth for XPS [147]. In this work, XPS was performed on PHOIBOS 100 (SPECS) hemispherical analyzer using Mg-Kα 1253.6 eV X-ray source. The spectrometer was calibrated on clean Ag, Cu, and Au samples for which the Ag $3d_{5/2}$, Cu $2p_{3/2}$, and Au $4f_{7/2}$ peak positions were determined at 368.3, 932.7, and 84 eV, respectively. The XP spectra were collected at 52° take-off angle using a pass energy of 7 eV. The adventitious C 1s peak set to 284.8 eV was used for charge referencing. Fitting was performed using XPS Peak Fit and Shirley background subtraction.

Ultraviolet photoelectron spectroscopy (UPS) has the same operating principle as XPS and is used to study the electronic structure of a material, as the Fermi edge and work function (WF) can be accurately determined. The emission of photoelectrons from the valence band of a material is carried out by ultraviolet (UV) radiation, most frequently He I radiation (21.22 eV) (Figure 2.10c). A typical UP spectrum consists of

emission peaks from the valence band, shallow core levels and the secondary electron background generated by inelastically scattered photoelectrons (Figure 2.10d). The WF is determined from the UP spectrum as WF= hν – ΔE, where ΔE is the width of the spectrum from the Fermi level to the secondary electron cut-off position [150]. In this work, the WF vs vacuum was calculated as the difference between the incident photon energy of 21.2 eV of the He I source and the secondary electron cut-off binding energy, which was determined from the intersection of the linear extrapolation of the spectrum edge with the baseline. Likewise, the energy difference E_F–E_{VBM} was determined from the intersection of the linear extension of the valence band edge near the Fermi level with the baseline. UPS also exhibits greater surface sensitivity than XPS because of the relatively shorter IMFP of emitted electrons at lower KE of 10–150 eV leading to an approximate information depth of 2-3 nm.

2.2.7 Photoluminescence spectroscopy

Photoluminescence (PL) spectroscopy is based on the emission of light following the radiative release of energy by a material that relaxes for excited electronic states in the ground state. It is a non-contact, nondestructive spectroscopic method that is widely applied in the case of semiconductor photocatalysts, as it is directly related to their electronic structure and especially to the presence of a direct or indirect energy gap and the photoinduced e^- – h^+ recombination that competes with the "beneficial" interfacial photocatalytic reactions. In this work, PL spectroscopy was applied in order to investigate the existence of charge separation phenomena. PL measurements were performed using the focused beam of a 405 nm laser diode as excitation, while the PL signal was collected through a long pass 435 nm filter (2" FGL435S, Thorlabs) by a fiber optic spectrometer (LR1, ASEQ Instruments).

2.2.8 Photocatalytic experiments

The photocatalytic activity of the films was studied by photodegradation experiments of water soluble pollutants under visible (Vis) radiation. In this work, the pharmaceutical substance salicylic acid (SA) was selected as model water pollutant. SA is a transformation product of acetylsalicylic acid, which is used in the production of anti-inflammatory and analgesic drugs such as aspirin, as well as an additive in cosmetics and food, and it is systematically detected in the effluents of treatment plants and in surface water near sewage treatment plants [151, 152]. Furthermore, SA is a colorless water pollutant with no electronic absorption in the visible range that presents research interest, as the photocatalytic evaluation of PCs has mainly been reported on colored dye pollutants [59]. In that case, photocatalytic decomposition can be induced by the visible light excitation of the dye molecules followed by electron transfer to the CB of the semiconductor such as TiO_2 (self-sensitization mechanism), which finally causes its self-decomposition [153]. This process can be enhanced for PC photocatalysts by the spectral matching of the dye electronic absorption with slow photon regions, precluding the validation of the photocatalyst's activity in the visible. SA, unlike dyes, absorbs at $\lambda < 330$ nm (Figure 2.11), well below the PCs' stop bands in water, and thus precludes any photonic enhancement by means of slow photon overlap with its absorbance.

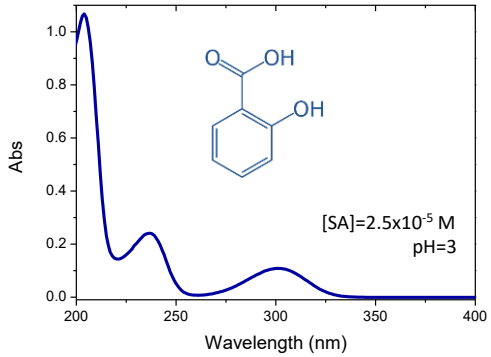

Figure 2.11 Absorbance spectrum of SA aqueous solution of 2.6 $\times 10^{-5}$ M at pH=3.

The experimental procedure is as follows: The PC films (area 1 cm^2) were placed horizontally at vials containing 3 ml of 25 μM SA aqueous solution, where they were left under stirring for 30 min in the dark to reach adsorption–desorption equilibrium. The solution pH was stabilized at 3 by dilute HCL in order to enhance SA adsorption on the $BiVO_4$ films. The illumination source was a 150 W Xe lamp (ORIEL 6255, ozone free) and UV-Vis irradiation was selected by a long-pass 305 nm filter to prevent high energy UV-vis (Newport 20CGA-305) and a heat reflective mirror in order to avoid heating by infrared radiation (Newport 20CLVS-3 CoolView™, T_{avg}=85% at 332-807 nm, R_{avg}=95% at 840-1500 nm) (Figure 2.12). Visible light was selected by an additional 400 nm long-pass filter (2" FGL400S, Thorlabs). The horizontally incident Xe beam was directed on the film via a UV-enhanced Al mirror (ValuMax, Newport, R_{avg}>90% at 250-600 nm) with power density of 70 mW/cm^2.

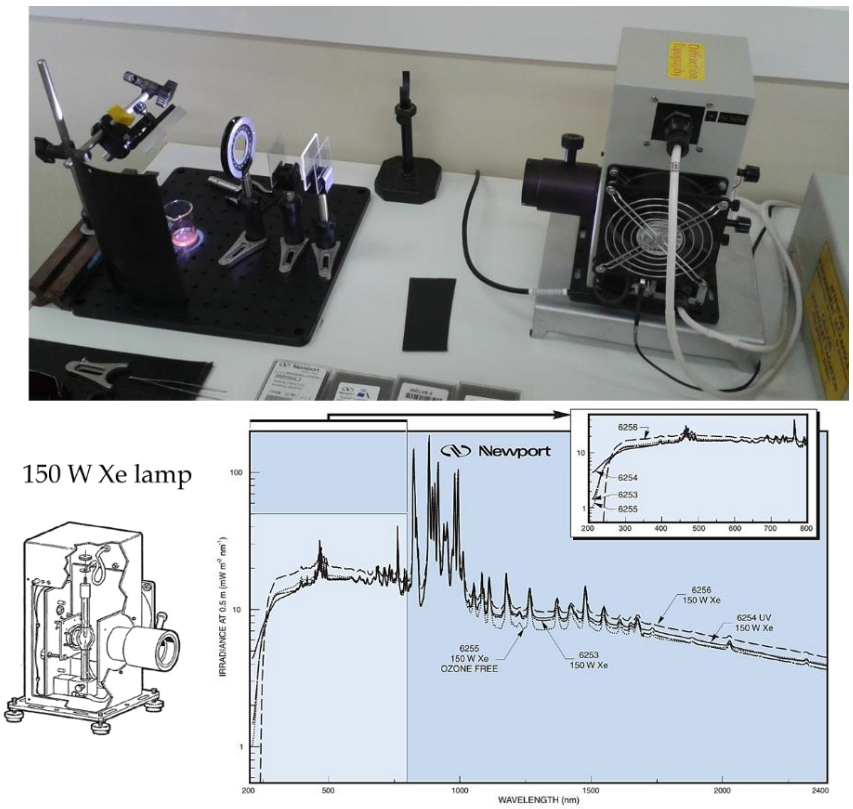

Figure 2.12 (top) Photocatalytic setup and (bottom) spectral irradiance of the 150 W Xe lamp.

Small (0.5 mL) aliquots of the pollutant solution were periodically withdrawn during photocatalytic tests and quantitatively analyzed by a 10 mm path length quartz microcell (HELMA Analytics 105B-QS, 500 μL) in the UV-Vis spectrometer. The SA concentration was determined spectrophotometrically by applying Lambert-Beer law for the SA absorption band at 300 nm. The photocatalytic experiments were performed in triplicate, and standard errors were calculated for the mean kinetic constants.

2.2.9 Photoelectrochemical experiments

Photocurrent density vs potential (J vs V) curves and electrochemical impedance spectroscopy (EIS) were employed to investigate the photoelectrochemical response and charge separation of the PC films. The former is based on the measurement of photocurrent density J produced by a photoelectrode in an electrolyte as a function of applied potential V under illumination, providing a direct metric of the semiconductor efficiency in water oxidation [6]. The experimental setup consists of a potentiostat usually connected to three electrodes (working, reference and counter), which are immersed in a solution containing the electrolyte. The potentiostat applies and maintains the potential between the working electrode and the reference one, while measuring the current that flows between the working and counter electrodes and is recorded by the appropriate software. Illumination of an n-type semiconductor with energy $h\nu \geq E_g$ results in e^- and h^+ generation, where electrons are transported to the cathode, while minority hole carriers are transported to the semiconductor-electrolyte interface initiating water oxidation. The potential at which the water splitting reaction begins signified the photocurrent onset potential (V_{on}), which is offset relative to the flat band potential V_{fb} by the required kinetic overpotentials for the reaction [154].

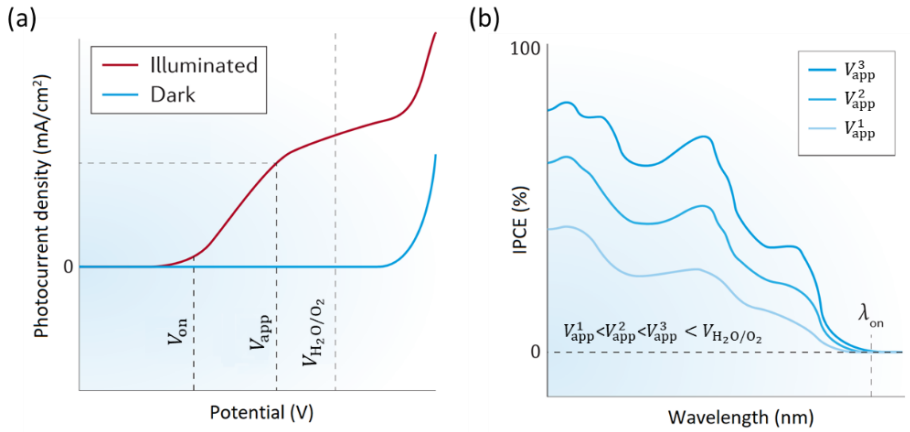

Figure 2.13 Schematic of (a) photocurrent density vs potential curves and (b) IPCE spectra at characteristic applied potentials V_{app} [6].

Quantum-efficiency metrics such as the Incident Photon-to-Current Efficiency (IPCE) is one of the most important figures of merit for photoelectrochemical systems, which describes the photocurrent collected per incident photon flux as a function of the illumination wavelength. IPCE takes into account efficiencies for three fundamental processes for water splitting, namely the fraction of e^--h^+ pairs generated per incident photon flux, charge transport to the semiconductor–liquid interface, and the efficiency of interfacial charge transfer, assuming that the counter electrode does not limit

current flow through the circuit. Thereby, IPCE is identical to the External Quantum Efficiency (EQE) that does not take into account losses due to photons that are not absorbed by the photoelectrode [154]. The IPCE spectral measurement is typically carried out using a Xe lamp as light source, which is coupled to a monochromator. The monochromatic beam is directed to the working electrode, between which and the counter electrode a bias V_{app} is applied. Then, the steady-state photocurrent is recorded using a potentiostat and is divided by the steady-state background photocurrent (under dark conditions) (Figure 2.13a). The IPCE is calculated as the ratio of this photocurrent (converted into electron rate) to the rate of incident photons:

$$\text{IPCE}\ (\lambda) = \frac{\text{electrons/cm}^2\ \text{/s}}{\text{photons/cm}^2\ \text{/s}} = \frac{1239.8(\text{V nm}) \times J(\text{mA/cm}^2)}{\lambda(\text{nm}) \times P_{\text{mono}}(\text{mW/cm}^2)}$$

where J is the photocurrent density in mA/cm^2, λ is the wavelength of incident light in nm, and P is the monochromatic light power density (mW/cm^2). The photocurrent onset wavelength (λ_{on}) is closely related to the semiconductor E_g. Moreover, the obtained IPCE (λ) spectra are correlated to the corresponding J vs V curves (Figure 2.13b), while they can be integrated to give an estimate of the expected J under the specific illumination conditions upon multiplication by the corresponding spectral distribution (usually AM 1.5G, 100 mW cm^{-2}) [6].

EIS is an alternating current (AC) technique that provides distinct information on the resistive and capacitive responses of metal oxide interfaces based on the frequency dependence of the observed current [155]. EIS is based on the application of a small amplitude sinusoidal potential $V(t) = V_0 \sin(\omega t)$ ($V_0 \sim 5 - 10$ mV) at a frequency $\omega = 2\pi f$, with f being the frequency in Hz. The resulting AC current $I(t) = I_0 \sin(\omega t + \varphi)$ at the same frequency, is offset by a phase angle (φ) depending on the parameters of the electrochemical circuit, and lead to the corresponding impedance:

$$Z(\omega) = \frac{V(t)}{I(t)} = |Z|e^{i\varphi} = |Z|(\cos\varphi + i\sin\varphi) = Z' + iZ''$$

$$\tan\varphi = Z''/Z'.$$

In a typical EIS experiment, f is varied over a wide frequency range e.g.~1 mHz to 1 MHz, for each value of applied DC bias V_{DC} superimposed on the AC modulation $V(t) = V_{DC} + V_0 \sin(\omega t)$. EIS data is analyzed using an equivalent electrical circuit that combines fundamental elements such as resistors, capacitors, inductors, constant phase elements, and diffusion elements [155]. The simplest equivalent circuit used to model MO interfaces, is the Randles one that consists of the electrolyte resistance R_S in series with the parallel combination of charge transfer resistance (R_{CT}) and the interfacial (double-layer) capacitance C_{int} at the MO/electrolyte interface (Figure 2.14a). The experimental EIS is then analyzed using different plots, the most common being the Nyquist one, where impedance is plotted as a complex number with the imaginary part Z'' along the y-axis and the real Z' along the x-axis (Figure 2.14a). The characteristic semicircle arc arises from the parallel combination of R_{CT} and C_{int}. Each data point in a Nyquist plot represents a different frequency with ω decreasing from left to right. At infinitely low frequencies, the applied potential is essentially constant (DC limit), where $Z = R_S + R_{CT}$.

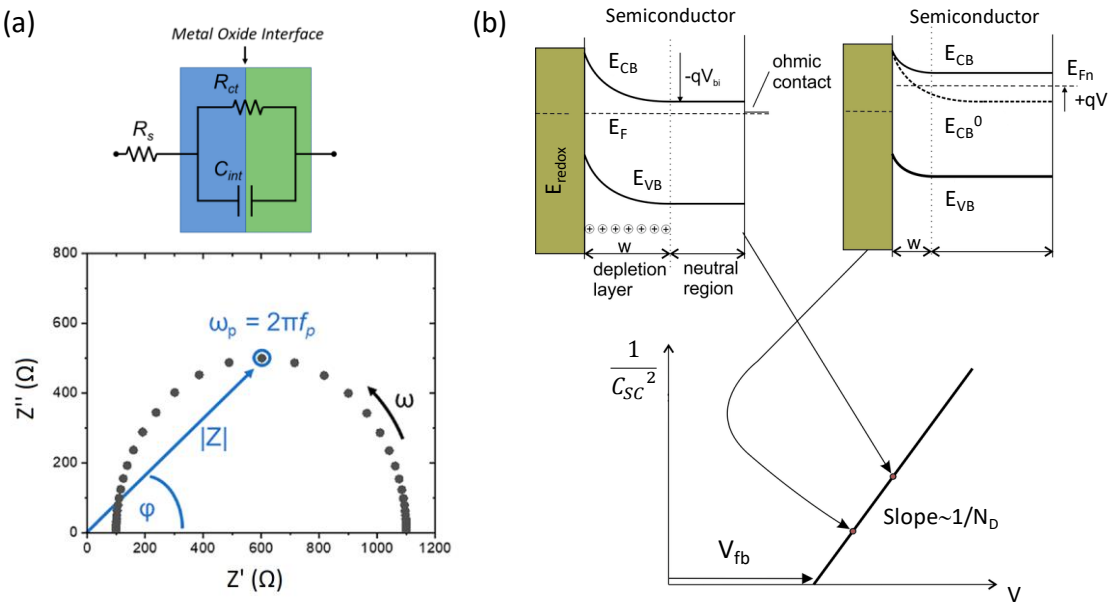

Figure 2.14 (a) Nyquist plots representing the EIS data simulated by a Randles equivalent circuit (top) for R_s = 100 Ω, Rct = 1000 Ω, C_{int} = 100 µF. The modulus |Z| and phase angle φ define the position of each frequency dependent data point in a complex plane [155]. (b) Semiconductor/electrolyte interface under equilibration leading to Schottky barrier and depletion layer or SCL of width w in the semiconductor. A positive voltage applied to the back contact in raises the Fermi level of electrons E_{Fn}, and decreases the size of the depletion region. Consequently, the capacitance of the junction increases, and the reciprocal square capacitance decreases leading to a linear Mott–Schottky plot [156].

EIS a can also be interpreted in terms of a frequency dependent and potential dependent capacitance. Just like impedance, capacitance can be defined as a complex number and determined from the imaginary component of the measured impedance, Z'', as $C_{\mathrm{int}}(\omega) = 1/i\omega Z(\omega)$. The total capacitance of the interfacial double layer, C_{int}, principally comprises contributions from the space charge layer in the semiconductor, C_{SC}, and the capacitance of the Helmholtz layer in the electrolyte, C_H, which are in series with each other [157]:

$$\frac{1}{C_{\mathrm{int}}} = \frac{1}{C_{\mathrm{SC}}} + \frac{1}{C_{\mathrm{H}}}.$$

The space charge capacitance varies with the extent of band bending, while the capacitance of the much narrower Helmholtz layer is expected to remain constant with much larger values $C_H \gg C_{SC}$ so that the total interfacial capacitance can be approximated as $C_{int} \approx C_{SC}$ [157]. The space charge capacitance is described by the Mott–Schottky equation, which for an n-type material is:

$$\frac{1}{{C_{SC}}^2} = \frac{2}{eA^2\varepsilon\varepsilon_0 N_{\mathrm{D}}}\left(V - V_{\mathrm{fb}} - \frac{kT}{e}\right)$$

where e is the elementary charge and A is the electrode area, N_D is the donor density, ε is the semiconductor permittivity and ε_0 the vacuum permittivity, V_{fb} is the flat band potential, T is the absolute temperature and k is Boltzman's constant. In that case, a plot of the reciprocal of the square of C_{int} versus applied potential (Mott–Schottky plot)

is expected to follow linear behavior over a potential range, which is used to estimate the V_{fb} and N_D values. Specifically, V_{fb} is determined from the intercept of the linear portion of the Mott–Schottky plot with the potential axis, $V_{fb} = (V - kT/e)_{y=0}$, while the donor concentration N_D may be derived from the slope of the Mott–Schottky plot, provided the relative permittivity is known (Figure 2.14 b).

In this work, photoelectrochemical experiments were performed in a three-electrode configuration on a CS350 potentiostat/galvanostat (Corrtest Instruments) using the PC films deposited on FTO substrates as working electrode (area 4 cm^2), Ag/AgCl and a Pt foil as reference and counter electrodes, respectively, in aqueous 0.5 M $NaHCO_3$ aqueous electrolyte. Visible light illumination was provided by a 300 W Xe lamp in combination with a 400 nm cutoff filter delivering 90 mW/cm^2 at the photoelectrode surface (Figure 2.15). The *J* vs *V* curves were recorded by linear sweep voltammetry performed at a potential scan rate of 10 $mV\ s^{-1}$ under dark conditions and front/back side illumination. The applied potential vs. Ag/AgCl was converted to reversible hydrogen electrode (RHE) scale by using

$$V_{RHE} = V_{Ag/AgCl} + 0.059\ pH + V^0_{Ag/AgCl}$$

where $V^0_{Ag/AgCl} = 0.1976$ V is the standard potential for Ag/AgCl at 25 °C. EIS was performed at the open-circuit voltage, in the 10^4–10^{-2} Hz frequency range with ac amplitude of 10 mV. IPCE measurements were also performed in 0.5 M $NaHCO_3$ aqueous electrolyte under back-side illumination at 1.23 V vs RHE potential using a 1 kW Xe lamp in combination with an Oriel 77200 1/4 monochromator and a calibrated Si photodiode. Mott-Schottky measurements were carried out at 500 Hz and a scan rate of 10 mV/s at each potential.

Figure 2.15 Experimental setup of photoelectrochemical measurements.

The photoelectrocatalytic activity of the photonic films was evaluated on the degradation of the pharmaceutical substances tetracycline (TC) and ciprofloxacin (CIP) antibiotics and the nonsteroidal anti-inflammatory drug ibuprofen (IBU), besides SA, which were selected as emerging water pollutants [158], whose residues and metabolites in water bodies present a major environmental hazard [159, 160]. PEC experiments were also carried out in three-electrode configuration with a 300 W Xe lamp in combination with a 400 nm long-pass filter (90 mW/cm^2) using 36 ml working

solution of 0.1 M $NaHCO_3$ supporting electrolyte under mild stirring, comprising the pharmaceutical pollutants: 22 mg/L of TC, 14 mg/L CIP, 7 mg/L IBU and 30 μM SA at pH=3. Dark adsorption of SA and CIP pollutants was negligible, while it reached 12% for TC after 30 min. Degradation kinetics was monitored by spectrophotometric detection for small aliquots periodically withdrawn from the reaction cell. Additional photoelectrocatalytic tests were carried out in the presence of 5 mM isopropanol (IPA) and formic acid (FA) as well as 1 mM 1,4-benzoquinone (BQ) as hydroxyl radical, hole and superoxide radical anion scavengers, respectively.

CHAPTER 3

Homojunction Mo-$BiVO_4$/Ca-$BiVO_4$ inverse opal photocatalysts

In this work*, the formation of nanoscale Mo-$BiVO_4$/Ca-$BiVO_4$ homojunctions in the skeletal walls of PBG engineered (Mo, Ca) doped $BiVO_4$ inverse opals is introduced as an advanced engineering approach to improve visible light harvesting along with electron transport and charge separation of nanostructured $BiVO_4$ photoelectrodes and extend their application potential to pharmaceutical photoelectrocatalytic degradation under visible light beyond water splitting. Light trapping optimization was firstly carried out by tuning the films PBG close to $BiVO_4$ electronic absorption edge, based on activity screening for the VLA photodegradation of salicylic acid (SA) as colorless recalcitrant water pollutant, attesting the diameter-selective performance of $BiVO_4$ PCs. Compositional tuning was pursued for the optimal photocatalytic films by Mo- and Ca- doping, which was exploited for the fabrication of nanostructured Mo-$BiVO_4$/Ca-$BiVO_4$ photoelectrodes by the successive infiltration of Mo and Ca-containing metal salt precursors in the colloidal template, leading to abundant interfaces and n-n^+ isotype homojunctions between differently doped $BiVO_4$ NPs. The nanostructured homojunction PC films were successfully applied on the VLA photoelectrocatalytic degradation of SA, TC and CIP antibiotics, whose residues and metabolites in wastewaters are a major environmental hazard, validating their application potential on water remediation by pharmaceutical contaminants.

3.1 Light trapping optimization

The fabrication of well-ordered $BiVO_4$ inverse opal films with approximately 2.1 μm thickness was evidenced by cross section SEM images (Figure 3.1), applying the liquid phase infiltration of the metal salt precursor based on bismuth nitrate $Bi(NO_3)_3{\cdot}5H_2O$ and ammonium vanadate NH_4VO_3 (section 2.1.1) followed by calcination of the impregnated colloidal templates in order to remove the PS matrix and crystallize $BiVO_4$ in the inverse replica structure. The chemical composition of the $BiVO_4$ photonic films was confirmed by TEM in combination with EDX analysis (Figure 3.2a), where the Bi, V and O elements were clearly identified in the local EDX spectrum and the corresponding elemental maps (Figure 3.2b).

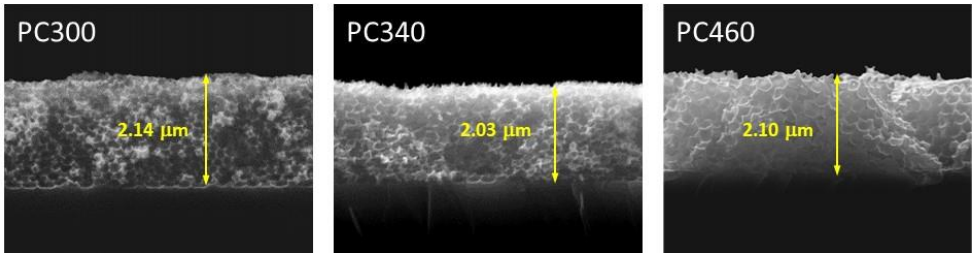

Figure 3.1 Cross section SEM images for the PC300, PC340 and PC460 inverse opals.

* This chapter has been published in ref. [134].

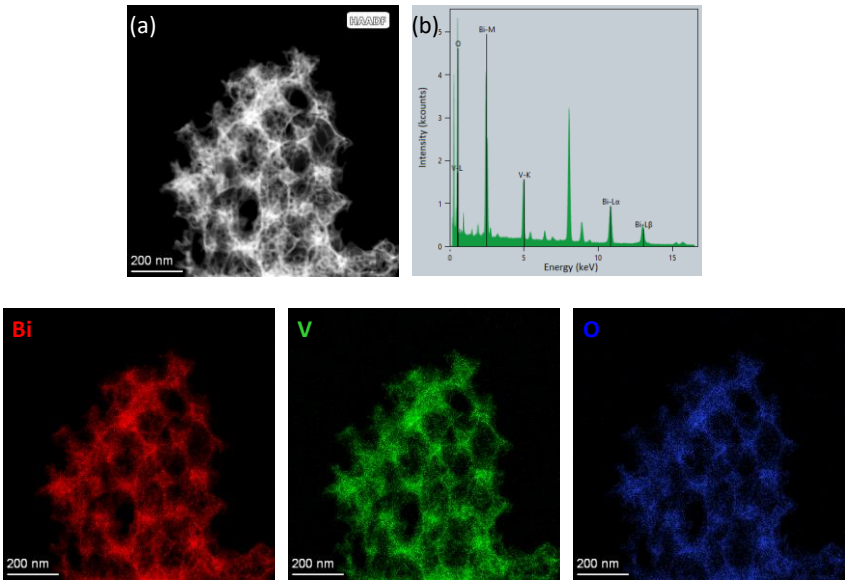

Figure 3.2 (a) TEM image of PC340 and the Bi, V, and O elemental maps obtained from the corresponding local (b) EDX spectrum.

All diffraction peaks in the corresponding XRD pattern (Figure 3.3a) could be indexed to the *ms* $BiVO_4$ phase (space group I2/a, JCPDS 014-0688), confirmed by the low-symmetry splitting of the (002) and (200) diffraction peaks at 34.5° and 35.2° as well as the (240) and (042) ones at 46.7° and 47.2° (insets of Figure 3.3a). This was verified by micro-Raman spectroscopy, where all the characteristic Raman-active modes of the *ms* phase were clearly identified with no traces of polymeric species or other polymorphic $BiVO_4$ phases (Figure 3.3b). The most intense Raman mode at 829 cm^{-1} arises from the symmetric V-O stretching (ν_s) band accompanied by the weak antisymmetric V-O stretching (ν_{as}) mode at about 710 cm^{-1} [161]. The symmetric (δ_s) and antisymmetric (δ_{as}) bending modes of the VO_4 tetrahedra were observed at 369 and 328 cm^{-1}, respectively, while the main external lattice modes appeared at 213 and 129 cm^{-1} [162]. Moreover, no sign of the tetrahedral stretching ν_s modes expected for the tetragonal scheelite or the tetragonal zircon $BiVO_4$ phases at lower (ca. 817 cm^{-1}) and higher (ca. 855 cm^{-1}) frequencies [163, 164], respectively, compared to the corresponding mode of the *ms* phase, was observed, excluding the formation of other $BiVO_4$ polymorphs.

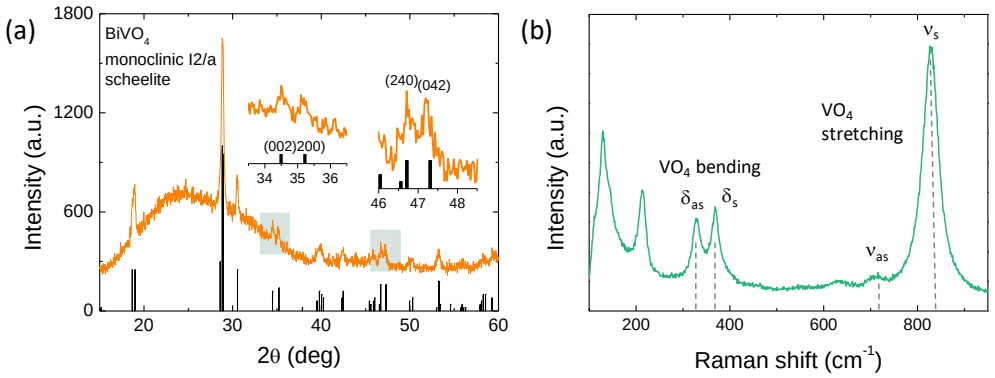

Figure 3.3 (a) XRD pattern and (b) Raman spectrum verifying the formation of the *ms* $BiVO_4$ phase for the PC340 film.

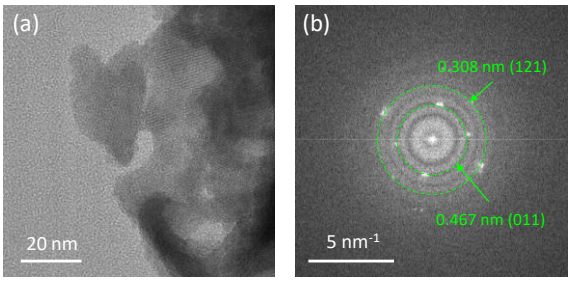

Figure 3.4 (a) TEM image and (b) the corresponding FFT pattern for PC340 showing diffraction spots that correspond to the (121) and (011) crystal planes of *ms* $BiVO_4$.

This was corroborated by the clear splitting of the VO_4 bending modes [165], verifying the crystallization of $BiVO_4$ PCs in the single *ms* phase. Application of the empirical relation $\nu_{stretch}[\mathrm{cm}^{-1}] = 21349\, e^{-1.9176\, \mathrm{R[Å]}}$, which correlates the V-O stretching frequencies ν_s and ν_{as} to the V-O bond lengths in vanadium oxides [166], yielded values of 1.694 and 1.775 Å, respectively, indicating appreciable deformation of the VO_4 tetrahedra for the $BiVO_4$ PCs. High-resolution TEM images of the inverse opal skeleton (Figure 3.4a) confirmed the presence of $BiVO_4$ nanocrystallites with *d*-spacings derived from the fast Fourier transform (FFT) patterns that matched the (121) and (011) planes of the *ms* phase (Figure 3.4b).

PBG engineering was performed by using PS colloidal spheres of different diameters in the range of 300 to 510 nm (Figure 3.5a-e). The formation of long-range ordered three dimensional inverse opals was clearly observed, corresponding to the (111) planes of an *fcc* lattice of spherical void macropores in the place of the sacrificial PS spheres, surrounded by a solid skeleton that fills the interstitial space. The large macropores were interconnected through smaller ones (dark circular areas within the large spherical voids) creating open windows at the contact points of adjacent PS spheres after calcination, which are essential for the mass transport within the pore network. SEM images of variable magnifications depict long range ordered inverse opal films, free of compact overlayers with domains extending over several micrometers (Figure 3.5f).

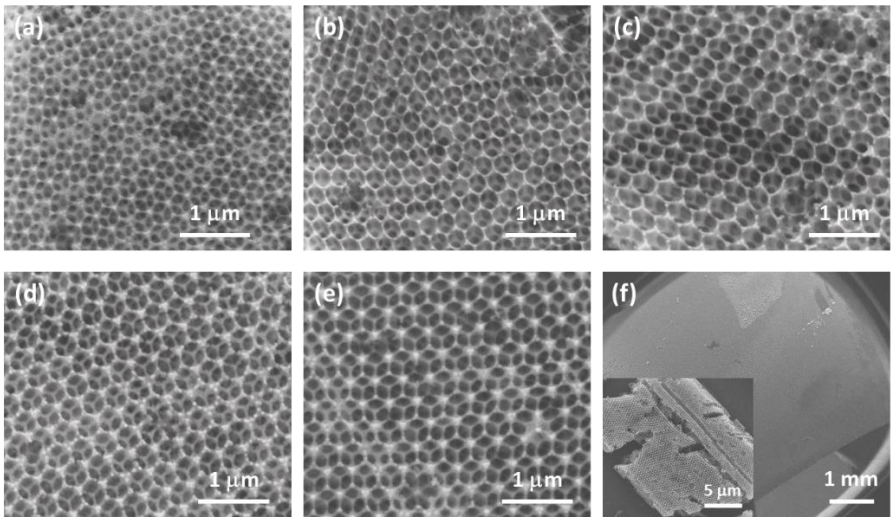

Figure 3.5 Top-view SEM images for (a) PC300, (b) PC340, (c) PC418, (d) PC460, and (e) PC510 inverse opal films. (f) Top view SEM images of PC460 at different magnifications.

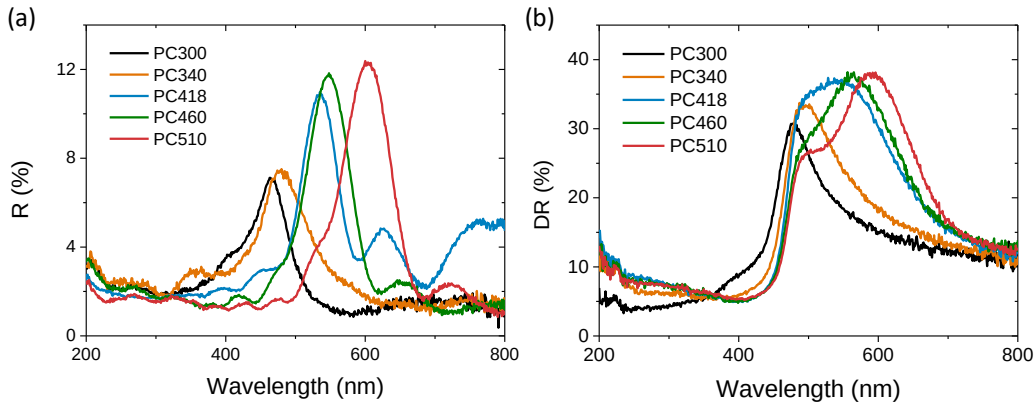

Figure 3.6 (a) Specular reflectance (R%) at 15° incidence angle and (b) diffuse reflectance (DR%) spectra for the $BiVO_4$ PC films of different macropore diameters.

However, cracks are still observed due to the calcination-induced cracking that persists in crystalline MOs via the amorphous-to-crystalline phase transition and the associated volume shrinkage of the inorganic matrix after thermal treatment [167]. The mean void diameters (D) determined by SEM, increased proportionally to the templating sphere size (Table 3.1), with the obtained values being about 62% smaller than those of the PS spheres, reflecting the crystallization of the inorganic precursor that fills the interstitial space of the opal templates after thermal treatment.

The PBG evolution for the $BiVO_4$ PC films was determined by specular reflectance (R%) measurements at 15° angle of incidence (Figure 3.6a), where a clear R% peak due to Bragg reflection was observed at wavelengths increasing with the macropore size (Table 3.1). This variation is characteristic for the incomplete PBG (stop band) along the [111] direction in the inverse opal films, distinctly different from the Fabry-Pérot interference fringes that appeared in the R% spectra of the disordered PC films, fabricated using a mixture of PS templating spheres of all diameters, where PBG is suppressed (Figure 3.7a).

Table 3.1 Structural and optical parameters for the BiVO4 inverse opal films.

Sample	D (nm)	λ_{exp} (15°) (air)	n_{eff} (air)	$1-f$	λ (0°) (air)	n_{eff} (H_2O)	λ (0°) (H_2O)
PC300	200	460	1,43	0,221	468	1,63	532
PC340	210	480	1,42	0,216	488	1,62	556
PC418	260	534	1,28	0,136	545	1,52	646
PC460	280	547	1,22	0,105	560	1,48	676
PC510	310	601	1,22	0,100	615	1,47	745

D = inverse opal macropore diameter determined from SEM.

λ_{exp} (15°) = stop band wavelength determined from R% spectra at 15° incidence angle.

λ (0°) = stop band wavelength according to the modified Bragg law at 0° incidence angle.

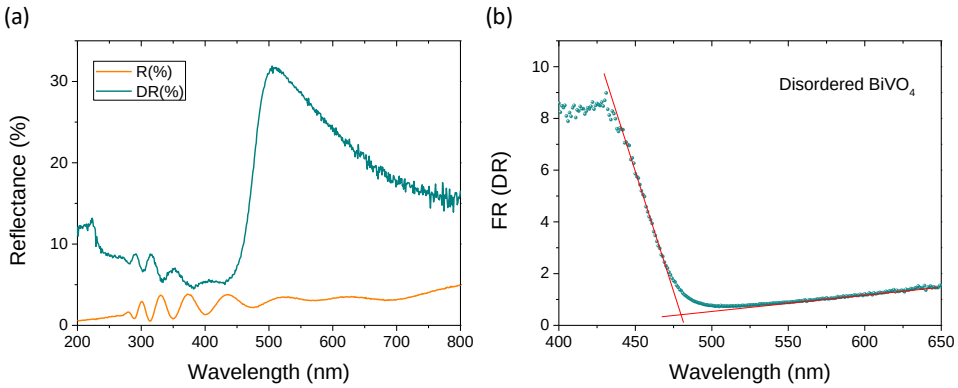

Figure 3.7 (a) Specular and diffuse reflectance spectra for the disordered $BiVO_4$ inverse opal films fabricated from colloidal templates assembled from a mixture of 300, 340, 418 and 460 nm PS spheres. (b) Absorbance spectra obtained from the Kubelka-Munk function F(DR) and absorption edge at 480 nm.

Stop band formation was confirmed by the broad peak in the diffuse reflectance (DR%) spectra of the PC films (Figure 3.6b). The DR% peak shifted to higher wavelengths with increasing macropore size, following closely the PBG variation observed in the R% spectra, in contrast to the constant electronic absorbance edge of $BiVO_4$ at about 480 nm (Figure 3.7b). Applying modified Bragg's law for the obtained stop band wavelengths at $\theta = 15°$ together with the measured inverse opal diameters D for the refractive indices of $BiVO_4$ ($n_{BiVO_4} = 2.4$) and air ($n_{air} = 1.0$) (Section 1.3), the effective refractive index n_{eff} and solid filling fraction $1 - f$ (f = 0.74 for the *fcc* lattice) were estimated (Table 3.1). The $1 - f$ values were appreciably smaller than the theoretical one of 0.26 for complete filling of the inverse *fcc* lattice, corroborating the nanocrystalline nature of the skeletal walls, while they decreased with increasing macropore diameter, in agreement with recent results for TiO_2 inverse opals [78].

The photocatalytic performance of $BiVO_4$ PCs was evaluated on SA degradation under visible light (Figure 3.8). SA is a colorless water contaminant, whose absorbance bands are well below the inverse opal PBGs (Figure 3.8a), and thus any slow photon contribution by spectral overlap with the molecular electronic absorption is not expected [168]. Blank experiments in the absence of $BiVO_4$ films, indicated negligible SA degradation under visible light, whereas illumination in the presence of PC films resulted in continuous decrease of SA concentration (C) with time (Figure 3.8b), which was determined spectrophotometrically by the characteristic SA band at 300 nm. The $\ln(C/C_0)$ vs. t plot, where C_0 is the initial SA concentration after dark adsorption, varied linearly with time (Figure 3.8c), indicating that SA photodegradation followed pseudo first-order kinetics. The apparent kinetic constant k_{Vis} were accordingly determined from the slopes of the linear $\ln(C/C_0)$ vs. t plots and the corresponding reaction rates were calculated as $r_{vis} = k_{Vis}C_0$ for low (<mM) pollutant concentrations in order to determine the films' activity independently of C_0 variations due to SA adsorption. The obtained r_{vis} rates varied markedly with the macropore size indicating significant differences in PC's light harvesting ability.

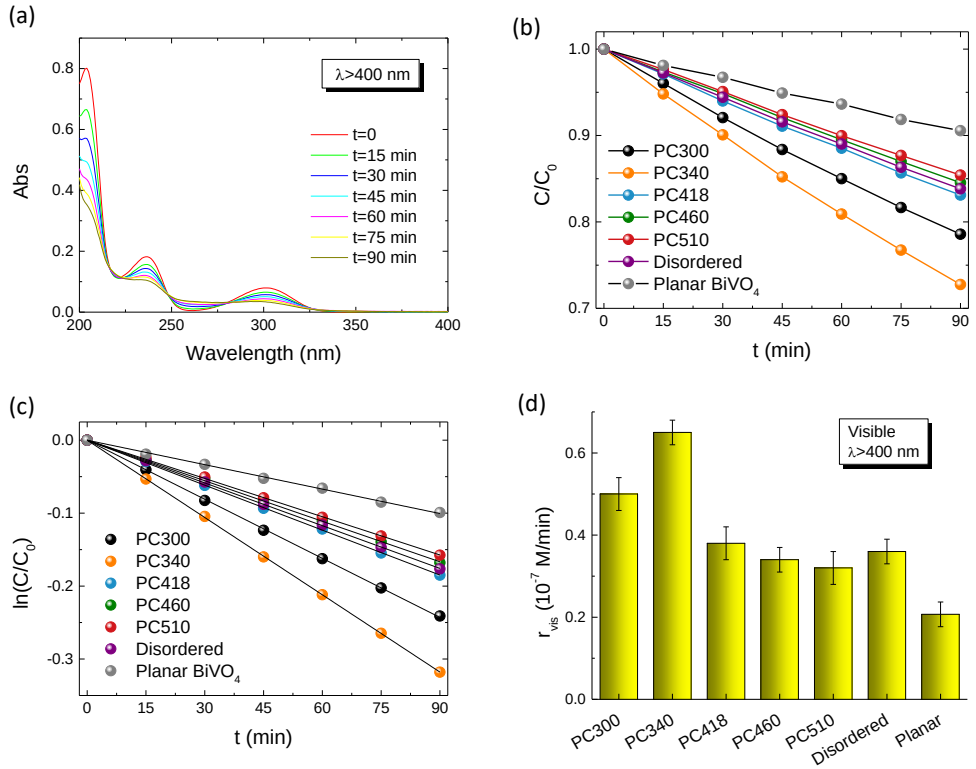

Figure 3.8 (a) SA absorbance spectra in the presence of PC340 under visible light. (b) (c) SA photodegradation kinetics and reaction rates r_{Vis} for the $BiVO_4$ PC films of different macropore diameters in comparison to the disordered and planar reference $BiVO_4$ films.

Specifically, PC340 exhibited the highest r_{vis}, followed closely by PC300, whereas larger diameter PCs presented successively lower activity reaching a two-fold decrease for PC510. This size-selective performance can be closely associated with the stop band variation and the concomitant slow light amplification effects, most prominent for PC340, whose PBG occurs at ca. 550 nm in water (Table 3.1). Assuming that the PBG spectral width is about the FWHM≈50 nm of the Bragg R% peak (Figure 3.6a), the PC340 stop band in water is expected at 556±25 nm. The corresponding blue-edge slow photons, which span a narrower spectral range of about 20-30 nm, will be roughly expected around 500 nm, approaching closely the electronic absorption edge of $BiVO_4$ at about 480 nm. Similar spectral matching is expected for PC300, whose slow photon region is predicted to blue-shift by about 20-30 nm (Table 3.1), leading to high photocatalytic activity. On the other hand, no appreciable slow light effects are expected for the larger diameter inverse opals, whose PBG in water is well above 600 nm (Table 3.1), where $BiVO_4$ does show any optical absorbance. Compared to disordered PCs as reference inverse opals that lack photonic effects, PC340 films presented a nearly two-fold improvement of r_{Vis}, which can be related to the enhanced light harvesting by blue-edge slow photons, in agreement with recent results on $BiVO_4$-TiO_2 inverse opals [169]. Even higher increase, by about 3.1 times, was obtained in comparison to the r_{Vis} of planar $BiVO_4$ films, confirming the beneficial role of the inverse opal structure in the enhanced performance of PC films. The PC340 films with optimal light trapping ability were accordingly selected for compositional tuning of $BiVO_4$ inverse opals by metal doping and homojunction fabrication.

3.2 Metal doping and homojunction formation

To improve electron transport and reduce electron-hole recombination for the $BiVO_4$ PCs, single metal doping was carried out by the incorporation of suitable metal sources in the sol-gel precursor, namely $(NH_4)_6Mo_7O_{24}{\cdot}4H_2O$, providing molybdenum dopants (*n*-doping) that can substitute for vanadium cations in $BiVO_4$ due to the closely matched ionic radii of V^{5+} (0.54 Å) and Mo^{6+} (0.62 Å) [40]. Furthermore, *p*-doping was pursued by the introduction of Ca^{2+} (0.99 Å) as acceptor at Bi^{3+} (1.11 Å) lattice sites by the controlled addition of $Ca(NO_3)_2$ in the precursor. Optimization of single Mo- and Ca-doping was performed by evaluating the photocatalytic activity of metal doped $BiVO_4$ PCs for different dopant concentrations of Mo (2, 3 and 4%) and Ca (2, 3, 4, and 5 %) on SA degradation under visible light (Figures 3.9 and 3.10). The optimal doping levels of 3% Mo and 4% Ca were thus determined and used for the synthesis of co-doped (Mo, Ca)-$BiVO_4$ PCs.

Homojunction deposition was further implemented by the successive infiltration of PC340 colloidal templates with Mo and Ca-containing sol gel precursors leading to Mo-$BiVO_4$/Ca-$BiVO_4$/Mo-$BiVO_4$ (Mo-Ca-Mo), where Mo-$BiVO_4$ and Ca-$BiVO_4$ hereafter designate the metal doped $BiVO_4$ PC340 films with nominal Mo:V and Ca:Bi molar ratios of 3% and 4%, respectively. In that case, the formation of abundant interfaces between differently doped, Mo-, Ca- or (Mo,Ca)-$BiVO_4$ nanoparticles could lead to the formation of nanoscale homojunctions in the skeletal walls.

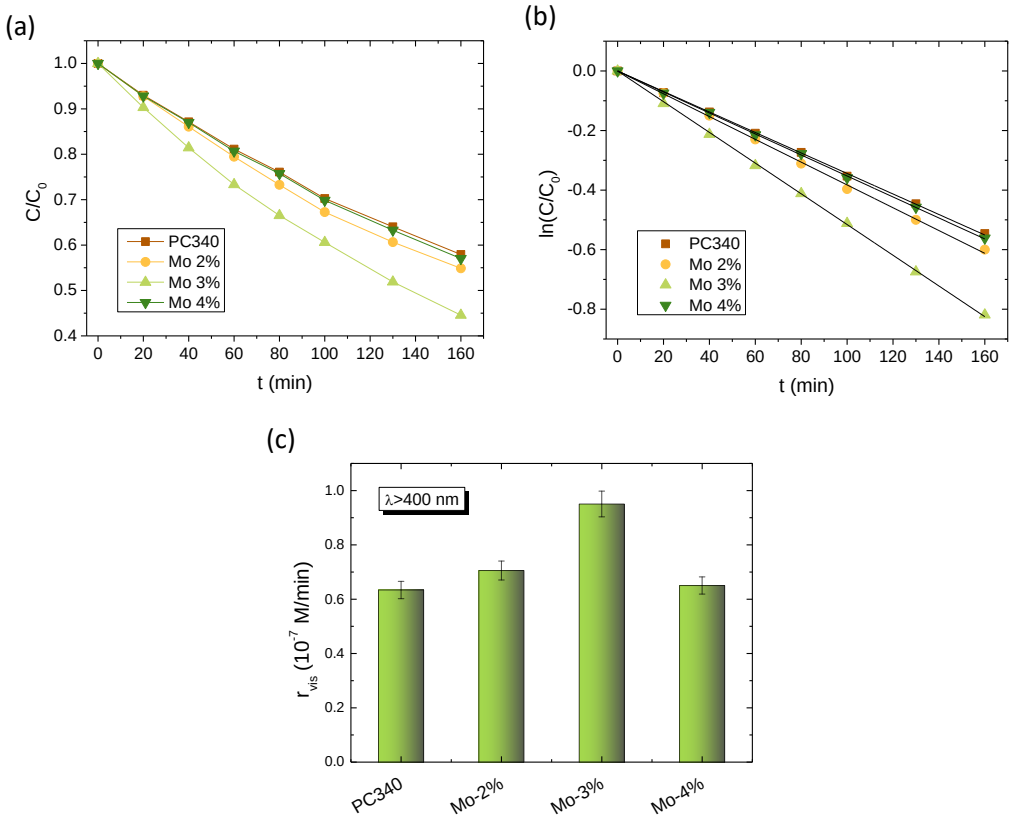

Figure 3.9 (a), (b) SA photodegradation kinetics and (c) the corresponding reaction rates r_{vis} as a function of Mo concentration for Mo-doped $BiVO_4$ PC340 inverse opal films under visible light illumination.

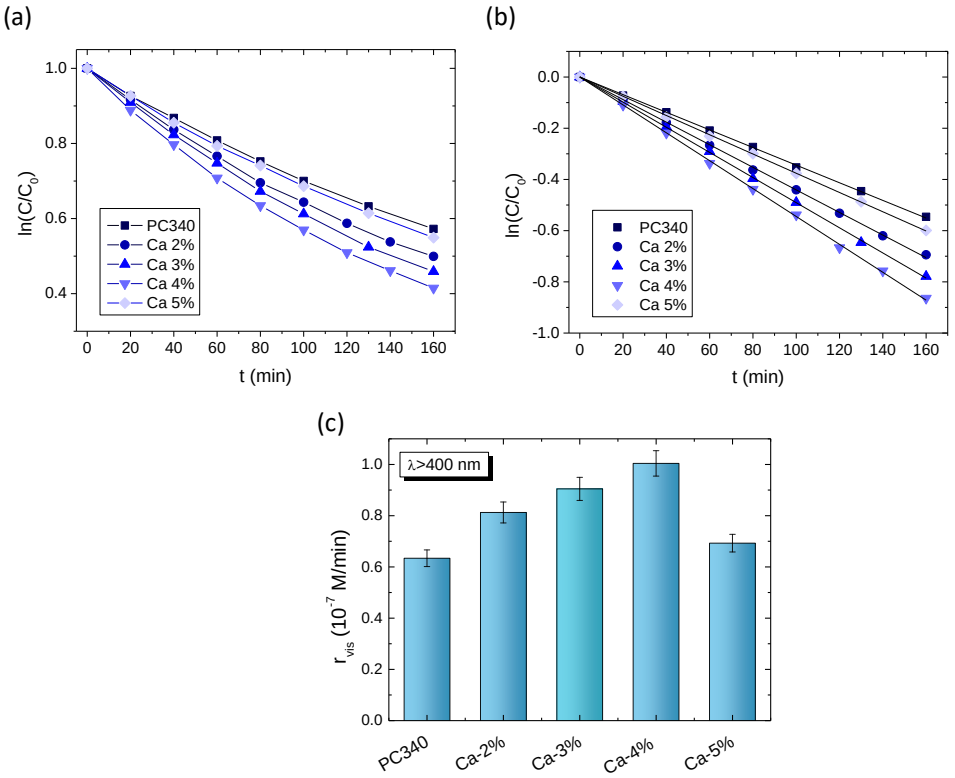

Figure 3.10 (a), (b) SA photodegradation kinetics and (c) the corresponding reaction rates r_{vis} as a function of Ca- doping concentrations for Ca-doped $BiVO_4$ PC340 inverse opal films under visible light illumination.

XRD measurements showed that both single Mo- and Ca-doped as well as the co-doped PC films and (Mo-Ca-Mo) ones retain the *ms* $BiVO_4$ phase (Figure 3.11). However, the characteristic low-symmetry splitting of (002)/(200) and (240)/(042) peaks is not clearly observed, especially for the (Mo,Ca)-$BiVO_4$, where severe spectral broadening and peak merging was observed, indicating that Mo/Ca-doping introduces disorder and averages the low-symmetry of the *ms* phase towards the tetragonal scheelite structure [44, 165]. This was supported by the corresponding Raman spectra variation (Figure 3.12).

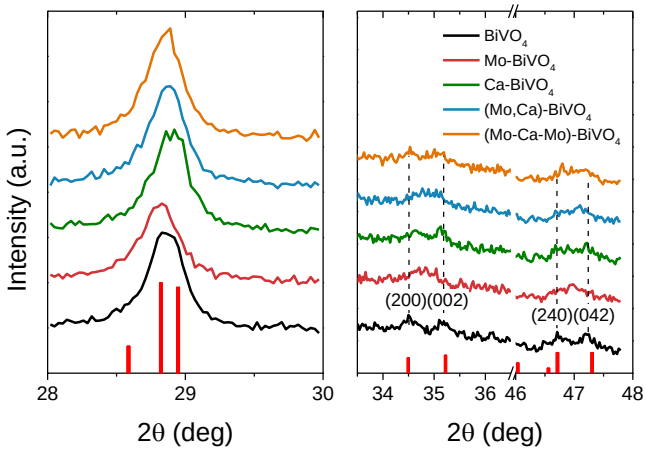

Figure 3.11 XRD patterns for the single-, co-doped and homojunction $BiVO_4$ PC films in comparison to the unmodified ones.

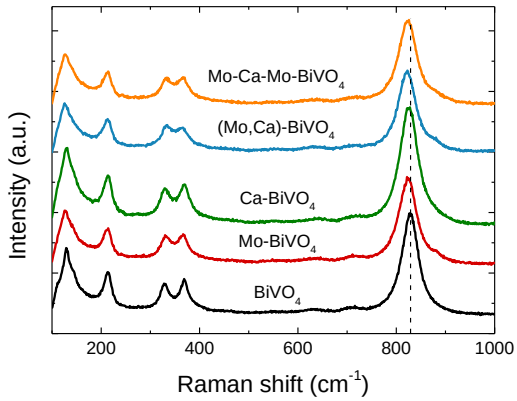

Figure 3.12 Raman spectra for the single-, co-doped and homojunction $BiVO_4$ PC films in comparison to the unmodified ones.

Specifically, the intense symmetric V-O stretching band ν_s shifted to lower wavenumbers, approaching the weak antisymmetric ν_{as} mode, as evidenced by spectral fitting (Figure 3.13). This resulted in the moderation of the difference between the two V-O bond lengths for the VO_4 tetrahedra in the *ms* phase that were calculated from the corresponding frequencies (Table 3.2). Likewise, the δ_s and δ_{as} VO_4 bending modes approached each other for the doped PCs (Figure 3.13), confirming the averaging of the monoclinic lattice distortion [161, 162]. This effect was more pronounced for the (Mo,Ca)-$BiVO_4$ PC films, where co-doping of *ms* $BiVO_4$ by Mo and Ca ions introduces structural disorder.

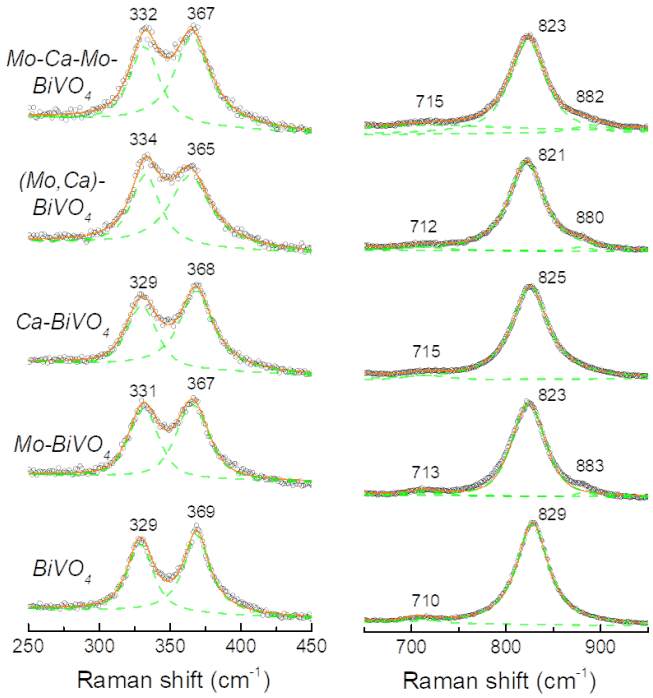

Figure 3.13 Spectral deconvolution (solid-dashed lines) of the bending (left) and stretching (right) vibrational VO_4 modes from the corresponding Raman spectra (open circles) for the single-, co-doped and Mo-Ca-Mo $BiVO_4$ PC films in comparison to the unmodified ones. The weak band at about 880 cm^{-1} for the Mo-doped $BiVO_4$ films indicates the MoO_4 stretching mode.

Table 3.2 V-O bond lengths, R_1 and R_2, derived from the frequencies of the symmetric (ν_s) and antisymmetric (ν_{as}) VO_4 stretching modes for the metal doped $BiVO_4$ inverse opal films.

PC film	ν_s (cm^{-1})	R_1 (V-O) (Å)	ν_{as} (cm^{-1})	R_2 (V-O) (Å)
$BiVO_4$	829	1,694	710	1,775
Mo-$BiVO_4$	823	1,698	713	1,773
Ca-$BiVO_4$	825	1,697	715	1,771
(Mo,Ca)-$BiVO_4$	821	1,699	712	1,773
Mo-Ca-Mo $BiVO_4$	823	1,698	715	1,771

However, the characteristic ν_s stretching modes for the tetragonal, scheelite or zircon, crystal phases could not be observed indicating the absence of mixed tetragonal-monoclinic $BiVO_4$ polymorphic phases by metal doping [163, 165]. This was corroborated by the corresponding ATR-FTIR spectra shown in Figure 3.14. In that case, the Bi-O stretching mode that was observed at about 638 cm^{-1} [170] shifted to higher frequencies and broadened appreciably for the metal doped $BiVO_4$ films. In addition, spectral fitting of the symmetric ν_s Raman mode revealed an additional weak shoulder at about 880 cm^{-1} for the Mo-doped $BiVO_4$ inverse opals, namely the single-, co-doped (Mo, Ca)- and Mo-Ca-Mo $BiVO_4$ PC films (Figure 3.13). This mode can be related to the MoO_4 stretching mode that is expected at higher frequency [165], indicative of Mo substitution in the VO_4 tetrahedra.

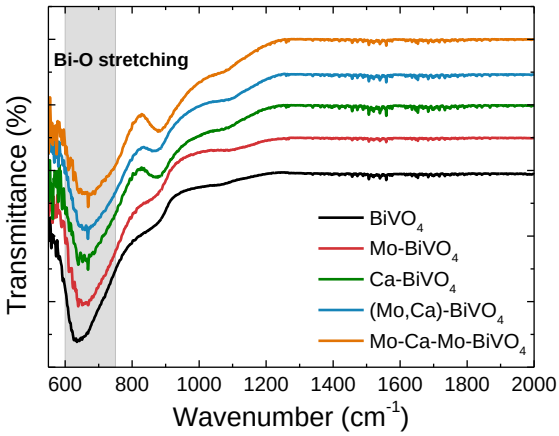

Figure 3.14 ATR-FTIR spectra for the single-, co-doped and Mo-Ca-Mo $BiVO_4$ PC films in comparison to the unmodified ones.

The chemical composition of the Mo- and Ca-doped $BiVO_4$ PC films was further supported by TEM-EDX analysis, where a homogeneous distribution of Mo (Figure 3.15a) and Ca (Figure 3.15b) was traced in the corresponding elemental maps along with the Bi, V and O elements.

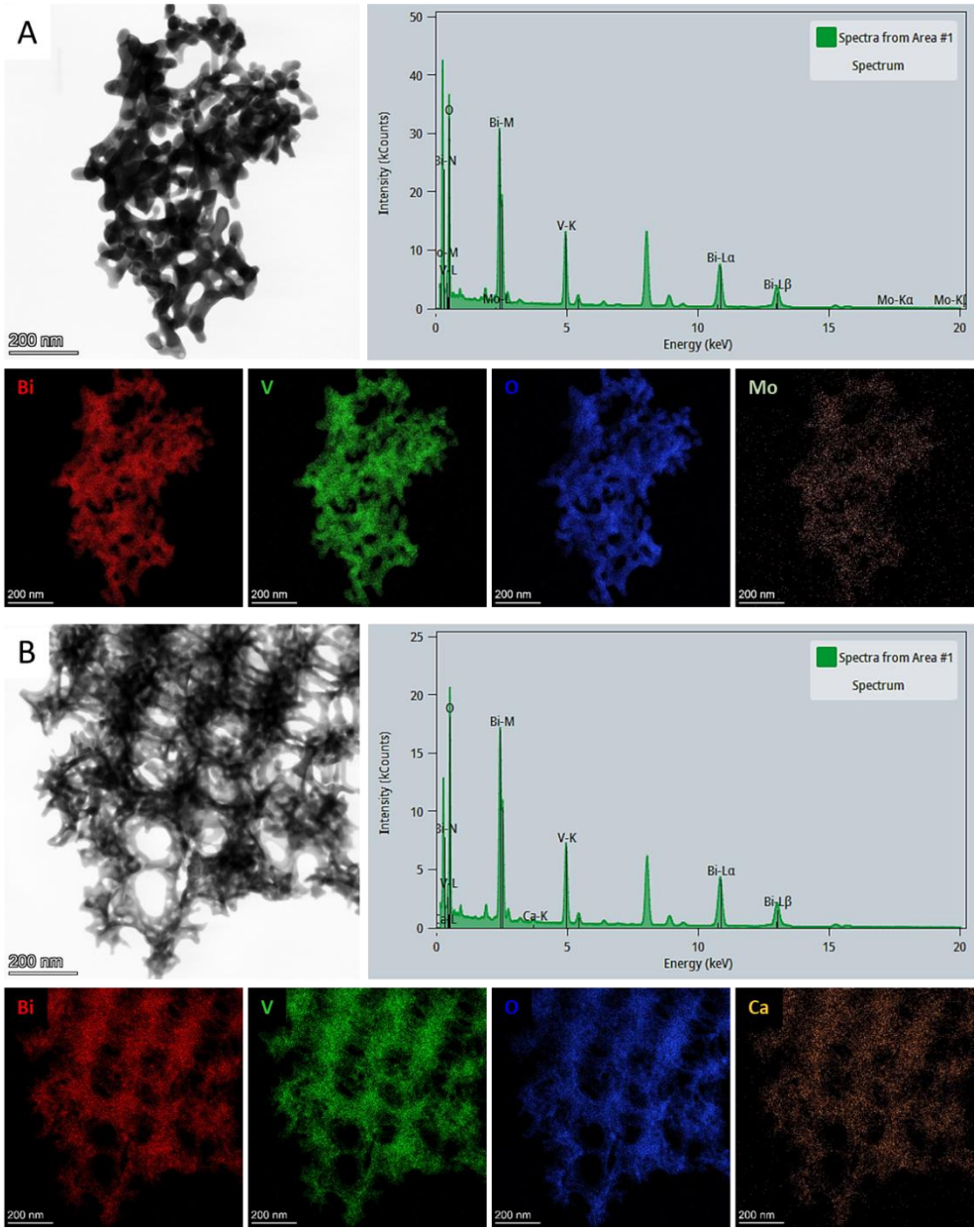

Figure 3.15 TEM images of (A) Mo-$BiVO_4$ and (B) Ca-$BiVO_4$ photonic films and the corresponding EDX spectra and elemental maps for Bi, V, O, Mo and Ca.

The surface composition of metal doped $BiVO_4$ PC films was investigated by XPS (Figure 3.16). The Bi 4f spectra for the pristine $BiVO_4$ PC showed a well separated $4f_{7/2}$ – $4f_{5/2}$ spin-orbit doublet at binding energies (BEs) of 159.4 and 164.7 eV (splitting Δ=5.3 eV), respectively, characteristic of Bi^{3+} ions [171]. The corresponding V $2p_{3/2}$ peak was detected at 517.1 eV, indicative of V^{5+} ions, while the O 1s peak was located at 530.2 eV with weak asymmetry towards higher BEs, typical of lattice oxygen and small amounts of adsorbed oxygen species [116]. For Mo-$BiVO_4$ PC films, two well-separated $3d_{5/2}$ and $3d_{3/2}$ spin-orbit components were observed at 232.6 and 235.9 eV (Δ=3.3 eV), respectively, verifying the presence of Mo^{6+} ions [44, 48]. In addition, the Ca $2p_{3/2}$ and $2p_{1/2}$ peaks were identified at 346.8 and 350.3 eV (Δ=3.5 eV) for the Ca-$BiVO_4$ PC, confirming the incorporation of Ca^{2+} ions in $BiVO_4$ [172].

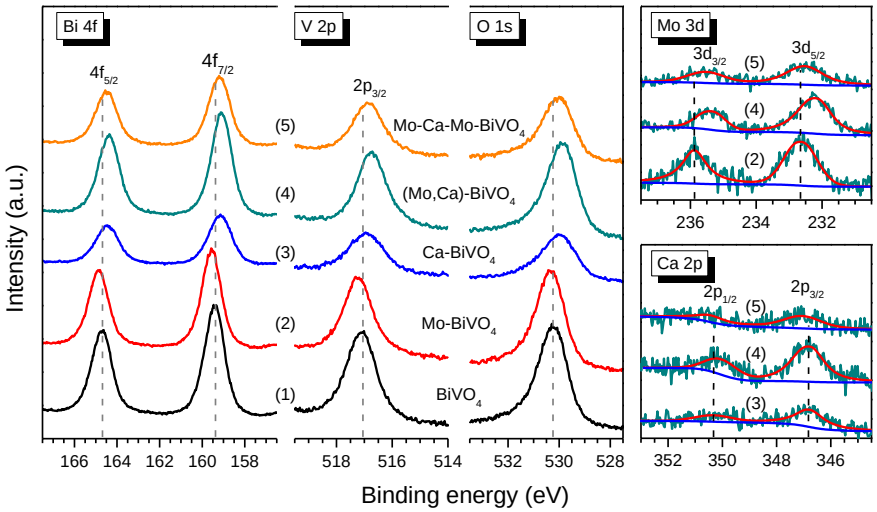

Figure 3.16 Variation of the Bi 4f, V 2p$_{3/2}$, O 1s, Mo 3d and Ca 2p core level spectra for (1) pristine, (2) Mo-doped, (3) Ca-doped, (4) (Mo,Ca) co-doped and (5) Mo-Ca-Mo homojunction $BiVO_4$ PC films.

The surface Mo and Ca elemental concentrations were determined from the observed spectral intensities to be 3.7% and 5.2% in Mo- and Ca-doped $BiVO_4$, respectively, following the relative variation of the nominal molar ratios. Similar Mo and Ca doping contents of 4.1% and 5.6% were derived for the co-doped (Mo,Ca)-$BiVO_4$, while the values of 3.6% and 3.2% were found for Mo-Ca-Mo-$BiVO_4$ consistent with the compositional variation for the homojunction films. Moreover, Mo doping resulted in a nearly constant increase of the Bi 4f, V 2p, and O 1s BEs by approximately 0.14 eV (Figure 3.16), indicating a shift of electronic origin. In particular, this behaviour can be related to a shift of the Fermi level position away from the VBM [171], in agreement with *n*-type doping for Mo-$BiVO_4$. On the other hand, the introduction of Ca^{2+} ions resulted in appreciable down shifts of the Bi 4f, V 2p, and O 1s BEs by 0.26, 0.14, 0.25 eV for Ca-$BiVO_4$, 0.30, 0.34, 0.35 eV for (Mo, Ca)-$BiVO_4$ and by ~0.2 eV for the Mo-Ca-Mo-$BiVO_4$ homojunction. This indicates that besides chemical shifts due to the lower electronegativity of Ca^{2+} ions compared to Bi^{3+}, the theoretically predicted acceptor sates close to the $BiVO_4$ valence band for Ca^{2+} doping [40] and compensation effects with other defects may lead to diverse shifts of electronic origin, especially for the co-doped (Mo, Ca)-$BiVO_4$ (*vide infra*).

Comparative PEC evaluation of the doped $BiVO_4$ PC photoelectrodes was carried out by linear sweep voltammetry at a potential scan rate of 10 mV s^{-1} under dark conditions and front-side illumination in 0.5 M $NaHCO_3$ aqueous electrolyte (Figure 3.17). All photonic films displayed a continuous increase of photocurrent density with applied potential under visible as well as UV-Vis illumination (Figure 3.17a, b), which was reproduced by the corresponding photocurrent transient curves under chopped visible light at 1.23 V vs RHE (Figure 3.17c). The homojunction Mo-Ca-Mo PC films presented markedly enhanced photocurrent density that outperformed all metal-doped PCs, including Mo-$BiVO_4$ by ca. 60%, reaching almost a six-fold increase compared to the unmodified PC340 photoelectrode.

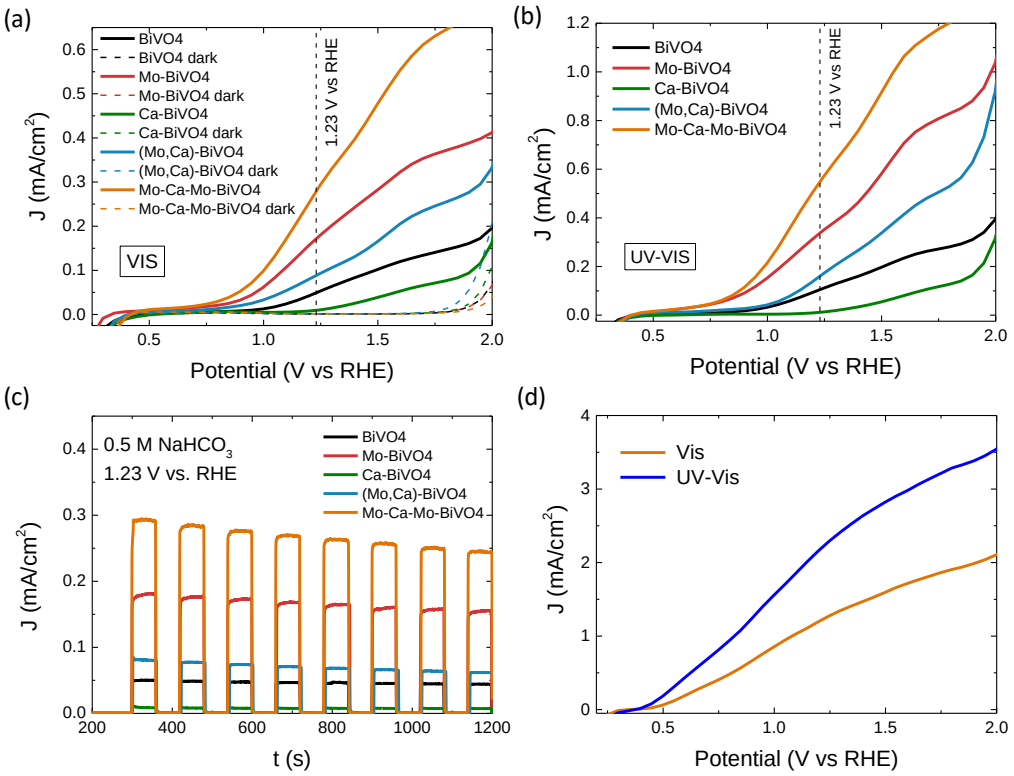

Figure 3.17 Current-potential curves for the metal-doped $BiVO_4$ PC films under (a) visible (solid lines) (dashed lines show the corresponding curves in the dark), and (b) UV-Vis light in 0.5 M $NaHCO_3$ electrolyte. (c) Chronoamperometry measurements under 60 s visible light-dark switching cycles. (d) Current-potential curves for the Mo-Ca-Mo PC films after the addition of 5% w/w EtOH in the electrolyte under visible and UV-Vis illumination.

More importantly, introduction of EtOH in the electrolyte as organic fuel, whose oxidation consumes photogenerated holes [14], resulted in marked enhancement of photocurrent density under both visible and UV-Vis light illumination (Figure 3.17d), indicating that Mo-Ca-Mo PCs could be applied as efficient photoanodes for PEC organic pollutant degradation and H_2 production.

VLA photocatalytic experiments showed that SA degradation (Figure 3.18a) followed pseudo first-order kinetics for all metal doped PCs (Figure 3.18b), from which the corresponding SA reaction rates r_{vis} were determined (Figure 3.18c). Significant increase of r_{vis} was observed for the homojunction Mo-Ca-Mo PC films, exceeding significantly all metal doped PCs (comparative SA degradation tests for the corresponding Ca-Mo-Ca PC films showed much lower photocatalytic activity). Comparison with bare PC340 films showed an enhancement factor of 2.05, which indicates a clear improvement of charge separation and transport for the Mo-Ca-Mo PCs besides light harvesting. Furthermore, the Mo- and Ca-doped $BiVO_4$ PC films presented markedly improved performance on both the photocurrent density in aqueous electrolyte and SA reaction rates r_{vis} in comparison with the corresponding planar films (Figure 3.19), reinforcing the synergy of metal doping and PC structuring in PEC performance amplification.

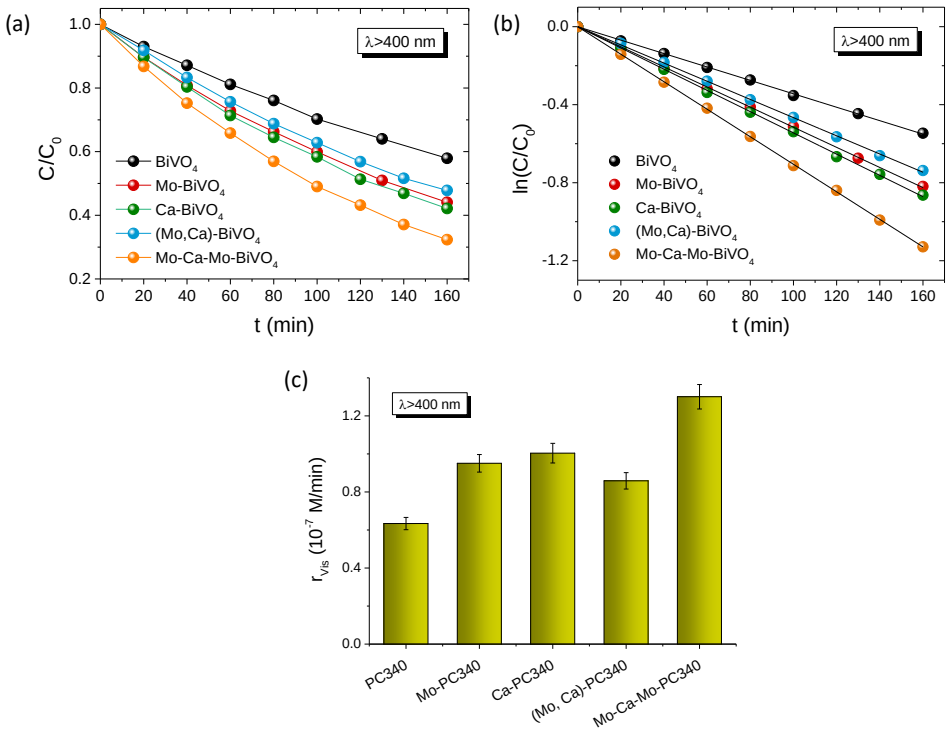

Figure 3.18 SA photodegradation kinetics (a),(b) and (c) the corresponding reaction rates r_{vis}, for the metal-doped $BiVO_4$ PC films under visible light.

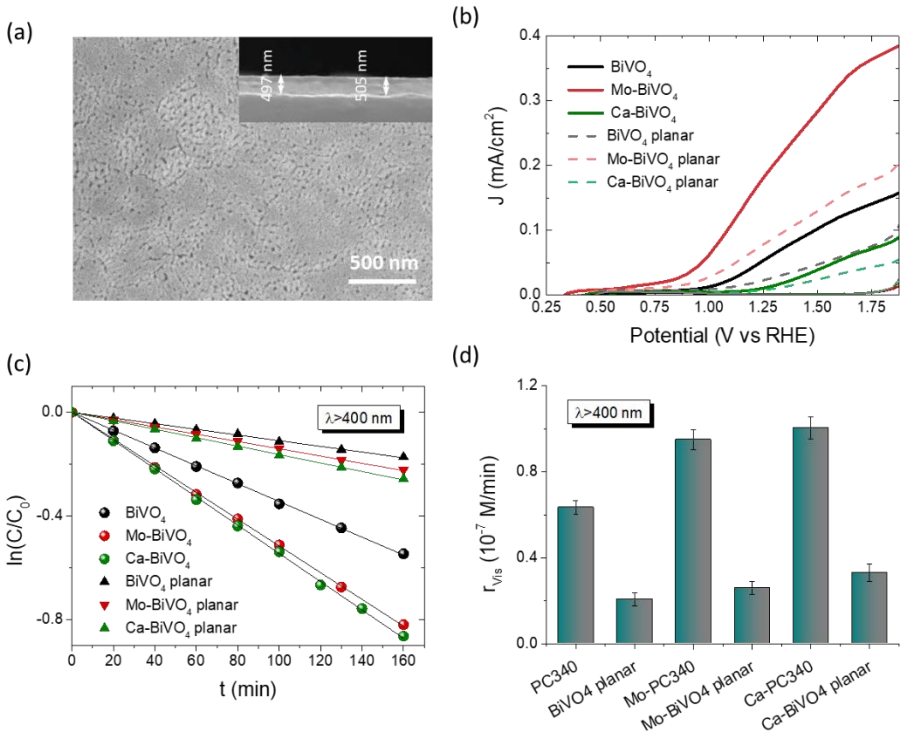

Figure 3.19 (a) SEM images of planar Mo-$BiVO_4$ films. Their thickness was approximately 500 nm leading to similar $BiVO_4$ mass loading to 2 μm-thick inverse opal films with solid filling factors $1 - f \leq 0.22$ (Table 3.1). Comparative (b) current density-potential curves in 0.5 M $NaHCO_3$ electrolyte, (c) SA photodegradation kinetics and (b) the corresponding reaction rates r_{vis} under visible light for the planar and PC $BiVO_4$ films.

Advanced application of the metal doped $BiVO_4$ PC films was carried out on PEC degradation of pharmaceutical emerging contaminants under visible light using TC and CIP, as representatives of tetracycline and quinolone antibiotics [173]. Initial PEC tests were carried out on SA degradation in 0.1 M $NaHCO_3$ supporting electrolyte using Mo-$BiVO_4$ PC films under no bias potential, +0.5 and +1.0 V vs Ag/AgCl under visible and UV-Vis illumination (Figure 3.20). A marked acceleration of SA photodegradation kinetics with applied potential was observed verifying its beneficial role in assisting photogenerated electron-hole separation [174]. In addition, linear sweep voltammetry and photoelectrocatalytic SA degradation experiments were performed on thicker Mo-$BiVO_4$ PC films under visible light (Figure 3.21). Increase of the inverse opal film thickness resulted in the decrease of both photocurrent density and SA kinetic constant, indicative of persistent electron transport limitations that depend on the films' morphology, similar to nanocrystalline Mo-$BiVO_4$ photoelectrodes for water splitting [24, 48].

The metal doped-$BiVO_4$ PCs were accordingly evaluated on the PEC degradation of SA (Figure 3.22) as well as TC (Figure 3.23) and CIP (Figure 3.24) antibiotics under visible light at +1.0 V vs Ag/AgCl.

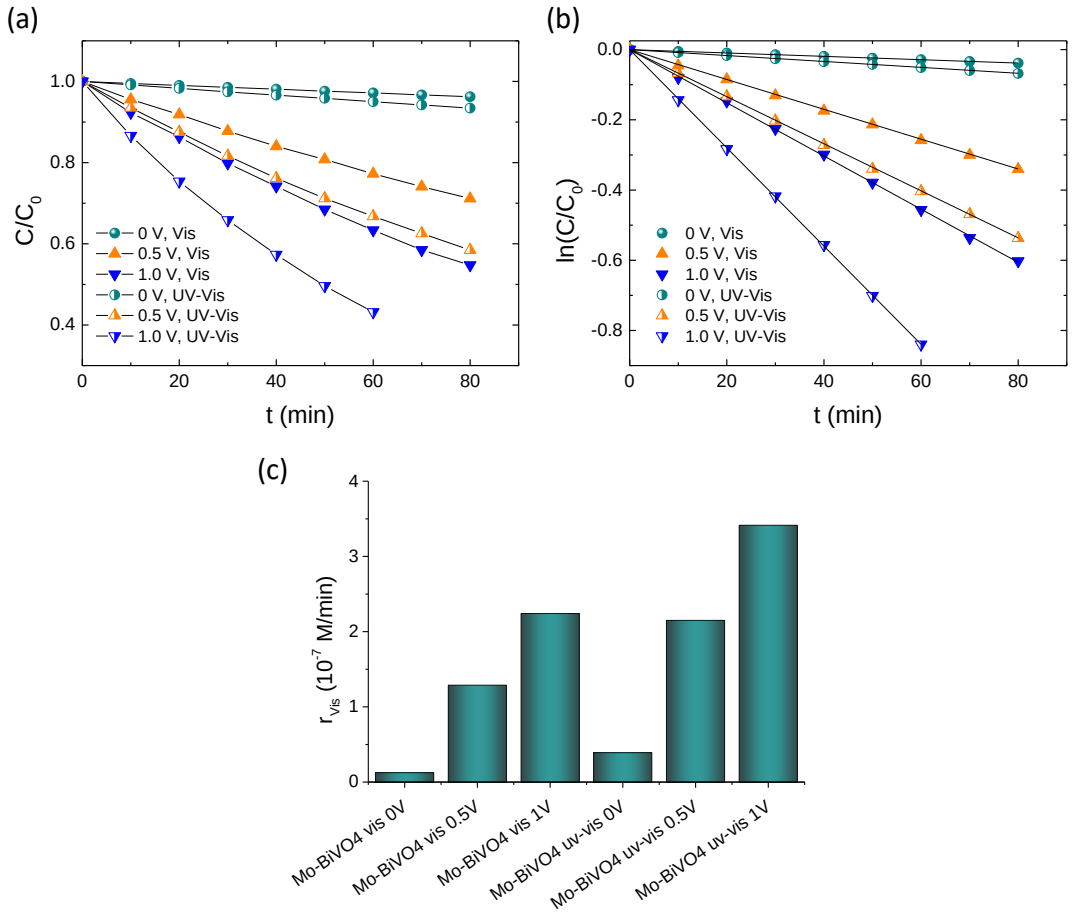

Figure 3.20 (a), (b) SA photoelectrocatalytic degradation kinetics and (c) the corresponding reaction rates r_{vis} for the Mo-$BiVO_4$ PC films in 0.1 M $NaHCO_3$ supporting electrolyte at bias potentials of 0, +0.5 and +1.0 V vs Ag/AgCl under visible and UV-Vis illumination.

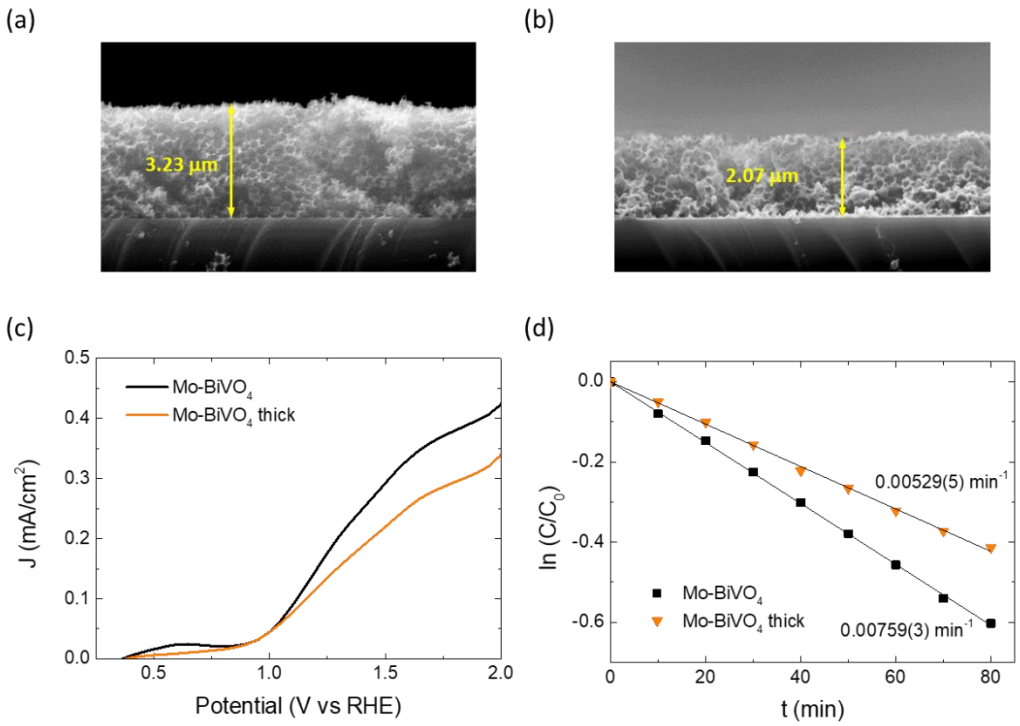

Figure 3.21 Cross section SEM images for (a) thick and (b) pristine Mo-BiVO$_4$ PC films. Comparative (c) current density-potential curves in 0.5 M NaHCO$_3$ electrolyte, and (d) SA photodegradation kinetics in 0.1 M NaHCO$_3$ for the thick and pristine Mo-BiVO$_4$ PC photoelectrodes under visible light at +1.0 V vs Ag/AgCl.

Photoelectrocatalytic SA degradation obeyed first-order kinetics with the homojunction PC photoelectrodes exhibiting greatly improved reaction rates r_{vis} (Figure 3.22), which followed closely the corresponding photocurrent variations under visible light (Figure 3.17a), indicating that SA degradation proceeds via photogenerated holes at acidic conditions similar to TiO$_2$ PCs [175]. On the other hand, Ca-BiVO$_4$ and Mo-Ca-Mo PC films showed the highest performance in TC photoelectrocatalytic degradation (Figure 3.23), though Mo-doping had a weak detrimental effect compared to pristine BiVO$_4$ PC films. Likewise, degradation rates of the more refractory CIP antibiotic were appreciably improved for Ca-BiVO$_4$ and Mo-Ca-Mo PC photoelectrodes (Figure 3.24), though in that case Mo- and Ca-doping resulted in increased r_{vis} compared to pristine BiVO$_4$ photonic films.

Despite the differences in the reaction mechanisms underlying pharmaceuticals degradation (*vide infra*), homojunction Mo-Ca-Mo PC photoelectrodes presented invariably the best PEC activity, similar to the results of photocurrent generation and plain photocatalysis (Figure 3.17). Performance comparison with literature results shows that the obtained kinetic constants were among the highest reported thus far for PEC degradation of TC by heterostructured BiVO$_4$ photoanodes (Table 3.3), while the relatively weaker activity obtained for CIP degradation compared to BiVO$_4$ heterojunction composites can be partly related to the different experimental conditions in the PEC experiments i.e. illumination conditions, bias potential, film area, pollutant concentration.

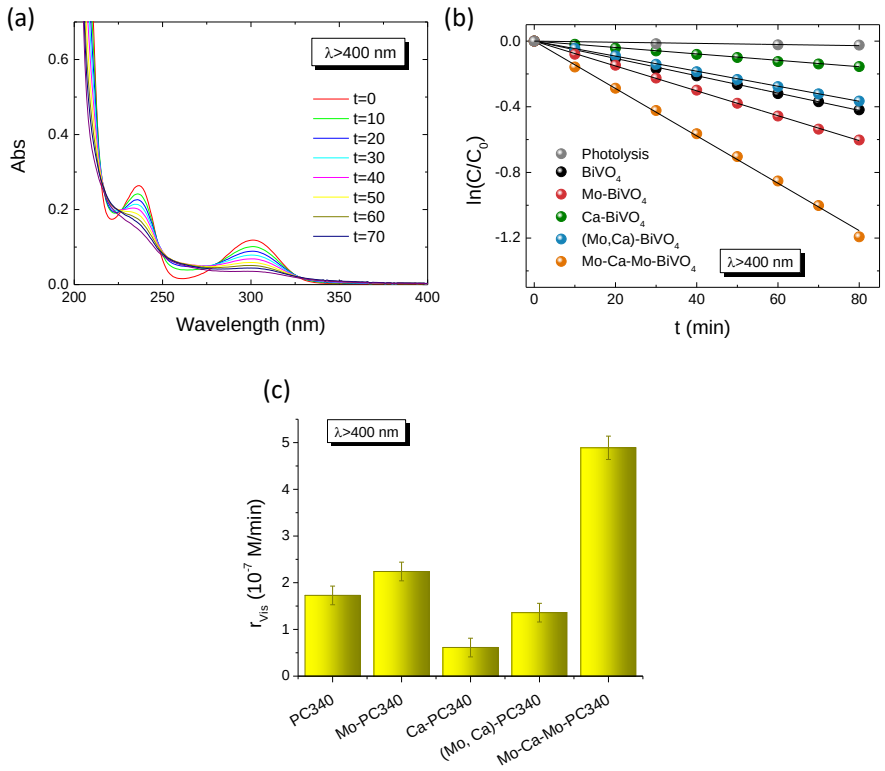

Figure 3.22 SA (a-c) absorbance spectra evolution in the presence of Mo-Ca-Mo PC electrodes, photodegradation kinetics, and reaction rates for the metal-doped $BiVO_4$ PC photoelectrodes at +1.0 V vs Ag/AgCl under visible light irradiation.

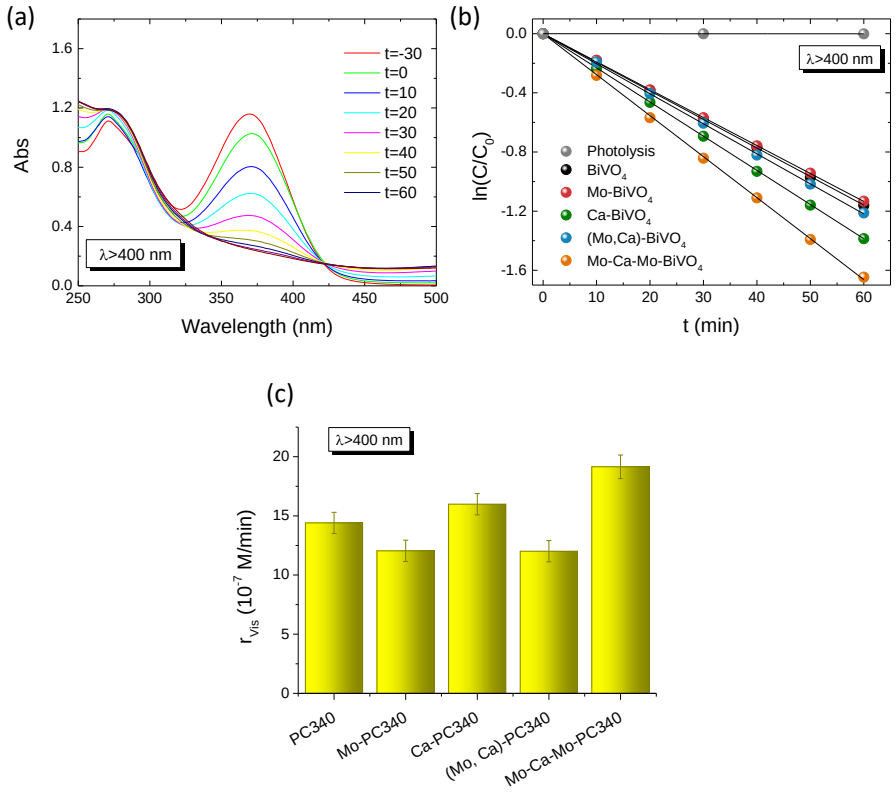

Figure 3.23 TC (d-f) absorbance spectra evolution in the presence of Mo-Ca-Mo PC electrodes, photodegradation kinetics, and reaction rates for the metal-doped $BiVO_4$ PC photoelectrodes at +1.0 V vs Ag/AgCl under visible light irradiation.

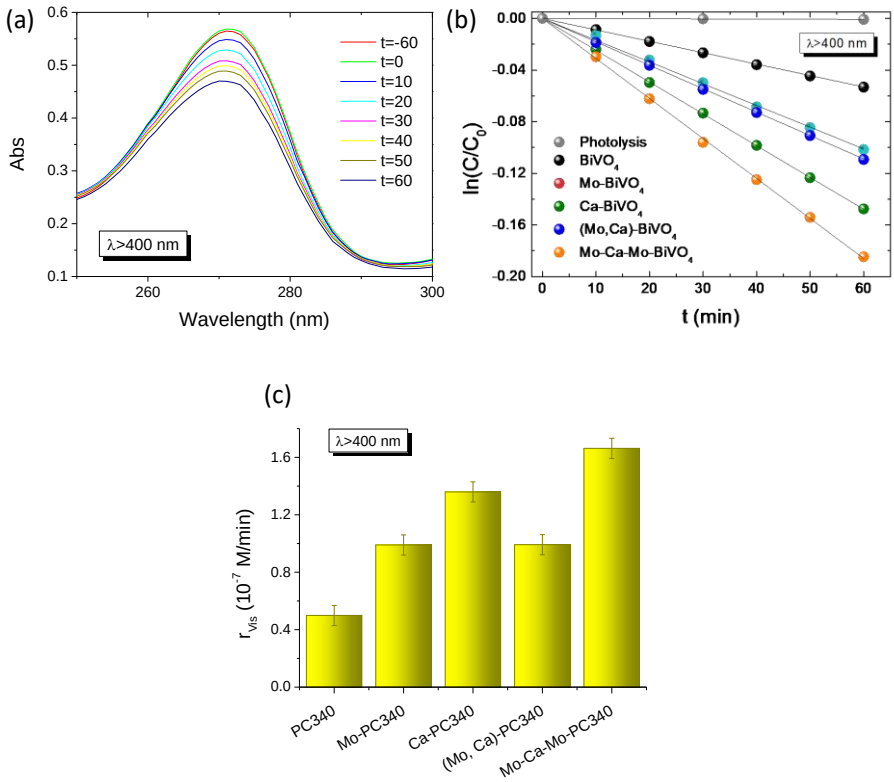

Figure 3.24 CIP (g-i) absorbance spectra evolution in the presence of Mo-Ca-Mo PC electrodes, photodegradation kinetics, and reaction rates for the metal-doped $BiVO_4$ PC photoelectrodes at +1.0 V vs Ag/AgCl under visible light irradiation.

Table 3.3 Performance comparison on tetracycline (TC), tetracycline hydrochloride (TCH) and ciprofloxacin (CIP) PEC degradation by $BiVO_4$-based photoelectrodes.

Photoanode composition	Catalyst morphology	Pollutant/ concentration	Irradiation conditions	Kinetic constant k (min^{-1})	Ref
WO_3/Mo-$BiVO_4$	Nanoplate arrays	TCH 10 mg/L	Xe 300 W AM 1.5 1V vs SCE	0.0114 min^{-1}	[176]
$BiVO_4$	Nanowires	TCH 10 mg/L	Xe 300 W AM 1.5 1 V vs Ag/AgCl	0.0035 min^{-1}	[177]
$BiVO_4$/ZnO	Nanorods	TC 20 mg/L	Xe 300 W λ>420 nm 0.8 V	0.00867 min^{-1}	[178]
F-$BiVO_4$@ NiFe-LDH	NPs/ nanoflakes	TCH 20 mg/L	Xe 300 W 100 mW/cm^2 0.5 V vs Ag/AgCl	0.0156 min^{-1}	[179]
FeOOH/1%Y-$BiVO_4$	warm-like	TCH 0.2 mg/L	PLS-SXE 300 W AM 1.5 0.7 V bias	0.00631 min^{-1}	[180]
SnO_2/Mo-$BiVO_4$	lichen-like morphology	TCH 5 mg/L	Xe 150 W AM 1.5G 1.23 vs RHE	0.0149 min^{-1}	[181]

$BiVO_4$/NiFe	nanoflowers	TC 20 mg/L	Xe 300W Visible light 0.6V vs SCE	pH= 7.5 0.01281 min^{-1} pH=6.5 0.02528 min^{-1}	[182]
Mo-Ca-Mo-$BiVO_4$	Inverse opals	TC 23 mg/L	Xe 300 W λ>400 nm 90 mW/cm^2 1 V vs Ag/AgCl	0.02772 min^{-1}	**This work**
$BiVO_4$/BiOI	Flower-like agglomerates	CIP 10 mg/L	Xe 100 W solar 1.5 V vs Ag/AgCl	0.00878 min^{-1}	[183]
$BiVO_4$/MnO_2	Agglomerated particles	CIP 10 mg/L	Xe 100 W solar 1.5 V vs Ag/AgCl	0.01053 min^{-1}	[184]
$BiVO_4$/Ag_2S	Nanowires	CIP 10 mg/L	Xe 150 W Solar 1.2 V vs Ag/AgCl	0.0137 min^{-1}	[185]
Mo-Ca-Mo-$BiVO_4$	Inverse opals	CIP 14 mg/L	Xe 300 W λ>400 nm 90 mW/cm^2 1 V vs Ag/AgCl	0.0031 min^{-1}	**This work**

In order to explore the role of reactive oxygen species in the photoelectrocatalytic activity of pristine and metal doped $BiVO_4$ PCs for TC (Figure 3.25) and SA (Figure 3.26) degradation, trapping experiments were performed by the addition of isopropanol (IPA), formic acid (FA) and 1,4 benzoquinone (BQ) scavengers in the reaction solution. The presence of IPA resulted in relatively weak effects on TC degradation kinetics, whereas the addition of BQ and FA caused significant drop of r_{vis}, especially for Ca-$BiVO_4$, indicating that superoxide radical anions ($O_2^{\bullet-}$) and holes (h^+) are the major species underlying TC degradation [173].

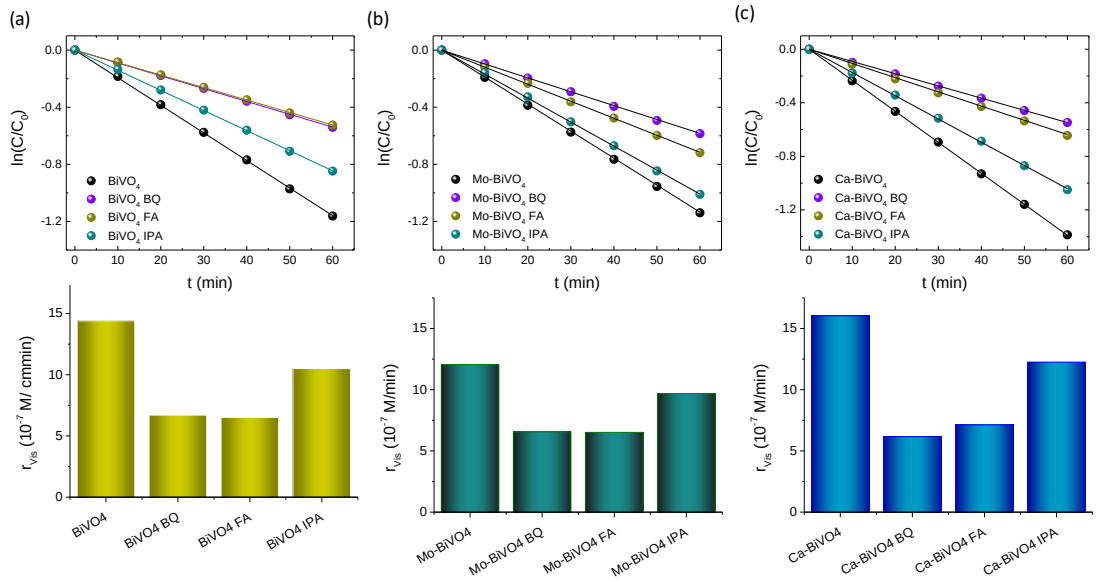

Figure 3.25 TC photoelectrocatalytic degradation kinetics and the corresponding reaction rates r_{vis} in the presence of IPA, FA and BQ radical scavengers for (a) $BiVO_4$, (b) Mo-$BiVO_4$ and (c) Ca-$BiVO_4$ PC films in 0.1 M $NaHCO_3$ supporting electrolyte under visible light at +1.0 V vs Ag/AgCl.

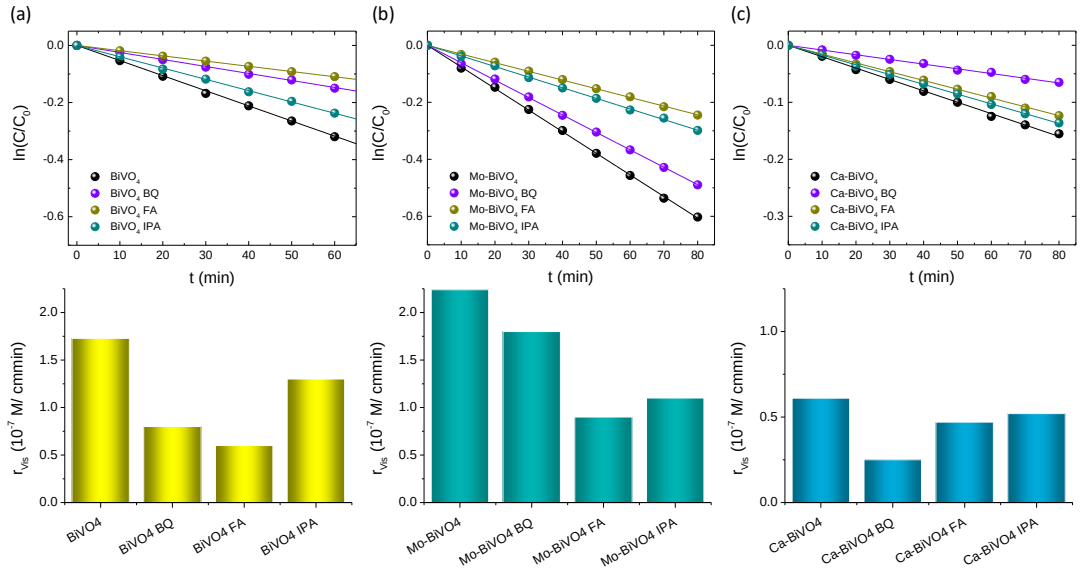

Figure 3.26 SA photoelectrocatalytic degradation kinetics and the corresponding reaction rates r_{vis} in the presence of IPA, FA and BQ radical scavengers for (a) $BiVO_4$, (b) Mo-$BiVO_4$ and (c) Ca-$BiVO_4$ PC films in 0.1 M $NaHCO_3$ supporting electrolyte under visible light at +1.0 V vs Ag/AgCl.

The suppression of TC degradation by BQ was more evident for Ca-$BiVO_4$ compared to the less reactive Mo-$BiVO_4$ PCs, indicating that $O_2^{\bullet-}$ radical formation is favored in the former case. In the case of SA degradation, the presence of FA resulted in the largest decrease of r_{vis} for both $BiVO_4$ and Mo-$BiVO_4$ PCs indicating that photogenerated valence band h^+ are the major reactive species. On the other hand, BQ's addition caused variable effects on the SA reaction rates that decreased in the order Ca-$BiVO_4$ >$BiVO_4$ >Mo-$BiVO_4$, indicating analogous shifts of the $BiVO_4$ conduction band CB potential with Mo- and Ca-doping relatively to that of single-electron O_2 reduction (O_2/O_2^- at -0.33 V *vs.* NHE) [126, 127]. The corresponding variations of $BiVO_4$ band edge variations with metal doping were subsequently studied by UPS analysis.

3.3 Electronic properties and charge separation

UPS measurements with He I excitation (21.22 eV) were accordingly carried out in order to investigate the electronic properties and band edge positions for the metal doped $BiVO_4$ PCs. The secondary electron cut-off (Figure 3.27a) and valence band spectral regions (Figure 3.27b) were used to determine the work function (WF) and VBM with respect to the Fermi level, respectively. The obtained WF and E_F-E_{VBM} together with the electronic band gaps (E_g), which were determined from Tauc plots (Figure 3.27c) for the $BiVO_4$ indirect band gap [33], derived from the corresponding Kubelka-Munk transforms of the diffuse reflectance DR% spectra (Figure 3.28), were used to construct the energy band diagram vs vacuum level (0 eV) for the metal-doped $BiVO_4$ PCs (Figure 3.27d). The obtained E_g values, which are summarized in Table 3.4, showed that $BiVO_4$ doping by either Mo^{6+} or Ca^{2+} ions, results in slight E_g narrowing, verifying the formation of shallow defect states.

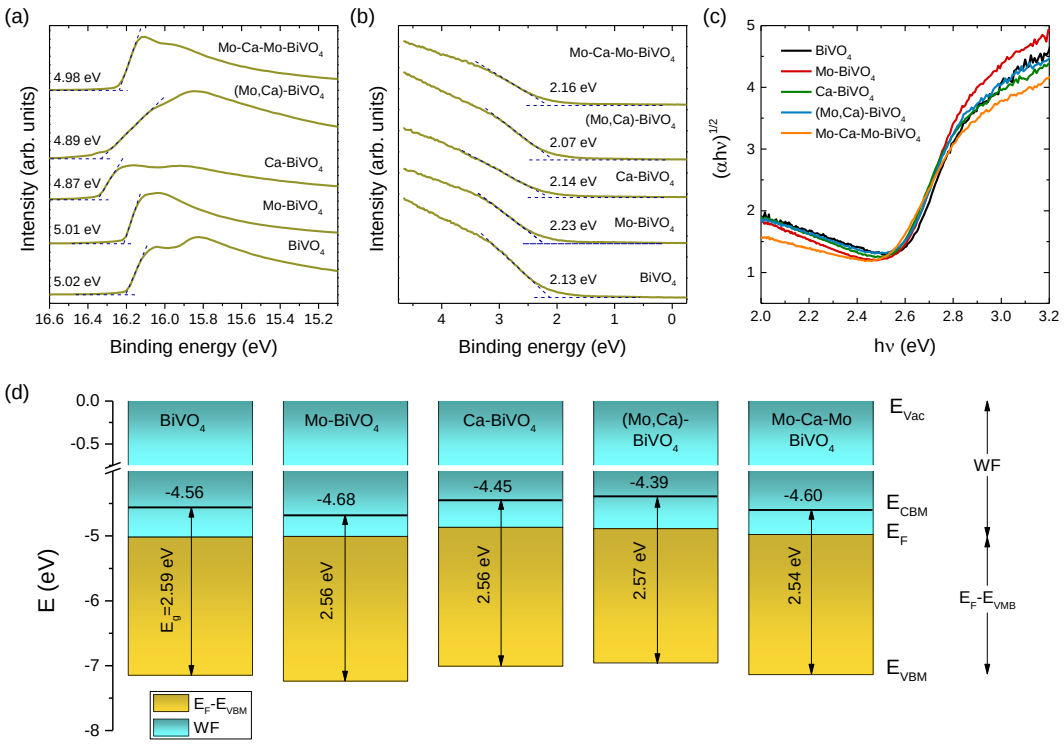

Figure 3.27 (a) Secondary electron cut-off, (b) valence band UP spectra, (c) Tauc plots and (d) energy band diagrams vs the absolute vacuum level taken as reference at 0 eV for the metal-doped $BiVO_4$ PCs.

A Fermi level shift towards the conduction band minimum E_{CBM} was observed for Mo-$BiVO_4$, in agreement with the formation of donor states, whereas an increase of E_F-E_{CBM} was observed for Ca-$BiVO_4$, indicative of acceptor states close to E_{VBM}. However, the latter value was close to the E_F-E_{CBM} of the bare $BiVO_4$ PCs indicating compensation effects by the simultaneous presence of intrinsic or extrinsic defects [40]. This was investigated by Mott–Schottky measurements (Figure 3.29), which confirmed that all metal-doped $BiVO_4$ films exhibited *n*-type semiconducting behavior with weakly varying flat band potentials, consistently with the E_F shifts derived from UPS analysis, though with largely different donor densities N_D.

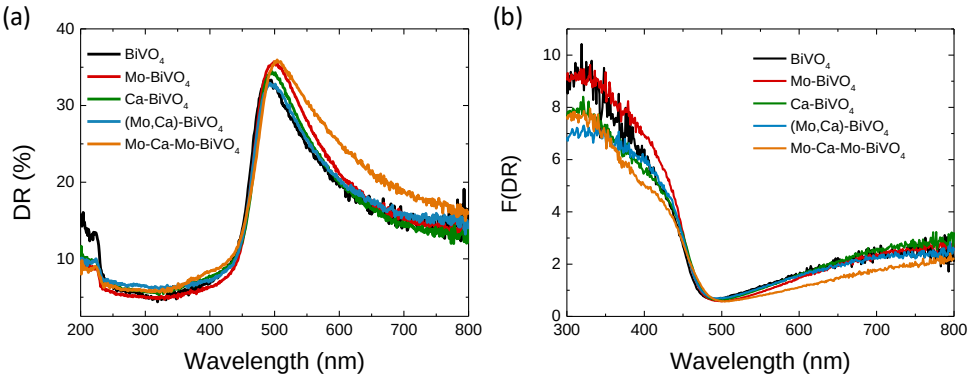

Figure 3.28 (a) Diffuse reflectance and (b) absorbance spectra obtained from the Kubelka-Munk function F(DR) for the metal doped $BiVO_4$ PC340 films.

Table 3.4 Absorption edge λ_{edge} and electronic band gaps E_g for the metal doped $BiVO_4$ PC films. The E_g values were determined from Tauc equation $(ahv)^n = A(hv - E_g)$ for $n = 1/2$, which corresponds to $BiVO_4$ indirect band gap [33].

PC film	λ_{edge} (nm)	E_g (eV)
$BiVO_4$	479	2,59
Mo-$BiVO_4$	484	2,56
Ca-$BiVO_4$	484	2,56
(Mo,Ca)-$BiVO_4$	482	2,57
Mo-Ca-Mo $BiVO_4$	488	2,54

The Mo-Ca-Mo and Mo-$BiVO_4$ PCs presented the highest N_D values of 1.87×10^{20} and 1.56×10^{20} cm^{-3}, which greatly exceeded those obtained for $BiVO_4$, Ca-$BiVO_4$ and (Mo, Ca)-$BiVO_4$, i.e. 2.18×10^{19}, 2.88×10^{19}, 3.20×10^{19} cm^{-3}. This variation shows that *p*-type doping was not realized for Ca-$BiVO_4$, most likely via the compensation of Ca^{2+} acceptor states by oxygen vacancies, similar to $BiVO_4$ doped by bivalent Co^{2+} [50] and Zn^{2+} ions [186]. Taking into account the successive infiltration of Mo- and Ca-containing metal salt precursors in the colloidal opal template, a broad distribution of n–n⁺ type-II homojunctions between Mo-$BiVO_4$, Ca-$BiVO_4$ and co-doped (Mo, Ca)-$BiVO_4$ nanocrystals that compose the inverse opal skeleton will occur for the Mo-Ca-Mo PCs. These nanoscale homojunctions can further promote charge separation and transport in the highly interconnected 3D $BiVO_4$ PC porous structure by confinement effects [124].

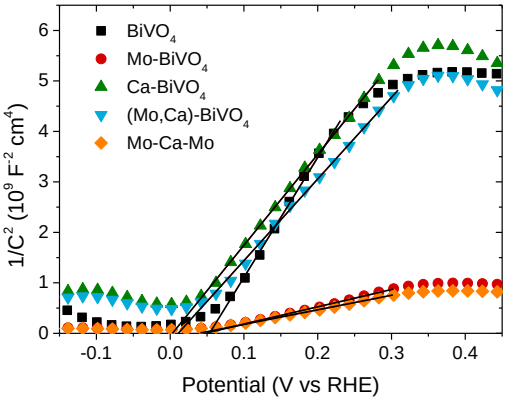

Figure 3.29 (a) Mott–Schottky plots for the metal-doped $BiVO_4$ PC photoelectrodes in the dark at 500 Hz.

The resulting energy band diagrams for the metal-doped $BiVO_4$ PCs vs RHE at pH=7 (Figure 3.30) show that Mo- and Ca- doping lead to substantial band offsets between differently doped $BiVO_4$ nanocrystals, whose band edges straddle the redox potentials for the generation of $OH^{\bullet}$ and $O_2^{\bullet-}$ reactive oxygen species and those for the O_2 and

H_2 evolution reactions. In particular, Ca-doping causes an upward shift of $BiVO_4$ band edge positions facilitating the generation of $O_2^{\bullet-}$ radicals, which are essential to TC and CIP antibiotics degradation (Figure 3.23 and 3.24), in agreement with the major quenching contribution of FA in TC scavengers' tests (Figure 3.25). Superoxide radical species though may not play a major role in the photoelectrocatalytic SA degradation by means of h^+ in acidic conditions (Figure 3.26), leading to the overall decrease of the corresponding reaction rates r_{vis} for Ca-$BiVO_4$ (Figure 3.22). On the other hand, Mo-doping causes a downward shift of $BiVO_4$ band edges that favor oxidation reactions either directly by valence band h^+ or $OH^\bullet$ radicals, complying with the results of trapping experiments for both TC (Figure 3.25) and SA (Figure 3.26) degradation, while at the same time improves carrier density and charge transport. More importantly, despite the differences in the reaction mechanisms for pharmaceuticals degradation, which stem from the variations of band edge positions relatively to the redox potential of reactive oxygen species, delineated by the trapping experiments and UPS analysis, Mo-$BiVO_4$/Ca-$BiVO_4$ PCs exhibited the highest photoelectrocatalytic reactivity. In that case, the formation of nanoscale n–n^+ type-II homojunctions and the associated electron transfer between differently doped $BiVO_4$ nanoparticles is expected to improve charge separation beyond that of single metal doped or co-doped $BiVO_4$ PCs and validate the enhanced PEC performance of homojunction PCs for all pharmaceutical micropollutants.

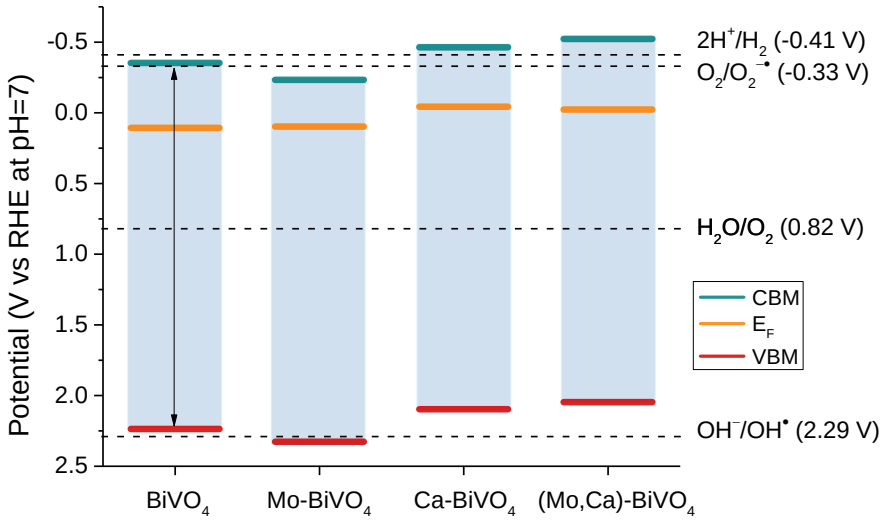

Figure 3.30 Energy band diagrams for the metal-doped $BiVO_4$ PCs compared to the redox potentials for the generation of hydroxyl ($OH^\bullet$) and superoxide ($O_2^{\bullet-}$) radical species and for the O_2 and H_2 evolution reactions relative to RHE at pH=7.

Charge carrier recombination in metal-doped $BiVO_4$ PCs was accordingly explored by EIS measurements (Figure 3.31). Metal doping resulted in a systematic decrease of charge-transfer resistance (R_{CT}) compared to the bare $BiVO_4$ PCs, indicated by the reduction of the capacitive arc radius at higher frequencies in the EIS plane, which was verified by fitting the experimental data to an equivalent Randles circuit under both dark (Figure 3.31a) and visible light illumination (Figure 3.31b).

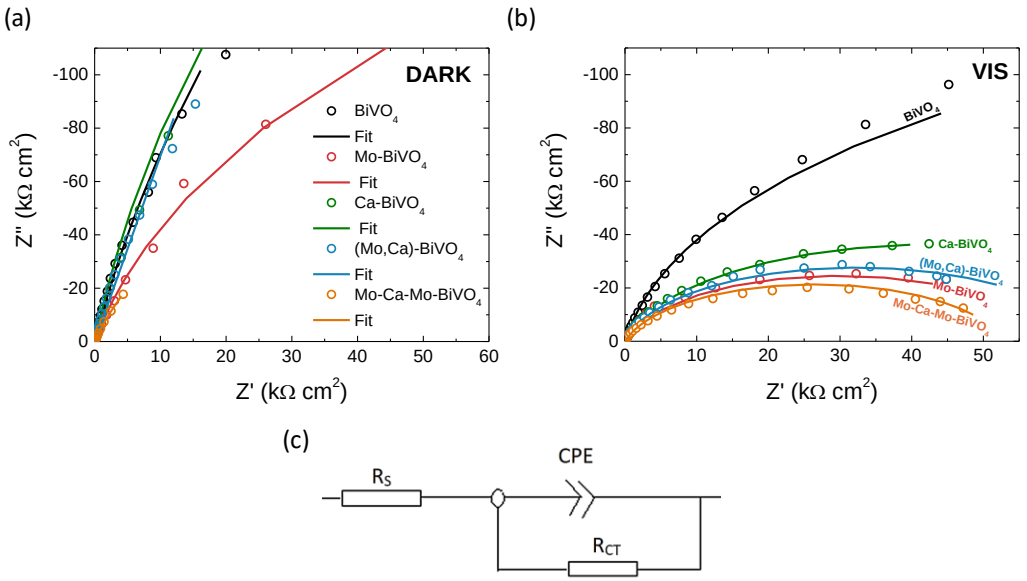

Figure 3.31 EIS Nyquist plots for the metal-doped $BiVO_4$ PCs under (a) dark conditions and (b) visible light. Solid lines depict the best fit curves to the modified Randles equivalent circuit (c) with parameters the series resistance R_S, the charge-transfer resistance R_{CT} and a constant phase element CPE [155].

Specifically, the obtained R_{CT} values, which are summarized in Table 3.5, decreased successively following the order Mo-Ca-Mo<Mo-$BiVO_4$<(Mo,Ca)-$BiVO_4$<Ca-$BiVO_4$<$BiVO_4$, confirming the enhanced charge separation in the Mo-Ca-Mo homojunction films.

Table 3.5 Parameters obtained by fitting the experimental impedance spectra to a modified Randles circuit for the metal doped $BiVO_4$ inverse opal films.

	Dark		Visible light (>400 nm)	
PC film	R_S (Ω cm^2)	R_{CT} (kΩ cm^2)	R_S (Ω cm^2)	R_{CT} (kΩ cm^2)
$BiVO_4$	35.8	1892	41.6	266
Mo-$BiVO_4$	32.2	509	26.3	59.7
Ca-$BiVO_4$	36.2	1818	32.4	86.6
(Mo,Ca)-$BiVO_4$	22.9	1500	32.0	64.7
Mo-Ca-Mo $BiVO_4$	25.5	306	33.5	52.9

Charge recombination in the metal doped $BiVO_4$ PC films was further investigated by PL spectroscopy (Figure 3.32) The PL spectra presented a broad peak at about 570 nm (ca 2.18 eV) for all metal doped PCs, which lies well below E_g (Table 3.4), indicating the absence of band edge emission and the presence of indirect band gap for $BiVO_4$ [33]. The observed PL complies with the excitation of donor-acceptor transitions that have been recently identified as the main radiative recombination process for $BiVO_4$ [187].

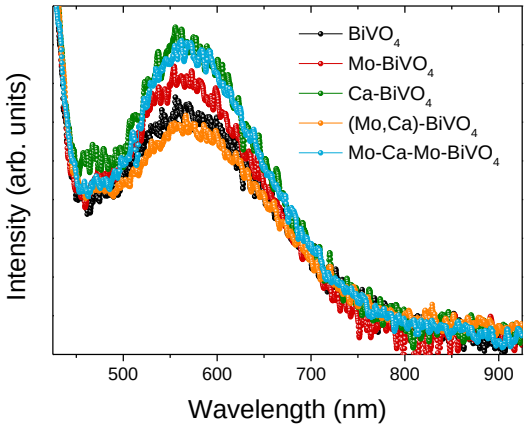

Figure 3.32 PL spectra for the metal-doped $BiVO_4$ PCs at 405 nm laser excitation.

In that case, temperature-dependent and time-resolved PL experiments revealed that radiative recombination competes with multi-phonon non-radiative processes via deep-level defects that become predominant for $BiVO_4$ photocarrier recombination at room temperature. In the present case, Ca-$BiVO_4$ and Mo-Ca-Mo-$BiVO_4$ showed the maximum PL intensity and thus the maximum radiative recombination, complying with the beneficial role of shallow acceptor levels in reducing non-radiative recombination [187]. On other hand, (Mo, Ca)-co-doping resulted in the reduction of PL intensity, most likely reflecting the decreased crystallinity of (Mo, Ca)- $BiVO_4$ PCs (Figures 3.11 and 3.12) and the formation of non-radiative recombination centers that shorten the carrier lifetime and decrease the hole diffusion length that deteriorate the PEC performance of (Mo,Ca)-$BiVO_4$.

3.4 Conclusions

In conclusion, the formation of nanoscale n-n^+ homojunctions between differently doped Mo-$BiVO_4$, Ca-$BiVO_4$ and co-doped (Mo, Ca)-$BiVO_4$ nanocrystals in the skeleton of PBG engineered inverse opal films is put forward as a highly competent approach to improve visible light trapping, electron transport and charge separation in nanostructured $BiVO_4$ photoelectrodes for the photoelectrocatalytic degradation of pharmaceutical contaminants of emerging concern. Light trapping optimization for $BiVO_4$ PCs with controlled PBGs along with compositional engineering by Mo- and Ca-doping allowed the deposition of Mo-$BiVO_4$/Ca-$BiVO_4$ nanoscale homojunctions by the successive infiltration of the optimal Mo and Ca-containing metal salt precursors in the colloidal templates. The introduction of shallow dopant states in $BiVO_4$ and abundant interfaces between Mo-, Ca-doped $BiVO_4$ nanoparticles with relatively weak structural distortions but significantly different donor concentrations was thereby achieved according to electrochemical measurements and photoelectron spectroscopy. This resulted in a broad distribution of n-n^+ type II homojunctions in the nanocrystalline inverse opal walls, which caused multifold performance enhancement for the Mo-Ca-Mo homojunction $BiVO_4$ PC films in VLA photocurrent generation and SA degradation rate compared to their individual constituents. Advanced application of the metal-doped $BiVO_4$ inverse opal films was demonstrated on the VLA photoelectrocatalytic degradation of emerging contaminants including TC and CIP

broad-spectrum antibiotics besides SA. Homojunction nanostructure-based $BiVO_4$ PC photoelectrodes presented invariably the highest rate for pharmaceuticals degradation due to the combination of enhanced visible light trapping and charge separation evading intrinsic limitations of single $BiVO_4$ nanomaterials for organics degradation under visible light.

CHAPTER 4

Plasmonic Ag, Au modified Mo-$BiVO_4$ inverse opal photoelectrocatalysts

In the present work†, PBG engineered Mo-doped $BiVO_4$ inverse opal photoelectrodes were applied as VLA photonic hosts for grafting plasmonic Ag and Au NPs both as single and dual co-catalysts aiming at the development of plasmonic-photonic photoelectrocatalysts for pharmaceuticals degradation. Aside from enhanced PEC activity due to improved visible light harvesting, electron transport and charge separation by Mo-doping, the selection of Mo-$BiVO_4$ PCs as semiconductor photonic substrate, which has a work function straddling those of the two noble metal NPs, allowed investigating the variation of the metal-semiconductor band alignment and thus the interplay of different plasmonic enhancement mechanisms in the metal-semiconductor heterostructure performance. Comparative evaluation of the (Ag, Au)/Mo-$BiVO_4$ PC films was carried out by photoelectrochemical measurements and visible light photoelectrocatalytic degradation of two pharmaceutical emerging contaminants in water bodies, namely tetracycline (TC) broad spectrum antibiotic and the highly refractory ibuprofen (IBU) nonsteroidal anti-inflammatory drug. Although a major contribution from local field enhanced electron-hole generation was inferred from the PEC response of the metal-decorated Mo-$BiVO_4$ PC photoelectrodes, different degradation mechanisms for the two pharmaceutical contaminants probed by scavenger tests, indicate additional contributions from interfacial electron transfer especially for the Ag-Au co-decorated plasmonic-photonic photoelectrocatalysts.

4.1 Structural and optical properties

SEM images (Figure 4.1a-d) showed that crystallization of the metal salt precursor in the interstices of the PS colloidal template prepared by the horizontal self-assembly method (Section 2.1.1) after calcination, resulted in well-ordered, interconnected inverse opal structures with macropore diameter (D) determined from that of the PS templating spheres and approximately 1.2 μm film thickness (Figure 4.1e). XRD measurements before and after surface modification with the metallic NPs (Figure 4.2), showed that the PC films crystallize in the *ms* $BiVO_4$ phase (space group I2/a, JCPDS 014-0688), identified by the splitting of the (002)/(200) diffraction peaks at 34.5° and 35.2° as well as the (240)/(042) ones at about 46.9° and 47.3° (Section 3.1) However, the observed splitting was considerably moderated and less resolved for all Mo-$BiVO_4$ films, indicating that the introduction of molybdenum dopants substituting for vanadium in the $BiVO_4$ lattice (Section 3.2), leads to the averaging of the *ms* low-symmetry toward the tetragonal scheelite structure [134].

† This chapter has been published in ref. [135].

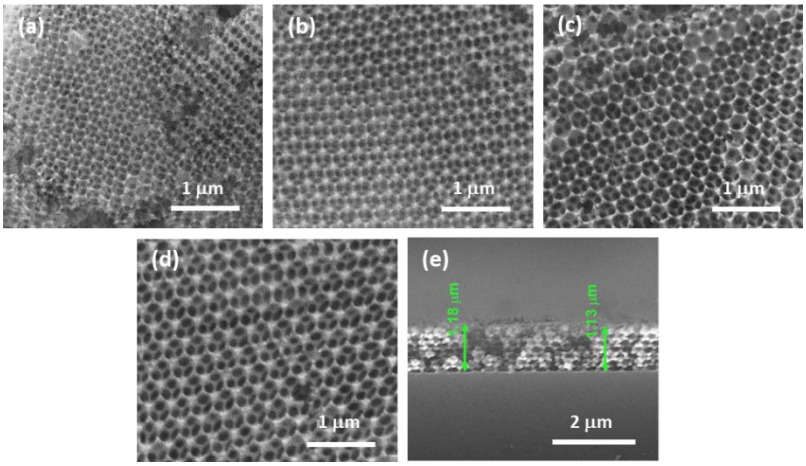

Figure 4.1 Plan view SEM images for (a) PC239, (b) PC287, (c) PC340, (d) PC418, and cross section for (e) PC340 inverse opal films.

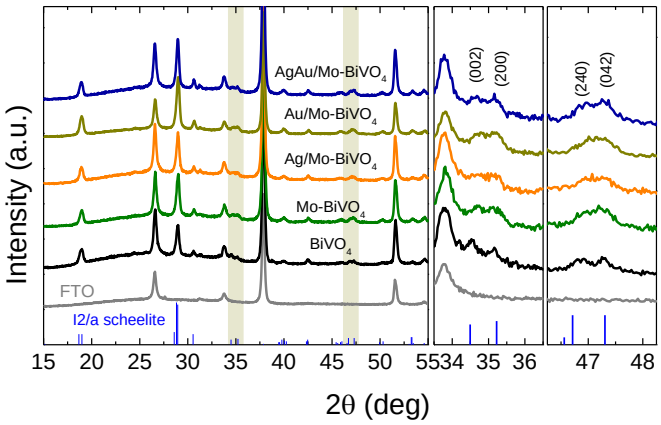

Figure 4.2 XRD patterns of Ag, Au-modified Mo-BiVO4 PC340 films compared to the pristine Mo-doped and undoped $BiVO_4$. The XRD patterns of the FTO substrate and the ms phase (JCPDS 014-0688) are also displayed, while the right panels depict in detail the shaded areas of the XRD patterns.

In addition, no sign of metallic Au and Ag NPs could be traced in the XRD patterns of the Ag, Au- modified PC films, indicative of their relatively low loading amount. Micro-Raman spectra for the Ag, Au- modified Mo-$BiVO_4$ films at 785 nm, displayed in all cases the characteristic vibrational modes of single-phase *ms* $BiVO_4$ with no sign of the tetragonal scheelite or zircon polymorphic phases [162]. Specifically, the strong symmetric (ν_s) along with the weak antisymmetric (ν_{as}) V-O stretching modes were identified at 824 and 712 cm^{-1}, respectively [161]. The monoclinic distortion of the scheelite structure was identified by the observation of two separate modes at 366 and 331 cm^{-1} (Figure 4.4) arising from the symmetric (δ_s) and antisymmetric (δ_{as}) bending modes of the VO_4 tetrahedra, as well as the two intense external (rotation/translation) lattice modes at 210 and 124 cm^{-1}. The presence of Mo^{6+} dopants substituting for V^{5+} cations in $BiVO_4$, was traced by the observation of an additional weak shoulder at about 882 cm^{-1} related to the corresponding MoO_4 stretching vibration [165], as well as the shift of the Raman peaks in comparison to the characteristic vibrational modes of pristine $BiVO_4$ PCs (Figure 4.3).

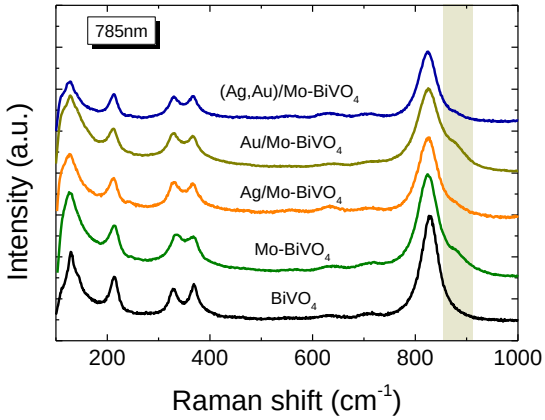

Figure 4.3 Raman spectra of Ag, Au-modified Mo-$BiVO_4$ PC340 films compared to pristine $BiVO_4$ PC films Mo-doped and undoped $BiVO_4$ at 785 nm.

Both the symmetric ν_s and antisymmetric ν_{as} stretching bands as well as the δ_s and δ_{as} bending modes of the VO_4 tetrahedra approached each other for the Mo-doped PCs, indicating the reduction of the *ms* lattice distortion towards the tetragonal phase. Using the exponential function $\nu = 21349\, e^{-1.9176\, R}$, which relates the V-O stretching frequencies (cm^{-1}) to V-O bond lengths (Å) in vanadium oxides [166], the values of 1.697 and 1.773 Å, were derived for the two V-O tetrahedral bond lengths in Mo-$BiVO_4$ in comparison to 1.694 and 1.775 Å, for the pristine $BiVO_4$ PCs, corroborating the averaging of the VO_4 tetrahedral deformation after Mo-doping. On the other hand, surface decoration of Mo-$BiVO_4$ inverse opals by Ag and/or Au NPs had no influence on the Raman frequencies apart from a weak intensity variation, most likely due to the reflectance of the metallic NPs.

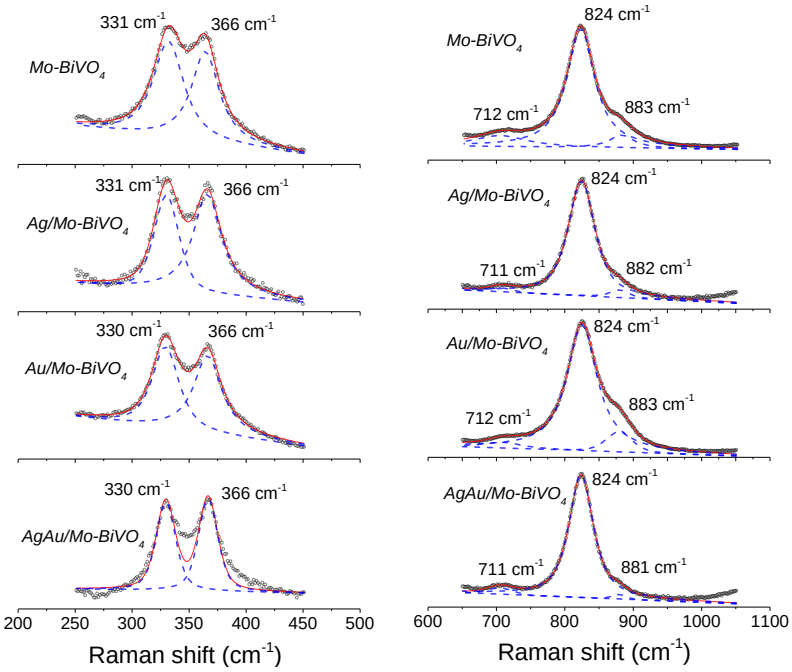

Figure 4.4 Spectral deconvolution (solid-dashed lines) of the bending (left) and stretching (right) VO_4 vibrational modes from the corresponding Raman spectra (open circles) for the single-, Ag-, Au- and (Ag,Au)-modified Mo $BiVO_4$ PC films.

The chemical composition of the PC films consisting of Bi, V, O and Mo elements, and their surface modification by Au and Ag NPs was investigated by EDX elemental maps of scanning TEM images. The uniform coverage and infiltration of the inverse opal skeleton by metallic NPs was thereby verified for the co-deposited (Ag,Au)/Mo-$BiVO_4$ (Figure 4.5a-d) as well as the singly-decorated Ag/Mo-$BiVO_4$ (Figure 4.6) and Au/Mo-$BiVO_4$ (Figure 4.7) PC340 films. The formation of high surface density of metallic NPs on the Mo-$BiVO_4$ walls with numerous clusters was directly observed in higher magnification TEM images (Figure 4.5e). The individual Ag and Au NPs of different sizes could be identified in the FFT patterns of high-resolution TEM images on the (Ag,Au)/Mo-$BiVO_4$ inverse opal walls (Figure 4.5f, g), where the *d*-spacing of 2.05 Å from the (200) *fcc* planes of ~10.5 nm Ag NPs was derived in contrast to the 2.36 Å interplanar spacing of (111) *fcc* planes for ~6 nm Au NPs. Likewise, the presence of Au NP aggregates was confirmed in high magnification TEM images of the Au/Mo-$BiVO_4$ inverse opal walls (Figure 4.7).

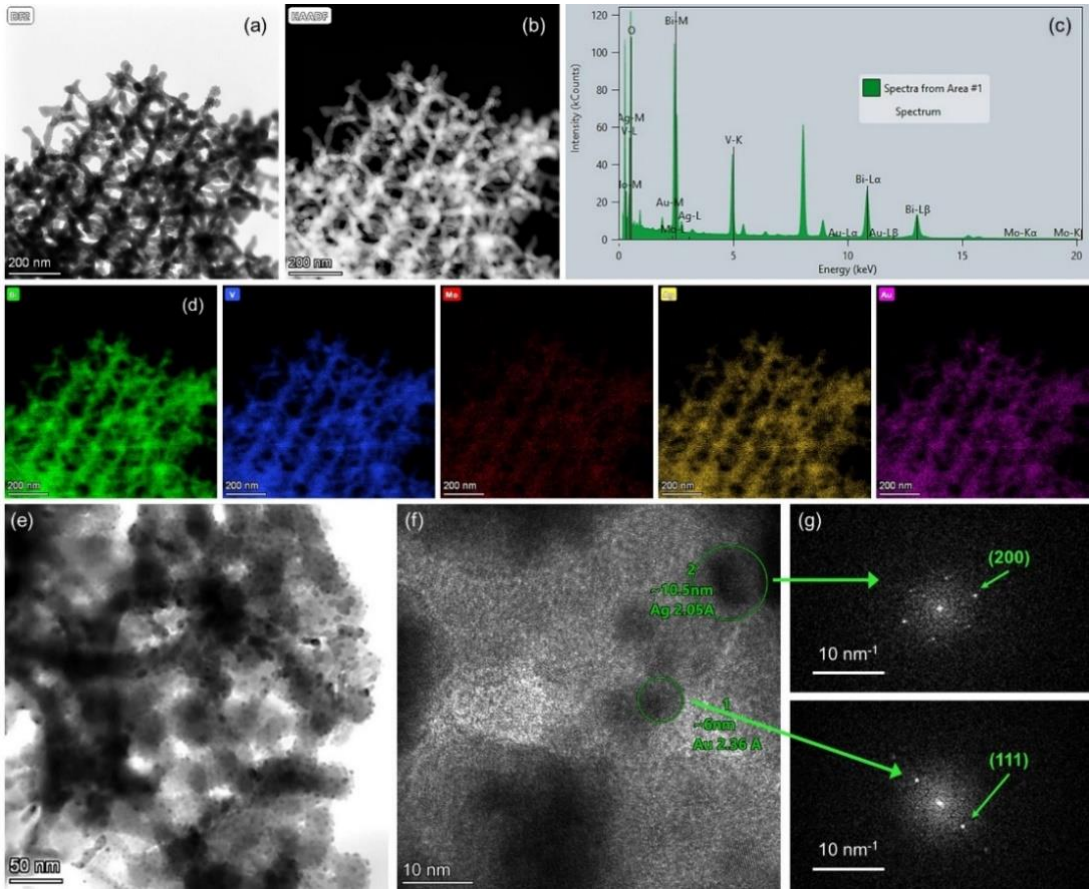

Figure 4.5 (a), (b) TEM images of (Ag, Au)/Mo-$BiVO_4$ PC340 films and (c) the corresponding local EDX spectrum and (d) Bi, V, O, Mo, Ag and Au elemental maps obtained from (e, f) Higher magnification TEM images of (Ag,Au)/Mo-$BiVO_4$ and (g) the FFT patterns of the encircled areas in (f), where individual Ag and Au NPs can be identified.

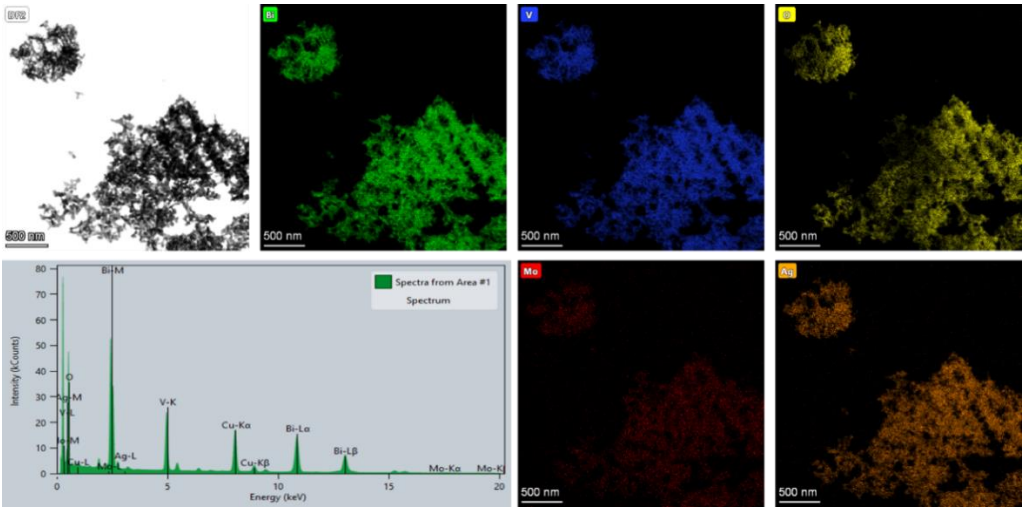

Figure 4.6 TEM image of Ag/Mo-$BiVO_4$ PCs and the corresponding Bi, V, O, Mo, and Ag elemental maps obtained from the corresponding local EDX spectra.

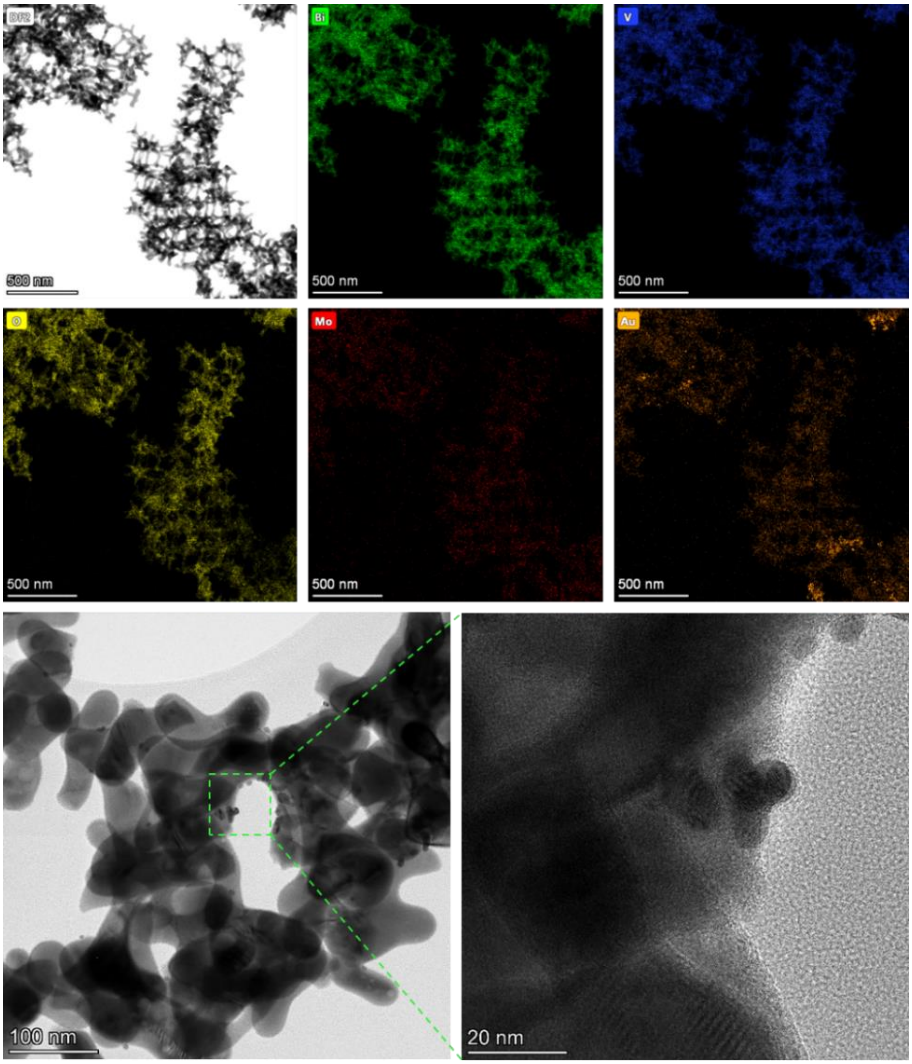

Figure 4.7 (Upper and middle panels) TEM image of Au/Mo-$BiVO_4$ PCs and the corresponding Bi, V, O, Mo, and Au elemental maps. (Bottom panel) TEM images at higher magnification showing the presence of Au NP aggregates decorating the large $BiVO_4$ nanocrystals.

The surface elemental composition of the plasmonic NP-modified Mo-$BiVO_4$ PCs films was determined by XPS measurements (Figure 4.8). The Bi 4f core level spectra for the Mo-$BiVO_4$ photonic substrate showed two distinct peaks at binding energies (BEs) of 159.3 and 164.5 eV (splitting Δ=5.2 eV), which correspond to the $4f_{7/2}$ – $4f_{5/2}$ spin-orbit doublet of Bi^{3+} ions [171]. The V 2p spectra presented the characteristic V $2p_{3/2}$ peak of V^{5+} ions at 516.9 eV, while the O 1s spectra showed an asymmetric broad peak at 530.1 eV arising from lattice oxygen and the presence of adsorbed oxygen species [116]. In addition, the presence of Mo^{6+} dopants was confirmed by the $3d_{5/2}$-$3d_{3/2}$ spin-orbit doublet at BEs of 232.4 and 235.6 eV (splitting Δ=3.2 eV) in the Mo 3d core level region [48]. The deposition of metallic NPs at the Mo-$BiVO_4$ inverse opal walls was identified in the respective Au 4f and Ag 3d core level spectra. The observed peaks at BEs of 368.1 and 374.2 eV (splitting Δ=6.1 eV) correspond to the $3d_{5/2}$-$3d_{3/2}$ spin-orbit doublet of metallic Ag [188], while the peaks at 87.3 and 83.6 eV (splitting Δ=3.7 eV) correspond to the $4f_{5/2}$ and Au $4f_{7/2}$ spin-orbit components of metallic Au [189]. Moreover, the Bi 4f, V 2p and O1s peaks for the plasmonic modified PC films shifted to lower BE's by about 0.2-0.4 eV compared to the unmodified ones, implying different Fermi level shifts toward the VBM of Mo-$BiVO_4$, especially for the (Ag, Au)/Mo-$BiVO_4$ PCs.

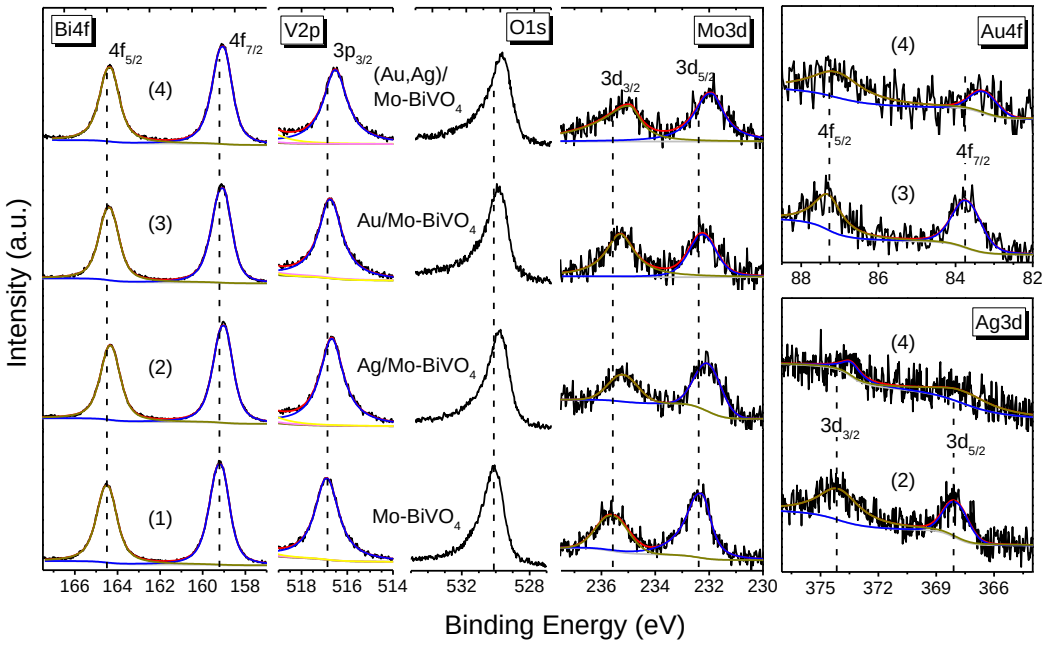

Figure 4.8 (a) Bi 4f, V 2p, O 1s, Mo 3d, Au 4f and Ag 3d core level XP spectra for (1) Mo-$BiVO_4$, (2) Ag/Mo-$BiVO_4$, (3) Au/Mo-$BiVO_4$, and (4) (Ag,Au)/Mo-$BiVO_4$ PC340 films.

Specular reflectance (R%) measurements at 15° angle of incidence showed the characteristic Bragg reflections due to the incomplete PBG formation along the [111] direction in the Mo-$BiVO_4$ inverse opal films (Figure 4.9a). The stop band positions shifted to higher wavelengths with the increase of the inverse opal void diameter allowing PBG engineering with respect to the Ag and Au NPs LSPR absorption peaks, which were determined from the extinction spectra of the corresponding NP dispersions at 406 and 520 nm, respectively (Figure 4.9c).

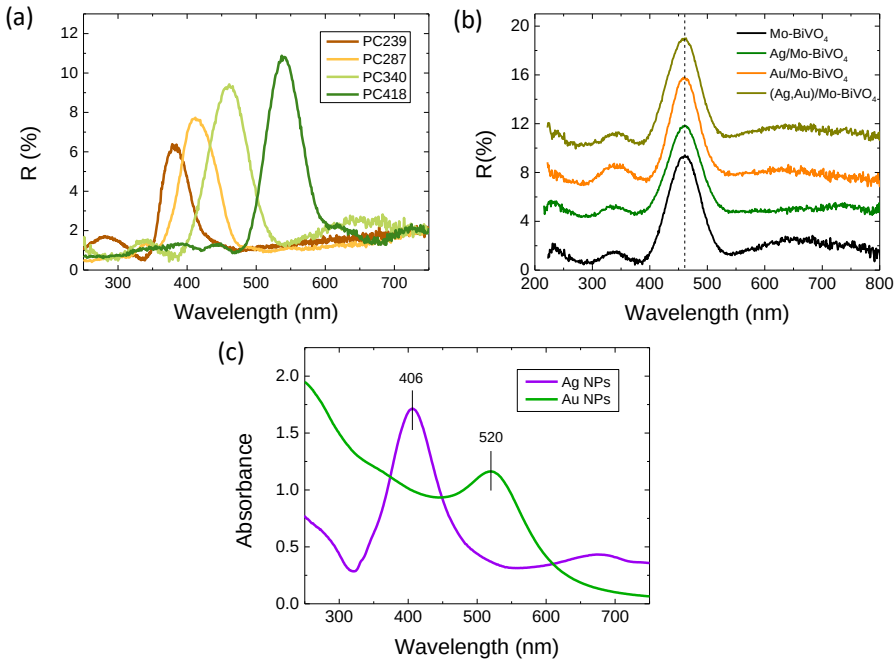

Figure 4.9 (a) Specular reflectance (R%) at θ=15° for (a) the Mo-$BiVO_4$ PC films and (b) the Ag and Au-modified Mo-$BiVO_4$ PC340 films. (c) LSPR absorbance of Ag and Au NP suspensions.

The R% Bragg intensities decreased with the decrease of PC macrospore size because of absorption losses that arise from the inherent electronic band gap absorption of Mo-$BiVO_4$ (*vide infra*). In addition, the stop band positions of the Ag and Au-modified Mo-BiVO4 PC340 films are independent of the presence of plasmonic NPs (Figure 4.9b). Applying modified Bragg's law for the obtained stop band wavelengths at 15°, which were not modified by the Ag and Au NP deposition (Figure 4.9c), together with the values of the PC macropore diameters D determined from SEM and the refractive indices of $BiVO_4$ ($n_{BiVO_4} = 2.4$) and air ($n_{\text{air}} = 1.0$), provided an estimate for the variation of the effective refractive index n_{eff} and the solid filling fraction $1 - f$ of the inverse opals. The obtained $1 - f$ values (Table 4.1) were smaller than the theoretical value of 0.26 for complete filling of the inverse *fcc* lattice indicative of the formation of nanocrystalline walls. Moreover, using the values for $1 - f$ and $n_{\text{H}_2\text{O}} = 1.33$, the stop band positions were estimated after PC infiltration with water, where the photocatalytic reaction takes place.

Table 4.1 Structural and optical parameters for the $BiVO_4$ PC films.

Film	D (nm)	λ_{exp} (15°) (air)	n_{eff} (air)	$1 - f$	λ (0°) (air)	n_{eff} (H_2O)	λ (0°) (H_2O)
PC239	165	382	1,44	0,226	388	1,63	440
PC287	185	413	1,39	0,197	420	1,60	483
PC340	210	462	1,37	0,185	470	1,58	543
PC418	260	534	1,28	0,136	545	1,52	646

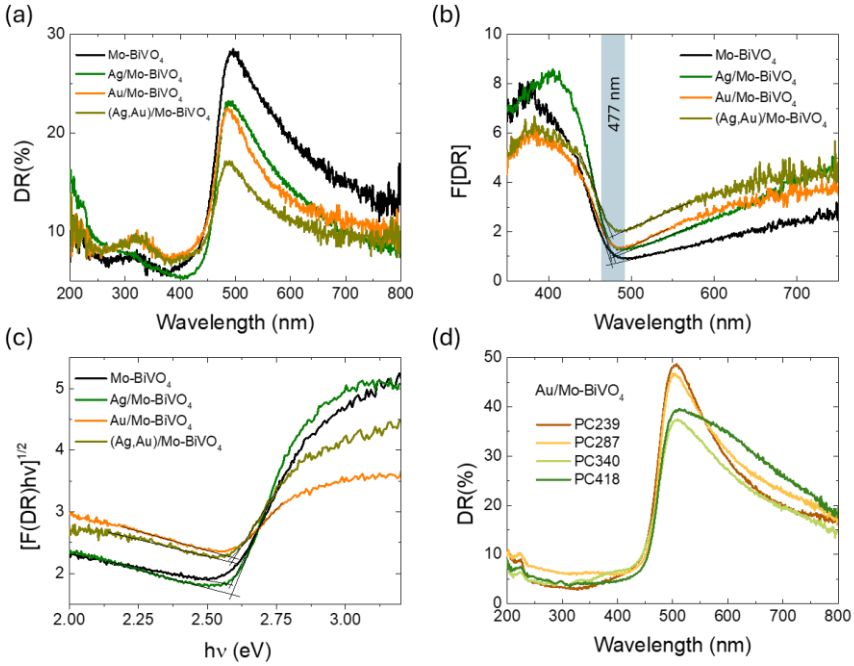

Figure 4.10 (a) Diffuse reflectance (DR%) and the corresponding (b) Kubelka-Munk transforms F(DR) and (c) indirect band gap Tauc plots for the Ag, Au-modified Mo-$BiVO_4$ PC340 films. (d) Diffuse reflectance (DR%) for the Au-modified Mo-$BiVO_4$ PC films.

Diffuse reflectance (DR%) spectra showed a nearly constant edge for the Ag, Au-modified PC340 films (Figure 4.10a), independent of the plasmonic NPs presence with no evident contribution of the Bragg reflection, which appears in the DR% spectra only for higher PC diameters where the spectral overlap of the stop band positions with the materials' electronic absorption is reduced (Figure 4.10d). An absorption edge of about 477 nm was accordingly derived from the Kubelka-Munk transforms F(DR) of the DR% spectra (Figure 4.10b), while the electronic bang gap E_g of 2.57 eV was estimated from the corresponding indirect band gap Tauc plots for the pristine and Ag, Au-modified Mo-$BiVO_4$ PC films (Figure 4.10c), in agreement with previous works on $BiVO_4$ inverse opals [116, 124]. Nevertheless, the DR% of the plasmonic NP-modified PCs decreased appreciably above the electronic absorption edge of Mo-$BiVO_4$, especially after surface modification by Au NPs (Figure 4.10a), indicating the appearance of visible light absorption extending beyond the narrow band LSPR bands of dispersed Ag and Au NPs (Figure 4.10b). This behavior indicates the excitation of higher-order plasmonic modes at longer wavelengths due to interparticle coupling effects in clusters consisting of closely spaced or touching metallic NPs on the $BiVO_4$ surface [190].

4.2 Photoelectrocatalytic evaluation

The Ag, Au-modified inverse opal films were comparatively evaluated on the photoelectrocatalytic degradation of TC (Figure 4.11a) and IBU (Figure 4.12a) pharmaceutical contaminants in 0.1 M $NaHCO_3$ supporting electrolyte at applied potential +1.0 vs Ag/AgCl under visible light illumination. Dark adsorption of TC molecules on the PC films reached approximately 12% after 30 min, while IBU adsorption was negligible.

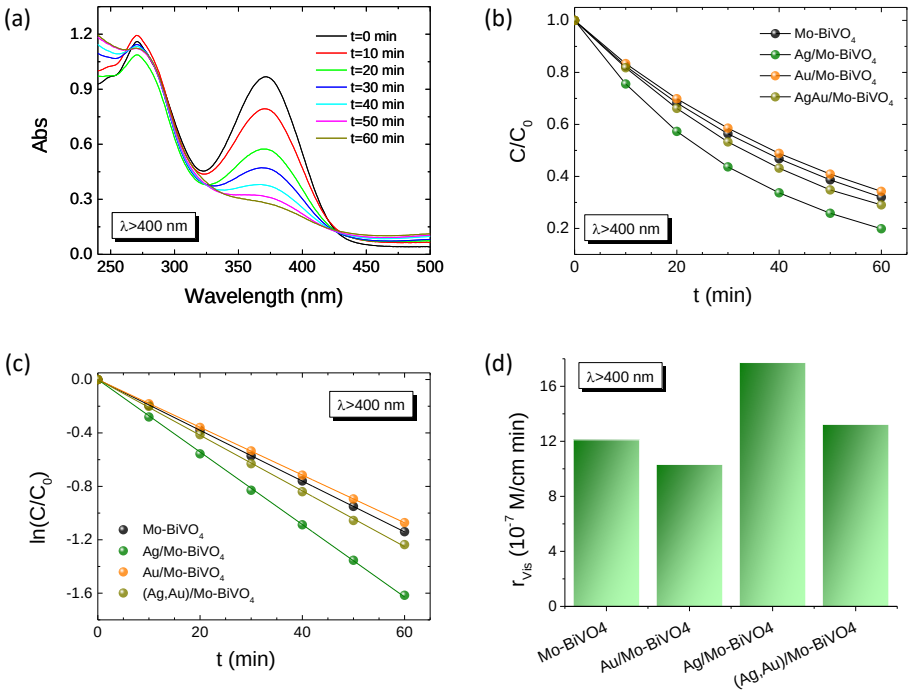

Figure 4.11 TC (a) absorbance spectra evolution, (b-c) photodegradation kinetics, and (d) reaction rates for the plasmonic modified Mo-BiVO4 PC340 photoelectrodes at +1.0 V vs Ag/AgCl under visible light irradiation.

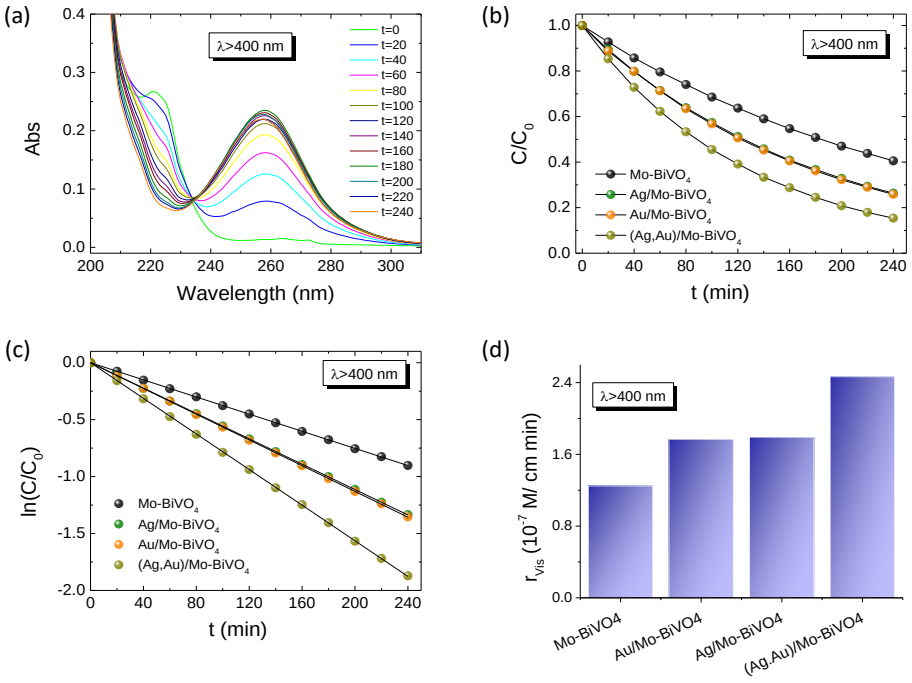

Figure 4.12 IBU (a) absorbance spectra evolution, (b-c) photodegradation kinetics, and (d) reaction rates for the plasmonic modified Mo-BiVO4 PC photoelectrodes at +1.0 V vs Ag/AgCl under visible light irradiation.

Blank tests without PC films, showed negligible TC or IBU degradation under visible light, whereas illumination in their presence led to the continuous temporal decrease of their concentration (C), monitored spectrophotometrically by the TC and IBU

absorption bands at 370 and 225 nm, respectively (Figure 4.11b and 4.12b). The $\ln(C/C_0)$ vs. t plot, where C_0 is the initial TC or IBU concentration after dark adsorption, varied linearly with time (Figure 4.11c and 4.12c), indicating first-order kinetics, with kinetic constants k (min^{-1}) derived from the corresponding linear slopes. The reaction rates r_{vis} were calculated as $r_{vis} = k\ C_0$, independent of concentration variations arising from dark adsorption. In the case of TC degradation, Ag/Mo-$BiVO_4$ showed the highest performance (Figure 4.11d), while Au NPs deposition resulted in slight deterioration of photoelectocatalytic activity toward TC degradation. The obtained kinetic constant k of 0.0271 min^{-1} exceeded that (0.01901 min^{-1}) of pristine Mo-$BiVO_4$ PC photoelectrodes by about 43%, and it is among the highest reported for TC photoelectrocatalytic degradation by $BiVO_4$-based photoanodes (Table 3.3) [132]. In the case of IBU degradation, plasmonic NPs deposition on Mo-$BiVO_4$ PCs resulted in enhanced photoelectocatalytic performance with the kinetic constants increasing from 1.2471 min^{-1} for Mo-$BiVO_4$ to 1.7686 and 1.7918 min^{-1} for Ag/Mo-$BiVO_4$ and Au/Mo-$BiVO_4$, while it reached an almost two-fold increase of 2.466 min^{-1} in the case of dual-deposited (Ag, Au)/Mo-$BiVO_4$ PC photoelectrodes (Figure 4.12d).

The reaction mechanisms for the best-performing plasmonic modified PC films on TC and IBU antibiotic degradation were investigated in comparison to the pristine Mo-$BiVO_4$ PC photoelectrodes by trapping experiments of superoxide radical anions ($^{\bullet}O_2^-$), holes (h^+) and hydroxyl radicals ($^{\bullet}OH$), by the addition of 1 mM 1,4 benzoquinone (Bq), 5 mM formic acid (FA) and 5 mM isopropanol (IPA) radical scavengers in the reaction solution, respectively. In the case of TC degradation by Mo-$BiVO_4$ PC films, the reaction rate r_{vis} was considerably reduced by the addition of Bq and FA (r_{vis} reduction by approximately 46% in both cases) (Figure 4.13a,b).

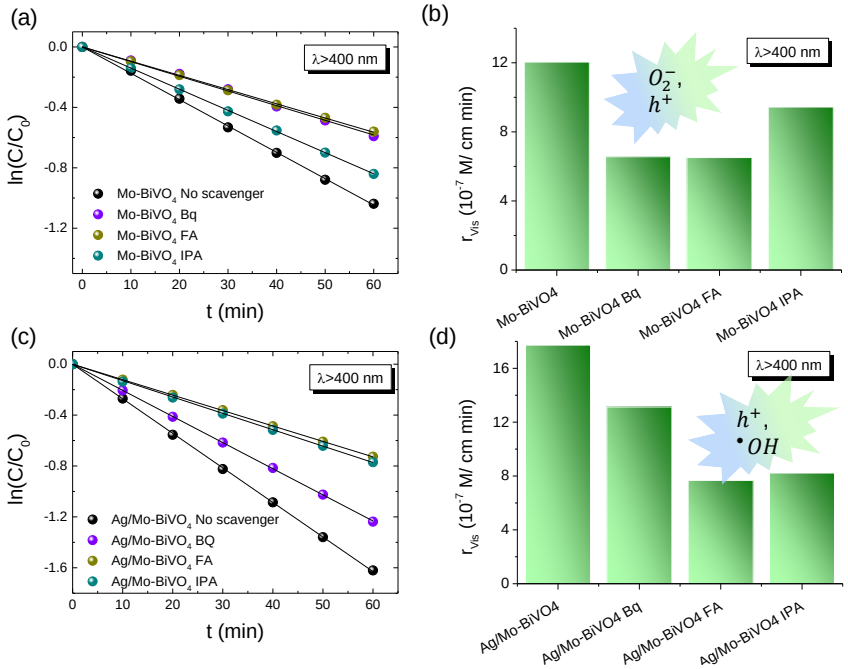

Figure 4.13 TC photoelectrocatalytic degradation kinetics and the corresponding reaction rates r_{vis} for (a), (b) Mo-$BiVO_4$ and (c), (d) Ag/Mo-$BiVO_4$ PC340 films in the presence of Bq, FA and IPA radical scavengers in 0.1 M $NaHCO_3$ supporting electrolyte at applied potential of +1.0 V vs Ag/AgCl under visible light.

On the other hand, weaker decrease of r_{vis} (by about 21%) was observed in the presence of IPA. These results indicated that h^+ and $^{\bullet}O_2^-$ radicals are the major species involved in the VLA TC degradation, whereas $^{\bullet}OH$ radicals play a minor role. In the case though of Ag/Mo-$BiVO_4$ PCs that presented the highest r_{vis} for TC degradation (Figure 4.11d), the addition of both FA and IPA resulted in significant inhibition of the photoelectrocatalytic reaction (r_{vis} decreased by 57% and 54% for FA and IPA, respectively), whereas the influence of Bq was significantly moderated (r_{vis} decreased by about 25%) (Figure 4.13c,d). This suggests a change of the reactive species nature underlying TC degradation upon Ag NPs deposition, which caused an increased contribution of $^{\bullet}OH$ against $^{\bullet}O_2^-$ radicals to the photocatalytic reaction, besides direct TC oxidation by photogenerated h^+.

In the case of IBU degradation, FA's addition caused a drastic r_{vis} reduction by 57% for the unmodified Mo-$BiVO_4$ PC films (Figure 4.14), whereas Bq and IPA scavengers had much weaker effects in the photocatalytic performance (r_{vis} decreased by about 15%), indicating that h^+ are the major reactive species [191, 192]. Similar behavior was observed for the dual-modified (Ag,Au)/Mo-$BiVO_4$ PCs that showed the highest performance on IBU degradation. In that case, where FA produced the most significant inhibitory effect (r_{vis} decrease by 63%), indicating that photogenerated h^+ remain the dominant reactive species.

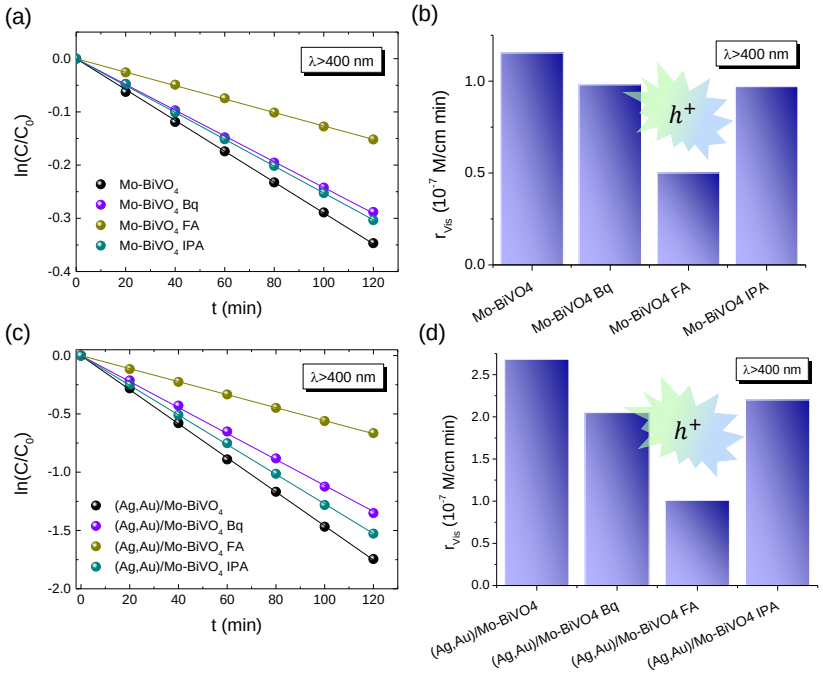

Figure 4.14 IBU photoelectrocatalytic degradation kinetics and the corresponding reaction rates r_{vis} for (a), (b) Mo-$BiVO_4$ and (c), (d) (Ag,Au)/Mo-$BiVO_4$ PC340 films in the presence of Bq, FA and IPA radical scavengers in 0.1 M $NaHCO_3$ supporting electrolyte at applied potential of +1.0 V vs Ag/AgCl under visible light.

The combination of LSPR with photonic amplification was investigated by comparative photoelectrocatalytic tests on TC degradation for the Ag- and Au-modified Mo-$BiVO_4$ PC films in 0.1 M $NaHCO_3$ at +1.0 V vs Ag/AgCl under

visible light (Figure 4.15, 4.16). The TC degradation rates showed a distinct size-dependence with respect to the PC periodicity with Ag/Mo-$BiVO_4$ PC340 presenting the highest r_{vis} value, followed by the PC239 films, whereas the PC418 and PC287 films showed much weaker activity (Figure 4.15c). This variation can be related to the optimal spectral overlap of the Ag NP LSPR and the Mo-$BiVO_4$ electronic absorption edge with the slow photons of the supporting PC340 scaffold, whose stop band is expected at ≈540 nm in water (Table 4.1).

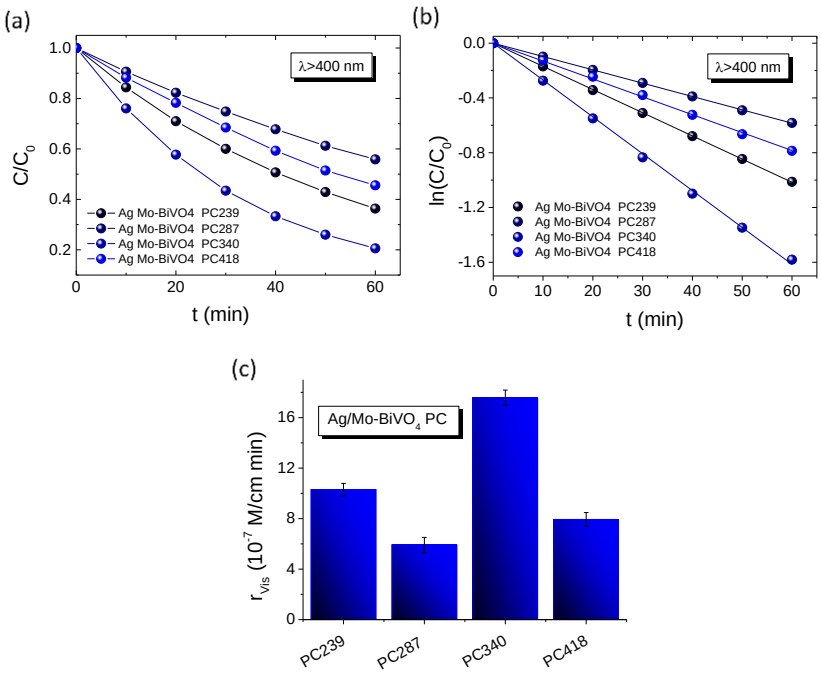

Figure 4.15 TC photodegradation kinetics and reaction rates for the Ag-modified Mo-$BiVO_4$ PC films in 0.1 M $NaHCO_3$ supporting electrolyte at +1.0 V vs Ag/AgCl under visible light irradiation as a function of the PC macropore diameter.

Assuming that the stop band spectral width is about 60 nm, i.e. the full width at half-maximum of the corresponding Bragg reflection (Figure 4.9a), the narrower blue-edge slow photon region will be roughly expected below 510 nm, approaching both the Mo-$BiVO_4$ absorption edge (≈480 nm) and the extended LSPR absorption of the Ag NP aggregates, observed in the DR% spectra (Figure 4.10a). On the other hand, the detrimental matching of the PC287 Bragg reflection in water at ≈ 480 nm (Table 4.1) with the Mo-$BiVO_4$ band gap complies with the lowest r_{vis} value, while PC418's stop band is expected at relatively high wavelengths (≈ 646 nm) to trigger slow photon effects. Significant overlap of red-edge slow photons with Ag LSPR and the semiconductor absorption edge is also expected for the ≈ 440 nm stop band (in water) of Ag/Mo-$BiVO_4$ PC239 (Table 4.1), whose performance may be compromised by absorption losses in the Mo-$BiVO_4$ band gap in comparison to the best performing PC340 films.

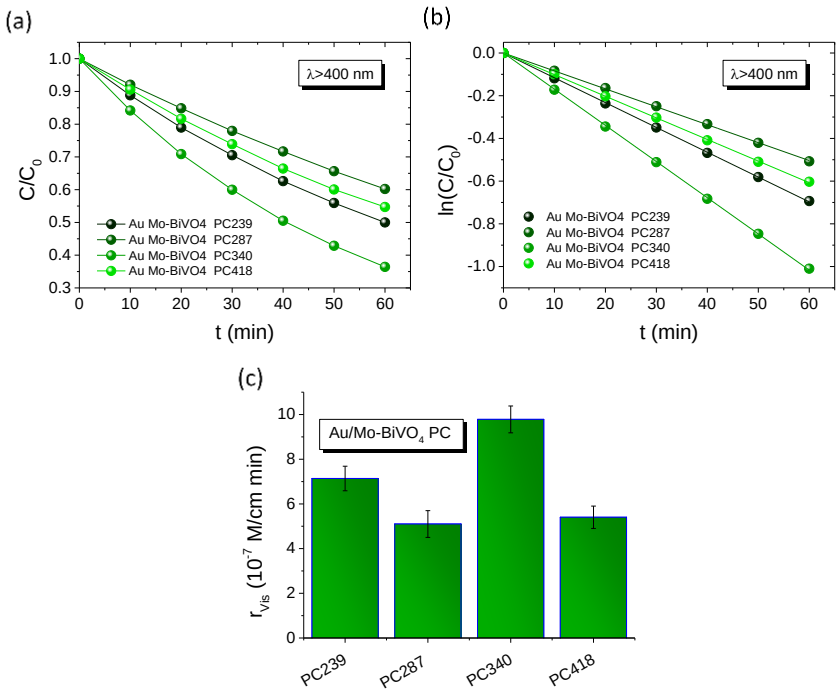

Figure 4.16 TC photodegradation kinetics and reaction rates for the Au-modified Mo-$BiVO_4$ PC films in 0.1 M $NaHCO_3$ supporting electrolyte at +1.0 V vs Ag/AgCl under visible light irradiation as a function of the PC macropore diameter.

Similar size-selective activity was observed for the Au-modified Mo-$BiVO_4$ PCs (Figure 4.16) but with less pronounced variations of the r_{vis} values compared to the Ag-modified PCs, which can be associated with the extended electronic absorbance of the Au NPs that moderate photonic effects.

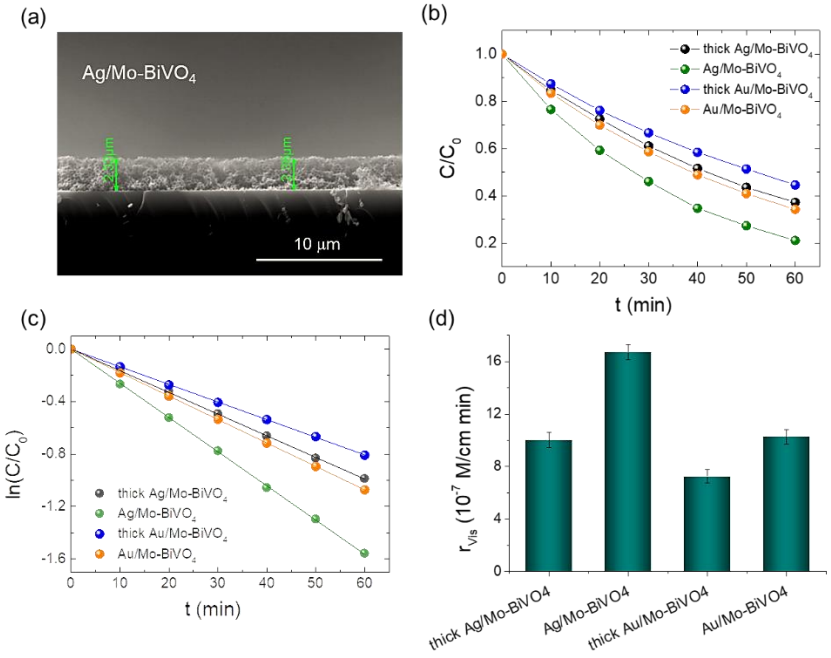

Figure 4.17 (a) Cross section SEM image of the thick Ag/Mo-$BiVO_4$ film. (b)-(d) Comparative TC photodegradation kinetics and reaction rates for the thick and thin (pristine) Ag- and Au-modified Mo-$BiVO_4$ PC films in 0.1 M $NaHCO_3$ supporting electrolyte at +1.0 V vs Ag/AgCl under visible light irradiation.

Furthermore, considering the modest uniformity of metal oxide inverse opals fabricated by wet chemical methods [167], compared to more robust plasmonic-photonic structures [193, 194], the activity of Ag- and Au-modified Mo-BiVO$_4$ PC340 on TC degradation was investigated for films of the same composition but higher thickness of ≈ 2.3 μm (Figure 4.17). The obtained results reproduced closely the relative variation of r_{vis} for the thin Ag- and Au-modified Mo-BiVO$_4$ PCs but with overall weaker photoelectrocatalytic performance, indicative of higher recombination losses for the thicker films [195].

4.3 PEC performance

The PEC response of the plasmonic modified Mo-BiVO$_4$ PC340 photoelectrodes was comparatively evaluated using linear sweep voltammetry at a potential scan rate of 10 mV s^{-1} both in the dark and under back-side visible (Figure 4.18a) and UV-Vis (Figure 4.18b) illumination in a 0.5 M $NaHCO_3$ aqueous electrolyte. Illumination from the back-side led to much higher photocurrent density compared to front-side one for Mo-BiVO4 PC340 (Figure 4.18c), indicative of the slow transport of photogenerated electrons at the semiconductor/electrolyte interface across the film thickness to reach the FTO substrate back contact [195, 196]. Significant photocurrent enhancement was also observed for the Mo-BiVO$_4$ PCs compared to approximately 500 nm thick-planar Mo-BiVO$_4$ films deposited by dip-coating of FTO substrates without the colloidal template (Figure 4.18d), which confirms the advantage of the inverse opal photonic structure.

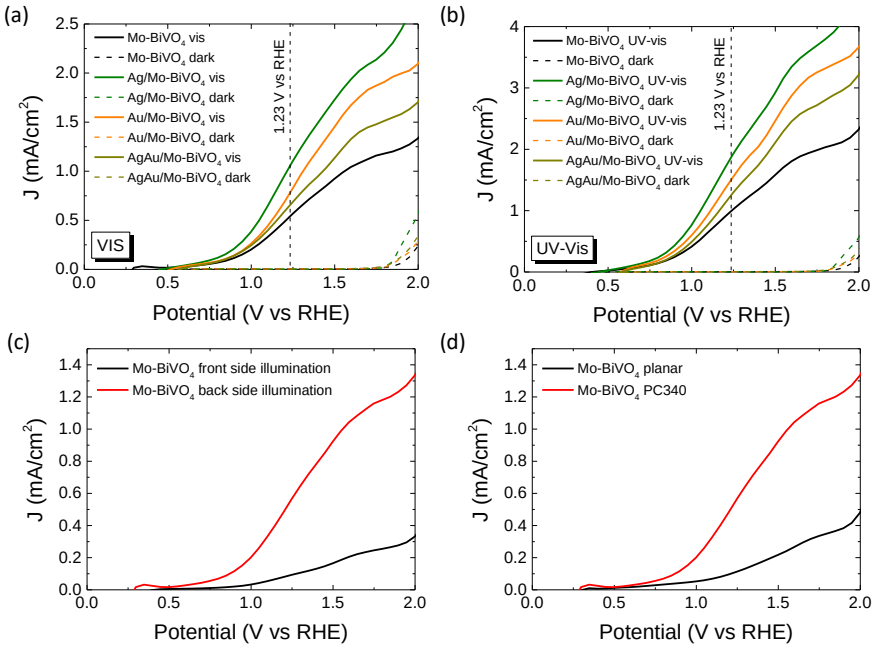

Figure 4.18. Current density-potential curves under (a) visible and (b) UV-Vis back-side illumination (solid lines) for the Ag and Au modified Mo-BiVO4 PC340 photoelectrodes. Dashed lines display the corresponding dark response. (c) Current density-potential curves for Mo-BiVO$_4$ PC340 films under front- and back-side visible light illumination. (d) Current density-potential curves for planar and Mo-BiVO$_4$ PC340 film under back-side visible light illumination. All PEC measurements were performed in 0.5 M $NaHCO_3$ aqueous electrolyte.

Decoration of plasmonic Ag and Au NPs on the inverse opal skeleton resulted in marked improvements of the photocurrent densities by about 44% (53%) and 94% (90%) at 1.23V vs RHE potential under visible (UV-Vis) back-side illumination for the Au/Mo-$BiVO_4$ and Ag/Mo-$BiVO_4$ PCs, respectively, while a relatively weaker increase of approximately 20% (28%) was observed for the co-deposited (Ag,Au)/Mo-$BiVO_4$ PCs, verifying the presence of plasmonic amplification effects.

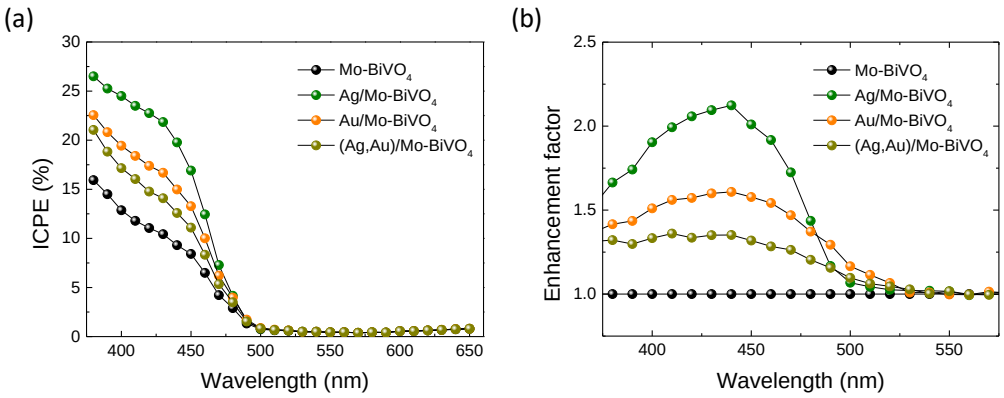

Figure 4.19 (a) IPCE spectra at 1.23 V vs RHE for the Ag and Au modified Mo-$BiVO_4$ PC photoelectrodes and (b) the corresponding enhancement factors with respect to the unmodified Mo-$BiVO_4$ PC). All PEC measurements were performed in 0.5 M $NaHCO_3$ aqueous electrolyte.

The enhanced PEC activity of Ag and Au modified Mo-$BiVO_4$ PC photoelectrodes was spectrally analyzed through IPCE measurements in 0.5 M $NaHCO_3$ aqueous electrolyte under back-side illumination at 1.23 V vs RHE (Figure 4.19a). Consistently with the LSV results, grafting of plasmonic NPs on Mo-$BiVO_4$ PCs resulted in significant enhancement of the ICPE spectra. The highest value was obtained for Ag/Mo-$BiVO_4$ followed by Au/Mo-$BiVO_4$ PCs, while the co-modified (Ag,Au)/Mo-$BiVO_4$ showed relatively weaker increase compared to the bare Mo-$BiVO_4$ photoelectrode. Moreover, the rise of IPCE was mainly observed below the absorption edge of Mo-$BiVO_4$ (<490 nm), as evidenced in the corresponding enhancement factors calculated with respect to the unmodified Mo-$BiVO_4$ PC (Figure 4.19b). In particular, a rapid decrease of ICPE was observed above 490 nm for Ag/Mo-$BiVO_4$, whereas the relatively lower ICPE values for Au/Mo-$BiVO_4$ and (Ag,Au)/Mo-$BiVO_4$ PCs extended spectrally up to longer wavelengths of about 530 nm. Considering the weak light scattering efficiency of 10 nm Ag [103] and 5 nm Au [100] NPs, the enhanced PEC response within the absorption range of Mo-$BiVO_4$ points to a major amplification effect by the local electromagnetic field enhancement from the metallic NPs promoting electron-hole generation at the interface with the $BiVO_4$ inverse opal skeleton. The near-field enhanced photocarrier production is more pronounced for Ag than Au NPs (Figure 4.19a), as the Ag LSPR absorption overlaps entirely with the $BiVO_4$ electronic absorption range, while it can be further intensified by the hot spots between the metallic NP aggregates. On the other hand, the weak ICPE enhancement above the absorption edge of $BiVO_4$ up to 530 nm for the Au/Mo-$BiVO_4$ and (Ag,Au)/Mo-$BiVO_4$ PCs, implies a much weaker plasmonic "sensitization" effect by hot-electron injection from Au NPs to the conduction band of Mo-$BiVO_4$.

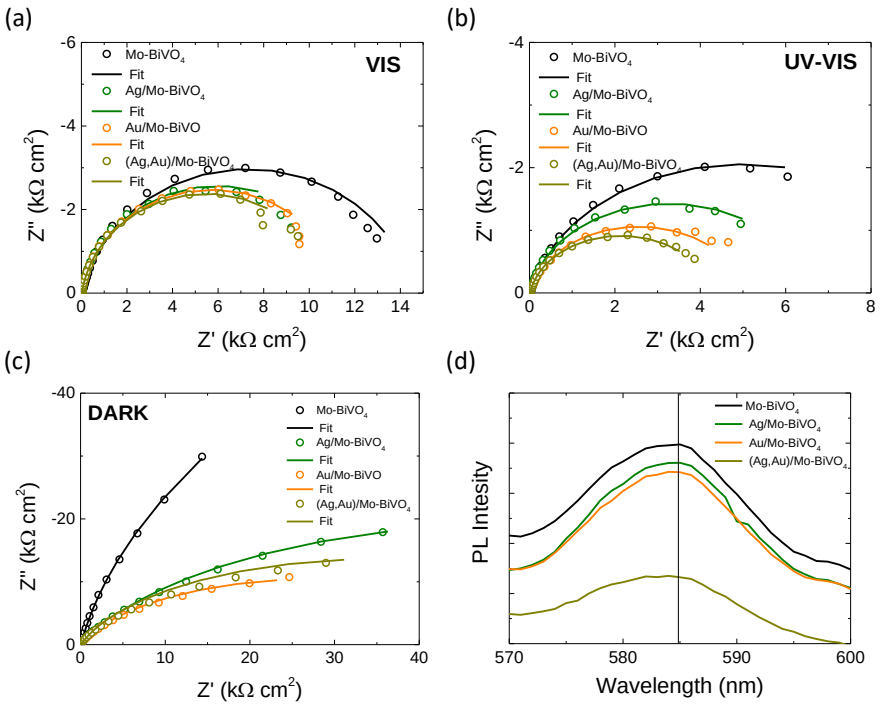

Figure 4.20 EIS Nyquist plots for the metal-doped Mo-$BiVO_4$ PC340 under (a) visible and (b) UV-Vis light as well as (c) dark conditions. Solid lines depict the best fit curves to the modified Randles equivalent circuit. All PEC measurements were performed in 0.5 M $NaHCO_3$ aqueous electrolyte. (d) PL spectra of the metal-doped Mo-$BiVO_4$ PC340.

In order to investigate charge separation at the photoelectrode/electrolyte interface for the Ag and Au modified Mo-$BiVO_4$ PCs, EIS measurements were performed under visible (Figure 4.20a) and UV-vis (Figure 4.20b) light as well in the dark (Figure 4.20c). The obtained Nyquist plots were fitted to a Randles equivalent circuit consisting of series resistance R_S, the charge-transfer resistance R_{CT} and a constant phase element CPE (Table 4.2). Light irradiation caused the decrease of the capacitive arc radius in the EIS plane, i.e. the charge transfer resistance, resulting in enhanced separation of photo-induced charge carriers. Moreover, infiltration of the Mo-$BiVO_4$ PC films with plasmonic NPs resulted in significant reduction of R_{CT}, with (Ag,Au)/Mo-$BiVO_4$ presenting the smallest value and consequently the lowest electron-hole recombination, especially under UV-Vis light.

Table 4.2 Parameters obtained by fitting the experimental impedance spectra to a modified Randles circuit.

	Dark		Visible light (>400 nm) UV-vis			
PC film	R_S (Ω cm^2)	R_{CT} (Ω cm^2)	R_S (Ω cm^2)	R_{CT} (Ω cm^2)	R_S (Ω cm^2)	R_{CT} (Ω cm^2)
Mo-$BiVO_4$	11.9	2.23x10^5	13.1	7292	12.1	4974
Ag/Mo-$BiVO_4$	11.0	0.54x10^5	10.7	5968	11.4	3254
Au/Mo-$BiVO_4$	9.3	0.28x10^5	9.3	5733	8.9	2536
(Ag,Au)/Mo-$BiVO_4$	10.4	0.35x10^5	10.4	5455	10.3	2122

This was supported by PL measurements (Figure 4.20d). A broad emission peak around 585 nm (approximately 2.12 eV) was observed, which is well above Mo-$BiVO_4$ PC's absorption edge, confirming the presence of indirect band gap. The PL intensity was reduced when metallic NPs were deposited on Mo-$BiVO_4$, indicating a decrease in electron-hole recombination with (Ag,Au)/Mo-$BiVO_4$ PCs presenting the weakest PL signal in agreement with the EIS analysis.

Depending on the difference between the metal work function ϕ_M and the semiconductor ϕ_S, the formation ($\phi_M - \phi_S > 0$) or not ($\phi_M - \phi_S < 0$) of a Schottky barrier $\phi_B = \phi_M - \chi_S$, where χ_S is the semiconductor electron affinity, is essential to the electron transfer path at the metal-semiconductor interface [197]. Using the ϕ_M values of 4.26 and 5.1 eV (absolute vacuum scale) for the Ag and Au NPs [198], the E_g value of 2.57 eV (Figure 4.10c) and χ_S of 4.68 eV determined for Mo-$BiVO_4$ PCs by UPS (Figure 3.27), the energy band diagrams can be derived for Ag/Mo-$BiVO_4$ (Figure 4.21a), Au/Mo-$BiVO_4$ (Figure 4.21b) and (Ag,Au)/Mo-$BiVO_4$ (Figure 4.21c) heterojunctions.

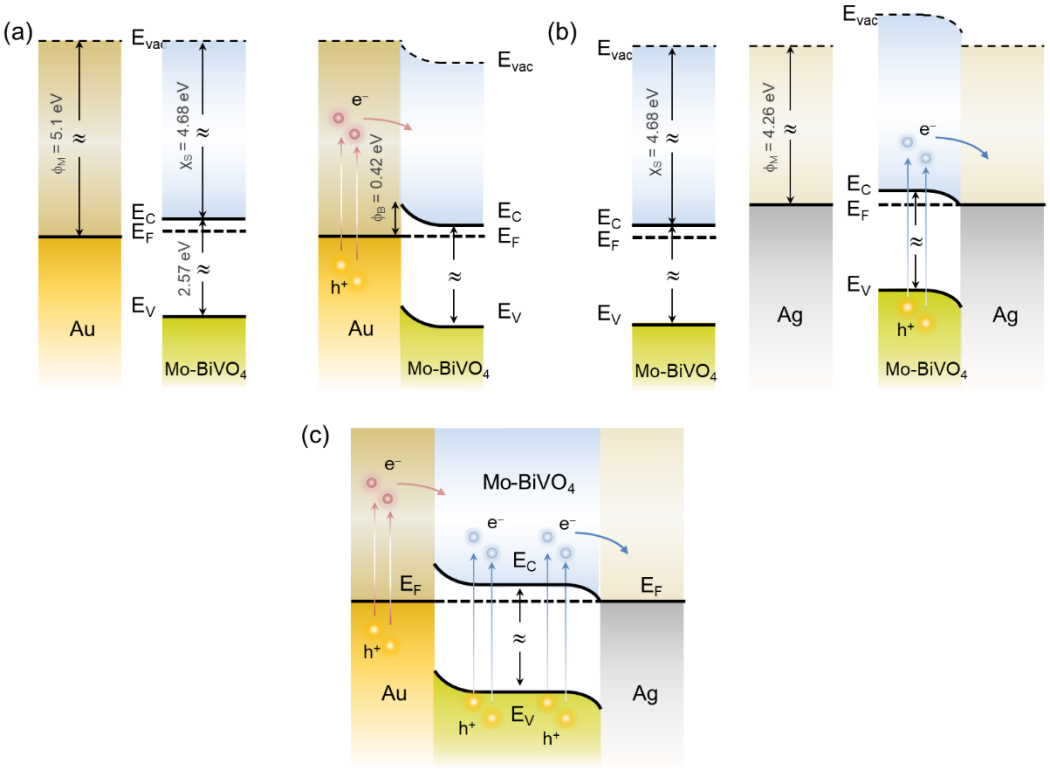

Figure 4.21 Schematic of the dominant charge transfer routes for (a) Au/Mo-$BiVO_4$, (b) Ag/Mo-$BiVO_4$ and (c) (Ag,Au)/Mo-$BiVO_4$ PCs.

In the case of Ag NPs, the metal work function is lower than that of Mo-$BiVO_4$ (ϕ_S=5.01 eV) precluding Schottky barrier formation (ϕ_B = - 0.42 eV<0) and favoring electron flow from the semiconductor to the Ag NPs under visible light excitation. The scavenging of photogenerated electrons by the metallic NPs may accordingly rationalize the suppression of $^{\bullet}O_2^-$ radicals from the observed reactive species in TC degradation for Ag/Mo-$BiVO_4$ (Figure 4.13). On the other hand, the work function ϕ_M for Au NPs is higher than ϕ_S of Mo-$BiVO_4$ leading to a Schottky barrier height ϕ_B = 0.42 eV, which is considerably lower than the corresponding $\phi_B \approx 1.1$ eV for Au-TiO_2

[109]. Hot electron flow from Au NPs to the semiconductor will be accordingly favored, which, however, according to the IPCE results produces a relatively weak PEC response at longer wavelengths compared to the Mo-$BiVO_4$ absorption edge (Figure 4.19a). In the case of dual-decorated Mo-$BiVO_4$ nanocrystals by both Ag and Au NPs, the injection of a relatively small fraction energetic hot electrons from Au NPs to the CB of Mo-$BiVO_4$ will be followed by intensified electron flow to the Ag NPs, leading to cascade charge transfer in the corresponding heterojunctions for (Ag,Au)/Mo-$BiVO_4$ PCs under visible light and UV-Vis excitation (Figure 4.21c). This can greatly reduce electron-hole recombination and promotes IBU degradation beyond the light concentration effects of the plasmonic NPs.

In order to explore plasmonic size effects, comparative photoelectrocatalytic experiments were carried out for Au-modified Mo-$BiVO_4$ PC340 films using 10, 50 and 80 nm Au NP citrate stabilized dispersions (Sigma Aldrich) on TC degradation at +1.0 V vs Ag/AgCl under visible light (Figure 4.22). Figure 4.23 show representative TEM images and the corresponding V and Au EDX elemental maps for Mo-$BiVO_4$ PC340 films surface modified by Au NPs of 50 and 80 nm diameters. The obtained results show that Mo-$BiVO_4$ PC films decorated by 10 nm Au NPs (Figure 4.24) present similar, slightly higher, r_{vis} rates to that of 5 nm Au NPs. Conversely, the TC degradation rates decreased for the surface modified $BiVO_4$ PCs with larger Au NPs, especially for the 50 nm diameter.

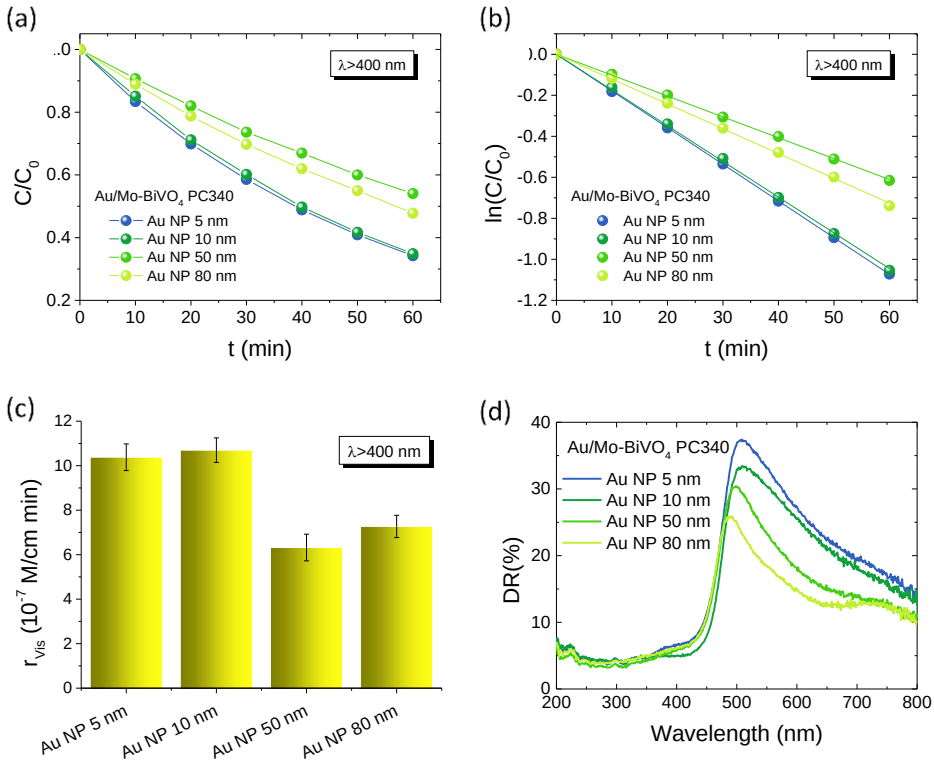

Figure 4.22 Size dependent TC (a)-(b) photodegradation kinetics and (c) degradation rates for the Au/Mo-$BiVO_4$ PC340 photoelectrodes with Au NPs of different diameters (5, 10, 50 and 80 nm) in 0.1 M $NaHCO_3$ supporting electrolyte at +1.0 V vs Ag/AgCl under visible light. (d) DR (%) spectra for the Au/Mo-$BiVO_4$ PC340 photoelectrodes with Au NPs of different diameters.

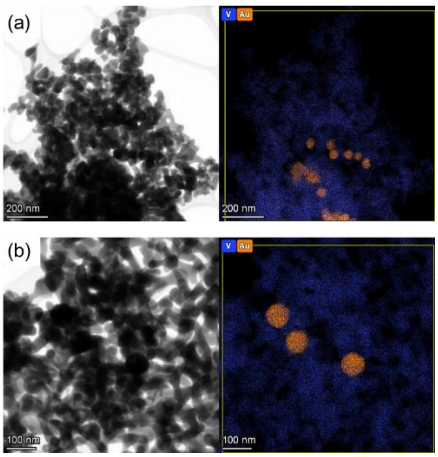

Figure 4.23 TEM images and the corresponding V and Au EDX elemental maps for Mo-$BiVO_4$ PC340 films surface modified by Au NPs of (a) 50 and (b) 80 nm diameters.

This variation can be related to the dominant local field enhancement for the smaller Au NPs characterized by large absorption cross sections [97, 100], along with the concomitant high surface coverage of the $BiVO_4$ PC walls that favors NP aggregation and hot spot formation, leading to enhanced electron-hole generation and electron transfer at the abundant metal-semiconductor interfaces. On the other hand, the enhanced scattering cross section of larger diameter Au NPs leads to appreciably higher extinction [97, 100], which underlies the decrease of DR% above the absorption edge of Mo-$BiVO_4$ with increasing NP size (Figure 4.22d), most pronounced for the 80 nm Au/Mo-$BiVO_4$. The preferential light scattering toward $BiVO_4$ by the large Au NPs is, though, not sufficient to promote the photocatalytic activity for the successively lower surface coverage of the PC skeleton by 50 nm (Figure 4.25) and 80 nm (Figure 4.26) Au NPs that also reduces the number of plasmonic metal-semiconductor heterojunctions.

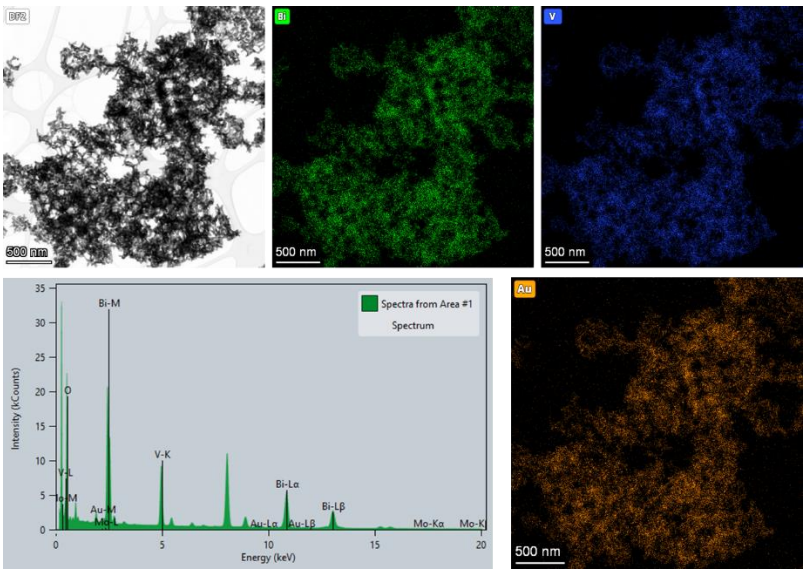

Figure 4.24 TEM image of 10 nm Au/Mo-$BiVO_4$ PC340 films and the corresponding Bi, V and Au elemental maps obtained from the corresponding local EDX spectra.

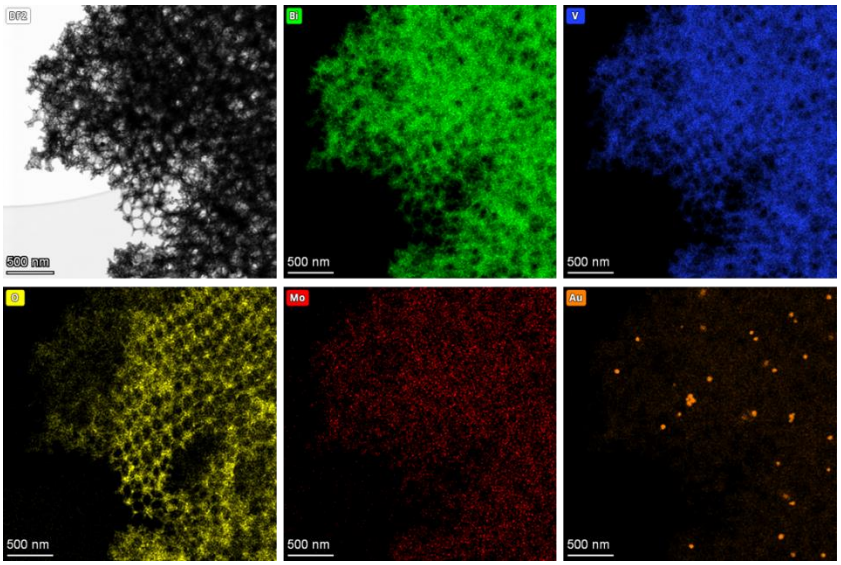

Figure 4.25 TEM image of 50 nm Au/Mo-$BiVO_4$ PC340 films and the corresponding Bi, V, O, Mo, and Au elemental maps.

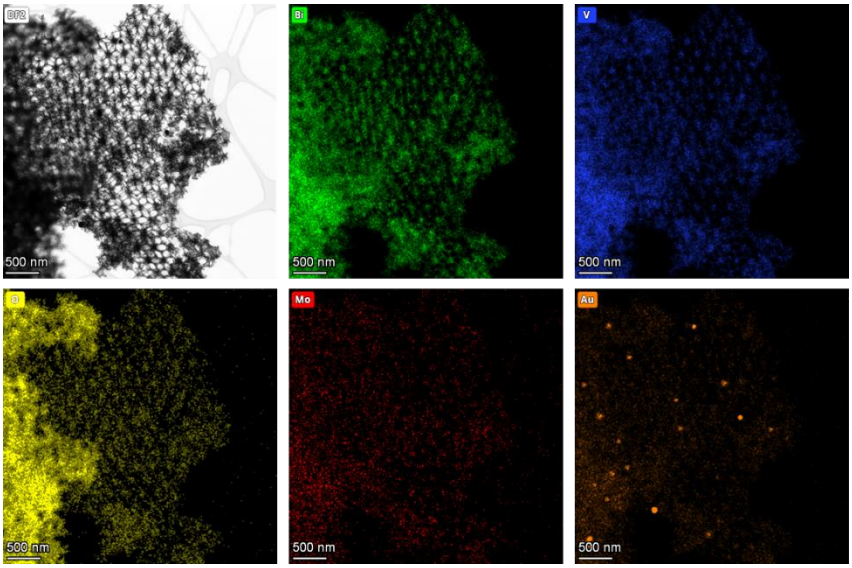

Figure 4.26 TEM image of 80 nm Au/Mo-$BiVO_4$ PC340 films and the corresponding Bi, V, O, Mo, and Au elemental maps.

4.3 Conclusions

In conclusion, surface decoration of Mo-$BiVO_4$ inverse opal photoelectrodes by single and dual plasmonic Ag and/or Au NPs is shown as a competent approach for the photoelectrocatalytic degradation of TC and IBU pharmaceutical contaminants. A major contribution from local field enhancement was concluded from the PEC response of the metal-decorated Mo-$BiVO_4$ PCs. This was most prominent for Ag/Mo-$BiVO_4$ due to the optimal spectral overlap of LSPR absorption of Ag NPs with the

semiconductor band gap. It was further assisted by slow photon propagation in the inverse opal structure and the formation of hot spots by the NP aggregates, whereas a weak sensitization effect by hot electrons was derived for the Au-modified PCs. More importantly, the variable band alignment at the metal-semiconductor interfaces resulted in different electron transfer pathways from Mo-$BiVO_4$ to Ag NPs and from Au NPs to Mo-$BiVO_4$, which in the case of co-decorated (Ag,Au)/Mo-$BiVO_4$ PCs may lead to cascade charge transfer in the corresponding heterojunctions. The former was found to intensify TC degradation for Ag/Mo-$BiVO_4$, while the latter underlined the enhanced IBU degradation via photogenerated holes for the (Ag,Au)/Mo-$BiVO_4$ PCs. Judicious combination of VLA semiconductor inverse opals and metallic NPs with favorable band alignment and PBG engineering is accordingly proposed as a versatile route for the rational design of competent plasmonic-photonic photoeletrocatalysts.

CHAPTER 5

Bilayer TiO_2/Mo-$BiVO_4$ photocatalysts

Heterostructuring $BiVO_4$ with benchmark semiconductor photocatalysts such as WO_3 and TiO_2 has been attracting significant attention as an efficient approach to enhance photocatalytic performance by improving visible light absorption and charge separation via interfacial charge transfer [24]. In the case of PC photocatalysts, post deposition of $BiVO_4$ NPs has been mostly applied as a means for the visible light sensitization of TiO_2 inverse opals for the photocatalytic degradation of dye pollutants [120, 121] or promote water splitting over WO_3 inverse opal photoanodes [199] as well as nanocrystalline layer on top of WO_3 [200] and TiO_2 [122] coated inverse opal photoelectrodes leading to outstanding photocurrent densities. Recently, $BiVO_4$ NP's deposition on single [169] and bilayer [201] TiO_2 inverse opals films resulted in markedly enhanced photocatalytic degradation rates of rhodamine B dye pollutants upon slow photon tuning, while significant enhancement of water oxidation was reported for a thin Mo-$BiVO_4$ photoanode when coated with a TiO_2 inverse opal layer with stop band to the red edge of/or coinciding with $BiVO_4$ electronic absorbance under back-side illumination [202].

In this work, an advanced TiO_2/Mo-$BiVO_4$ bilayer photoelectode was fabricated by the deposition of a mesoporous TiO_2 overlayer using the benchmark Aeroxide® P25 titania catalyst on top of the Mo-$BiVO_4$ PC340 films as supporting layer that intrinsically absorbs visible light below 490 nm, while offering improved charge transport. A porous heterostructured P25/Mo-$BiVO_4$ bilayer structure was produced from the collapse of the inverse opal underlayer after post thermal annealing, which was evaluated on the photoelectrocatalytic degradation of IBU non-steroidal anti-inflammatory drug under back-side illumination by visible and UV-Vis light. Significantly enhanced photocatalytic performance was achieved for the bilayer structure with respect to the additive effect of the constituent layers, which was related to the improved light harvesting due to backscattering from the P25 TiO_2 layer in combination with the favorable charge transfer at the TiO_2/Mo-$BiVO_4$ interface.

5.1 Morphological, structural, and photoelectrochemical properties

A Mo-doped $BiVO_4$ PC340 layer was initially deposited on FTO glass substrates using the liquid phase infiltration of a colloidal opal template of 340 nm diameter PS spheres with the appropriate metal salt precursor and optimized composition followed by calcination at 400 °C (Section 2.1.4), which provides the highest photoelectrocatalytic performance. The horizontal colloidal crystallization method was applied in order to rapidly deposit the PS opal template without consuming large amounts of colloidal suspension that is commonly used in conventional self-assembly. Subsequently, a mesoporous TiO_2 layer was deposited on top of the Mo-doped $BiVO_4$ film by spin-coating a paste of the benchmark Aeroxide® P25 mixed phase catalyst, followed by drying at 120 °C and post-annealing at 450 °C to remove the organic ingredients. Thermal treatment resulted in the formation of a porous bilayer structure comprising

a nanocrystalline Mo-$BiVO_4$ bottom layer produced from the collapse of the inverse opal structure after the second thermal annealing and a mesoporous titania overlayer consisting of interconnected P25 aggregates. Each layer was of about 500 nm thickness (Figure 5.1 a-c).

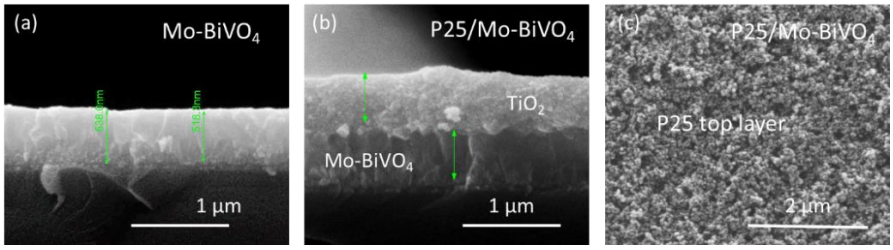

Figure 5.1 Cross section of the (a) bottom Mo-$BiVO_4$ layer and (b) cross and (c) top-view of the bilayer structure.

The phase composition of the individual layers and the bilayer structure was identified by micro-Raman spectroscopy at 785 nm (Figure 5.2). The individual P25 layers showed the characteristic Raman-active phonons of anatase TiO_2 at approximately 144 (E_g), 196 (E_g), 397 (B_{1g}), 519 (A_{1g}+B_{1g}), and 638 cm^{-1} (E_g), superimposed on the parasitic glass substrate fluorescence under the near-infrared laser excitation [203, 204]. The Mo-$BiVO_4$ films showed a series of Raman bands at 124, 210, 331, 366, 707, and 825 cm^{-1} that arise from the slightly shifted vibrational modes of *ms* $BiVO_4$ due to Mo doping, while the additional peak at 880 cm^{-1} corresponds to the MoO_4 stretching mode (Section 3.2). Specifically, the peaks at 825 and 707 cm^{-1} correspond to the V-O stretching modes and the peaks at 366 and 331 cm^{-1} correspond to the VO_4 bending vibrations, while 210 and 124 cm^{-1} are the external modes [161].

Figure 5.3 shows the DR% and T% spectra of the P25/Mo-$BiVO_4$ bilayer films compared to the individual layers. Both DR% and T% measurements showed the superposition of the absorption edges of the two constituent Mo-$BiVO_4$ and TiO_2 metal oxides, which were clearly resolved in the corresponding absorbance spectra obtained from the Kubelka-Munk transforms of the DR% spectra.

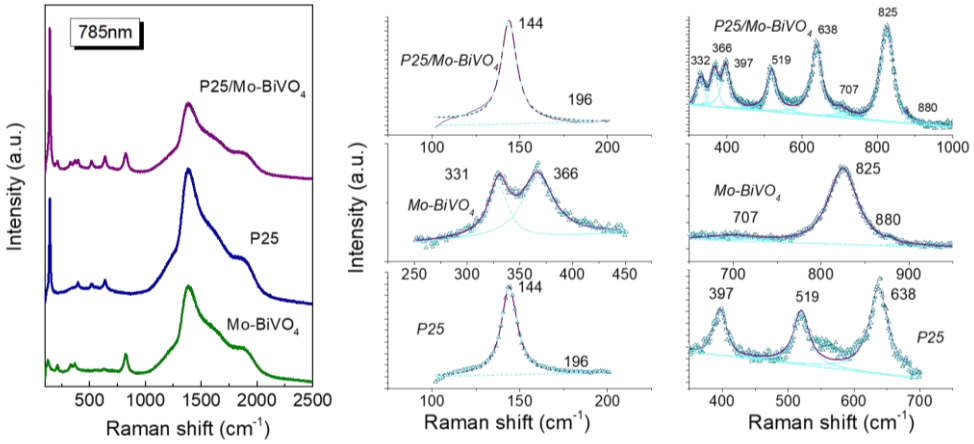

Figure 5.2 (left) Raman spectra of the P25/Mo-$BiVO_4$ bilayer and the constituent layers, and (middle and right panel) the corresponding spectral deconvolution at 785 nm.

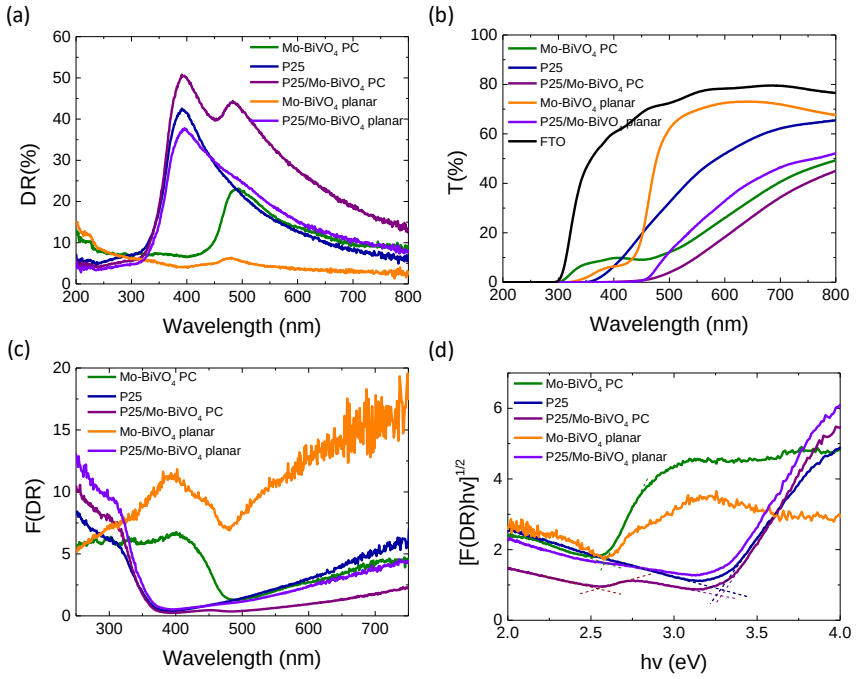

Figure 5.3 (a) Diffuse reflectance (DR%), (b) transmittance (T%) and the corresponding (c) Kubelka–Munk absorbance and (d) Tauc plots of the individual layers and the P25/Mo-$BiVO_4$ bilayers.

The derived Tauc plots for indirect band gap indicated E_g values of 3.28 and 2.59 eV for the individual P25 and Mo-$BiVO_4$ layers, respectively (Figure 5.3d). The corresponding E_g values for the P25/Mo-$BiVO_4$ bilayer indicated a slight narrowing of E_g to 2.56 eV for Mo-$BiVO_4$ that may be associated with the post thermal annealing and the enhanced crystallinity in contrast to the identical value for the P25 upper layer. Comparison was also made with nanocrystalline Mo-$BiVO_4$ planar films and the corresponding bilayers, which were deposited on FTO glass substrates using the same procedure without the colloidal template, in order to validate the role of the inverse opal structure in the film's performance. These reference films showed qualitatively similar optical spectra though with considerably reduced DR% and enhanced T% arising from the marked reduction of DR% for the planar Mo-$BiVO_4$ underlayer in comparison to inverse opal supporting layer due to its reduced surface roughness and porosity.

The photoelectrochemical performance of the bilayer structures and the constituent layers was subsequently investigated by photocurrent density-potential curves in 0.5 M $NaHCO_3$ aqueous electrolyte under visible and UV-vis back-side illumination (Figure 5.4a,b). The P25/Mo-$BiVO_4$/FTO bilayer showed much higher photocurrent density than the reverse Mo-$BiVO_4$/P25 bilayer structure under both illumination conditions. This can be firstly related to the improved charge transport for the Mo-$BiVO_4$ photoelectrodes due to n-doping provided by Mo^{6+} ions that substitute for V^{5+} cations in $BiVO_4$ [48]. Photogenerated charge transport can be further enhanced under back-side illumination when electrons created at the semiconductor/electrolyte interface, have to travel a short distance to reach the FTO conductive substrate as for the P25/Mo-$BiVO_4$ bilayer incorporating a thin Mo-$BiVO_4$ layer.

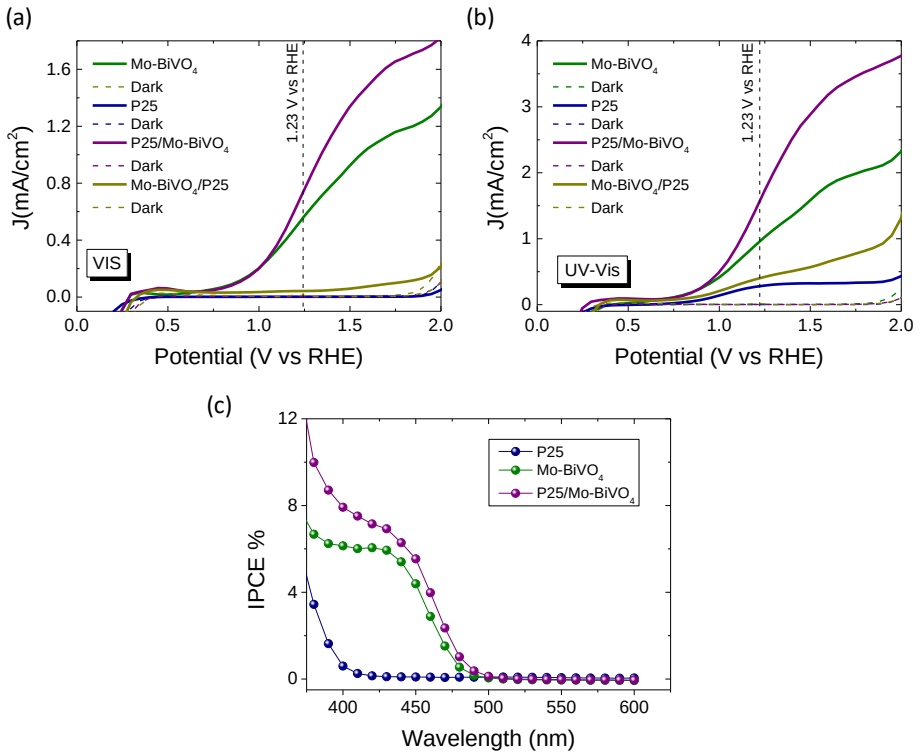

Figure 5.4 Photocurrent density-potential (J-V) curves for the P25/Mo-$BiVO_4$/FTO and Mo-$BiVO_4$/P25/FTO films in comparison to the individual layers under (a) visible and (b) UV-vis back-side illumination in 0.5 M $NaHCO_3$ aqueous electrolyte. (c) IPCE spectra at 1.23 V vs RHE potential for the P25/Mo-$BiVO_4$/FTO bilayer with respect to the P25/FTO and Mo-$BiVO_4$/FTO constituent layers.

On the other hand, charge transport and collection efficiency are greatly obstructed when the P25 layer is deposited directly on the FTO substrate even under UV-Vis illumination, reflecting its weaker PEC performance for water oxidation compared to Mo-$BiVO_4$ photoanodes [24]. The photocurrent density of the Mo-$BiVO_4$/P25 bilayer exceeded the corresponding sums of the individual Mo-$BiVO_4$ and P25 layers by about 31% under both visible and UV-Vis light, indicating improved PEC performance by enhanced light capture and/or charge separation. The former was corroborated by IPCE measurements that showed appreciable enhancement for the P25/Mo-$BiVO_4$ bilayer films, especially below the absorption edge of Mo-$BiVO_4$ at $\lambda < 490$ nm down to about 440 nm (Figure 5.4c). This suggests improved light harvesting by the Mo-$BiVO_4$ layer from the backscattering of light that reached the mesoporous P25 film, which shows significant diffuse reflectance in this spectral range (Figure 5.3a).

Charge transfer between the metal oxide layers was investigated by Mott-Schottky measurements, which were used for the estimation of the flat band potentials V_{fb} and donor densities N_D of the bilayer film with respect to its individual constituents (Figure 5.5). The Mo-$BiVO_4$ and P25 films, as well as the bilayer P25/Mo-$BiVO_4$ presented positive slopes, indicative of n-type semiconducting behavior with considerably higher donor density N_D for the n-doped Mo-$BiVO_4$ films [134]. The V_{fb} of Mo-$BiVO_4$, P25 layers and P25/Mo-$BiVO_4$ bilayer were determined from the intercept of the Mott-Schottky plots with the potential axis to be 0.179, -0.451 and 0.154 V in the dark, respectively.

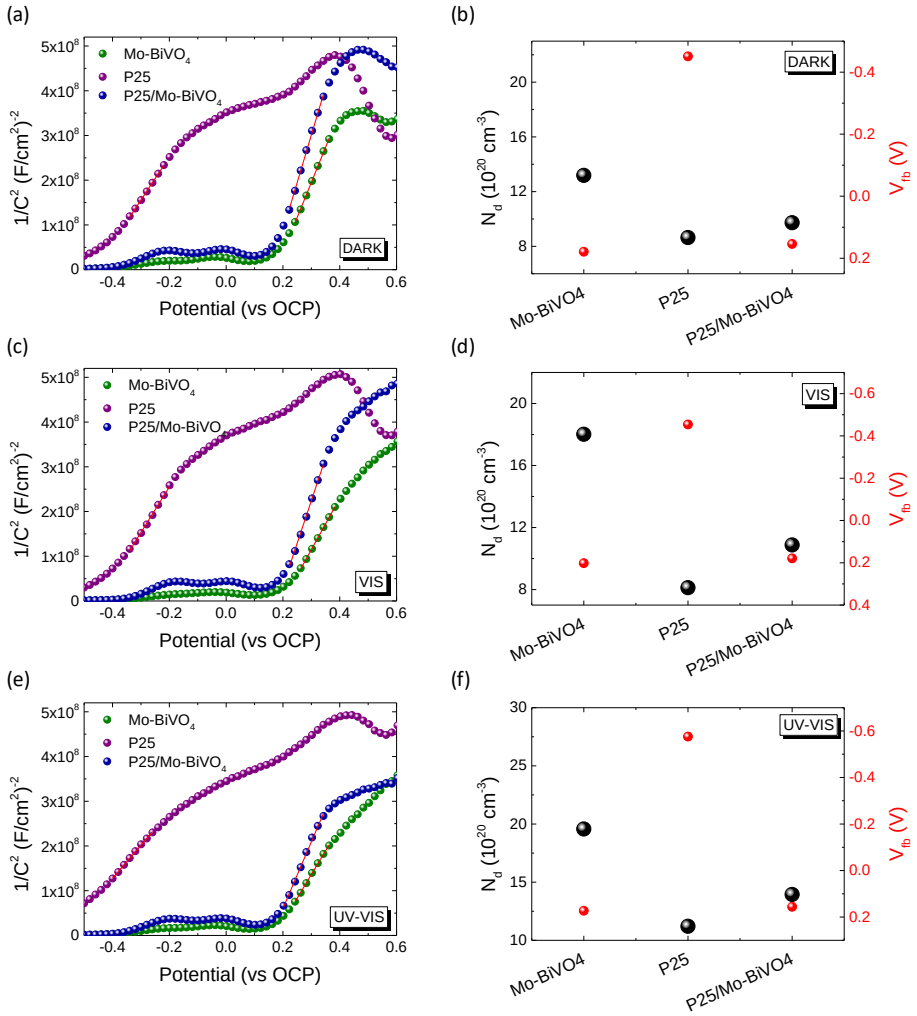

Figure 5.5 Mott-Schottky plots and the corresponding V_{fb} and N_D values derived for the Mo-$BiVO_4$ and P25 individual films in comparison to the P25/Mo-$BiVO_4$ bilayer under (a), (b) dark, (c),(d) visible and (e), (f) UV-Vis light illumination in 0.5 M $NaHCO_3$ aqueous electrolyte.

The resulting V_{fb} values indicate that the band alignment of the P25/Mo-$BiVO_4$ heterojunction is of staggered type II. In that case, photogenerated e^- would preferably transfer from the conduction band (CB) of titania nanoparticles to the corresponding CB of Mo-$BiVO_4$ under UV-Vis excitation, while photogenerated h^+ would transfer from the valence band (VB) of Mo-$BiVO_4$ to the VB of TiO_2 nanoparticles under both visible and UV-Vis light at the corresponding interface.

In order to further investigate charge carrier recombination of the samples, EIS experiments were performed under visible and UV-vis light as well in the dark for the P25/Mo-$BiVO_4$ bilayer compared to the individual layers (Figure 5.6). The Nyquist plots were fitted to a Randles equivalent circuit consisting of a series resistance R_S, the charge-transfer resistance R_{CT} at the electrode/electrolyte interface and a constant phase element CPE (Table 5.1). Under light irradiation, the films presented lower charge transfer resistance compared to dark conditions due to the generation of electron−hole pairs. Visible light irradiation resulted in markedly reduced R_{CT} values for the Mo-$BiVO_4$ and P25/Mo-$BiVO_4$ bilayer in comparison to P25 films.

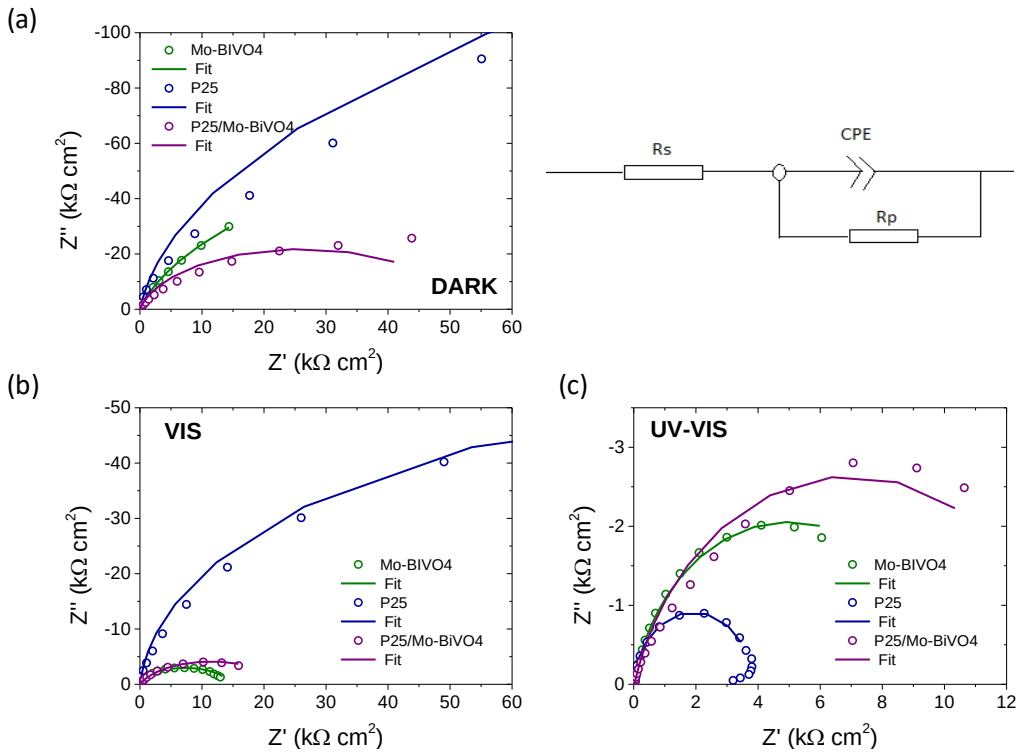

Figure 5.6 EIS Nyquist plots for the P25/Mo-$BiVO_4$ bilayer in comparison to Mo-$BiVO_4$ and P25 films under (a) dark, (b) visible and (c) UV-Vis back-side illumination in 0.5 M $NaHCO_3$ aqueous electrolyte.

This variation can be associated with the weak visible light absorption of the mixed-titania phase of P25 nanocatalysts consisting of (10 – 20%) rutile nanocrystals with band gap of ~3.0 eV besides the major (80 – 90%) anatase phase with smaller (20 nm) nanoparticles and larger band gap of 3.2 eV [15]. Nevertheless, the charge transfer resistance for the single P25 layer was greatly reduced under UV-Vis light in comparison to the Mo-$BiVO_4$ and P25/Mo-$BiVO_4$ bilayer, indicating that under these illumination conditions at open-circuit charge separation and transport are not major obstacles in the PEC performance.

Table 5.1 Parameters obtained by fitting the experimental impedance spectra to a modified Randles circuit for the P25/Mo-$BiVO_4$ bilayer in comparison to Mo-$BiVO_4$ and P25 films.

Film	Dark		Visible light (>400 nm)		UV-vis light	
	R_S (Ω)	R_{CT} (Ω)	R_S (Ω)	R_{CT} (Ω)	R_S (Ω)	R_{CT} (Ω)
Mo-$BiVO_4$	11.9	2.23x10^5	13.1	7292	12.1	4974
P25	9.0	4.62x10^5	20.6	1x10^5	9.1	1909
P25/Mo-$BiVO_4$	4.8	26034	9.4	11498	9.4	6979

5.2 Photocatalytic performance

Advanced application of the P25/Mo-$BiVO_4$ bilayer films was performed on the photoelectrocatalytic degradation of the pharmaceutical emerging contaminant ibuprofen (IBU), a non-steroidal anti-inflammatory drug that is widely used as analgestic and antipyretic [205]. It is the third consumable drug and highly detected in many water bodies [206]. It has been shown that IBU is selectively metabolized in humans and animals and the excretion, which is more toxic than the parent molecule, enters into river, lake, oceans, ground water etc. Initial photodegradation tests were performed on IBU degradation in 0.1 M $NaHCO_3$ supporting electrolyte using the bare P25 films at zero bias potential, +0.5 and +1.0 V vs Ag/AgCl under UV-vis light (Figure 5.7), indicating that the applied potential promoted electron-hole separation and pollutant degradation.

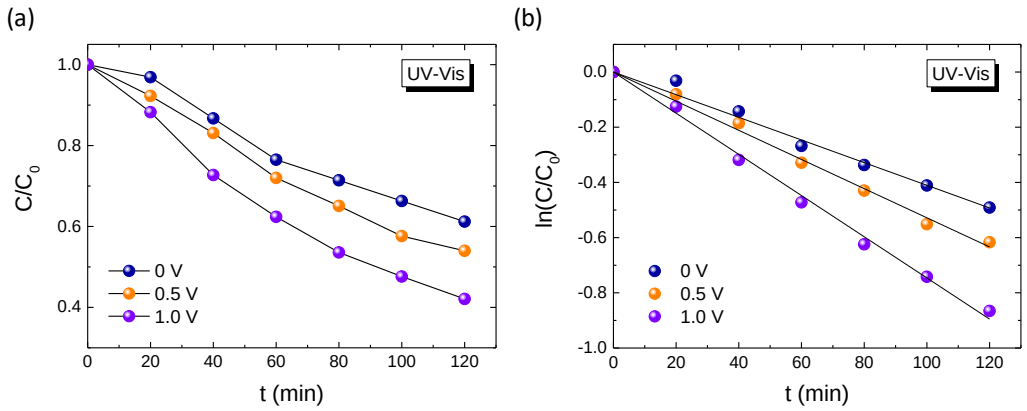

Figure 5.7 IBU photoelectrocatalytic degradation kinetics for the Mo-$BiVO_4$ PC films in 0.1 M $NaHCO_3$ supporting electrolyte at bias potentials of 0, +0.5 and +1.0 V vs Ag/AgCl under UV-Vis illumination.

IBU photodegradation was accordingly performed in 0.1 M $NaHCO_3$ supporting electrolyte at applied potential +1.0 vs Ag/AgCl under visible and UV-vis light (Figure 5.8). IBU degradation was detected by UV-Vis spectroscopy monitoring the main aromatic 222 nm absorbance band [207], which degraded rapidly following pseudo first-order kinetics for which the corresponding initial reaction rates r_{Vis} and $r_{UV\text{-}Vis}$ were calculated (Figure 5.8f). The photodegradation of IBU was accompanied by the appearance of a new red-shifted absorption band at about 257 nm, indicative of the formation of reaction intermediates, the most prominent being 4-isobutylacetophenone [208]. The corresponding band reached maximum intensity after 80 min of photocatalytic treatment by UV-Vis light (Figure 5.8a), while illumination for longer times resulted in its continuous reduction signaling the side group oxidation and oxidative opening of IBU benzene ring towards mineralization [207, 208]. P25 films showed rather weak reactivity due to the inherently low visible light absorbance of the TiO_2 polymorphic phases [209], which increased considerably under UV-Vis light.

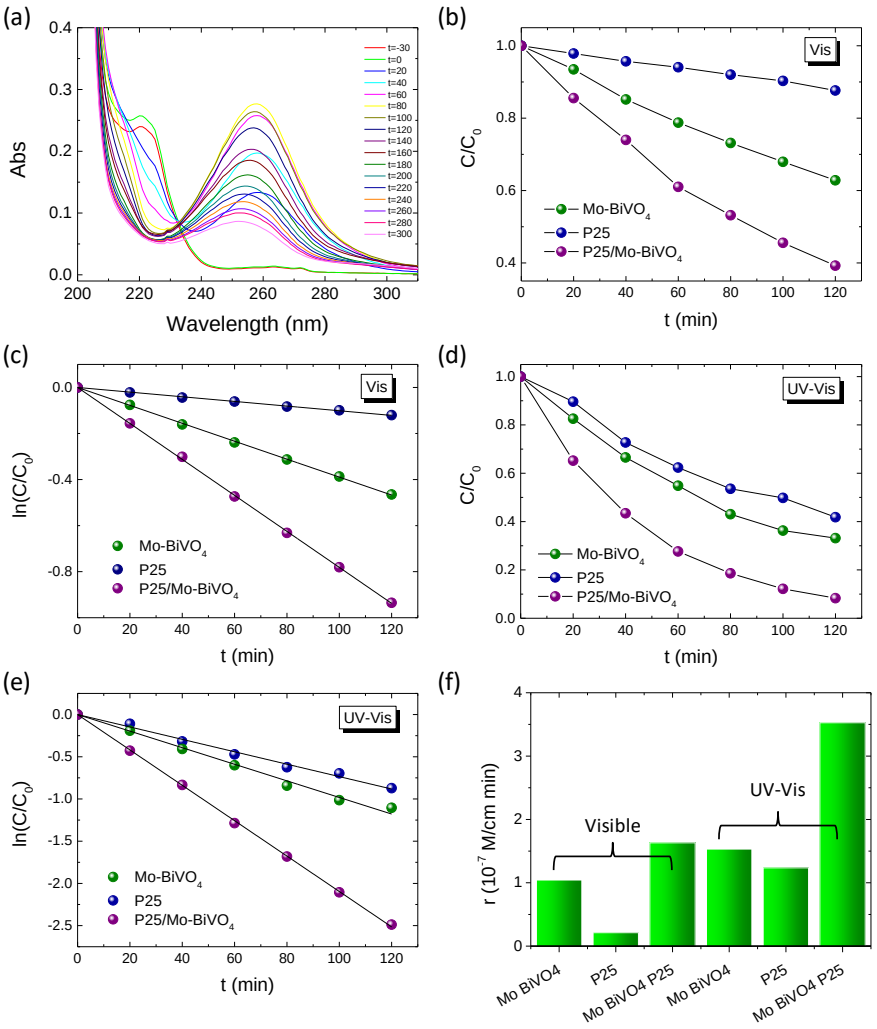

Figure 5.8 (a) IBU absorbance spectra under UV-Vis illumination in the presence of P25/Mo-$BiVO_4$. IBU photodegradation kinetics under (b), (c) visible and (d), (e) UV-Vis light as well as the corresponding (f) reaction rates for the individual constituents and the P25/Mo-$BiVO_4$ bilayer photoelectrodes at +1.0 V vs Ag/AgCl.

The pristine Mo-$BiVO_4$ photoelectrodes showed smaller differences in their photocatalytic activity under visible and UV-Vis light, reflecting their intrinsic visible light activation below 490 nm. More importantly, the P25/Mo-$BiVO_4$ bilayers presented the highest performance that exceeded the reaction rate sums for the individual P25 and Mo-$BiVO_4$ layers by approximately 30 and 28%, under visible and UV-Vis light, respectively.

In order to validate the bilayer performance, IBU degradation was also monitored by high-performance liquid chromatography (HPLC) for P25/Mo-$BiVO_4$ under UV-Vis light for 5 h (Figure 5.9). The total run was 15 min and the retention time was 6.3 min for IBU. At 5.4 min, a degradation product of IBU was detected after 1 h, which according to the corresponding UV-Vis spectra (Figure 5.9a,b) may arise from 4-isobutylacetophenone [208]. The obtained results showed that IBU was completely removed after 2 h (Figure 5.9e), whereas the degradation of the intermediate reaction product that appeared after 1 h (Figure 5.9d) reached 94% after 5 h (Figure 5.9f) under UV-Vis light, supporting the high photocatalytic activity of the bilayer films.

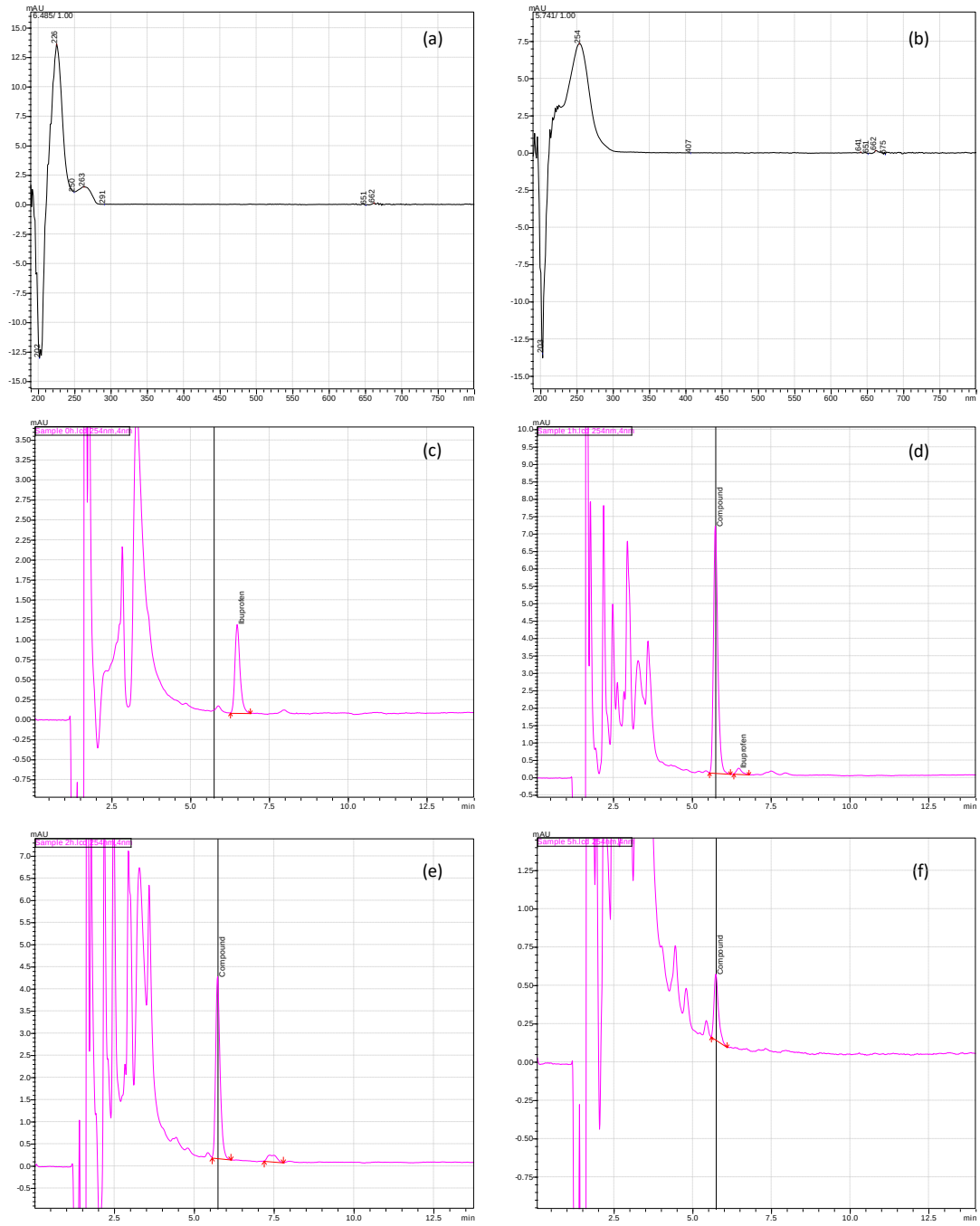

Figure 5.9 Absorbance spectra of (a) IBU and (b) the degradation product. HPLC chromatograms of IBU degradation in the presence of P25/Mo-$BiVO_4$ films under UV-Vis light irradiation for (c) 0, (d) 1, (e) 2 and (f) 5 h. The bottom figure shows the corresponding TC degradation kinetics up to 3 h.

Based on these results, the enhanced photocatalytic performance of the TiO_2/Mo-$BiVO_4$ bilayer photoanode can be primarily related to the improved light harvesting due to backscattering by the mesoporous TiO_2 layer in combination with the interfacial cascade electron transfer from the upper TiO_2 layer to Mo-$BiVO_4$ and finally to the FTO substrate and photogenerated hole transfer to the TiO_2 valence band (Figure 5.10) that promotes the photoelectrocatalytic degradation of IBU, which presents a highly refractory water pollutant of emerging concern.

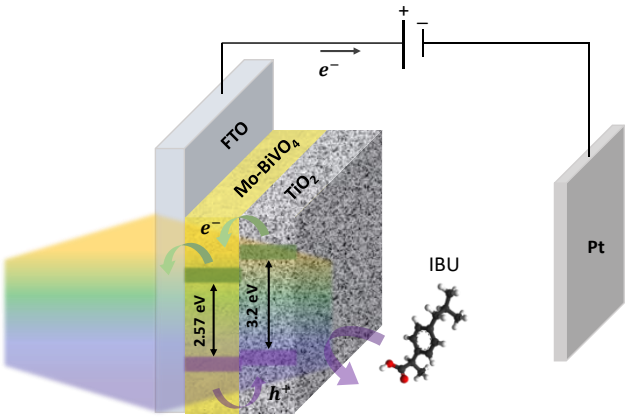

Figure 5.10 Schematic charge transfer in the of P25/Mo-$BiVO_4$ photoelectrode for IBU degradation under back side illumination.

5.3 Conclusions

Advanced bilayer photoelectodes were fabricated utilizing the best performing Mo-$BiVO_4$ PC films as supporting layer that intrinsically absorbs visible light below 490 nm, while offering improved charge transport due to Mo-doping. Spin coating of a mesoporous P25 titania overlayer resulted in a porous heterostructured P25/Mo-$BiVO_4$ bilayer structure produced from the collapse of the inverse opal underlayer after the second thermal annealing. The bilayer film performance was evaluated on the photoelectrocatalytic degradation of IBU non-steroidal anti-inflammatory drug under back-side illumination by visible and UV-Vis light. Significantly enhanced photocatalytic performance was achieved for the bilayer structure with respect to the additive effect of the constituent layers, which was related to the improved light harvesting due to backscattering from the P25 TiO_2 layer in combination with the favorable interfacial charge transfer at the TiO_2/Mo-$BiVO_4$ heterojunction.

Conclusions

In this thesis, the development of $BiVO_4$ PCs with tailored optical properties was investigated in order to combine slow photon assisted light trapping with targeted compositional modifications for visible light photocatalysis. The deposition of well-ordered $BiVO_4$ inverse opal films was successfully implemented by the liquid phase infiltration of a complex inorganic precursor of $Bi(NO_3)_3{\cdot}5H_2O$ and NH_4VO_3 salts on colloidal opal templates prepared by the self-assembly of monodisperse polystyrene microspheres. Systematic analysis of the PC films structural and optical properties showed the formation of periodic inverse opal structures in the *ms*-$BiVO_4$ phase with E_g of 2.59 eV and variable PBG in the visible range. Comparative photocatalytic evaluation of PBG engineered $BiVO_4$ inverse opals on SA degradation showed selective enhancement of the photocatalytic process validating the presence of slow photon amplification effects, which were identified in the case of resonance of the high-energy slow light spectral region (blue slow photons) with the electronic absorption of *ms*-$BiVO_4$, allowing to determine the optimal PC structure for visible light harvesting. Compositional tuning was then pursued for the optimal photocatalytic PC films by Mo- and Ca- doping. Thorough investigations of the modified $BiVO_4$ inverse opals with different experimental techniques showed the incorporation of Mo^{6+} and Ca^{2+} ions replacing V^{5+} and Bi^{3+} ions in *ms*-$BiVO_4$ with weak structural distortions. Metal doping resulted in the introduction of shallow donor and acceptor states for Mo-$BiVO_4$ and Ca-$BiVO_4$, respectively, which caused slight Eg narrowing and shifts of the CB and VB potentials along with significant variation in the donor concentrations. Optimization of the Mo and Ca doping concentrations was determined by comparative photocatalytic evaluation in SA degradation. The optimally doped $BiVO_4$ films were applied for the fabrication of nanostructured Mo-$BiVO_4$/Ca-$BiVO_4$ photoelectrodes by the successive infiltration of the Mo and Ca-containing metal salt precursors in the optimal colloidal template, leading to abundant interfaces and n-n^+ isotype homojunctions between differently doped $BiVO_4$ NPs. The nanostructured homojunction PC films were successfully applied on the VLA photoelectrocatalytic degradation of SA, TC and CIP antibiotics, validating their application potential on water remediation by pharmaceutical contaminants.

The surface modification of $BiVO_4$ PC films with plasmonic Ag and Au NPs was also investigated as a promising means to further improve light harvesting and charge separation aiming to enhance the photo(electro)catalytic degradation of TC and IBU antibiotics in the visible range. For this modification, the optimal Mo-$BiVO_4$ PC was chosen, whose WF lies between the corresponding values for Ag and Au metallic NPs, allowing the investigation of different charge transfer mechanisms at the metal-semiconductor interface to enhance photocatalytic activity. Inverse opal fabrication was carried out by applying the material saving horizontal deposition method using smaller amounts of colloidal suspensions, followed by surface modification using aqueous suspensions of Ag and Au NPs with LSPR at 406 and 520 nm, respectively. Comparative structural analysis of the Ag/Mo-$BiVO_4$, Au/Mo-$BiVO_4$, and Ag-Au/Mo-$BiVO_4$ PC photoelectrodes with TEM-EDX, XRD, Raman and XPS showed

uniform distribution of the metal NPs on the walls of the Mo-BiVO4 PCs, while UV-visible DR% spectroscopy showed significant reduction in reflectivity due to plasmonic absorption. Photoelectrochemical evaluation by J-V, IPCE, EIS and Mott-Schottky analysis combined with PL showed enhanced visible light collection and improved charge separation. Specifically, performance evaluation in photocurrent generation showed significant contributions from local field enhancement, particularly for the Ag/Mo-$BiVO_4$ PCs due to the spectral overlap of plasmonic with the electronic absorption and the blue slow photons, in contrast to the weak plasmonic sensitization (hot electron injection) for the Au/Mo-$BiVO_4$ PC films. The Ag/Mo-$BiVO_4$ and Ag-Au/Mo-$BiVO_4$ films exhibited the highest efficiencies in the TC and IBU PEC degradation, respectively, under visible light at +1.0 vs. Ag/AgCl. This difference was attributed to the corresponding shifts in the energy bands of the surface-modified PC films resulting from changes in the alignment of the Fermi energies at the metal-semiconductor heterojunction due to the different WFs of the Ag and Au NPs relative to Mo-$BiVO_4$, which affect interfacial electron transfer, in agreement with the results of trapping experiments of reactive oxygen species. It is concluded that the relative positions of energy bands and PBG tuning are crucial factors in designing efficient plasmonic-photonic photoelectrocatalysts based on heterojunctions of VLA semiconductor PCs and plasmonic NPs.

Alternatively, heterostructured TiO_2/Mo-$BiVO_4$ bilayer films were fabricated and evaluated with the aim of enhancing light collection and photocatalytic activity in the visible and UV spectral regions. The films were fabricated by horizontal deposition of the optimal Mo-$BiVO_4$ inverse opal as photonic substrate that exhibits strong intrinsic absorption at $\lambda<490$ nm and improved charge transport due to Mo doping. Deposition of a mesoporous layer of nanocrystalline titania Aeroxide P25 exhibiting high near-UV photocatalytic performance resulted in a porous P25/Mo-$BiVO_4$ bilayer that formed by the collapse of the inverse opal structure of the substrate after the second thermal annealing due to the growth of the $BiVO_4$ crystallites. The structural and optical properties of the films were studied by SEM, TEM combined with elemental EDX analysis, Raman, diffuse and specular spectroscopies and photoelectrochemical measurements of J-V curves, IPCE, EIS and Mott- Schottky, while comparative evaluation of the photocatalytic activity of mono- and bi-layer films was carried out in the PEC degradation of IBU under visible and UV illumination. The bilayer films showed significantly improved performance in the IBU PEC degradation compared to the additive performance of their components, which is related to improved light harvesting via backscattering from the mesoporous TiO_2 layer coupled with electron transfer at the heterojunction interface of TiO_2 and Mo-$BiVO_4$, which promotes charge separation and photocatalytic activity.

References

[1] A. Fujishima, X. Zhang, and D. A. Tryk, TiO_2 photocatalysis and related surface phenomena, Surf. Sci. Rep. **63**, 515 (2008).

[2] J. Schneider, D. Bahnemann, J. Ye, G. Li Puma, and D. D. Dionysiou, *RCS Energy and Environment Series No. 14, Photocatalysis: Fundamentals and Perspectives*, (The Royal Society of Chemistry, Cambridge, 2016).

[3] S. Giménez, and J. Bisquert, *Photoelectrochemical Solar Fuel Production: From Basic Principles to Advanced Devices*, (Springer, New York, 2016).

[4] D. Bahnemann, P. Robertson, C. Wang, W. Choi, H. Daly, M. Danish, H. de Lasa, S. Escobedo, C. Hardacre, T. H. Jeon, B Kim, H. Kisch, W. Li, M. Long, M. Muneer, N. Skillen, and J. Zhang 2023 roadmap on photocatalytic water splitting, J. Phys. Energy **5,** 012004 (2023).

[5] B. C. Hodges, E. L. Cates, and J. Kim, Challenges and prospects of advanced oxidation water treatment processes using catalytic nanomaterials. Nature Nanotechnology **13**, 642 (2018).

[6] K. Sivula, and R. van de Krol, Semiconducting materials for photoelectrochemical energy conversion, Nat. Rev. Mater. **1**, 15010 (2016).

[7] Q. Wang, and K. Domen, Particulate photocatalysts for light-driven water splitting: mechanisms, challenges, and design strategies. Chem. Rev. **120**, 919 (2020).

[8] X. Li, J. Yu, and M. Jaroniec, Hierarchical photocatalysts, Chem. Soc. Rev. **45**, 2603 (2016).

[9] S. Banerjee, S. C. Pillai, P. Falaras, K. E. O'Shea, J. A. Byrne, and D. D. Dionysiou, J. Phys. Chem. Lett. **5**, 2543 (2014).

[10] H. Kisch, *Semiconductor Photocatalysis*, (Wiley-VCH Verlag GmbH & Co. KGaA, Germany, 2015).

[11] A. Fujishima, and K. Honda, Electrochemical photolysis of water at a semiconductor electrode. Nature **238**, 37 (1972).

[12] Kubacka, A.; Fernandez-Garcia, M.; Colon, G. Advanced nanoarchitectures for solar photocatalytic applications. Chem. Rev. ***112***, 1555 (2012).

[13] Y. Xu, and M. A. A. Schoonen, The absolute energy positions of conduction and valence bands of selected semiconducting minerals, American Mineralogist **85**, 543 (2000).

[14] P. Lianos, Review of recent trends in photoelectrocatalytic conversion of solar energy to electricity and hydrogen, Appl. Catal. B: Environ. **210**, 235 (2017).

[15] V. Likodimos, A. Chrysi, M. Calamiotou, C. Fernández-Rodríguez, J.M. Doña-Rodríguez, D.D. Dionysiou, and P. Falaras, Microstructure and charge trapping

assessment in highly reactive mixed phase TiO_2 photocatalysts, Appl. Catal. B: Environ. **192**, 242 (2016).

[16] S. McMichael, P. Fernández-Ibáñez, and J. A. Byrne, A review of photoelectrocatalytic reactors for water and wastewater treatment. Water **13**, 1198 (2021).

[17] S. Garcia-Segura, and E. Brillas, Applied photoelectrocatalysis on the degradation of organic pollutants in wastewaters, J. Photochem. Photobiol. C: Photochem. Rev. **31**, 1 (2017).

[18] M. G. Walter, E. L. Warren, J. R. McKone, S. W. Boettcher, Q. Mi, E. A. Santori, and N. S. Lewis, Solar water splitting cells, Chem. Rev. **110**, 6446 (2010).

[19] C. Jiang, S. J. A. Moniz, A. Wang, T. Zhang, and J. Tang, Photoelectrochemical devices for solar water splitting-materials and challenges, Chem. Soc. Rev. **46**, 4645 (2017).

[20] H. Wu, H. L. Tan, C. Y. Toe, J. Scott, L. Wang, R. Amal, and Y. H. Ng, Photocatalytic and photoelectrochemical systems: similarities and differences, Adv. Mater. **32**, 1904717 (2020).

[21] R. Tang, S. Zhou, Z. Zhang, R. Zheng, and J. Huang, Engineering nanostructure–interface of photoanode materials toward photoelectrochemical water oxidation, Adv. Mater. **33**, 2005389 (2021).

[22] H. Tong, S. Ouyang, Y. Bi, N. Umezawa, M. Oshikiri, and J. Ye, Nano-Photocatalytic materials: possibilities and challenges, Adv. Mater. **24**, 229 (2012).

[23] D. K. Lee, D. Lee, M. A. Lumley, and K. S. Choi, Progress on ternary oxide-based photoanodes for use in photoelectrochemical cells for solar water splitting, Chem. Soc. Rev. **48**, 2126 (2019).

[24] J. H. Kim and J. S. Lee, Elaborately modified $BiVO_4$ photoanodes for solar water splitting, Adv. Mater. **31**, 1806938 (2019).

[25] A. Kudo, K. Ueda, H. Kato, and I. Mikami, Photocatalytic O_2 evolution under visible light irradiation on $BiVO_4$ in aqueous $AgNO_3$ solution, Catal. Lett. **53**, 229 (1998).

[26] A. Kudo, K. Omori, and H. Kato, A novel aqueous process for preparation of crystal form-controlled and highly crystalline $BiVO_4$ powder from layered vanadates at room temperature and its photocatalytic and photophysical properties, J. Am. Chem. Soc. **121**, 11459 (1999).

[27] S. Tokunaga, H. Kato, and A. Kudo, Selective preparation of monoclinic and tetragonal $BiVO_4$ with scheelite structure and their photocatalytic properties, Chem. Mater. **13**, 4624 (2001).

[28] D. Zhou, L. X. Pang, D. W. Wang, and I. M. Reaney, $BiVO_4$ based high k microwave dielectric materials: a review, J. Mater. Chem. C **6**, 9290 (2018).

[29] F. F. Abdi, S. P. Berglund, and R. van de Krol, *Multinary metal oxide photoelectrodes*, in Photoelectrochemical Solar Fuel Production, eds. S. Gimenez, J. Bisquert, Springer, (2016).

[30] Y. Park, K. J. McDonald, and K.-S. Choi, Progress in bismuth vanadate photoanodes for use in solar water oxidation, Chem. Soc. Rev. **42**, 2321 (2013).

[31] J. D. Bierlein and A. W. Sleight, Ferroelasticity in $BiVO_4$, Sol. St. Commun. **16**, 69 (1975).

[32] J. K. Cooper, S. Gul, F. M. Toma, L. Chen, P.-A. Glans, J. Guo, J. W. Ager, J. Yano, and I. D. Sharp, Electronic structure of monoclinic $BiVO_4$, Chem. Mater. **26**, 5365 (2014).

[33] J. K. Cooper, S. Gul, F. M. Toma, L. Chen, Y. S. Liu, J. Guo, J. W. Ager, J. Yano, and I. D. Sharp, Indirect bandgap and optical properties of monoclinic bismuth vanadate, J. Phys. Chem. C **119**, 2969 (2015).

[34] J. Wiktor, F. Ambrosio, and A. Pasquarello, Role of polarons in water splitting: the case of $BiVO_4$, ACS Energy Lett. **3**, 1693 (2018).

[35] F. F. Abdi, T. J. Savenije, M. M. May, B. Dam, and R. van de Krol, The origin of slow carrier transport in $BiVO_4$ thin film photoanodes: a time-resolved microwave conductivity study, J. Phys. Chem. Lett. **4**, 2752 (2013).

[36] A. J. E. Rettie, H. C. Lee, L. G. Marshall, J.-F. Lin, C. Capan, J. Lindemuth, J. S. McCloy, J. Zhou, A. J. Bard, and C. B. Mullins, Combined charge carrier transport and photoelectrochemical characterization of $BiVO_4$ single crystals: intrinsic behavior of a complex metal oxide, J. Am. Chem. Soc. **135**, 11389 (2013).

[37] J. A. Seabold, K. Zhu, and N. R. Neale, Efficient solar photoelectrolysis by nanoporous Mo:$BiVO_4$ through controlled electron transport, Phys. Chem. Chem. Phys. **16**, 1121 (2014).

[38] K. E. Kweon and G. S. Hwang, Structural phase-dependent hole localization and transport in bismuth vanadate, Phys. Rev. B: Condens. Matter Mater. Phys. **87**, 205202 (2013).

[39] A. J. Rettie, W. D. Chemelewski, D. Emin, and C. B. Mullins, Unravelling small-polaron transport in metal oxide photoelectrodes, J. Phys. Chem. Lett. **7**, 471 (2016).

[40] W.-J. Yin, S.-H. Wei, M. M. Al-Jassim, J. Turner, and Y. Yan, Doping properties of monoclinic $BiVO_4$ studied by first-principles density-functional theory, Phys. Rev. B **83**, 155102 (2011).

[41] N. Österbacka, F. Ambrosio, and J. Wiktor, Charge Localization in defective $BiVO_4$, J. Phys. Chem. C **126**, 2960 (2022).

[42] H. S. Park, K. E. Kweon, H. Ye, E. Paek, G.S. Hwang, and A. J. Bard, Factors in the metal doping of $BiVO_4$ for improved photoelectrocatalytic activity as studied by scanning electrochemical microscopy and first-principles density-functional calculation, J. Phys. Chem. C **115**, 17870 (2011).

[43] K. P. S. Parmar, H .J. Kang, A. Bist, P. Dua, J. S. Jang, and J. S. Lee, Photocatalytic and photoelectrochemical water oxidation over metal-doped monoclinic $BiVO_4$ photoanodes, ChemSusChem **5**, 1926 (2012).

[44] W. J. Jo, H. J. Kang, K.-J. Kong, Y. S. Lee, H. Park, Y. Lee, T. Buonassisi, K. K. Gleason, and J. S. Lee, Phase transition-induced band edge engineering of $BiVO_4$ to split pure water under visible light, Proc. Natl. Acad. Sci. U. S. A. **112**, 13774 (2015).

[45] J.H. Kim, Y. Jo, J. H. Kim, J. W. Jang, H. J. Kang, Y. H. Lee, D. S. Kim, Y. Jun, and J.S. Lee, Wireless solar water splitting device with robust cobalt-catalyzed, dual-doped $BiVO_4$ photoanode and perovskite solar cell in tandem: a dual absorber artificial leaf, ACS Nano, **9**, 11820 (2015).

[46] S. Wang, P. Chen, Y. Bai, J. H. Yun, G. Liu, and L. Wang, New $BiVO_4$ dual photoanodes with enriched oxygen vacancies for efficient solar-driven water splitting, Adv. Mater. **30**, 1800486 (2018).

[47] S. Jin, X. Ma, J. Pan, C. Zhu, S. E. Saji, J. Hu, X. Xu, L. Sun, and Z. Yin, Oxygen vacancies activating surface reactivity to favor charge separation and transfer in nanoporous $BiVO_4$ photoanodes, Appl. Catal. B: Environ. **281**, 119477 (2021).

[48] W. Zhang, F. Wu, J. Li, D. Yan, J. Tao, Y. Ping, and M. Liu, Unconventional relation between charge transport and photocurrent via boosting small polaron hopping for photoelectrochemical water splitting, ACS Energy Lett. **3**, 2232 (2018).

[49] F. F. Abdi, L. Han, A. H. M. Smets, M. Zeman, B. Dam, and R. van de Krol, Efficient solar water splitting by enhanced charge separation in a bismuth vanadate-silicon tandem photoelectrode, Nat. Commun. **4**, 2195 (2013).

[50] B. Zhang, H. Zhang, Z. Wang, X. Zhang, X. Qin, Y. Dai, Y. Liu, P. Wang, Y. Li, and B. Huang, Doping strategy to promote the charge separation in $BiVO_4$ photoanodes. Appl. Catal. B: Environ. **211**, 258 (2017).

[51] J. M. Lee, H. Baek, M. Gill, X. Shi, S. Lee, I.-S. Cho, H. S. Jung, and X. Zheng, A $Zn:BiVO_4/Mo:BiVO_4$ homojunction as an efficient photoanode for photoelectrochemical water splitting, J. Mater. Chem. A, **7**, 9019 (2019).

[52] S. Bera, S. A. Lee, W.-J. Lee, J.-H. Kim, C. Kim, H. G. Kim, H. Khan, S. Jana, H. W. Jang, and S.-H. Kwon, Hierarchical nanoporous $BiVO_4$ photoanodes with high charge separation and transport efficiency for water oxidation, ACS Appl. Mater. Interfaces **13**, 14291 (2021).

[53] J. W. Yang, I. J. Park, S. A. Lee, M. G. Lee, T. H. Lee, H. Park, C. Kim, J. Park, J. Moon, J. Y. Kim, and H. W. Jang, Near-complete charge separation in tailored $BiVO_4$-based heterostructure photoanodes toward artificial leaf, Appl. Catal. B Environ. **293**, 120217 (2021).

[54] X. Shi, I. Y. Choi, K. Zhang, J. Kwon, D. Y. Kim, J. K. Lee, S. H. Oh, J. K. Kim and J. H. Park, Efficient photoelectrochemical hydrogen production from bismuth vanadate-decorated tungsten trioxide helix nanostructures, Nat. Commun. **5**, 4775 (2014).

[55] Y. Pihosh, I. Turkevych, K. Mawatari, J. Uemura, Y. Kazoe, S. Kosar, K. Makita, T.Sugaya, T. Matsui, D. Fujita, M. Tosa, M. Kondo, and T. Kitamori, Photocatalytic generation of hydrogen by core-shell $WO_3/BiVO_4$ nanorods with ultimate water splitting effiency, Sci. Rep. **5**, 11141 (2015).

[56] L. Zhou, C. Zhao, B. Giri, P. Allen, X. Xu, H. Joshi, Y. Fan,L. V. Titova, and P. M. Rao, High light absorption and charge separation efficiency at low applied voltage from Sb-Doped $SnO_2/BiVO_4$ core/shell nanorod-array photoanodes, Nano Lett. **16**, 3463 (2016).

[57] J. Resasco, H. Zhang, N. Kornienko, N. Becknell, H. Lee, J. Guo, A. L. Briseno, and P. Yang, $TiO_2/BiVO_4$ Nanowire heterostructure photoanodes based on type II band alignment, ACS Cent. Sci. **2**, 80 (2016).

[58] G. von Freymann, V. Kitaev, B. V. Lotsch, G. A. Ozin, Bottom-up assembly of photonic crystals, Chem. Soc. Rev. **42**, 2528 (2013)

[59] V. Likodimos, Photonic crystal-assisted visible light activated TiO_2 photocatalysis, Appl. Catal. B Environ. **230**, 269 (2018).

[60] E. Yablonovitch, Inhibited spontaneous emission in solid-state physics and electronics, Phys. Rev. Lett. **58**, 2059 (1987).

[61] S. John, Strong localization of photons in certain disordered dielectric superlattices, Phys. Rev. Lett. **58**, 2486 (1987).

[62] J. D. Joannopoulos, S. G. Johnson, J. N. Winn and R. D. Meade, *Photonic Crystals: Molding the Flow of Light*, (Princeton University Press, 2008).

[63] F. Marlow, Muldarisnur, P. Sharifi, R. Brinkmann, and C. Mendive, Opals: status and prospects, Angew. Chem. **48**, 6212 (2009).

[64] A. Stein, B. E. Wilson, and S. G. Rudisill, Design and functionality of colloidal-crystal-templated materials-chemical applications of inverse opals, Chem. Soc. Rev. **42**, 2763 (2013).

[65] D. J. Norris and Y. A. Vlasov, Chemical approaches to three-dimensional semiconductor photonic crystals, Adv. Mater. **13**, 371 (2001).

[66] A. Toumazatou, M. K. Arfanis, P.-A. Pantazopoulos, A. G. Kontos, P. Falaras, N. Stefanou, and V. Likodimos, Slow-photon enhancement of dye sensitized TiO_2 photocatalysis, Mat. Lett. **197**, 123 (2017).

[67] K. Busch and S. John, Photonic band gap formation in certain self-organizing systems, Phys. Rev. E **58**, 3896 (1998).

[68] J. F. Galisteo-López, "An optical study of opal based photonic crystals," PhD Thesis, (2005).

[69] S. J. Yeo, G. H. Choi, and P. J. Yoo, Multiscale-architectured functional membranes utilizing inverse opal structures, *J. Mater. Chem. A* **5**, 17111 (2017).

[70] B. Hatton, L. Mishchenko, S. Davis, K. H. Sandhage, and J. Aizenberg, Assembly of large-area, highly ordered, crack-free inverse opal films, Proc. Natl. Acad. Sci. U. S. A. **107**, 10354 (2010).

[71] Q. Yan, Z. Zhou, and X. S. Zhao, Inward-growing self-assembly of colloidal crystal films on horizontal substrates, Langmuir **21**, 3158 (2005).

[72] G. E. Jellison, L. A. Boatner, J. D. Budai, B.-S. Jeong, and D. P. Norton, Spectroscopic ellipsometry of thin film and bulk anatase (TiO_2), J Appl Phys **93**, 9537 (2003).

[73] G. I. N. Waterhouse, and M. R. Waterland, Opal and inverse opal photonic crystals: Fabrication and characterization, Polyhedron **26**, 356 (2007).

[74] A. Lonergan, C. Hu, and C. O' Dwyer, Filling in the gaps: the nature of light transmission through solvent-filled inverse opal photonic crystals, Phys. Rev. Mater. **4**, 065201 (2020).

[75] N. Stefanou, V. Yannopoulos, and A. Modinos, Heterostructures of photonic crystals: frequency bands and transmission coefficients, Computer Phys. Commun. **113**, 49 (1998).

[76] N. Stefanou, V. Yannopapas, and A. Modinos, MULTEM2: A new version of the program for transmission and band-structure calculations of photonic crystals, Comput. Phys. Commun. **132**, 189 (2000).

[77] R. C. Schroden, M. Al-Daous, C. F. Blanford, and A. Stein, Optical properties of inverse opal photonic crystals, Chem. Mater. **14**, 3305 (2002).

[78] A. Toumazatou, M. Antoniadou, E. Sakellis, D. Tsoutsou, S. Gardelis, G. Em. Romanos, N. Ioannidis, N. Boukos, A. Dimoulas, P. Falaras, V. Likodimos, Boosting visible light harvesting and charge separation in surface modified TiO_2 photonic crystal catalysts with CoO_x nanoclusters, Mater. Adv. **1**, 2310 (2020).

[79] S. Nishimura, N. Abrams, B. A. Lewis, L. I. Halaoui, T. E. Mallouk, K. D. Benkstein, J. van de Lagemaat, and A. J. Frank, Standing wave enhancement of red absorbance and photocurrent in dye-sensitized titanium dioxide photoelectrodes coupled to photonic crystals, J. Am. Chem. Soc. **125**, 6306 (2003).

[80] L.I. Halaoui, N. Abrams, and T.E. Mallouk, Increasing the conversion efficiency of dye-sensitized TiO_2 photo-electrochemical cells by coupling to photonic crystals, J. Phys. Chem. B **109**, 6334 (2005).

[81] S. Guldin, S. Huttner, M. Kolle, M. E. Welland, P. Muller-Buschbaum, R. H. Friend, U. Steiner, and N. Tetreault, Dye-sensitized solar cell based on a three-dimensional photonic crystal, Nano Lett. **10**, 2303 (2010).

[82] J. I. Chen, G. von Freymann, S. Y. Choi, V. Kitaev, and G. A. Ozin, Amplified photochemistry with slow photons, Adv.Mater. **18**, 1915 (2006).

[83] X. Zhang, and S. John, Enhanced photocatalysis by light-trapping optimization in inverse opals. J. Mater. Chem. A **8**, 18974 (2020).

[84] M. El Harakeh, and L. Halaoui, Enhanced conversion of light at TiO_2 photonic crystals to the blue of a stop band and at TiO_2 random films sensitized with Q-CdS: order and disorder. J. Phys. Chem. C **114**, 2806 (2010).

[85] K. R. Phillips, G. T. England, S. Sunny, E. Shirman, T. Shirman, N. Vogel, and J. Aizenberg, A colloidoscope of colloid-based porous materials and their uses, Chem. Soc. Rev. **45**, 281 (2016).

[86] J. Liu, H. Zhao, M. Wu, B. Van der Schueren, Y. Li, O. Deparis, J. Ye, G. A. Ozin, T. Hasan, and B.-L. Su, Slow photons for photocatalysis and photovoltaics, Adv. Mater. **29**, 1605349 (2017).

[87] A. Lonergan and C. O'Dwyer, Many facets of photonic crystals: from optics and sensors to energy storage and photocatalysis, Adv. Mater. Technol. **8**, 2201410 (2023).

[88] L. Mascaretti, A. Dutta, Š. Kment, V. M. Shalaev, A. Boltasseva, R. Zboril, and A. Naldoni, Plasmon-enhanced photoelectrochemical water splitting for efficient renewable energy storage, Adv. Mater. **31**, 1805513 (2019).

[89] H. A. Atwater and A. Polman, Plasmonics for improved photovoltaic devices, Nat. Mater. **9**, 205 (2010).

[90] S. Linic, P. Christopher, and D. B. Ingram, Plasmonic-metal nanostructures for efficient conversion of solar to chemical energy, Nat. Mater. **10**, 911 (2011).

[91] C. Clavero, Plasmon-induced hot-electron generation at nanoparticle/metal-oxide interfaces for photovoltaic and photocatalytic devices, Nat. Photonics **8**, 95 (2014).

[92] Y. Zhang, S. He, W. Guo, Y. Hu, J. Huang, J. R. Mulcahy, and W. D. Wei, Surface-plasmon-driven hot electron photochemistry, Chem. Rev. **118**, 2927 (2018).

[93] S. K. Cushing, J. Li, F. Meng, T. R. Senty, S. Suri, M. Zhi, M. Li, A. D. Bristow, and N. Wu, Photocatalytic activity enhanced by plasmonic resonant energy transfer from metal to semiconductor, J. Am. Chem. Soc. **134**, 15033 (2012).

[94] J. Li, S. K. Cushing, F. Meng, T. R. Senty, A. D. Bristow, and N. Wu, Plasmon-induced resonance energy transfer for solar energy conversion, Nat. Photonics **9**, 601 (2015).

[95] K. L. Kelly, E. Coronado, L. L. Zhao, and G. C. Schatz, The Optical properties of metal nanoparticles: the influence of size, shape, and dielectric environment, J. Phys. Chem. B **107**, 668 (2003).

[96] D. Paramelle, A. Sadovoy, S. Gorelik, P. Free, J. Hobleya, and D. G. Fernig, A rapid method to estimate the concentration of citrate capped silver nanoparticles from UV-visible light spectra, Analyst **139**, 4855 (2014).

[97] A. Derkachova, K. Kolwas, and I. Demchenko, Dielectric function for gold in plasmonics applications: size dependence of plasmon resonance frequencies and damping rates for nanospheres, Plasmonics **11**, 941 (2016).

[98] P. K. Jain, K. S. Lee, I. H. El-Sayed, and M. A. El-Sayed, Calculated absorption and scattering properties of gold nanoparticles of different size, shape, and composition: applications in biological imaging and biomedicine, J. Phys. Chem. B **110**, 7238 (2006).

[99] L. Driencourt and B. Gallinet, Design guidelines for enhanced activity of water splitting photoelectrodes with plasmonic nanoparticles, J. Phys. Chem. C **126**, 1701 (2022).

[100] L. Zhang, L. O. Herrmann, and J. J. Baumberg, Size dependent plasmonic effect on $BiVO_4$ photoanodes for solar water splitting, Sci. Rep. **5**, 16660 (2015).

[101] D. B. Ingram, and S. Linic, Water splitting on composite plasmonic-metal/semiconductor photoelectrodes: evidence for selective plasmon-induced formation of charge carriers near the semiconductor surface, J. Am. Chem. Soc. **133**, 5202 (2011).

[102] Z. Liu, W. Hou, P. Pavaskar, M. Aykol, and S. B. Cronin, Plasmon resonant enhancement of photocatalytic water splitting under visible illumination, Nano Lett. **11**, 1111 (2011).

[103] M. Valenti, E. Kontoleta, I. A. Digdaya, M. P. Jonsson, G. Biskos, A. Schmidt-Ott and W. A. Smith, The role of size and dimerization of decorating plasmonic silver nanoparticles on the photoelectrochemical solar water splitting performance of $BiVO_4$ photoanodes, ChemNanoMat **2**, 739 (2016).

[104] D. Derkacs, S. H. Lim, P. Matheu, W. Mar, and E. T. Yu, Improved performance of amorphous silicon solar cells via scattering from surface plasmon polaritons in nearby metallic nanoparticles, Appl. Phys. Lett. **89**, 093103 (2006).

[105] P. Peerakiatkhajohn, T. Butburee, J.-H. Yun, H. Chen, R. M. Richards and L. Wang, A hybrid photoelectrode with plasmonic $Au@TiO_2$ nanoparticles for enhanced photoelectrochemical water splitting, J. Mater. Chem. A **3**, 20127 (2015).

[106] Y. Shiraishi, N. Yasumoto , J. Imai , H. Sakamoto , S. Tanaka , S. Ichikawa , B. Ohtani, and T. Hirai, Quantum tunneling injection of hot electrons in Au/TiO_2 plasmonic photocatalysts, Nanoscale, **9**, 8349 (2017).

[107] C. Jia, X. Li, N. Xin, Y. Gong, J. Guan, L. Meng, S. Meng, and X. Guo, Interface-engineered plasmonics in metal/semiconductor heterostructures, Adv. Energy Mater. **6**, 1600431 (2016).

[108] S. Y. Moon, H. C. Song, E. H. Gwag, I. I. Nedrygailov, C. Lee, J. J. Kim, W. H. Doh and J. Y. Park, Plasmonic hot carrier-driven oxygen evolution reaction on Au nanoparticles/TiO_2 nanotube arrays, Nanoscale **10**, 22180 (2018).

[109] D. C. Ratchford, A. D. Dunkelberger, I. Vurgaftman, J. C. Owrutsky, and P. E. Pehrsson, Quantification of efficient plasmonic hot-electron injection in gold nanoparticle–TiO_2 Films, Nano Lett. **17**, 6047 (2017).

[110] J. W. Ha, T. P. A. Ruberu, R. Han, B. Dong, J. Vela, and N. Fang, Super-resolution mapping of photogenerated electron and hole separation in single metal–semiconductor nanocatalysts, J. Am. Chem. Soc. **136**, 1398 (2014).

[111] X. Yu, A. Shavel, X. An, Z. Luo, M. Ibanez, and A. Cabot, Cu_2ZnSnS_4-Pt and Cu_2ZnSnS_4-Au heterostructured nanoparticles for photocatalytic water splitting and pollutant degradation, J. Am. Chem. Soc. **136**, 9236 (2014).

[112] S. K. Dutta, S. K. Mehetor, and N. Pradhan, Metal semiconductor heterostructures for photocatalytic conversion of light energy, J. Phys. Chem. Lett. **6**, 936 (2015).

[113] M. Zhou, H. B. Wu, J. Bao, L. Liang, X. W. Lou, Y. Xie, Ordered Macroporous $BiVO_4$ architectures with controllable dual porosity for efficient solar water splitting, Angew. Chem. Int. Ed. **52**, 8579 (2013).

[114] M. Zho, J. Bao, Y Xu, J. Zhang, J. Xie, M. Guan, C. Wang, L. Wen, Y. Lei, and Y. Xie, Photoelectrodes based upon Mo:$BiVO_4$ inverse opals for photoelectrochemical water splitting, ACS Nano **8**, 7088 (2014).

[115] L. W. Zhang, C. Y. Lin, V. K. Valev, E. Reisner, U. Steiner, and J. J. Baumberg, Plasmonic enhancement in $BiVO_4$ photonic crystals for efficient water splitting, Small **10**, 3970 (2014).

[116] Y.X. Liu, H.X. Dai, J.G. Deng, L. Zhang, and C.T. Au, Three-dimensional ordered macroporous bismuth vanadates: PMMA-templating fabrication and excellent visible light-driven photocatalytic performance for phenol degradation, Nanoscale **4**, 2317 (2012).

[117] K. Ji, H. Dai, J. Deng, H. Zang, H. Arandiyan, S. Xie, and H. Yang, 3DOM BiVO4 supported silver bromide and noble metals: High-performance photocatalysts for the visible-light-driven degradation of 4-chlorophenol, Appl. Catal. B: Environ. **168-169**, 274 (2015).

[118] L. Fang, F. Nan, Y. Yang, and D. Cao, Enhanced photoelectrochemical and photocatalytic activity in visible-light-driven Ag/$BiVO_4$ inverse opals, Appl. Phys. Lett. **108**, 093902 (2016).

[119] F. Nan, Z. Kang, J. Wang, M. Shen, and L. Fang, Carbon quantum dots coated $BiVO_4$ inverse opals for enhanced photoelectrochemical hydrogen generation, Appl. Phys. Lett. **106**, 153901 (2015).

[120] M. Zalfani, B. Van Der Schueren, Z.Y. Hu, J. Rooke, R. Bourguiga, M. Wu, Y. Li, G. Van Tendeloo, and B.L. Su, Novel 3DOM $BiVO_4/TiO_2$ nanocomposites for highly enhanced photocatalytic activity, J. Mater. Chem. A **3**, 21244 (2015).

[121] M. Zalfani, Z.-Y. Hu, W.-B. Yu, M. Mahdouani, R. Bourguiga, M. Wu, Y. Li, G. Van Tendeloo, Y. Djaoued, B.-L. Su, $BiVO_4$/3DOM TiO_2 nanocomposites: Effect of $BiVO_4$ as highly efficient visible light sensitizer for highly improved visible light photocatalytic activity in the degradation of dye pollutants, Appl. Catal. B: Environ. **205**, 121 (2017).

[122] H. Zhang, and C. Cheng, Three-Dimensional FTO/TiO_2/$BiVO_4$ composite inverse opals photoanode with excellent photoelectrochemical performance ACS Energy Lett. **2**, 813 (2017).

[123] H. F. Zhang, W. W. Zhou, Y. P. Yang, and C. W. Cheng, 3D WO_3/$BiVO_4$/cobalt phosphate composites inverse opal photoanode for efficient photoelectrochemical water splitting, Small **13**, 1603840 (2017).

[124] H. Wu, R. Irani, K. Zhang, L. Jing, H. Dai, H. Y.Chung, F. F. Abdi, and Y. H. Ng, Unveiling carrier dynamics in periodic porous $BiVO_4$ photocatalyst for enhanced solar water splitting, ACS Energy Lett. **6**, 3400 (2021).

[125] S. Kohtani, K. Yoshida, T. Maekawa, A. Iwase, A. Kudo, H. Miyabe, and R. Nakagaki, Loading effects of silver oxides upon generation of reactive oxygen species in semiconductor photocatalysis, Phys. Chem. Chem. Phys. **10**, 2986 (2008).

[126] N.C. Castillo, L. Ding, A. Heel, T. Graule, and C. Pulgarin, On the photocatalytic degradation of phenol and dichloroacetate by $BiVO_4$: The need of a sacrificial electron acceptor, J. Photochem. Photobiol. A Chem. **216**, 221 (2010).

[127] T. Saison, N. Chemin, C. Chanéac, O. Durupthy, L. Mariey, F. Maugé, V. Brezová, and J.-P. Jolivet, New insights into $BiVO_4$ properties as visible light photocatalyst, J. Phys. Chem. C **119**, 12967 (2015).

[128] O.F. Lopes, K.T.G. Carvalho, G.K. Macedo, V.R. de Mendonça, W. Avansi, and C. Ribeiro. Synthesis of $BiVO_4$ via oxidant peroxo-method: insights into the photocatalytic performance and degradation mechanism of pollutants, New J. Chem. **39**, 6231 (2015).

[129] J. Sun, X. Li, Q. Zhao, M.O. Tadé, and S. Liu, Quantum-sized $BiVO_4$ modified TiO_2 microflower composite heterostructures: Efficient production of hydroxyl radicals towards visible light-driven degradation of gaseous toluene, J. Mater. Chem. A **3**, 21655 (2015).

[130] K. Zhu, W. Wang, B. Zhang, X. Chen, D. Ma, X. Wang, R. Zhang, Y. Liu, P. Dong, and X. Xi, Interface engineering of a 2D/2D $BiVO_4$/$Bi_4V_2O_{10}$ heterostructure with improved photocatalytic photoredox activity, Langmuir **38**, 7558 (2022).

[131] A. Malathi, J. Madhavan, M. Ashokkumar, and P. Arunachalam, A review on $BiVO_4$ photocatalyst: activity enhancement methods for solar photocatalytic applications, Appl. Catal. A **555**, 47 (2018).

[132] B. O. Orimolade and O. A. Arotiba, Bismuth vanadate in photoelectrocatalytic water treatment systems for the degradation of organics: a review on recent trends, J. Electroanal Chem. **878**, 114724 (2020).

[133] K. Ordon, V. I. Merupo, S. Coste, O. Noel, N. Errien, M. Makowska-Janusik, and A. Kassiba, Charge-transfer peculiarities in mesoporous $BiVO_4$ surfaces with anchored indoline dyes, Appl. Nanosci. **8**, 1895 (2018).

[134] M. Pylarinou, E. Sakellis, P. Tsipas, G. Em. Romanos, S. Gardelis, A. Dimoulas and V. Likodimos, Mo-$BiVO_4$/Ca-$BiVO_4$ Homojunction nanostructure-based inverse opals for photoelectrocatalytic pharmaceutical degradation under visible light, ACS Appl. Nano Mater. **6**, 6759 (2023).

[135] M. Pylarinou, E. Sakellis, P. Tsipas, S. Gardelis, V. Psycharis, A. Dimoulas, T. Stergiopoulos, and V. Likodimos, Light concentration and electron transfer in plasmonic–photonic Ag,Au modified Mo-$BiVO_4$ inverse opal photoelectrocatalysts, Nanoscale **16**, 10366 (2024).

[136] M. Antoniadou, P. Bouras, N. Strataki, and P. Lianos, Hydrogen and electricity generation by photoelectrochemical decomposition of ethanol over nanocrystalline titania, Int. J. of Hydrogen Energy **33**, 5045 (2008).

[137] S. Ito, P. Chen, P. Comte, M. K. Nazeeruddin, P. Liska, P. Pechy, and M. Grätzel, Fabrication of screen-printing pastes from TiO_2 powders for dye-sensitised solar cells, Progress in Photovoltaics **15**, 603 (2007).

[138] B.J. Inkson, *2 - Scanning electron microscopy (SEM) and transmission electron microscopy (TEM) for materials characterization*, in Materials characterization using nondestructive evaluation (NDE) methods (Woodhead Publishing, 2016).

[139] N. W. Ashcroft and N. D. Mermin, *Solid State Physics* (Saunders College Publishing, Philadelphia, 1976).

[140] J. R. Ferraro, K. Nakamoto and C. W. Brown, *Introductory Raman Spectroscopy* (Second edition), (Elsevier Science, 2003).

[141] https://www.renishaw.com/en/what-is-raman-scattering--25805.

[142] P. R. Griffiths and J. A. De Haseth, *Fourier Transform Infrared Spectrometry* (John Wiley & Sons, 2007).

[143] T. Owen, *Fundamentals of Modern UV-visible Spectroscopy* (Agilent Technologies, 2000).

[144] P. Kubelka and F. Munk, Ein beitrag zur optik der farbanstriche, Z. Techn. Phys. **12**, 593 (1931).

[145] H. G. Hecht, The interpretation of diffuse reflectance spectra, J. Res. Natl. Bur. Stand. A Phys. Chem. **80A**, 567 (1976).

[146] S. Landi Jr, I.R. Segundo, E. Freitas, M. Vasilevskiy, J. Carneiro, and C.J. Tavares, Use and misuse of the Kubelka-Munk function to obtain the band gap energy from diffuse reflectance measurements, Solid State Commun. **341**, 114573 (2022).

[147] F. A. Stevie and C. L. Donley, Introduction to X-ray photoelectron spectroscopy, J. Vac. Sci. Technol. A **38**, 063204 (2020).

[148] https://grimmgroup.net/research/xps/background/

[149] Y. Hermans, S. Murcia-Lopez, A. Klein, R. van de Krol, T. Andreu, J. R. Morante, T. Toupance, and W. Jaegermann, Analysis of the interfacial characteristics of

$BiVO_4$/metal oxide heterostructures and its implication on their junction properties, Phys. Chem. Chem. Phys. **21**, 5086 (2019).

[150] K. Ozawa, *Ultraviolet photoelectron spectroscopy, Compendium of Surface and Interface Analysis,* (Springer, Singapore, 2018).

[151] N. Stamatis and I. Konstantinou, Occurrence and removal of emerging pharmaceutical, personal care compounds and caffeine tracer in municipal sewage treatment plant in Western Greece, J. Environ. Sci. Health B **48**, 800 (2013).

[152] E. Evgenidou, I. Konstantinou and D. Lambropoulou, Occurrence and removal of transformation products of PPCPs and illicit drugs in wastewaters: A review, Sci. Total Environ. **505**, 905 (2015).

[153] I. K. Konstantinou and T. A. Albanis, TiO_2-assisted photocatalytic degradation of azo dyes in aqueous solution: kinetic and mechanistic investigations: a review, Appl. Catal. B: Environ. **49**, 1 (2004).

[154] Z. Chen, H. N. Dinh, and E. Miller, *Photoelectrochemical Water Splitting*: *Standards Experimental Methods, and Protocols,* (Springer, New York, 2013).

[155] A. R. C. Bredar, A. L. Chown, A. R. Burton, and B. H. Farnum, Electrochemical Impedance Spectroscopy of Metal Oxide Electrodes for Energy Applications, ACS Appl. Energy Mater. **3**, 66 (2020).

[156] J. Bisquert, *Nanostructured Energy Devices: Equilibrium Concepts and Kinetics* (CRC Press, Boca Raton, 2014).

[157] A. Hankin, F. E. Bedoya-Lora, J. C. Alexander, A. Regoutz and G. H. Kelsall, Flat band potential determination: avoiding the pitfalls, J. Mater. Chem. A **7**, 26162 (2019).

[158] M. Patel, R. Kumar, K. Kishor, T. Mlsna, C. U. Pittman, and D. Mohan, Pharmaceuticals of emerging concern in aquatic systems: chemistry, occurrence, effects, and removal methods, Chem. Rev. **119**, 3510 (2019).

[159] S. Wu, and Y. H. Hu, A comprehensive review on catalysts for electrocatalytic and photoelectrocatalytic degradation of antibiotics, Chem. Eng. J. **409**, 127739 (2021).

[160] J.-y. Lin, Y. Zhang, Y. Bian, Y.-x. Zhang, R.-z. Du, M. Li, Y. Tan and X.-s. Feng, Non-steroidal anti-inflammatory drugs (NSAIDs) in the environment: Recent updates on the occurrence, fate, hazards and removal technologies, Sci. Total Environ. **904**, 166897 (2023).

[161] F. D. Hardcastle, I. E. Wachs, H. Eckert, and D. A. Jefferson, Vanadium(V) Environments in Bismuth Vanadates: A Structural investigation using Raman spectroscopy and solid state ^{51}V NMR, J. Solid State Chem. **90**, 194 (1991).

[162] J. Pellicer-Porres, D. Vázquez-Socorro, S. López-Moreno, A. Muñoz, P. Rodríguez-Hernández, D. Martínez-García, S. N. Achary, A. J. E. Rettie, and C. Buddie Mullins, Phase transition systematics in $BiVO_4$ by means of high-pressure–high-temperature Raman experiments, Phys. Rev. B **98**, 214109 (2018).

[163] A. Minato, Z. Pan, K. Katayama, and W. Yong Sohn, Enhancement of photoelectrochemical performance of bismuth vanadate ($BiVO_4$)-based photoanode by building phase-junction configurations, J. Photochem. Photobiol. A **434**, 114252 (2023).

[164] T. S. Dabodiya, P. Selvarasu, and A.V. Murugan, Tetragonal to monoclinic crystalline phases change of $BiVO_4$ via microwave-hydrothermal reaction: in correlation with visible-light-driven photocatalytic performance, Inorg. Chem. **58**, 5096 (2019).

[165] D. Zhou, L.-X.Pang, J. Guo, H. Wang, X. Yao, and C. Randall, Phase evolution, phase transition, Raman spectra, infrared spectra, and microwave dielectric properties of low temperature firing $(K_{0.5x}Bi_{1\ -0.5x})(Mo_xV_{1-x})O_4$ ceramics with scheelite related structure, Inorg. Chem. **50**, 12733 (2011).

[166] F. D. Hardcastle, and I. E. Wachs, Determination of vanadium-oxygen bond distances and bond orders by Raman spectroscopy, J. Phys. Chem. **95**, 5031 (1991).

[167] K. R. Phillips, T. Shirman, E. Shirman, A. V. Shneidman, T. M. Kay, and J. Aizenberg, Nanocrystalline precursors for the co-assembly of crack-free metal oxide inverse opals, Adv. Mater. **30**, 1706329 (2018).

[168] A. Diamantopoulou, E. Sakellis, G. E. Romanos, S. Gardelis, N. Ioannidis, N. Boukos, P. Falaras, and V. Likodimos, Titania photonic crystal photocatalysts functionalized by graphene oxide nanocolloids, Appl. Catal. B Environ. **240**, 277 (2019).

[169] T. L. Madanu, S. R. Mouchet, O. Deparis, J. Liu, Y. Li, and B.-L. Su, Tuning and transferring slow photons from TiO_2 photonic crystals to $BiVO_4$ nanoparticles for unprecedented visible light photocatalysis, J. Colloid Interface Sci. **634**, 290 (2023).

[170] R. L. Frost, D. A. Henry, M. L. Weier, and W. Martens, Raman spectroscopy of three polymorphs of $BiVO_4$: Clinobisvanite, dreyerite and pucherite, with comparisons to $(VO_4)_3$ – bearing minerals: namibite, pottsite and schumacherite, J. Raman Spectrosc. **37**, 722 (2006).

[171] Y. Hermans, A. Klein, K. Ellmer, R. van de Krol, T. Toupance, and W. Jaegermann, Energy-band alignment of $BiVO_4$ from photoelectron spectroscopy of solid-state interfaces, J. Phys. Chem. C **122,** 20861 (2018).

[172] J.F. Moulder, W.F. Stickle, P.E. Sobol, and K.D. Bomben, K. *Handbook of X-Ray Photoelectron Spectroscopy*, (Perkin-Elmer Corporation, Physical Electronics Division, Eden Prairie, Minnesota 55344, United States of America, 1992).

[173] W. Shi, M. Li, X. Huang, H. Ren, F. Guo, Y. Tang, and C. Lu, Construction of $CuBi_2O_4/Bi_2MoO_6$ p-n heterojunction with nanosheets-on-microrods structure for improved photocatalytic activity towards broad-spectrum antibiotics degradation, Chem. Eng. J. **394**, 125009 (2020).

[174] B.O. Orimolade and O. A. Arotiba, Enhanced photoelectrocatalytic degradation of diclofenac sodium using a system of Ag-$BiVO_4$/BiOI anode and Ag-BiOI cathode, Sci. Rep. **12**, 4214 (2022).

[175] M. Pylarinou, A. Toumazatou, E. Sakellis, E. Xenogiannopoulou, S. Gardelis, N. Boukos, A. Dimoulas, and V. Likodimos, Visible light trapping against charge recombination in FeO_x–TiO_2 photonic crystal photocatalysts, Materials **14**, 7117 (2021).

[176] Q. Zeng, J. Li, L. Li, J. Bai, L. Xia, and B. Zhou, Synthesis of WO_3/$BiVO_4$ photoanode using a reaction of bismuth nitrate with peroxovanadate on wo_3 film for efficient photoelectrocatalytic water splitting and organic pollutant degradation, Appl. Catal. B: Environ. **217**, 21 (2017).

[177] L. Xia, J. Li, J. Bai, L. Li, Q. Zeng, Q. Xu, and B. Zhou, Preparation of a $BiVO_4$ nanoporous photoanode based on peroxovanadate reduction and conversion for efficient photoelectrochemical performance, Nanoscale **10**, 2848 (2018).

[178] J. Feng, L. Cheng, J. Zhang, O. K. Okoth, and F. Chen, Preparation of $BiVO_4$/ZnO composite film with enhanced visible-light photoelectrocatalytic activity, Ceram. Int. **44**, 3672 (2018).

[179] J. Liu, J. Li, Y. Li, J. Guo, S.-M. Xu, R. Zhang, and M. Shao, Photoelectrochemical water splitting coupled with degradation of organic pollutants enhanced by surface and interface engineering of $BiVO_4$ photoanode, Appl. Catal. B: Environ. **278**, 119268 (2020).

[180] Y. Guo, W. Han, K. Zhao, S. Hao, S. Shi, and Y. Ding, Promoting effects of Y doping and FeOOH loading for efficient photoelectrochemical activity on $BiVO_4$ electrodes, New J. Chem. **46**, 13178 (2022).

[181] S. Kahng, and J. H. Kim, Heterojunction photoanode of SnO_2 and Mo-doped $BiVO_4$ for boosting photoelectrochemical performance and tetracycline hydrochloride degradation, Chemosphere **291**, 132800 (2022).

[182] S. Cong, J. Yu, B. Liu, W. Teng, and Y. Tang, Preparing a dual-function $BiVO_4$/NiFe-LDH Composite photoanode for enhanced photoelectrocatalytic wastewater treatment and simultaneous hydrogen evolution, New J. Chem. **46**, 15227 (2022).

[183] B. O. Orimolade, B. A. Koiki, G. M. Peleyeju, and O. A. Arotiba, Visible light driven photoelectrocatalysis on a FTO/$BiVO_4$/BiOI anode for water treatment involving emerging pharmaceutical pollutants, Electrochim. Acta **307**, 285 (2019).

[184] B. O. Orimolade, B. N. Zwane, B. A. Koiki, L. Tshwenya, G. M. Peleyeju, N. Mabuba, M. Zhou, and O. A Arotiba, Solar photoelectrocatalytic degradation of ciprofloxacin at a FTO/$BiVO_4$/MnO_2 anode: kinetics, intermediate products and degradation pathway studies, J. Environ. Chem. Eng. **8**, 103607 (2020).

[185] J.E. Carrera-Crespo, I. Fuentes-Camargo, R.E. Palma-Goyes, U.M. García-Pérez, J. Vazquez-Arenas, I. Chairez, and T. Poznyak, Unrevealing the effect of transparent fluorine-doped tin oxide (FTO) Substrate and irradiance configuration to unmask the activity of FTO-$BiVO_4$ heterojunction, Mat. Sci. Semicon. Proc. **128**, 105717 (2021).

[186] Q. Pan, K. Yang, G. Wang, D. Li, J. Sun, B. Yang, Z. Zou, W. Hu, K. Wen, and H. Yang, $BiVO_4$ nanocrystals with controllable oxygen vacancies induced by Zn-doping

coupled with graphene quantum dots for enhanced photoelectrochemical water splitting, Chem. Eng. J. **372**, 399 (2019).

[187] I. Abdellaoui, M. M. Islam, M. Remeika, Y. Higuchi, T. Kawaguchi, T. Harada, C. Budich, T. Maeda, T. Wada, S. Ikeda, and T. Sakurai, Photocarrier recombination dynamics in $BiVO_4$ for visible light–driven water oxidation, J. Phys. Chem. C **124**, 3962 (2020).

[188] J. Ginter and I. Piwoński, Evaluation of the synergistic effect between slow photons and electron trapping on the photocatalytic properties of TiO_2 photonic crystals, Matter. Res. Bull. **107**, 100 (2018).

[189] T. G. U. Ghobadi, A. Ghobadi, M. C. Soydan, M. B. Vishlaghi, S. Kaya, F. Karadas, and E. Ozbay, Strong light–matter interactions in Au plasmonic nanoantennas coupled with prussian blue catalyst on $BiVO_4$ for photoelectrochemical water splitting, ChemSusChem **13**, 2577 (2020).

[190] N. Stefanou and A. Modinos, Optical properties of thin discontinuous metal films, J. Phys.: Condens. Matter. **3**, 8149 (1991).

[191] X. Zhang, Y. Ma, L. Xi, G. Zhu, X. Li, D. Shi, and J. Fan, Highly efficient photocatalytic removal of multiple refractory organic pollutants by $BiVO_4/CH_3COO(BiO)$ heterostructured nanocomposite, Sci. Total Environ. **647**, 245 (2019).

[192] M. Jiménez-Salcedo, M. Monge, and M. T. Tena, Combination of Au-Ag plasmonic nanoparticles of varied compositions with carbon nitride for enhanced photocatalytic degradation of ibuprofen under visible light, Materials **14**, 3912 (2021).

[193] L. M. Otto, E. A. Gaulding, C. T. Chen, T. R. Kuykendall, A. T. Hammack, F. M. Toma, D. F. Ogletree, S. Aloni, B. J. H. Stadler, and A. M. Schwartzberg, Methods for tuning plasmonic and photonic optical resonances in high surface area porous electrodes, Sci. Rep. **11**, 7656 (2021).

[194] H. N. Q. Tran, K. N. Tran, S. Gunenthiran, J. Wang, C. S. Law, S. Y. Lim, Y. C. G. Lim, A. D. Abell, L. F. Marsal, and A. Santos, Tailoring Tamm plasmon resonances in dielectric nanoporous photonic crystals, ACS Appl. Mater. Interfaces **16**, 11787 (2024).

[195] L. Zhang, E. Reisner, and J. J. Baumberg, Al-doped ZnO inverse opal networks as efficient electron collectors in $BiVO_4$ photoanodes for solar water oxidation, Energy Environ. Sci. **7**, 1402 (2014).

[196] Y. Liang, T. Tsubota, L. P. A. Mooij, and R. van de Krol, Highly improved quantum efficiencies for thin film $BiVO_4$ photoanodes, J. Phys. Chem. C **115**, 17594 (2011).

[197] Z. Zhang and J. T. Yates Jr, Band bending in semiconductors: chemical and physical consequences at surfaces and interfaces, Chem. Rev. **112**, 5520 (2012).

[198] A. Meng, L. Zhang, B. Cheng, and J. Yu, Dual cocatalysts in TiO_2 photocatalysis, Adv. Mater. 31, 1807660 (2019).

[199] Y. Taga, Z. Pan, K. Katayama, and W. Y. Sohn, $BiVO_4$ - Dotted WO_3 photoanode with an inverse opal underlayer for photoelectrochemical water splitting, ACS Appl. Energy Mater. **5**, 5750 (2022).

[200] M. Ma, J. K. Kim, K. Zhang, X. Shi, S. J. Kim, J. H. Moon, and J. H. Park, Double-deck inverse opal photoanodes: efficient light absorption and charge separation in heterojunction, Chem. Mater. **26**, 5592 (2014).

[201] T. L. Madanu, L. Chaabane, S. R. Mouchet, O. Deparis, and B.-L. Su, Manipulating multi-spectral slow photons in bilayer inverse opal TiO_2@$BiVO_4$ composites for highly enhanced visible light photocatalysis, J. Colloid Interface Sci. **647**, 233 (2023).

[202] M. Al Rammal, K. Akkaoui, and L. I. Halaoui, Multijunction photoanode of Mo:$BiVO_4$ layered with TiO_2 inverse opal and NiB_i oxygen evolution catalyst to trap light and enhance water splitting, J. Phys. Chem. C **126**, 6960 (2022).

[203] V. Likodimos, T. Stergiopoulos, P. Falaras, J. Kunze, and P. Schmuki, Phase composition, size, orientation and antenna effects of self-assembled anodized titania nanotube arrays: a polarized micro-Raman investigation, J. Phys. Chem. C **112**, 12687 (2008).

[204] D. Papadakis, A. Diamantopoulou, P. A. Pantazopoulos, D. Palles, E. Sakellis, N. Boukos, N. Stefanou, and V. Likodimos, Nanographene oxide-TiO_2 photonic films as plasmon-free substrates for surface-enhanced Raman scattering, Nanoscale **11**, 21542 (2019).

[205] H-R. Buser, T. Poiger, and M. D. Müller, Occurrence and environmental behavior of the chiral pharmaceutical drug ibuprofen in surface waters and in wastewater, Environ. Sci. Technol. **33**, 2529 (1999).

[206] N. C. Huynh, T. T. T. Nguyen, D. T. C. Nguyen, and T. V. Tran, Occurrence, toxicity, impact and removal of selected non-steroidal anti-inflammatory drugs (NSAIDs): A review, Sci. Total Environ. **898**, 165317 (2023).

[207] J. Choina, H. Kosslick, C. Fischer, G.-U. Flechsig, L. Frunza, and A. Schulz, Photocatalytic decomposition of pharmaceutical ibuprofen pollutions in water over titania catalyst, Appl. Catal. B Environ. **129**, 589 (2013).

[208] M. O. Miranda, W. E. C. Cavalcanti, F. F. Barbosa, J. A. de Sousa, F. I. da Silva, S. B. C. Pergher, and T. P. Braga, Photocatalytic degradation of ibuprofen using titanium oxide: insights into the mechanism and preferential attack of radicals, RSC Adv. **11**, 27720 (2021).

[209] T. M. Khedr, S. M. El-Sheikh, A. Hakki, A. A. Ismail, W. A. Badawy, and D. W. Bahnemann, Highly active non-metals doped mixed-phase TiO_2 for photocatalytic oxidation of ibuprofen under visible light, J. Photochem. Photobiol. A Chem. **346**, 530 (2017).